DAMAGE PROGRESSION IN COMPOSITE BOLTED JOINTS

A thesis submitted in fulfilment of the requirements for the degree of Master of Engineering

Maajid Chishti

B. Eng (Aero) (Hon I) RMIT

School of Aerospace, Mechanical & Manufacturing Engineering

Science, Engineering and Health Portfolio

RMIT University

February, 2011

DECLARATION

I certify that except where due acknowledgement has been made, the work is that of the author alone; the work has not been submitted previously, in whole or in part, to qualify for any other academic award; the content of the thesis is the result of work which has been carried out since the official commencement date of the approved research program; any editorial work, paid or unpaid, carried out by a third party is acknowledged; and, ethics procedures and guidelines have been followed.

_____

Maajid Chishti

ACKNOWLEDGEMENTS

I would like to acknowledge relentless guidance and support of my First supervisor Dr Adrian Orifici (RMIT), Second supervisor Prof. Chun Wang (RMIT) and Consultant Dr Rodney Thomson of Cooperative Research Centre for Advanced Composite Structures (CRC-ACS) without which it would be impossible to complete this project. I would also like to thank A/Prof. Javid Bayandor my initial supervisor for making me understand the importance of postgraduate studies and his initial support. I would like to give special thanks to Prof. Adrian Mourtiz and Dr Adrian Orifici for supporting me through the difficult time of changing project direction and guidance.

I would also like to thank Prof. Nicholas Mileshkin, A/Prof. Lachlan Thomson, Dr Stefanie Feih, Dr Caleb White, Dr Ferry Dharmawan, and Mr David Elder (CRC-ACS) for helping in various aspects of the project. The technical expertise of Mr Peter Tkatchyk, Mr. Robert Ryan, Mr Patrick Wilkins and Mr Daniel Bitton (CRC-ACS) helped me greatly in conducting my experimental work. The administrative support of Mrs Lina Bubic, Ms Melissa Sigismondo and Ms Sandy Bowers is also greatly acknowledged.

I would also like to thank my friends and fellow post graduate students (Sawan Shah, Minki Kim, Minoo Rathnasabapathy, Andrew Litchfield, Anthony Zammit, PongPat Thavornpattanapong, I Gusti Agung Aditya Jaya, Harun Chowdhary, Sunny Lok Hin Chan, Loren Yeo, Paul Norman Simon, Heng-Yi Chou (Ken), Emrira Abdullah, Sridhar Ravi) who were there for me in good times and bad. I am greatly indebted to my friends Mr Malinda Wijesinghe, Mr Siddharth Dhingra, Ms Wendy Ng, Mr Suhaib Mohammad Ali, Mr Sanidhaya Tak and Mr Tejpal Firoda for their continuous emotional and professional support. I would like to make special mention of my good friend *Late Mr Ashish Miranda* (Boeing Australia) with whom I did my undergraduate and who also acted as an industry advisor for my work.

The financial support provided by Australian Postgraduate Award is also greatly acknowledged. Additional support for material procurement was provided by CRC-ACS. The high powered computing facilities provided by RMIT-HPC and Victorian Partnership for Advanced Computing is also greatly acknowledged.

I owe everything I have been able to achieve to parents, Capt. Ghulam Chishti and Mrs Farhat Chishti. They have always motivated me to be a better person. I would like to specially acknowledge the role of my friend and guide, my elder brother Mr Faaiz Chishti, who has always supported me since I came to Australia. I also like to thank my siblings Miss Farheen Chishti, Miss Zaineb Chishti and Abdul Rafai for their continuous support and love. Most importantly I would like to thank God for giving me this opportunity and helping me in being successful.

ABSTRACT

Despite the many advantages of adhesive bonding, bolted joints are still used to fasten composite aircraft structures because of the ease of assembly/disassembly, minimal surface preparations, use of common tools between metal and composite structures and airworthiness certification. Joining or repairing external aircraft structures inevitably involves the use of countersunk fasteners, which can induce complex three-dimensional stress fields near the bolt hole. Since bolted joints incur significant penalty of low strength compared to pristine composite laminates, it is important to understand the damage mechanisms and develop design tools to enable better design and optimisation of composite joints so as to take full advantage of composite structures.

This investigation focuses on single lap joints using countersunk fasteners, using both experimental testing and computational simulation techniques. Joints were tested in shear to failure at a range of bolt torques, hole clearances and countersunk depths to thickness ratio levels. To assist the development of predictive tools, straight-shank bearing tests were carried out to calibrate model parameters. Detailed microscopy analysis of failed specimens was conducted to characterise the through-thickness failure profile of countersunk bolted joints. Detailed finite element analyses using Abaqus/Explicit were conducted to gain insight into the behaviour of the single lap joints. The models accounted for in-plane and through-thickness composite damage, frictional contact, bolt torque and secondary bending effects in bolted joints under shear.

The experimental investigation and finite element analyses showed that the through-thickness damage contained mainly interlaminar and intralaminar shear cracks and delamination. The variations in selected parameters had marginal effects on ultimate failure load of the joints; however the bearing load was significantly affected. The variation in bolt-hole clearance and countersunk depth to thickness ratio can produce significant variation in the through-thickness damage profile. As the countersunk depth to thickness ratio increased, the damage to the bearing plane of the joint increased. Catastrophic bending failure occurred for the highest ratio of countersunk depth to thickness. The finite element investigation showed that stress concentration factor at the hole edge increases with hole clearance. A detailed analysis of initiation and progression of damage, in the plane and through the thickness of the laminate has been performed. A review of the literature indicates that the detailed investigation of damage mechanisms and joint

parameters presented in this thesis appears to be the first for joints involving countersunk fasteners.

The present research also highlights a new method for determining the fracture energy associated with composite compression failure. The issues associated with the use of literature in determining material properties, friction coefficient and other modelling parameters are identified and discussed. The implications of capturing the overall effect of damage modes without a true mechanistic representation are also discussed. These new findings demonstrate that whilst capturing the overall behaviour and effect of joint parameters is possible, reliable predictive capability such as that required for aerospace design purposes remains a critical aspect for ongoing research.

TABLE OF CONTENTS

DECLARATION ..... **I**
ACKNOWLEDGEMENTS ..... **II**
ABSTRACT ..... **IV**
TABLE OF CONTENTS ..... **VI**
LIST OF FIGURES ..... **VIII**
LIST OF TABLES ..... **XII**
NOMENCLATURE ..... **XIII**
1 INTRODUCTION **1**
1.1 BACKGROUND 1
1.2 OBJECTIVE 5
1.3 METHODOLOGY 5
1.4 THESIS ORGANISATION 5
1.5 OUTCOMES 6
2 LITERATURE REVIEW **7**
2.1 COMPOSITE JOINTS 7
2.1.1 Joint failure *7*
2.1.2 Effects of countersunk *12*
2.1.3 Effects of bolt torque *15*
2.1.4 Effects of clearance *18*
2.2 FAILURE CRITERIA 22
2.2.1 Point stress failure criteria *22*
2.2.2 Maximum stress criterion *24*
2.2.3 Hashin failure criteria *25*
2.3 DAMAGE PROGRESSION 27
2.4 COHESIVE ZONE MODELLING 27
2.5 CONCLUSION 29
3 EXPERIMENT METHODS **31**
3.1 TESTING PREPARATIONS 31
3.2 TEST SETUP 33
3.3 MICROSCOPY 36
3.4 CONCLUSION 38
4 EXPERIMENT RESULTS **39**
4.1 BEARING TEST 39
4.2 EFFECTS OF BOLT TORQUE 45
4.3 EFFECTS OF CLEARANCE 57
4.4 EFFECTS OF COUNTERSUNK DEPTH TO THICKNESS RATIO 69
4.5 CONCLUSION 79
5 NUMERICAL ANALYSIS METHODOLOGY **81**
5.1 SOLVER 81
5.2 ELEMENT TYPE 81
5.3 COMPOSITE FAILURE MODEL 84
5.4 MATERIAL PROPERTIES 85
5.5 COHESIVE MODELLING 92
5.6 CONTACT 94
5.6.1 Friction *95*
5.7 BOLT TORQUE 96
5.8 MESH DENSITY 97
5.9 MASS SCALING 102
5.10 HOURGLASS CONTROL 104
5.11 MAXIMUM DAMAGE INDEX 104

5.12 BOUNDARY CONDITIONS 105
5.13 CONCLUSION 105

6 NUMERICAL ANALYSIS RESULTS 106

6.1 EXPERIMENTAL COMPARISON 106
6.2 EFFECT OF COUNTERSUNK 113
6.3 EFFECTS OF CLEARANCE 116
6.3.1 Conclusion 121
6.4 EFFECTS OF COUNTERSUNK DEPTH TO THICKNESS RATIO 122
6.4.1 Conclusion 129
6.5 EFFECTS OF BOLT TORQUE 129
6.5.1 Conclusion 132
6.6 MODELS WITH COHESIVE ELEMENTS 133
6.7 CONCLUSIONS 135

7 DISCUSSION 137

7.1 MATERIAL PROPERTIES 137
7.2 MODELLING PARAMETERS 137
7.3 DAMAGE MODELLING 138
7.4 FAILURE ENERGIES 138
7.5 DELAMINATION 139
7.6 EARLY TERMINATION 140

8 CONCLUSIONS AND RECOMMENDATIONS 141

8.1 CONCLUSIONS 141
8.2 FUTURE WORK 142

REFERENCES 144

APPENDIX I. 153

APPENDIX II. 166

LIST OF FIGURES

FIGURE 1-1 STRUCTURAL DESIGN PROCEDURE, (IREMAN 1998) 2
FIGURE 1-2 CENTRE WING BOX AND OUTER WING BOX ATTACHMENT FOR WIDE BODY AIRCRAFT, (ROSKAM, 1986) 2
FIGURE 1-3 FASTENED ATTACHMENTS, (ROSKAM, 1986, BRUHN, 1973 AND FLABEL 1997) 3
FIGURE 1-4 STRUCTURAL EFFICIENCY OF VARIOUS JOINT TYPES, (NELSON ET AL. 1981) 4
FIGURE 1-5 STRAIGHT SHANK AND COUNTERSUNK LAMINATE 5
FIGURE 2-1 TYPES OF MECHANICAL JOINTS 7
FIGURE 2-2 FAILURE MODES OF COMPOSITE MECHANICALLY FASTENED JOINTS, (HART-SMITH 1978) 8
FIGURE 2-3 LOADS ACTING ON A PLATE, (EKH ET AL. 2006) 9
FIGURE 2-4 DAMAGED SECTION ALONG THE 0^{O} CUTTING PLANE, (IREMAN ET AL. 2000) 10
FIGURE 2-5 DETAILED MICROGRAPHS OF FAILURE MODES, (KELLY ET AL. 2004) 11
FIGURE 2-6 EFFECT OF COUNTERSUNK ANGLE ON "K" FOR A WIDE PLATE, (BHARGAVA ET AL. 2007) 13
FIGURE 2-7 EFFECT OF HT RATIO ON K FOR A WIDE PLATE (T/R=1), (BHARGAVA ET AL. 2007) 13
FIGURE 2-8 CONTACT STRESS DISTRIBUTION FOR PROTRUDING HEAD LAMINATE, (IREMAN 1998) 14
FIGURE 2-9 CONTACT STRESS DISTRIBUTION FOR CSK LAMINATE, (IREMAN 1998) 14
FIGURE 2-10 LOAD TRANSFER CURVES FOR TORQUE SET BOLTS, (STARIKOV ET AL. 2001) 15
FIGURE 2-11 FAILURE IN BEARING CUTTING PLANE FOR BOLT-HOLE 2, (STARIKOV ET AL. 2001) 15
FIGURE 2-12 VARIATION OF FAILURE LOAD WITH BOLT CLAMPING LOAD, (STOCKDALE ET AL. 1976) 17
FIGURE 2-13 FAILURE LOAD VARIATION, (COOPER ET AL. 1995) 18
FIGURE 2-14 CONTACT ANGLE FOR BOLT-HOLE LOADING, (KELLY ET AL. 2004) 19
FIGURE 2-15 RADIAL STRESS DISTRIBUTION FOR ZERO DOMINATED LAYUP, (MCCARTHY ET AL. 2005) 20
FIGURE 2-16 EFFECT OF BOLT-HOLE CLEARANCE ON PIN-LOADED LAMINATES, (KELLY ET AL. 2004) 21
FIGURE 2-17 EFFECT OF BOLT-HOLE CLEARANCE ON CLAMPED LAMINATES, (KELLY ET AL. 2004) 21
FIGURE 2-18 CHARACTERISTIC CURVE FOR PIN-LOADED COMPOSITE, (WHITWORTH ET AL. 2003) 23
FIGURE 2-19 BEARING STRENGTH COMPARISON, (WHITWORTH ET AL. 2003) 24
FIGURE 3-1 SINGLE LAP JOINT GEOMETRY 32
FIGURE 3-2 FILLED HOLE SPECIMEN DIMENSIONS (MM) 33
FIGURE 3-3 ASSEMBLED SINGLE LAP JOINT 34
FIGURE 3-4 MODIFIED EXTENSOMETER 34
FIGURE 3-5 EXPERIMENTAL SETUP FOR BEARING TEST 35
FIGURE 3-6 EXTENSOMETER ATTACHMENT FOR BEARING TEST 35
FIGURE 3-7 SINGLE LAP TEST SET UP 36
FIGURE 3-8 EXTENSOMETER ATTACHMENT AND STRAIN GAUGES FOR SINGLE LAP JOINT 36
FIGURE 3-9 SECTIONS FOR POST PROCESSING 37
FIGURE 3-10 INSPECTED REGIONS OF SINGLE LAP SPECIMENS 37
FIGURE 3-11 UNDAMAGED LAMINATES 38
FIGURE 4-1 LOAD-DISPLACEMENT CURVE OF SPECIMEN 1 UNDER BEARING 40
FIGURE 4-2 LOAD-DISPLACEMENT CURVES FOR BEARING TEST 41
FIGURE 4-3 STRAIN DATA FOR SPECIMEN LOADED UP TO THE LINEAR LOAD 41
FIGURE 4-4 STRAIN DATA FOR BEARING TEST 42
FIGURE 4-5 DAMAGED EDGE FOR SPECIMEN LOADED UP TO LINEAR LOAD 43
FIGURE 4-6 DAMAGED EDGE FOR SPECIMEN LOADED UP TO ULTIMATE LOAD 44
FIGURE 4-7 LOAD-DISPLACEMENT BEHAVIOUR FOR JOINTS WITH 0 NM TORQUE 45
FIGURE 4-8 LOAD-DISPLACEMENT BEHAVIOUR FOR JOINTS WITH 2.103 NM TORQUE 45
FIGURE 4-9 LOAD-DISPLACEMENT BEHAVIOUR FOR JOINTS WITH 4.206 NM TORQUE 46
FIGURE 4-10 EFFECTS OF VARIATION OF BOLT TORQUE 47
FIGURE 4-11 EFFECT OF BOLT TORQUE ON ULTIMATE FAILURE LOAD 48
FIGURE 4-12 EFFECT OF BOLT TORQUE ON BEARING LOAD 48
FIGURE 4-13 DAMAGED UPPER LAMINATE AT 0^{O} SECTION FOR JOINTS WITH 0 NM BOLT TORQUE 50
FIGURE 4-14 DAMAGED UPPER LAMINATE AT 0^{O} SECTION FOR JOINTS WITH 2.103 NM BOLT TORQUE 51
FIGURE 4-15 DAMAGED UPPER LAMINATE AT 0^{O} SECTION FOR JOINTS WITH 4.206 NM BOLT TORQUE 52
FIGURE 4-16 DAMAGED UPPER LAMINATE AT 45^{O} SECTION FOR JOINTS WITH 4.206 NM BOLT TORQUE 52
FIGURE 4-17 DAMAGED LOWER LAMINATE AT 0^{O} SECTION FOR JOINTS WITH 2.103 NM BOLT TORQUE 53
FIGURE 4-18 DAMAGED LOWER LAMINATE AT 0^{O} SECTION FOR JOINTS WITH 4.206 NM BOLT TORQUE 54
FIGURE 4-19 DAMAGED LOWER LAMINATES AT 45^{O} SECTION 55
FIGURE 4-20 EFFECTS OF BOLT TORQUE ON THE DAMAGE PROFILE OF UPPER AND LOWER LAMINATES AT 0^{O} 56
FIGURE 4-21 CLEARANCE FOR COUNTERSUNK JOINT 57
FIGURE 4-22 LOAD-DISPLACEMENT BEHAVIOUR FOR JOINTS WITH 220 MM CLEARANCE 58
FIGURE 4-23 LOAD-DISPLACEMENT BEHAVIOUR FOR JOINTS WITH 440 MM CLEARANCE 59

FIGURE 4-24 CHANGE IN STIFFNESS DURING INITIAL LOADING 61
FIGURE 4-25 EFFECT OF VARIATION OF CLEARANCE 61
FIGURE 4-26 EFFECTS OF CLEARANCE ON THE ULTIMATE FAILURE LOAD 62
FIGURE 4-27 EFFECTS OF CLEARANCE ON BEARING LOAD 62
FIGURE 4-28 DAMAGED UPPER LAMINATE AT 0^O SECTION FOR JOINTS WITH 220 MM CLEARANCE 64
FIGURE 4-29 DAMAGED UPPER LAMINATE AT 0^O SECTION FOR JOINTS WITH 440 MM CLEARANCE 65
FIGURE 4-30 BEARING DAMAGE (CIRCLED) IN CLEARANCE LAMINATES AFTER TESTING 65
FIGURE 4-31 LOADING SEQUENCE DUE TO CLEARANCE 65
FIGURE 4-32 DAMAGED UPPER LAMINATE AT 45^O SECTION FOR JOINTS WITH 220 MM CLEARANCE 67
FIGURE 4-33 DAMAGED LOWER LAMINATE AT 0^O SECTION FOR JOINTS WITH 220 MM CLEARANCE 67
FIGURE 4-34 DAMAGED LOWER LAMINATE AT 0^O SECTION FOR JOINTS WITH 440 MM CLEARANCE 68
FIGURE 4-35 DAMAGED LOWER LAMINATE AT 45^O SECTION 68
FIGURE 4-36 EFFECTS OF CLEARANCE ON THE DAMAGE PROFILE OF UPPER AND LOWER LAMINATES AT 0^O 68
FIGURE 4-37 LOAD-DISPLACEMENT BEHAVIOUR FOR JOINTS WITH COUNTERSUNK DEPTH TO THICKNESS RATIO OF 0.64 70
FIGURE 4-38 LOAD-DISPLACEMENT BEHAVIOUR FOR JOINTS WITH COUNTERSUNK DEPTH TO THICKNESS RATIO OF 0.76 71
FIGURE 4-39 EFFECTS OF VARIATION OF COUNTERSUNK DEPTH TO THICKNESS RATIO 72
FIGURE 4-40 EFFECTS OF COUNTERSUNK DEPTH TO THICKNESS RATIO ON ULTIMATE FAILURE STRESS 73
FIGURE 4-41 EFFECTS OF COUNTERSUNK DEPTH TO THICKNESS RATIO ON BEARING STRESS 73
FIGURE 4-42 UNDAMAGED UPPER LAMINATES 74
FIGURE 4-43 DAMAGED UPPER LAMINATE AT 0^O SECTION FOR JOINTS WITH COUNTERSUNK DEPTH TO THICKNESS RATIO OF 0.64 75
FIGURE 4-44 DAMAGED UPPER LAMINATE AT 0^O SECTION FOR JOINTS WITH COUNTERSUNK DEPTH TO THICKNESS RATIO OF 0.76 76
FIGURE 4-45 TOP VIEW OF BENDING FAILURE IN UPPER LAMINATE FOR JOINTS WITH COUNTERSUNK DEPTH TO THICKNESS RATIO OF 0.76 76
FIGURE 4-46 DAMAGED LOWER LAMINATE AT 0^O SECTION FOR JOINTS WITH COUNTERSUNK DEPTH TO THICKNESS RATIO OF 0.76 77
FIGURE 4-47 DAMAGED LOWER LAMINATE AT 45^O SECTION 78
FIGURE 4-48 EFFECTS OF COUNTERSUNK DEPTH TO THICKNESS RATIO ON THE DAMAGE PROFILE OF UPPER AND LOWER LAMINATE AT 0^O 78
FIGURE 5-1 MODELLING APPROACHES FOR COMPOSITE LAMINATE 82
FIGURE 5-2 VARIATION OF INITIAL PROPERTIES 88
FIGURE 5-3 STRESS-DISPLACEMENT RELATION FOR HASHIN FAILURE CRITERIA, (ABAQUS USER MANUAL 2010) 91
FIGURE 5-4 LOAD-DISPLACEMENT CURVES FOR DIFFERENT FIBRE FAILURE FRACTURE TOUGHNESS VALUES 91
FIGURE 5-5 TRACTION-SEPARATION LAW FOR COHESIVE ELEMENTS, (ABAQUS USER MANUAL 2010) 92
FIGURE 5-6 CONTACT REGION FOR BEARING MODEL, (CHISHTI ET AL. 2010) 95
FIGURE 5-7 CONTACT REGION FOR SINGLE LAP MODEL, (CHISHTI ET AL. 2010) 95
FIGURE 5-8 STEPS TO APPLY BOLT TORQUE 97
FIGURE 5-9 DIFFERENT IN-PLANE MESH DENSITY REGIONS FOR BEARING AND SINGLE LAP JOINT LAMINATE 98
FIGURE 5-10 DIFFERENT MESH DENSITIES FOR BEARING AND SINGLE LAP JOINT LAMINATE 99
FIGURE 5-11 MESH DENSITY CLOSE TO THE HOLE (D1) 99
FIGURE 5-12 NUMBER OF ELEMENTS FOR MESH DENSITY M2 100
FIGURE 5-13 EFFECT OF THROUGH-THICKNESS MESH DENSITY ON CL3 JOINT 100
FIGURE 5-14 ISOMETRIC VIEW OF BOLT AND NUT MESH 100
FIGURE 5-15 NUMBER OF ELEMENTS FOR BOLT AND NUT 101
FIGURE 5-16 BEARING MODEL 101
FIGURE 5-17 SINGLE LAP MODEL 101
FIGURE 5-18 EFFECTS OF VARIATION OF MS FACTOR ON INTERNAL ENERGY 103
FIGURE 5-19 EFFECTS OF VARIATION OF MS FACTOR ON KINETIC ENERGY 103
FIGURE 5-20 VARIATION OF MAXIMUM DAMAGE INDEX 104
FIGURE 5-21 BEARING TEST BOUNDARY CONDITIONS 105
FIGURE 5-22 SINGLE LAP JOINT BOUNDARY CONDITIONS 105
FIGURE 6-1 LOAD-DISPLACEMENT RESULT FOR JOINT WITH 2.103 NM BOLT TORQUE 107
FIGURE 6-2 LOAD-DISPLACEMENT RESULTS OF BEARING JOINT 108
FIGURE 6-3 LOAD-DISPLACEMENT RESULT FOR JOINT WITH 220 MM CLEARANCE 109
FIGURE 6-4 LOAD-DISPLACEMENT RESULT FOR JOINT WITH COUNTERSUNK DEPTH TO THICKNESS RATIO OF 0.64 109
FIGURE 6-5 SCALE FOR DAMAGE PLOTS 110
FIGURE 6-6 DAMAGE AT 45^O CUTTING PLANE AT FIRST NON-LINEAR LOAD (SEE FIGURE 6-5 FOR DAMAGE SCALE) 111
FIGURE 6-7 DAMAGED AT 0^O CUTTING PLANE AT FIRST NON-LINEAR LOAD (SEE FIGURE 6-5 FOR DAMAGE SCALE) 111
FIGURE 6-8 FIBRE COMPRESSIVE DAMAGE IN UPPER LAMINATE OF JOINT WITH 0 NM BOLT TORQUE AT 0^O CUTTING PLANE (SEE FIGURE 6-5 FOR DAMAGE SCALE) 112

FIGURE 6-9 FIBRE COMPRESSIVE DAMAGE IN LOWER LAMINATE OF JOINT WITH 0 NM BOLT TORQUE AT 0^O CUTTING PLANE (SEE FIGURE 6-5 FOR DAMAGE SCALE) 112
FIGURE 6-10 ENERGY VARIATION FOR JOINT WITH 0 NM BOLT TORQUE 113
FIGURE 6-11 LAYERS USED FOR STRESS CONCENTRATION FACTOR DISTRIBUTION 114
FIGURE 6-12 EFFECT OF COUNTERSUNK ON RADIAL STRESS CONCENTRATION FACTOR IN UPPER LAMINATE AT ~1.5 KN 114
FIGURE 6-13 DISTRIBUTION OF Σ_{33} (MPA) IN THE COUNTERSUNK LAMINATE 115
FIGURE 6-14 DISTRIBUTION OF Σ_{13} (MPA) IN THE COUNTERSUNK LAMINATE 115
FIGURE 6-15 DAMAGE PROGRESSION AT SELECTED PLY LOCATIONS IN BEARING AND SINGLE LAP JOINT 116
FIGURE 6-16 DAMAGE PROGRESSION FOR UPPER LAMINATE OF JOINT WITH 0 NM BOLT TORQUE (SEE FIGURE 6-5 FOR DAMAGE SCALE) 116
FIGURE 6-17 EFFECTS OF VARIATION OF CLEARANCE 117
FIGURE 6-18 EFFECTS OF CLEARANCE ON FULLY DEVELOPED CONTACT AREA 117
FIGURE 6-19 EFFECT OF CLEARANCE ON RADIAL STRESS CONCENTRATION FACTOR AT SHEAR PLANE (0^O PLY) IN UPPER LAMINATES AT ~1.5 KN 118
FIGURE 6-20 EFFECT OF CLEARANCE ON THROUGH-THICKNESS FIBRE COMPRESSIVE DAMAGE PROGRESSION AT THE HOLE EDGE 119
FIGURE 6-21 EFFECT OF CLEARANCE ON THROUGH-THICKNESS FIBRE COMPRESSIVE DAMAGE AT BEARING LOAD AT 0^O CUTTING PLANE (SEE FIGURE 6-5 FOR DAMAGE SCALE) 120
FIGURE 6-22 EFFECT OF CLEARANCE ON THROUGH-THICKNESS FIBRE COMPRESSIVE DAMAGE AT 2 MM AT 0^O CUTTING PLANE (SEE FIGURE 6-5 FOR DAMAGE SCALE) 120
FIGURE 6-23 EFFECT OF CLEARANCE ON FIBRE COMPRESSIVE DAMAGE AT 2 MM IN 0^O PLIES (SEE FIGURE 6-5 FOR DAMAGE SCALE) 121
FIGURE 6-24 EFFECT OF VARIATION OF CLEARANCE 122
FIGURE 6-25 THROUGH-THICKNESS DISPLACEMENT OF VARIOUS JOINTS AT 2 MM DISPLACEMENT 123
FIGURE 6-26 FIBRE TENSILE FAILURE PROGRESSION IN THE BOTTOM PLY OF THE UPPER LAMINATE AT THE NET SECTION PLANE 124
FIGURE 6-27 EFFECT OF COUNTERSUNK DEPTH TO THICKNESS RATIO ON RADIAL STRESS CONCENTRATION FACTOR AT SHEAR PLANE (0^O PLY) IN UPPER LAMINATES AT ~1.5 KN 125
FIGURE 6-28 EFFECT OF COUNTERSUNK DEPTH TO THICKNESS RATIO ON THROUGH-THICKNESS FIBRE COMPRESSIVE DAMAGE PROGRESSION 126
FIGURE 6-29 EFFECT OF COUNTERSUNK DEPTH TO THICKNESS RATIO ON THROUGH-THICKNESS FIBRE COMPRESSIVE DAMAGE AT BEARING LOAD AT 0^O CUTTING PLANE (SEE FIGURE 6-5 FOR DAMAGE SCALE) 127
FIGURE 6-30 EFFECT OF COUNTERSUNK DEPTH TO THICKNESS RATIO ON THROUGH-THICKNESS FIBRE COMPRESSIVE DAMAGE AT 2 MM AT 0^O CUTTING PLANE (SEE FIGURE 6-5 FOR DAMAGE SCALE) 127
FIGURE 6-31 EFFECT OF COUNTERSUNK DEPTH TO THICKNESS RATIO ON FIBRE COMPRESSIVE DAMAGE AT 2 MM IN 0^O PLIES (SEE FIGURE 6-5 FOR DAMAGE SCALE) 128
FIGURE 6-32 EFFECTS OF VARIATION OF BOLT TORQUE 129
FIGURE 6-33 EFFECTS OF BOLT TORQUE ON FIBRE COMPRESSIVE DAMAGE PROGRESSION AT THE HOLE EDGE IN 0^O DIRECTION 130
FIGURE 6-34 EFFECTS OF BOLT TORQUE ON THROUGH-THICKNESS FIBRE COMPRESSIVE DAMAGE AT 2 MM AT 0^O CUTTING PLANE (SEE FIGURE 6-5 FOR DAMAGE SCALE) 131
FIGURE 6-35 EFFECTS OF BOLT TORQUE ON THROUGH-THICKNESS FIBRE COMPRESSIVE DAMAGE AT ULTIMATE FAILURE LOAD AT 0^O CUTTING PLANE (SEE FIGURE 6-5 FOR DAMAGE SCALE) 131
FIGURE 6-36 EFFECTS OF BOLT TORQUE ON FIBRE COMPRESSIVE DAMAGE AT 2 MM IN 0^O PLIES (SEE FIGURE 6-5 FOR DAMAGE SCALE) 132
FIGURE 6-37 LOAD-DISPLACEMENT BEHAVIOUR OF JOINT WITH 0 NM BOLT TORQUE 134
FIGURE 6-38 FIBRE COMPRESSIVE DAMAGE IN STRAIGHT SHANK REGION JUST BEFORE SIGNIFICANT LOAD DROP 134
FIGURE 6-39 DELAMINATION AND DAMAGE INDEX FOR FINITE ELEMENT MODEL WITH DELAMINATION 135
FIGURE I - 1 FILLED HOLE SPECIMEN DIMENSIONS (MM) 155
FIGURE I - 2 SINGLE LAP JOINT GEOMETRY 156
FIGURE I - 3 BOLT AND NUT GEOMETRY 156
FIGURE I - 4 STRAIN GAUGE NUMBERING AND EXTENSOMETER TAB LOCATION (MM) 156
FIGURE I - 5 DETAILED LAYOUT OF A PANEL 158
FIGURE I - 6 PANEL CUTTING PLAN 158
FIGURE I - 7 DEBULKING OF THE LAMINATE 160
FIGURE I - 8 VACUUM BAGGING (BASSO 2006) 160
FIGURE I - 9 AUTOCLAVE CURING CYCLE (BASSO 2006) 160
FIGURE I - 10 DRILLING RIG (TOP VIEW) 161
FIGURE I - 11 EFFECT OF OVER SIZING ON CSK TOOL 162
FIGURE I - 12 UNTREATED OVER SIZED EDGE COMPARISON 162
FIGURE I - 13 TREATED OVER SIZED EDGE COMPARISON 163
FIGURE I - 14 EDGE SANDING 163

FIGURE I - 15 CONVENTIONAL TORQUE WRENCH 164
FIGURE I - 16 MODIFIED TORQUE WRENCH 164
FIGURE I - 17 ATTACHMENTS FOR DIFFERENT BOLT/NUT ASSEMBLIES 164
FIGURE I - 18 TORQUE WRENCH CALIBRATION DEVICE 165
FIGURE II- 1 LAYERS USED TO PLOT STRESS CONCENTRATION FACTOR DISTRIBUTION 166
FIGURE II- 2 RADIAL STRESS CONCENTRATION FACTOR IN SHEAR PLANE OF BT1 JOINT AT ~1.5 KN 166
FIGURE II- 3 TANGENTIAL STRESS CONCENTRATION FACTOR IN SHEAR PLANE OF BT1 JOINT AT ~1.5 KN 167
FIGURE II- 4 RADIAL STRESS CONCENTRATION FACTOR AT START OF CSK OF BT1 JOINT AT ~1.5 KN 167
FIGURE II- 5 TANGENTIAL STRESS CONCENTRATION FACTOR AT START OF CSK OF BT1 JOINT AT ~1.5 KN 168
FIGURE II- 6 RADIAL STRESS CONCENTRATION FACTOR IN SHEAR PLANE OF BT2 JOINT AT ~1.5 KN 168
FIGURE II- 7 TANGENTIAL STRESS CONCENTRATION FACTOR IN SHEAR PLANE OF BT2 JOINT AT ~1.5 KN 169
FIGURE II- 8 RADIAL STRESS CONCENTRATION FACTOR AT START OF CSK OF BT2 JOINT AT ~1.5 KN 169
FIGURE II- 9 TANGENTIAL STRESS CONCENTRATION FACTOR AT START OF CSK OF BT2 JOINT AT ~1.5 KN 170
FIGURE II- 10 RADIAL STRESS CONCENTRATION FACTOR IN SHEAR PLANE OF BT3 JOINT AT ~1.5 KN 170
FIGURE II- 11 TANGENTIAL STRESS CONCENTRATION FACTOR IN SHEAR PLANE OF BT3 JOINT AT ~1.5 KN 171
FIGURE II- 12 RADIAL STRESS CONCENTRATION FACTOR AT START OF CSK OF BT3 JOINT AT ~1.5 KN 171
FIGURE II- 13 TANGENTIAL STRESS CONCENTRATION FACTOR AT START OF CSK OF BT3 JOINT AT ~1.5 KN 172
FIGURE II- 14 RADIAL STRESS CONCENTRATION FACTOR IN SHEAR PLANE OF CL2 JOINT AT ~1.5 KN 172
FIGURE II- 15 TANGENTIAL STRESS CONCENTRATION FACTOR IN SHEAR PLANE OF CL2 JOINT AT ~1.5 KN 173
FIGURE II- 16 RADIAL STRESS CONCENTRATION FACTOR AT THE START OF CSK OF CL2 JOINT AT ~1.5 KN 173
FIGURE II- 17 TANGENTIAL STRESS CONCENTRATION FACTOR AT THE START OF CSK OF CL2 JOINT AT ~1.5 KN 174
FIGURE II- 18 RADIAL STRESS CONCENTRATION FACTOR IN SHEAR PLANE OF CL3 JOINT AT ~1.5 KN 174
FIGURE II- 19 TANGENTIAL STRESS CONCENTRATION FACTOR IN SHEAR PLANE OF CL3 JOINT AT ~1.5 KN 175
FIGURE II- 20 RADIAL STRESS CONCENTRATION FACTOR AT THE START OF CSK OF CL3 JOINT AT ~1.5 KN 175
FIGURE II- 21 TANGENTIAL STRESS CONCENTRATION FACTOR AT THE START OF CSK OF CL3 JOINT AT ~1.5 KN 176
FIGURE II- 22 RADIAL STRESS CONCENTRATION FACTOR IN SHEAR PLANE OF HT1 JOINT AT ~1.5 KN 176
FIGURE II- 23 TANGENTIAL STRESS CONCENTRATION FACTOR IN SHEAR PLANE OF HT1 JOINT AT ~1.5 KN 177
FIGURE II- 24 RADIAL STRESS CONCENTRATION FACTOR AT THE START OF CSK OF HT1 JOINT AT ~1.5 KN 177
FIGURE II- 25 TANGENTIAL STRESS CONCENTRATION FACTOR AT THE START OF CSK OF HT1 JOINT AT ~1.5 KN 178
FIGURE II- 26 RADIAL STRESS CONCENTRATION FACTOR IN SHEAR PLANE OF HT3 JOINT AT ~1.5 KN 178
FIGURE II- 27 TANGENTIAL STRESS CONCENTRATION FACTOR IN SHEAR PLANE OF HT3 JOINT AT ~1.5 KN 179
FIGURE II- 28 RADIAL STRESS CONCENTRATION FACTOR AT THE START OF CSK OF HT3 JOINT AT ~1.5 KN 179
FIGURE II- 29 TANGENTIAL STRESS CONCENTRATION FACTOR AT THE START OF CSK OF HT3 JOINT AT ~1.5 KN 180
FIGURE II- 30 RADIAL STRESS CONCENTRATION FACTOR IN SHEAR PLANE OF HT3FE JOINT AT ~1.5 KN 180
FIGURE II- 31 TANGENTIAL STRESS CONCENTRATION FACTOR IN SHEAR PLANE OF HT3FE JOINT AT ~1.5 KN 181
FIGURE II- 32 RADIAL STRESS CONCENTRATION FACTOR AT THE START OF CSK OF HT3FE JOINT AT ~1.5 KN 181
FIGURE II- 33 TANGENTIAL STRESS CONCENTRATION FACTOR AT THE START OF CSK OF HT3FE JOINT AT ~1.5 KN 182

LIST OF TABLES

TABLE 1-1 CONTROL SYSTEM LOADS (AIAA, 2003) 3
TABLE 2-1 BEARING FAILURE GEOMETRIC RESTRICTIONS 8
TABLE 3-1 SPECIMEN DETAILS 32
TABLE 3-2 DIMENSIONS OF SINGLE LAP JOINT (MM) 32
TABLE 4-1 BEARING TEST RESULTS 40
TABLE 4-2 SUMMARY OF BOLT TORQUE RESULTS 48
TABLE 4-3 SUMMARY OF CLEARANCE RESULTS 61
TABLE 4-4 COMPARISON OF COUNTERSUNK DEPTH TO THICKNESS RATIO 73
TABLE 5-1 ELEMENT SELECTION TABLE 84
TABLE 5-2 FIBRE AND MATRIX PROPERTIES 86
TABLE 5-3 CALCULATED INITIAL MATERIAL PROPERTIES OF UD PLIES 87
TABLE 5-4 MATERIAL PROPERTIES OF UD PLIES 89
TABLE 5-5 IN-PLANE FAILURE FRACTURE TOUGHNESS VALUES 91
TABLE 5-6 BOLT TORQUE DISPLACEMENT 97
TABLE 5-7 MESH DENSITY COMPARISON TABLE 99
TABLE 5-8 MASS SCALING COMPARISON 103
TABLE 6-1 EXPERIMENT AND FE COMPARISON 107
TABLE I - 1 DIMENSIONS OF SINGLE LAP JOINT (MM) 155
TABLE I - 2 BOLT DIMENSIONS (MM) 155
TABLE I - 3 NUT DIMENSIONS (MM) 155
TABLE I - 4 TEST MATRIX 157
TABLE I - 5 TORQUE CALIBRATION TABLE 165

NOMENCLATURE

Abbreviation	Definition
3D	Three-dimensional
ALLAE	Artificial strain energy or Hourglass energy
ALLIE	Internal energy
ALLKE	Kinetic energy
ALLMW	Work done due to Mass scaling
ALLVD	Viscous damping energy
BC	Boundary condition
BT	Bolt torque
CC	Compact compression
CCT	Centre cracked tension
CL	Bolt-hole clearance
CLT	Classical Laminate Theory
CNC	Centre notched compression
CPT	Classical Plate Theory
CSK	Countersunk
CT	Bearing test/Compact tension
CZM	Cohesive Zone Modelling
DENT	Double edge notched tension
ENF	End notch flexural
FC	Fibre compressive failure
FD	Failure displacement
FE	Finite Element
FEM	Finite element modelling
FL	Specimen loaded to failure
FNL	First non-linearity load
FT	Fibre tensile failure
Gc	Critical strain energy release rate
HT	Countersunk depth to thickness ratio
LL	Specimen loaded to first non-linear load
MC	Matrix compressive failure
MD	Maximum damage parameter
MS	Mass scaling
MT	Matrix tensile failure
OL	Overlap length
PFA	Progressive failure analysis
SG	Strain gauge
SLB	Strain gauge location on bottom laminate

SLT	Strain gauge location on the top laminate
Treated edge	Sanded edge after over-sizing to provide smooth hole edge
UD	Unidirectional
UFL	Ultimate failure load
UFS	Ultimate failure stress
VCCT	Virtual Crack Closure Technique

Term	**Definition**
σ	Stress
X, S	Strength
τ	Interfacial strength
ν	Poisson ratio
V	Volume fraction
$\overline{\tau^0}$	Modified interfacial strength
N_e^0	Number of elements in the cohesive zone
l_e	Length of the element in the delamination direction
p	Thread pitch
ρ	Density
F_i	Bolt Preload
K	Torque coefficient
A	Bolt cross sectional area
d	Diameter of the hole
D	Bolt diameter
e	Edge distance
E	Young's modulus
G	Shear modulus
L	Specimen length
m	Friction coefficient in nut and bolt
t	Thickness of the laminate
w	Width of the specimen
θ	Rotation angle of the disc

Subscript	**Definition**
1,2,3	Ply coordinate system, fibre, matrix and through-thickness direction
t, T	Tensile property and thread coefficient for friction
c, C	Compressive property and collar coefficient for friction
f	Fibre
m	Matrix

1 INTRODUCTION

1.1 Background

The aerospace industry has one of the highest safety requirements in operations while being economically efficient in today's world. In order to build safe aerospace structures, safe-life and damage tolerance concepts need to be considered in design. In the safe-life concept, a structure is designed to have a minimum life during which it is predicted that no catastrophic failure will occur. The damage-tolerant structure must withstand damage and subsequently, all expected stresses until a flaw is detected at a regular scheduled maintenance. Generally, it is more economical to design some parts of the structure to be damage tolerant than to have long safe life, since such structures can be lighter. The use of composite materials in the aerospace industry has seen a steady rise in the past decade. Fibre reinforced composites are an attractive alternative to aluminium and other metals because of their low density, high strength, high stiffness and capability to tailor their design according to the load path. These advantages can provide weight saving and improved design for advanced aerospace structures. However, the advantages would be lost if the structure was not designed using optimal design methodologies. The damage tolerant approach used to design composite structures can realise the advantages discussed earlier.

An aircraft structure is an assembly of different parts (skin, spar, stiffener etc.) joined together to define a load transmission path. The structural design procedure is explained pictographically in Figure 1-1. The initial step requires the determination of load distribution in the joint. Then, the local stress distribution around the fastener is determined. Finally, the strength is predicted using an appropriate approach. The degree of detailed modelling is determined by the significance of the structure. For critical joints it is preferred to carry out a three-dimensional (3D) analysis of the isolated region. Joints can be classified as mechanically fastened (bolted or riveted), adhesively bonded (polymeric adhesive) and hybrid (fasteners and adhesive) joints. Advantages such as ease of assembly/disassembly, simple joint configuration, ease of inspection and through-thickness reinforcement are the reasons that mechanical fastening remains the primary means of joining composite components in modern aircraft structures (Padhi et al. 2002). The single-lap configuration is more representative than the double-lap configuration of the most critical aircraft bolted joint applications (MIL-HDBK-17 2002). Single-lap joints

result in significant stress concentrations in the thickness direction and lower bearing strengths.

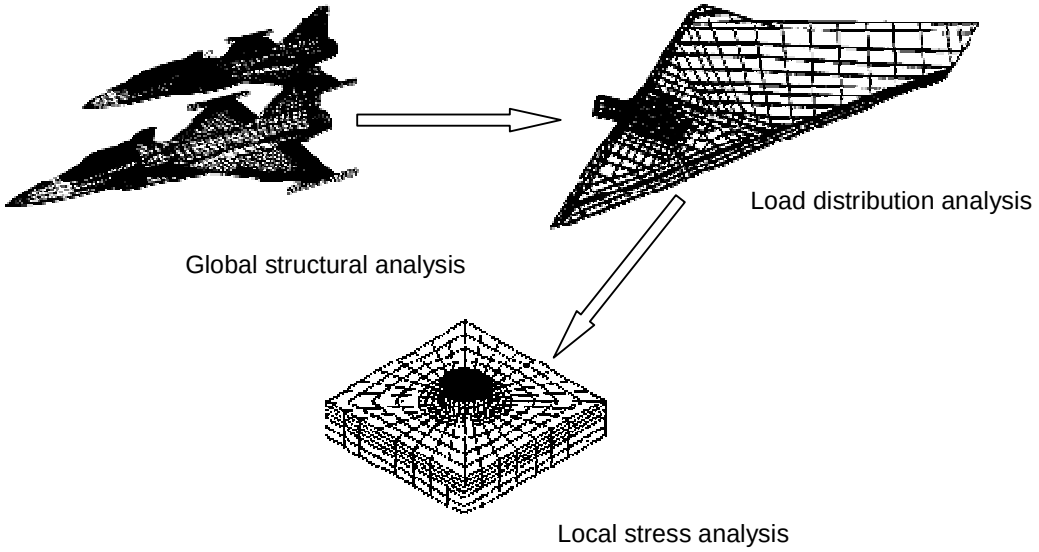

Figure 1-1 Structural design procedure, (Ireman 1998)

Fastened joints can be seen in several locations in an aircraft. Figure 1-2 shows a section of the heavily loaded centre wing box (CWB) and outer wing box (OWB) attachment for a wide body aircraft. The fastened joints and connections can also be found in several other locations such as control surface attachments, engine fittings, skin-stringer attachment, tail assembly etc. as shown in Figure 1-3. A summary of control system loads is provided in Table 1-1 (AIAA, 2003).

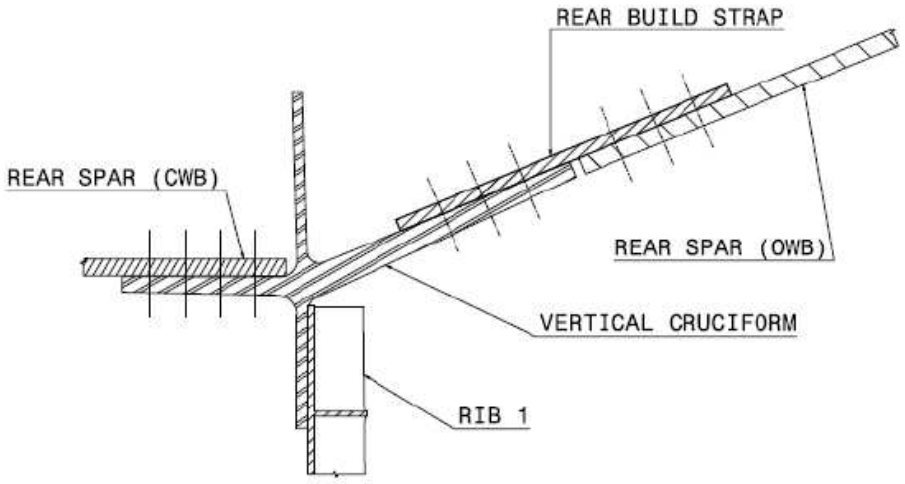

Figure 1-2 Centre wing box and outer wing box attachment for wide body aircraft, (Roskam, 1986)

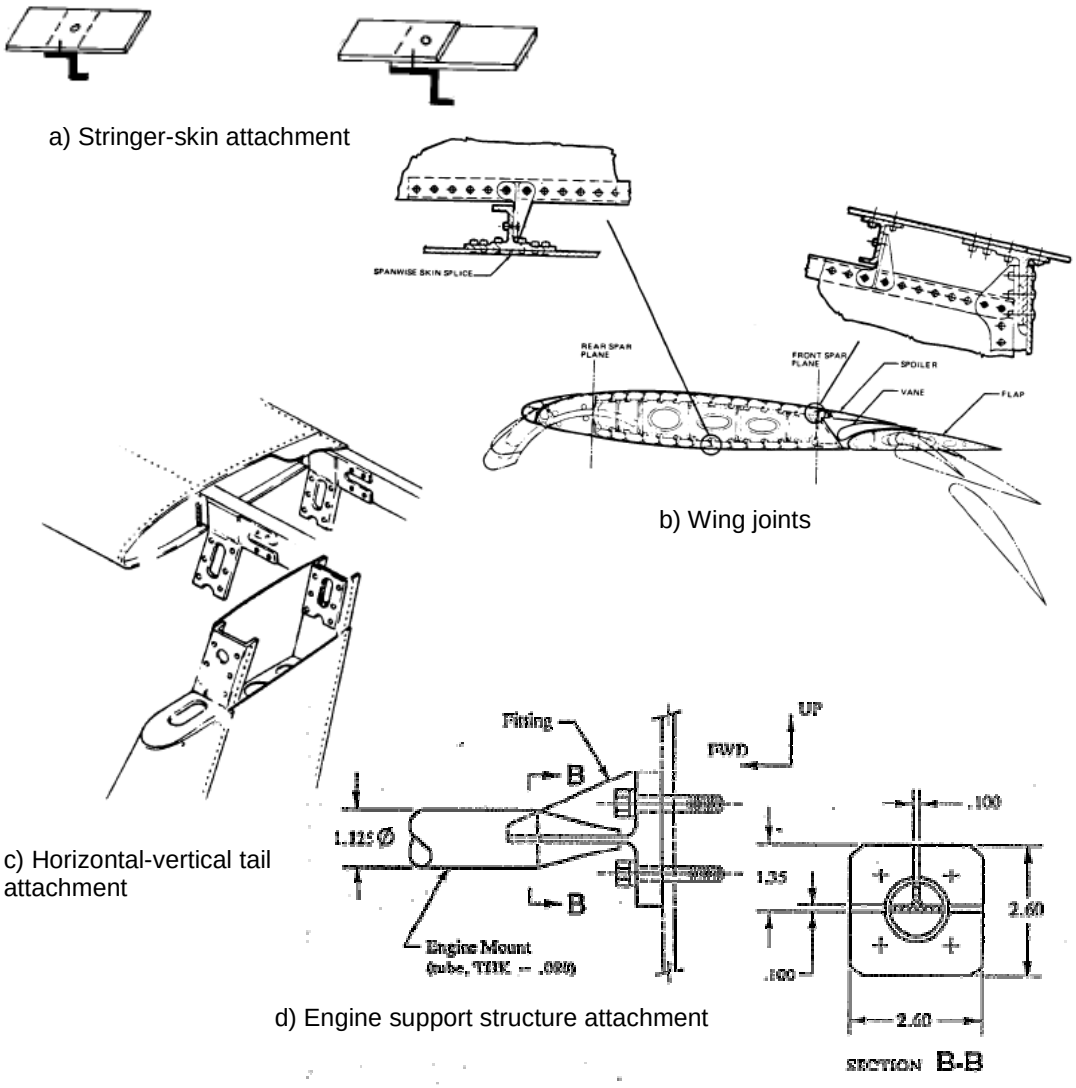

Figure 1-3 Fastened attachments, (Roskam, 1986, Bruhn, 1973 and Flabel 1997)

Table 1-1 Control system loads (AIAA, 2003)

Control system	Type	Ultimate design load, lb
Elevator	Stick	450/375
	Wheel	450
Aileron	Stick	150
	Wheel	240
Rudder and brake	Pedal	450
Flap, tab, stabilizer, spoiler, landing gear, arresting hook, wing-fold controls.	Crank, wheel, or lever operated by push or pull	**Error! Objects cannot be created from editing field codes.**
	Small wheel or knob	200 in-lb[c,d] 150[a,e]

[a]R = Radius of wheel or length of lever.

[b]Applied at circumference of wheel, or grip of crack, or lever, and allowed to be active at any angle within 20^{o} of plane of control.

[c]But not less than 75 lb or more than 255 lb.

[d]If operated only by twist.

[e]If operated by push or pull.

The joints being the weakest points in the airframe, determine its structural efficiency (Baker et al. 2004). With composites becoming the material of choice in the aerospace industry, composite joints require special attention. The maximum bearing joint efficiency of a composite bolted joint (~40%) is significantly less compared to fastened metal joints (>60%) as shown in Figure 1-4. Fastened joint configurations have complex stress distributions due to the presence of stress concentration and singularities at the hole edge. The failure of a composite joint is a three-dimensional phenomenon involving in-plane and through-thickness effects. The presence of a countersunk (CSK) hole leads to further complication in stress distribution and damage progression in single lap joints. Significantly higher stress concentration factor occurs at the start of the countersink. Figure 1-5 compares a cross section view of straight shank and countersunk laminates. Research has been conducted in the field of fastened composite joints to establish a standard design procedure. However, the majority of the current design procedures are empirical and rely extensively on expensive and time consuming testing procedures. The procedures may lead to inefficient joint design. Further investigation is required to develop a robust and reliable methodology capable of accurately predicting joint behaviour.

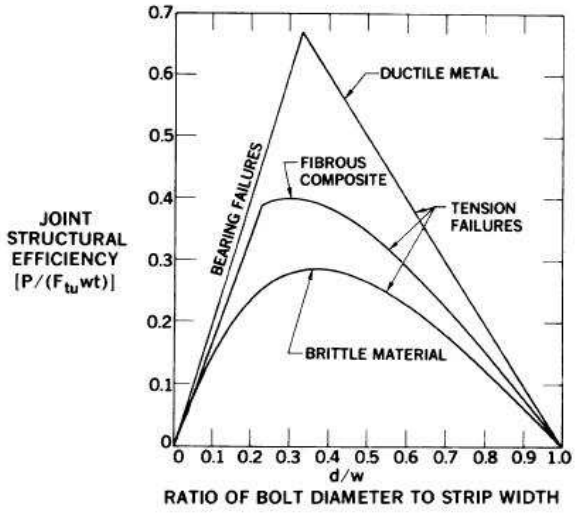

Figure 1-4 Structural efficiency of various joint types, (Nelson et al. 1981)

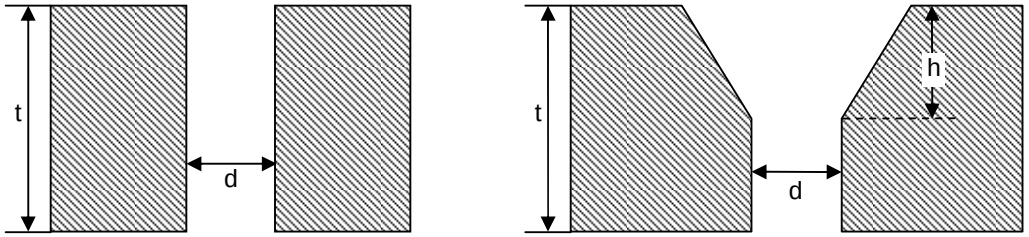

a) Straight hole laminate b) Countersunk hole laminate

Figure 1-5 Straight shank and countersunk laminate

1.2 Objective

The aims of this study are (1) to investigate the effects of bolt torque, bolt-hole clearance and ratio of countersunk depth to thickness on the failure mechanisms of composite single lap joints, and (2) to develop a validated computational technique to accurately predict the behaviour of damage initiation and progression in composite countersunk bolted joints.

1.3 Methodology

Detailed experimental testing was conducted to characterise the effects of bolt torque (BT), bolt-hole clearance (CL) and countersunk depth to thickness (HT) ratio on characteristics (ultimate failure load, through-thickness damage profile, etc.) of composite single lap joints. Experimental results were used to develop a validated finite element (FE) approach. The approach was used to further examine the effects of bolt torque, bolt-hole clearance and countersunk depth to thickness ratio on the stress distribution and initiation and progression of damage in composite single lap joints.

1.4 Thesis organisation

The thesis document is organised in the following chapters:

- *Literature Review* chapter provides a detailed summary of previous experimental and FE approaches used in analysis of single lap countersunk composite joints.
- *Experiment Methods* chapter provides a description of tests conducted and microscopy analysis.
- *Experimental Results* chapter provides a detailed analysis of the experimental results.
- *Numerical Analysis Methodology* chapter provides a detailed discussion of finite element modelling methodology.
- *Numerical Analysis Results* chapter provides a detailed analysis of the finite element analysis results.
- *Discussion* chapter summarises the adopted modelling methodology together with suggestions for improvement.

- *Conclusion and Recommendations* chapter summarises the major findings together with suggestions for future work.
- *Appendix I* discusses specimen preparation, hole over-sizing and other experimental procedures.
- *Appendix II* provides tangential and radial stress plots for the tested joints at various locations.

1.5 Outcomes

The following are the outcomes of the conducted research:

- An experimental investigation characterised the behaviour of single lap countersunk composite bolted joints with regards to bolt torque, clearance and countersunk depth to thickness ratio.
- Detailed microscopy analysis showed that the variation in tested parameters alters the through-thickness damage profile of single lap joint. A similar investigation has not been reported in literature.
- A validated computational technique to model bolted joint was developed. The technique was capable of accounting for complicated frictional contact, damage initiation and progression in a composite single lap joint.
- A new approach to calculate fibre failure energy in compression has been proposed.
- The work has also resulted in peer-reviewed conference papers:
    - Chishti, M, Wang, C H, Thomson, R S, and Orifici, A C, 2010, 'Progressive damage in single lap countersunk composite joints', in 9th World Congress on Computational Mechanics, Sydney, Australia, 19-23 July 2010.
    - Chishti, M, Wang, C H, Thomson, R S, and Orifici, A C, 2010, 'The effect of clearance on single lap countersunk composite joints', in 3rd Asia-Pacific International Symposium on Aerospace Technology, Melbourne, Australia, February 28 – March 3, 2011.

2 LITERATURE REVIEW

A summary of analytical and experimental approaches used to evaluate the effects of various parameters such as bolt torque, clearance, different bolt type etc. on the behaviour of composite bolted joints is provided below, followed by a final conclusion.

2.1 Composite joints

Significant work on mechanically fastened composite joints has been done by several authors. The current body of knowledge can be divided into pin-loaded laminates, protruding head single and double lap bolted joints, and countersunk single and double lap bolted joints. Extensive experimental, analytical, and numerical investigations have been conducted on the first two types of mechanical joints listed above. The available knowledge on the behaviour of countersunk joints is much less compared to other types of joints. The following section provides a summary of available literature on joints.

2.1.1 Joint failure

In spite of the advancement in bonding technology, mechanical fastening is usually the only feasible or economical means of joining highly loaded composite components. Load transfer in mechanical joints occurs by compression of the faces of the holes passing through the joint members by shear of the fasteners. Some of the load is also transferred through friction between the joint members and fastener, if the clamping force imposed by the fastener is sufficient. The most common form of mechanical joints are single lap and double lap joints as shown in Figure 2-1. The composite joints loaded as shown in Figure 2-1 experience stress concentration at the boundary of the hole. The single lap joint configuration is affected by secondary bending which leads to a complex three-dimensional stress and contact state at the hole. The secondary bending occurs because the load in a single lap joint is offset from the principal axis of the joint as shown in Figure 2-1.

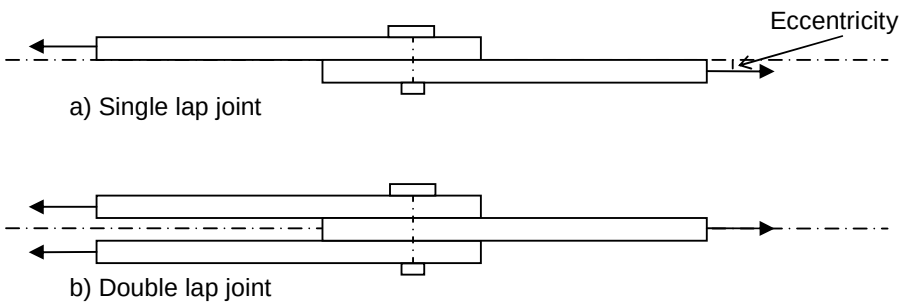

Figure 2-1 Types of mechanical joints

The type of failure that occurs in a mechanical joint depends on the following parameters; shown in Table 2-1 (ASTM D5961 2007):

- Ratio of the width to the diameter of the fastener hole, *w/d*.
- Ratio of the edge distance to the diameter, *e/d*.

Figure 2-2 shows different failure modes experienced by a mechanically fastened joint. The shear out, tension and cleavage failure modes are not recommended for aerospace structures as they are catastrophic failure modes. The failure mode accepted by the aerospace industry is bearing failure mode as it is a non-catastrophic failure mode, providing time to detect and repair damaged components. The geometric restrictions required to promote bearing failure together with other standard design practices are shown in Table 2-1.

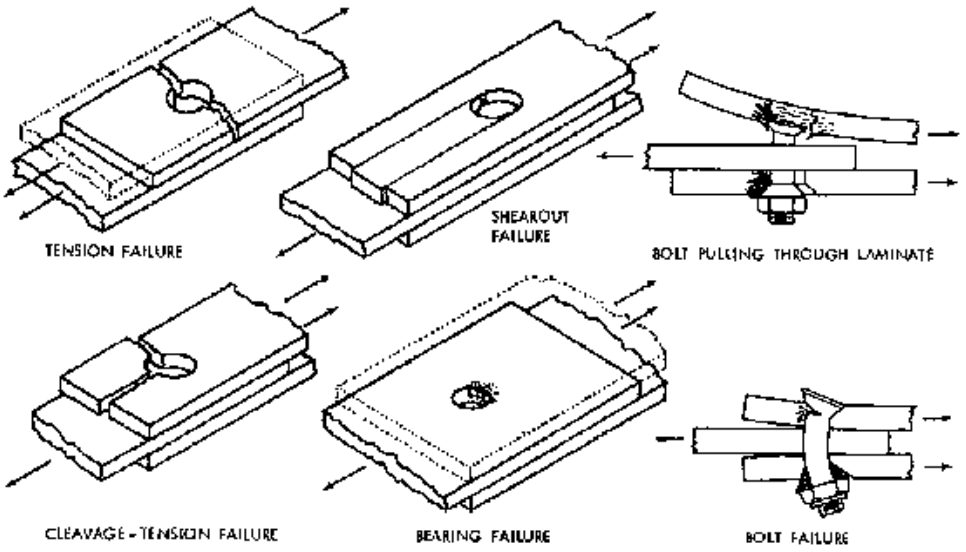

Figure 2-2 Failure modes of composite mechanically fastened joints, (Hart-Smith 1978)

Table 2-1 Bearing failure geometric restrictions

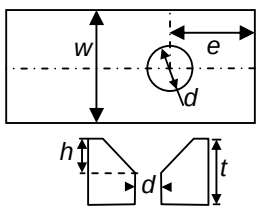	$w/d > 4$	Promotes bearing failure from ASTMD5961
	$e/d > 3$	Promotes bearing failure from ASTMD5961
	$1.5 \le d/t \le 3.0$	Reduces the possibility of fastener failure from ASTMD5961
	$0 \le h_{CSK}/t \le 0.7$	Industry standard from ASTMD5961

Fundamentally, bearing failure is a local compressive failure which occurs due to contact and frictional forces acting on the surface of the hole. Failure modes in the vicinity of loaded bolt holes in laminated composite materials include tensile, compressive and shear failure of fibres and matrix, and delamination between the plies. Essentially, bearing failure is progressive accumulation of in-plane damage modes, together with delamination damage (Xiao et al. 2001).

Failure in bolted joints is related to the local stress field in the vicinity of fastener holes. Stresses at a particular hole are affected by several factors such as the amount of load reacted by the fastener and the amount of load running through the plate cross-section which is reacted elsewhere in the joint (Ekh et al. 2006). These loads are referred to as bearing load, P_b, and bypass load, P_{bp}, respectively and are shown in Figure 2-3. Additionally, properties such as contact area and friction may have a significant effect on the local stress field. This is more significant for single shear lap joints due to the non-uniform distribution of contact stress in the thickness direction caused by the eccentric load path.

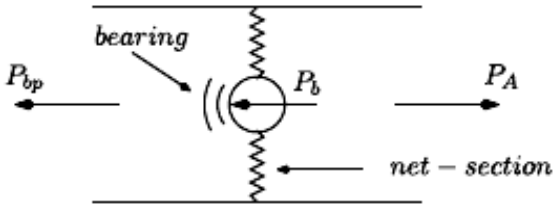

Figure 2-3 Loads acting on a plate, (Ekh et al. 2006)

The design of bolted joints in composite materials involves a greater degree of complexity than in metals due to the almost infinite combinations of composite materials, complex 3D stress and strain distributions, the existence of failure modes that may not exist in conventional metallic bolted joints and the fact that bolted joints in composites may fail at loads that are not predicted by either perfectly elastic or perfectly plastic assumptions (Nelson et al. 1981).

Wang et al. (1996) and Camanho et al. (1998) showed that the primary failure modes in pin-bearing damage were shear cracks formed by accumulated compression failure in each individual ply of the laminate. A microscopy investigation showed that the principal failure modes of the shear cracks were fibre kinking, fibre-matrix shearing and matrix

compression. A detailed investigation of failure progression in single-lap bolted composite-metal joints was undertaken by Ireman et al. (2000). The specimen was examined at different load levels using acoustic emissions, X-rays and microscopy. It was found that the failure initiated with an occurrence of matrix cracking and single fibre fracture at low loads (3-5 kN). This was followed by increased fibre fracture, fibre matrix chip-out and delamination initiation at medium load levels of 6-8 kN. At high load levels up to ultimate failure the fibre and matrix damage increased significantly in the circumferential and through-thickness direction together with an increase in delamination. The major failure modes included matrix cracking, fibre fracture, delamination and kinking.

An example of a damaged section at a 0^o cutting plane is shown in Figure 2-4. The figure shows accumulated shear and compression damage (kinking) forming a band extending from ply 6 to ply 9. At the interface between plies 18 and 19, the kinking mode converted to delamination (Ireman et al. 2000). Similarly, Kelly et al. (2004) performed microscopy analysis on a pin-loaded laminate. Inspection of the laminates revealed the dominant micromechanical failure modes as matrix compression, interlaminar and intralaminar matrix shear cracking, fibre micro-buckling and fibre shear fracture. Detailed micrographs of fibre micro-buckling, shear cracking and fibre compressive failure (kinking) are shown in Figure 2-5.

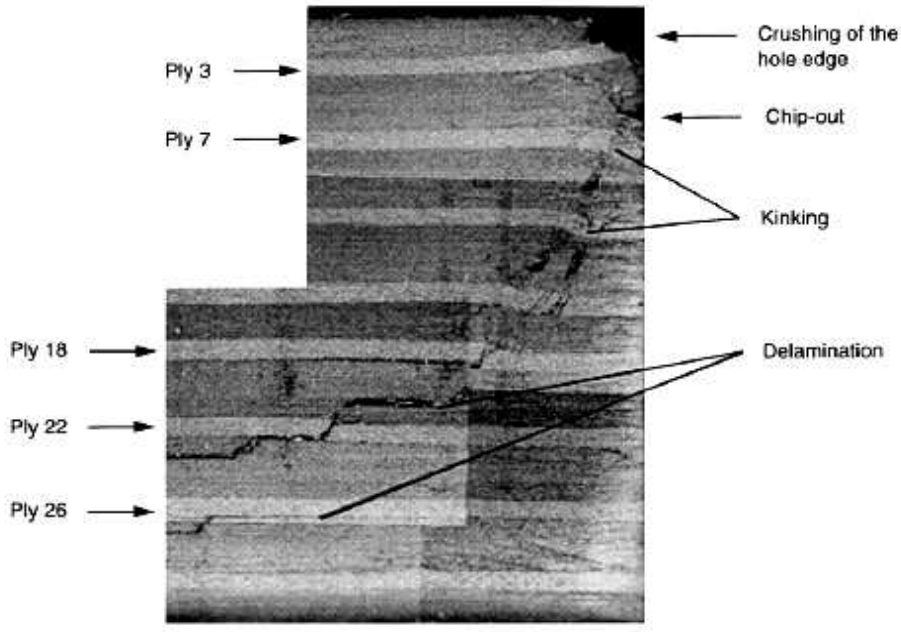

Figure 2-4 Damaged section along the 0^o cutting plane, (Ireman et al. 2000)

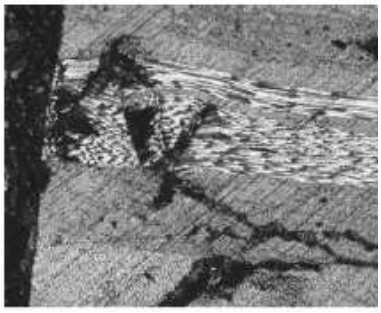

a) Fibre microbuckling and shear cracking

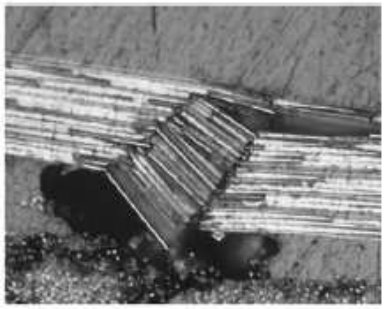

b) Fibre compressive fracture (Kinking)

Figure 2-5 Detailed micrographs of failure modes, (Kelly et al. 2004)

Tserpes et al. (2001) developed a three-dimensional progressive damage model for bolted joints. Failure analysis and degradation of material properties were implemented using Hashin (1980) failure criteria and a set of degradation rules respectively. A knock-down approach was used for material properties degradation. The authors analysed the effect of bolt position and friction (in the washer area) upon damage accumulation and residual strength. The authors showed that for protruding head bolted joints, the position of the bolt significantly affected the strength of the composite joint. The effect of friction in the washer area was not significant. The authors applied a user-defined subroutine to perform a three-dimensional analysis. Camanho et al. (1999) proposed a three-dimensional progressive damage model for composite bolted joints. Hashin (1980) failure criteria were used for damage initiation and Tan et al. (1989; 1991; 1993) and Nuismer et al. (1988) approaches were used to provide material property degradation laws. The model showed good comparison with literature and experimental results. However, the model did not account for delamination failure.

A progressive failure analysis of an open hole composite plate under compression was undertaken by Labeas et al. (2008). A three-dimensional model was developed using user-defined subroutine comprised of Hashin (1980) failure criteria and two different knock-down property degradation laws. In the first property degradation law the corresponding material properties were reduced to zero, however, in the second approach the properties were reduced by a certain percentage. The developed approach showed a good comparison with experimental results. The author concluded that the two different property degradation approaches did not significantly affect the results for the compressively loaded plate.

2.1.2 Effects of countersunk

The presence of a countersunk in a single lap joint further complicates the problem as acknowledged by several authors (Ireman 1998; Padhi et al. 2002; Thoppul et al. 2009; Aronsson 1993; Bhargava et al. 2007; Shivakumar et al. 1992). However, countersunk fasteners are vital for aerospace applications as they provide aerodynamic smoothness to the joint. All mechanical joints exposed to airflow use countersunk fastener systems. The stress distribution at the countersunk hole is affected by various parameters (Bhargava et al. 2007; Khashaba et al. 2005; McCarthy et al. 2005) including the following:

- Countersink depth
- Plate thickness
- Countersunk angle
- Bolt torque
- Washer size
- Clearance
- Laminate layup sequence
- Load type

Bhargava et al. (2007) discussed the effects of countersunk angle, countersunk depth and hole radius to thickness ratio on stress concentration factor (*K*). The effect of countersunk angle can be seen in Figure 2-6. Figure 2-6 also shows that maximum stress concentration factor for the selected geometry of the plate occurred at the start of the countersink. For the range of countersunk depth to thickness ratios tested, the stress concentration factor monotonically increased with an increase in countersunk depth to thickness ratio, as shown in Figure 2-7. Again the maximum stress concentration factor occurred at the start of the countersunk.

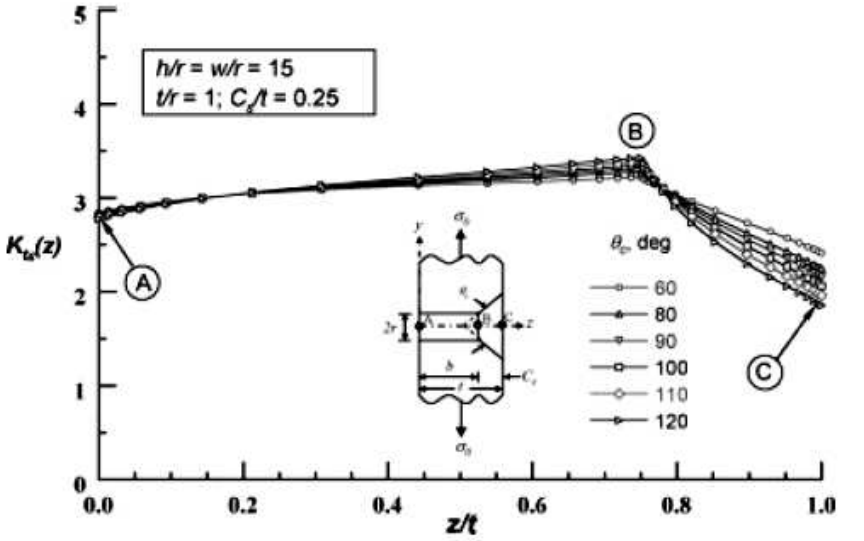

Figure 2-6 Effect of countersunk angle on "K" for a wide plate, (Bhargava et al. 2007)

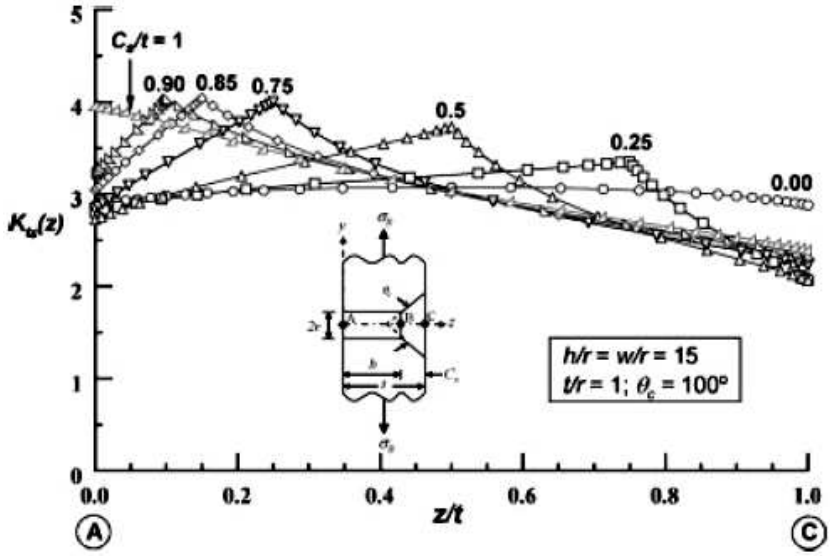

Figure 2-7 Effect of HT ratio on K *for a wide plate (t/r=1), (Bhargava et al. 2007)*

Ireman (1998) experimentally and numerically examined the stress distribution through the thickness of bolted composite laminates. Protruding head and countersunk bolted joints were analysed in the study. A quasi isotropic stacking sequence of $[(\pm 45/0/90)_4]_S$ was used for laminate A. The major outcome of the study was the stress distribution along the hole in the countersunk and straight shank bolt. It was shown that the significant contact stress concentration occurred in the straight shank region of the countersunk hole.

Contact stress distribution along the shanks of the protruding head and countersunk bolt are shown in Figure 2-8 and Figure 2-9 respectively. The angle α in the plot defines the

angle along the circumference of the hole. The angle starts from the centre line of the hole opposite to the contact area between bolt and hole. Therefore 180^o represents the location of the bearing plane. The z/t_1 coordinate defines the through-thickness location along the bolt hole, i.e. z/t_1 = 0 represents the shear plane of the joint and z/t_1 = 1 represents the top surface of the laminate. It can be seen from the figures that the contact stress concentration at the shear plane is higher for the countersunk hole compared to the straight shank hole. The contact stress immediately drops when the countersunk region starts. The top of the countersunk hole had higher contact stress concentration compared to the other parts of the countersunk region of the hole. This contact stress distribution becomes really significant in the presence of clearance, as discussed in the later part of this report.

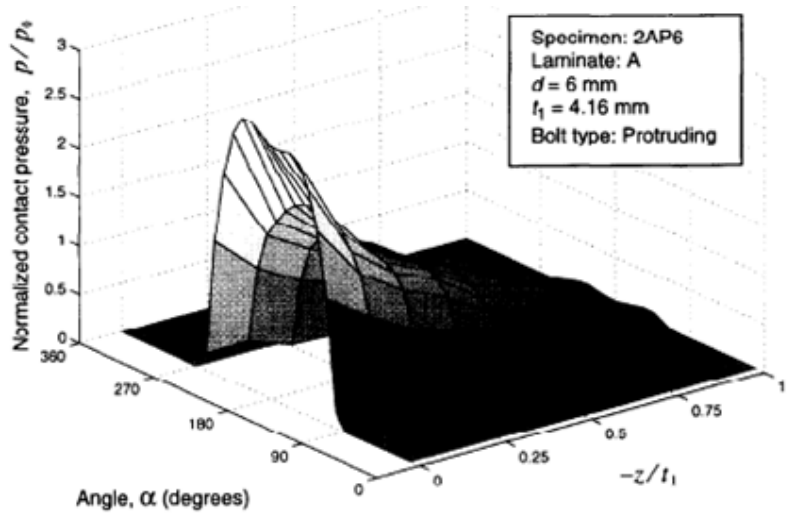

Figure 2-8 Contact stress distribution for protruding head laminate, (Ireman 1998)

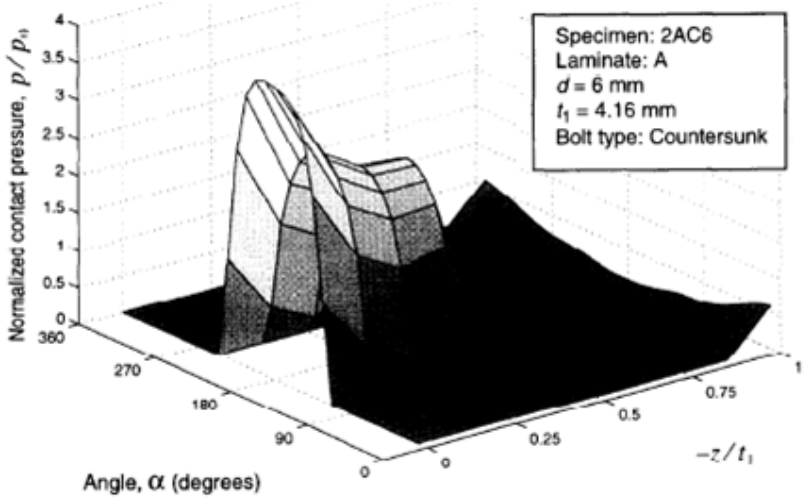

Figure 2-9 Contact stress distribution for CSK laminate, (Ireman 1998)

Starikov et al. (2001) investigated the effects of different types of countersunk bolts in a multi-bolt composite joint. Titanium torque-set, titanium Huck-comp and composite countersunk fasteners were used in the investigation. Double lap joints were tested in tension and compression with lateral support. All the joints failed in either net section failure or bolt failure. The study showed that multi-bolt joints experienced variable load transfer ratio between each bolt row. Initially the third bolt row transferred maximum load followed by the first and second bolt row. The load transfer curves for torque set bolts are shown in Figure 2-10.The failure in the countersunk hole is shown in Figure 2-11. Some damage can be seen in the straight shank section of the hole. Delamination was reported in the bottom layer of the composite.

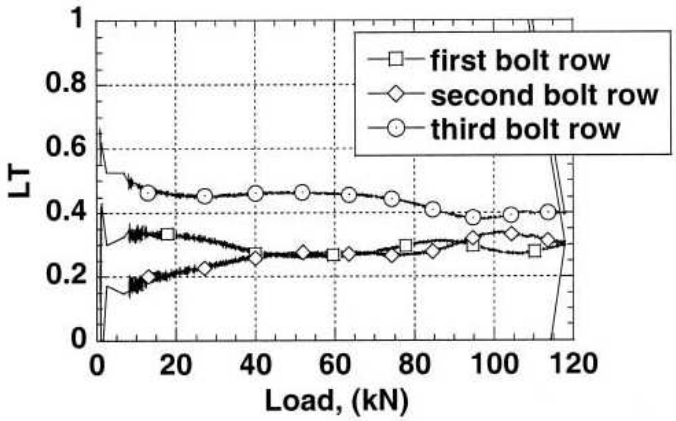

Figure 2-10 Load transfer curves for torque set bolts, (Starikov et al. 2001)

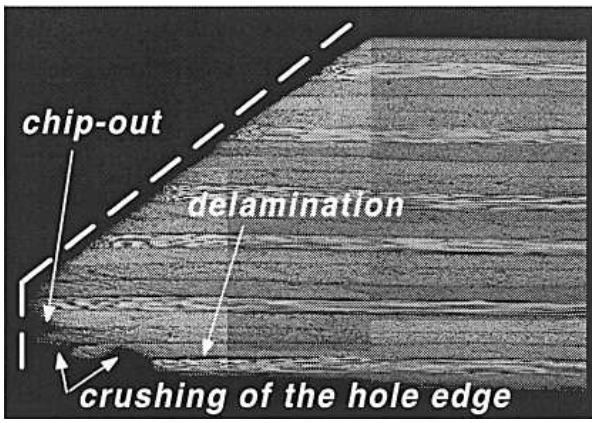

Figure 2-11 Failure in bearing cutting plane for bolt-hole 2, (Starikov et al. 2001)

2.1.3 Effects of bolt torque

The effect of bolt torque on the behaviour of double lap straight shank joints with protruding head bolts has been studied in detail. An improvement in the bearing strength of the carbon fibre reinforced polymer (CFRP) laminate due to increased lateral (i.e.

through-thickness) compressive stress around the loaded hole was shown by Collings (1977). For (0/±45) laminates, improvement from 60% to 170% according to hole size were achieved with constraint pressure of up to 22 MPa. Further increase in the constraint pressure led to only marginal improvements. It was assumed that lack of through-thickness compression at the contact zone could lead to premature in-plane compression failure. Failure occurred by initiation of shear cracks at the hole edge and subsequent propagation to the edge of the clamped region.

A similar effect was reported by Kretsis et al. (1985) in glass fibre-reinforced composites. For laterally restrained laminates, the zone under the washers developed shear cracks but was unable to expand under compression. This led to lateral expansion spreading into a wider area that lay outside the washer boundary. For high values of clamping pressure the bearing strength versus clamping pressure relation was almost constant, suggesting the existence of an optimum value of pressure. Ireman (1998) performed a three-dimensional numerical study on the effect of bolt torque on stress-strain distribution of the joint. No failure was modelled; however, the analysis showed that the secondary bending and strain level reduced with an increase in bolt torque. The bolt torque was simulated using a thermal expansion coefficient calibrated using a special instrumented bolt. The author also pointed out that higher strain levels were generally observed in the specimens with countersunk bolts compared to specimens with protruding head bolts.

Stockdale et al. (1976) examined the effects of increased bolt clamping pressure on the bearing load of glass fibre composites. Two different laminates a = [0/90/0/90/0/90/0] and b = [90/0/90/0/90/0/90], were tested with pin, finger tight (0 N), 4905 N, 9810 N and 14715 N clamping force. The experiments showed a 40% increase in the initial bearing load for finger tight specimens compared to pin-loaded specimens. A 100% increase in initial failure load for the pin-loaded specimen to the maximum bolt load specimen can be seen in Figure 2-12. The figure also shows that the lay-up significantly affected the failure load of the specimen. The final failure for pin-loaded specimens was reported to be compressive failure leading to crushing and delamination. However, the use of bolt clamping (even finger tight) load prevented delamination from occurring in the tested specimen (Stockdale et al. 1976).

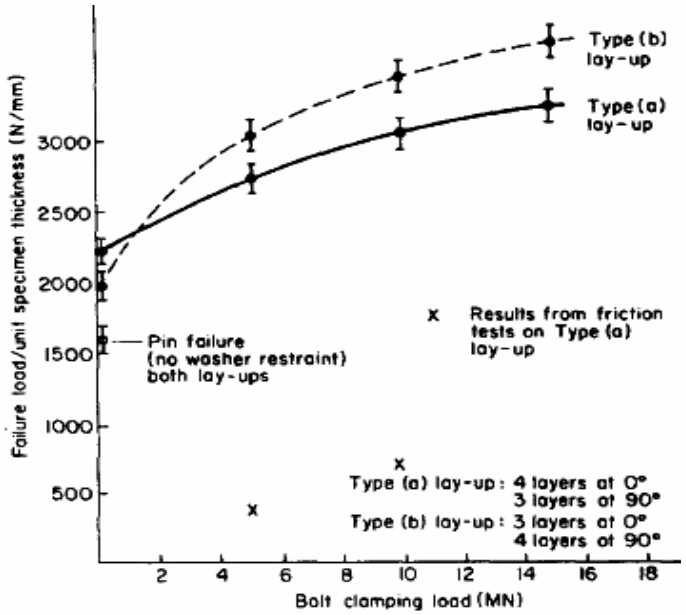

Figure 2-12 Variation of failure load with bolt clamping load, (Stockdale et al. 1976)

Cooper et al. (1995) investigated the effects of changing *e/d, w/d* and bolt torque on a double lap single bolt joint. The ranges of $1.5 \leq e/d \leq 7$ and $2 \leq w/d \leq 10$ were tested in the experimental investigation. Three values of 0 Nm, 3 Nm and 30 Nm were used for bolt torque. The author found that increasing bolt torque from 0 to 3 Nm led to an improvement of approximately 45% in bearing failure load. Similarly 30 Nm bolt torque led to approximately 80% improvement in bearing failure load.

The study also showed that for low values of *e/d* and *w/d,* failure load was almost insensitive to the variation in bolt torque. The failure loads were almost directly proportional to *e/d* and *w/d* up to critical *e/d* and *w/d* as shown in Figure 2-13. The figure also shows that critical *e/d* and *w/d* ratios increased with an increase in bolt torque. The variation of stiffness with *e/d* and bolt torque was found to be marginal, however, *w/d* significantly affected the stiffness of the bearing laminate. The bolt movement was also shown to reduce with an increase in the bolt torque. An extensive review of studies on the effects of bolt torque on fastened joints is provided in Camanho et al. (1997) and Thoppul et al. (2009).

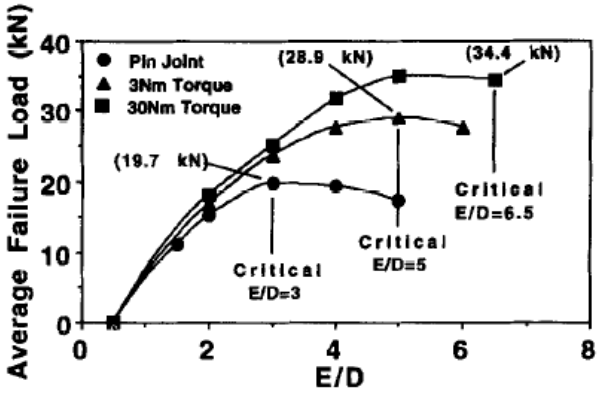

a) Variation of failure load with e/d and bolt torque.

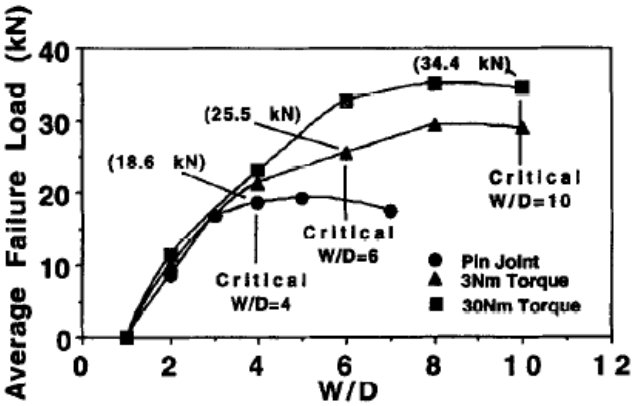

b) Variation of failure load with w/d and bolt torque.

Figure 2-13 Failure load variation, (Cooper et al. 1995)

2.1.4 Effects of clearance

As the use of composite material increases, it is important to establish the effects manufacturing imperfections on the characteristics of the structure. The bolt-hole clearance is one such imperfection which can alter the behaviour of composite joints. The principal effect of clearance is the reduction in the contact angle between bolt and hole. The bolt hole contact angle can be seen in Figure 2-14. Hyer et al. (1987) examined the effects of pin elasticity, clearance and friction on the stress state of pin-loaded joints. Friction and clearance significantly affected both the distribution and magnitude of the stresses around the hole. A neat fit and 40 μm clearance were used with 4 mm hole diameter. The 40 μm clearance resulted in a 22% reduction in the contact area and 12% reduction in the joint strength. Hyer et al. (1987) also reported a shift in the maximum tangential stress from the net-section plane towards the bearing plane due to clearance.

Similarly DiNicola et al. (1993) investigated the effect of clearance on pin-loaded joints with clearance of 0 μm (neat fit), 76 μm, 152 μm, 276 μm. The bearing strength at 4%

hole deformation had significant reduction with an increase in clearance. However, unlike Hyer et al. (1987) the ultimate bearing strength showed limited dependence on the clearance.

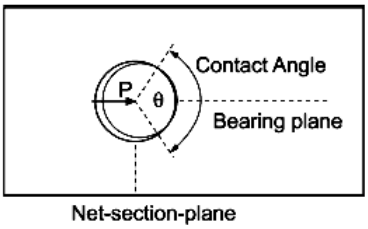

Figure 2-14 Contact angle for bolt-hole loading, (Kelly et al. 2004)

McCarthy et al. (2005) conducted a detailed experimental and numerical analysis of single lap bolted composite joints. Quasi-isotropic and zero dominated lay-ups were evaluated using an 8 mm protruding head bolt. Clearances of 0 µm, 80 µm, 160 µm and 240 µm were tested with a finger tight torque of 0.5 Nm. A three-dimensional model of a protruding head bolted joint was used for the analysis. The authors used Hashin (1980) failure criteria for damage initiation. The model was not able to account for progression of damage. The initial linear response of the model correlated well with the experimental results. The authors also highlighted the importance of correct contact definition and high mesh density in the contact region to avoid “overhanging nodes”.

Clearance was reported to increase bolt rotation, reduce bolt-hole contact area and decrease joint stiffness. The joint with clearance had a gradual increase in stiffness as the applied load was increased. This behaviour was not seen in neat fit joints. Clearance also led to three-dimensional variations in the stress distribution of single lap joint. Similar to Hyer et al. (1987) the maximum radial stress was shown to increase with an increase in clearance as shown in Figure 2-15. A shift in the location of maximum tangential stress towards the bearing plane was also reported.

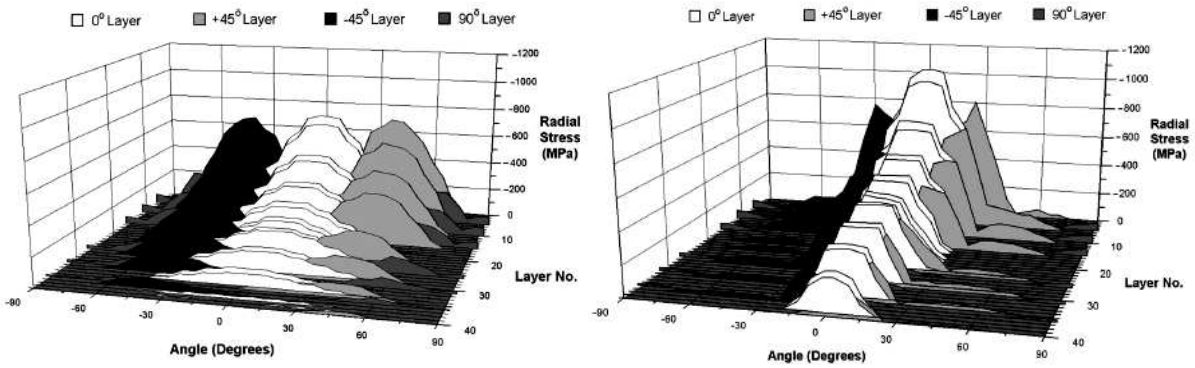

a) Neat fit laminate

b) 240 µm clearance laminate

Figure 2-15 Radial stress distribution for zero dominated layup, (McCarthy et al. 2005)

Kelly et al. (2004) investigated the effects of clearance on the laminate bearing strength for both pinned and clamped joints. Clearances of 0 µm, 100 µm and 200 µm were used with a nominal bolt diameter of 6.35 mm. A three-dimensional finite element model was developed to determine the stress field around the hole. The model showed that the radial stress concentration factor increased significantly with an increase in clearance. The distribution of stresses was found to be affected by the presence of clearance. The model showed that through-thickness stress distribution was also affected by the presence of clearance. The model was not able to account for composite failure.

The bolt-hole clearance influenced the hole deformation behaviour (Kelly et al., 2004). The neat fit specimen immediately transferred load in comparison to the clearance fit specimen where the initial clearance led to delay in load transfer. For pin-loaded specimens, a slight reduction in stiffness was reported with an increased clearance. The variation of bearing strength at 4% hole deformation and ultimate bearing strength of pin-loaded specimen with clearance can be seen in Figure 2-16. Effects on two different laminates are shown in the figure. The $[0/45/90/-45]_{2s}$ laminate showed some variation in ultimate bearing strength but no significant variation was reported for bearing strength at 4% hole deformation. The $[0/45/90/-45]_{s}$ laminate showed significant variation in both ultimate bearing strength and bearing strength at 4% hole deformation.

A similar comparison for clamped joints is shown in Figure 2-17. The lateral clamping force increased the value of bearing strength at 4% hole deformation by approximately 20% compared to pin-loaded laminate. The authors reported almost 110% improvement in the ultimate bearing strength of the clamped joint compared to pin-loaded laminate. The

variation in the strengths due to clearance was less for clamped laminates compared to the pin-loaded laminates. The ultimate bearing strength of both the laminates was practically independent of the bolt-hole clearance. The bearing strength at 4% hole deformation showed some reduction with increased clearance as seen with pin-loaded laminates.

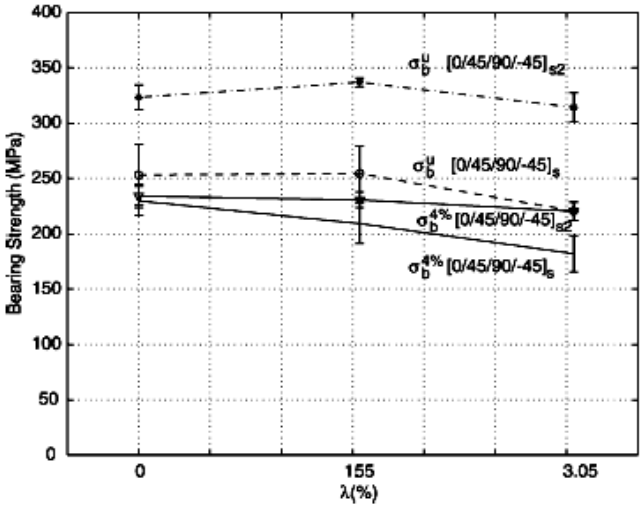

Figure 2-16 Effect of bolt-hole clearance on pin-loaded laminates, (Kelly et al. 2004)

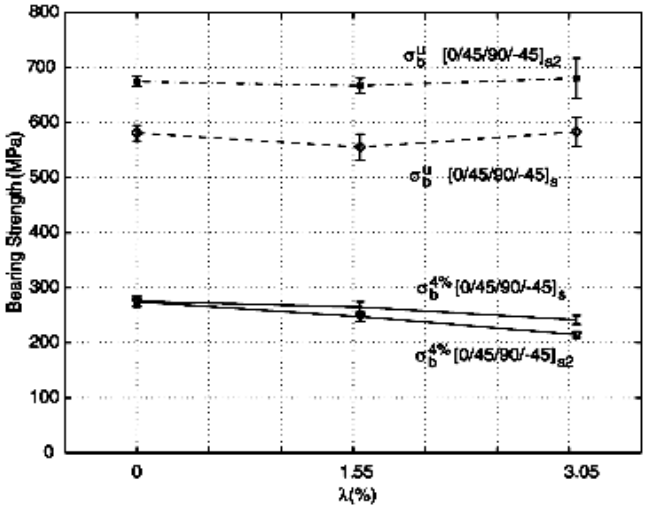

Figure 2-17 Effect of bolt-hole clearance on clamped laminates, (Kelly et al. 2004)

McCarthy et al. (2002) examined the effects of clearance on single lap protruding head and countersunk bolted joints. A quasi-isotropic and zero dominated lay-up were tested with finger tight (0.5 Nm) and 16 Nm bolt torque. The authors pointed out that the presence of countersunk affected the load-carrying capacity of the laminate leading to the straight shank of the countersunk laminate reacting to the applied load. The authors also

found that the 2% offset strength showed limited variation with clearance for finger tight protruding head bolted joints. No such dependency was noted for countersunk and fully torqued joints. The ultimate bearing strength showed no statistically significant variation with clearance as was pointed out by DiNicola et al. (1993). A reduction of approximately 10% in stiffness was noted for a protruding head finger tight joint with 240 μm clearance. A similar reduction in stiffness was noted for a countersunk finger tight joint. The study analysed only protruding head torqued bolts. The countersunk bolted joints were not torqued.

2.2 Failure criteria

The initiation of damage has been predicted using damage initiation criteria or failure models. Fibre-reinforced composites present a large variety of failure behaviour, and a large number of failure models have been proposed. The majority of available models are either micro- or meso-level models. Models can also be classified either as phenomenological (Hashin criteria, Puck criteria etc.) or interaction (Tsai-Wu, Von mises, Yamada Sun etc.) based failure models. The phenomenological models are derived based on the underlining phenomena, which promote a better understanding and more realistic failure models. Major failure mechanisms for continuous fibre composites are:

- Fibre breakage
- Fibre buckling
- Fibre kinking
- Matrix crushing
- Matrix cracking
- Fibre pullout

The large quantity of failure modes significantly increases the complexity in predicting composite failure. A comprehensive review of the available failure models was provided by Echaabi et al. (1996) and Orifici et al. (2008). In this report, point stress failure criteria, maximum stress failure criteria and Hashin failure criteria are discussed to exemplify the major categories of the failure models currently utilised.

2.2.1 Point stress failure criteria

Whitworth et al. (2003) performed a theoretical analysis to evaluate the bearing strength of pin-loaded composite joints. The analysis was based on Chang et al. (1982) strength prediction model and the point stress failure criterion was used to evaluate the

characteristic lengths in tension and compression. A two–dimensional finite element analysis was used to evaluate the stress distribution in the vicinity of the joint. Yamada (1978) failure criterion was used in the analysis. The criterion was defined as:

$$\left(\frac{\sigma_1}{X_L}\right)^2 + \left(\frac{\tau_{12}}{S}\right)^2 = e^2$$

where

σ_1 = Longitudinal stress

τ_{12} = Shear stress

X_L = Ply longitudinal strength

S = Ply in-plane shear strength

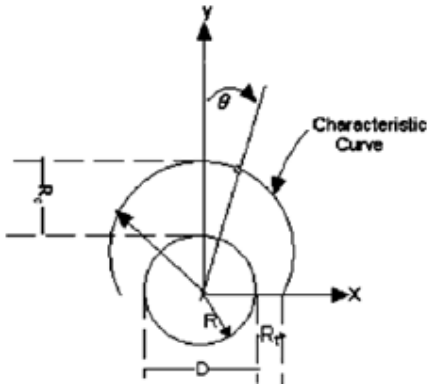

Figure 2-18 Characteristic curve for pin-loaded composite, (Whitworth et al. 2003)

The value of e greater than or equal to unity led to failure. The characteristic curve is shown in Figure 2-18 and can be expressed as

$r_c(\theta) = R + R_t + (R_c - R_t)\cos\theta$,

where

R_t = Characteristic dimension in tension

R_c = Characteristic dimension in compression

θ = Ranges from -90^o to 90^o

The parameters R_t and R_c were evaluated by applying the point stress failure criterion to a plate with an open hole loaded in tension and a plate with an inclusion loaded in compression. The point stress failure criterion assumed that failure would occur when the transverse stress at some distance R_t and/or R_c, away from the opening reached the un-

notched tensile or compressive strength of the material respectively. The developed approach was used to predict strength of a joint with finite element models. Finite element analysis was conducted using a cosine fastener contact load distribution and a constant displacement at one end of the plate. The results obtained from the analysis were compared with available experimental data for composite pinned joints made from AS4/3501-6 carbon/epoxy laminates utilising steel pins. A comparison of experimental (dots) and FE (solid line) results is provided in Figure 2-19. The initial comparison was good, however, as the *e/d* ratio increased the error increased.

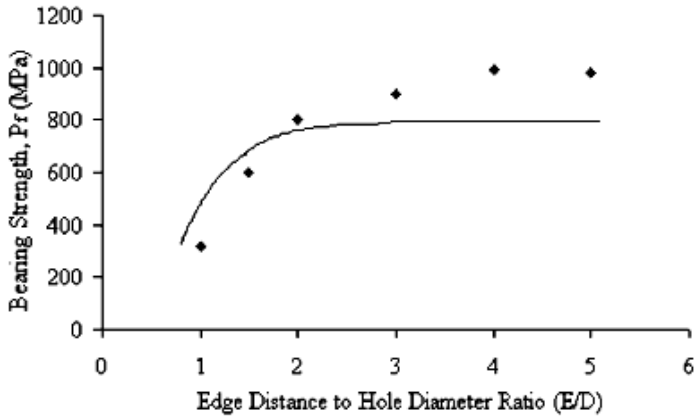

Figure 2-19 Bearing strength comparison, (Whitworth et al. 2003)

2.2.2 Maximum stress criterion

The maximum stress criterion is simple and therefore one of the most widely used failure criteria. The geometric shape of this criterion is a rectangle in σ_{11}-σ_{22} plane. The criterion is based on the following approach:

Fibre Failure

If $\sigma_{11} > 0, X = X_t$; otherwise, $X = X_c$

Matrix Failure

If $\sigma_{22} > 0, Y = Y_t$; otherwise, $Y = Y_c$

The maximum stress failure criterion requires that

$$I_f = \max\left(\frac{\sigma_{11}}{X}, \frac{\sigma_{22}}{Y}, \left|\frac{\sigma_{12}}{S}\right|\right) = 1$$

where

X_t = Longitudinal tensile strength

X_c = Longitudinal compressive strength

Y_t = Transverse tensile strength

Y_c = Transverse compressive strength

S = Shear Strength

I_f = Failure Index

Failure occurs once the failure index is equal to 1. This criterion is capable of predicting some of the failure modes of composite structures, however it suffers from the following disadvantages:

- Over estimation of the failure stresses in the corners of the stress rectangle
- Only linear behaviour can be described as the failure envelope is represented by a set of straight lines
- Interaction between stresses or failure modes is not permitted

2.2.3 Hashin failure criteria

The failure criteria were developed for transversally isotropic unidirectional (UD) laminates. They are quadratic polynomial failure criteria that take into account physical considerations. Due to the presence of two dissimilar phases in the composite, failure occurs in different modes. Hashin and Rotem (1973) and Hashin (1980) considered that these different modes cannot be represented by a simple smooth function and proposed separate failure criteria accounting for fibre and matrix failure separately. The Hashin 3D damage model (1980) can be written as:

Fibre tension ($\sigma_{11} \geq 0$)

$$\left(\frac{\sigma_{11}}{X_t}\right)^2 + \frac{1}{S^2}\left(\sigma_{12}^2 + \sigma_{13}^2\right) = 1$$

Fibre compression ($\sigma_{11} < 0$)

$$\frac{|\sigma_{11}|}{X_c} = 1$$

Matrix tension $(\sigma_{22} + \sigma_{33}) > 0$

$$\frac{1}{Y_t^2}(\sigma_{22} + \sigma_{33})^2 + \frac{1}{S_T^{\,2}}\left(\sigma_{23}^2 - \sigma_{22}\sigma_{33}\right) + \frac{1}{S^2}\left(\sigma_{12}^2 + \sigma_{13}^2\right) = 1$$

Matrix compression $(\sigma_{22} + \sigma_{33}) < 0$

$$\frac{1}{Y_c}\left[\left(\frac{Y_c}{2S_T}\right)^2 - 1\right](\sigma_{22} + \sigma_{33}) + \frac{1}{4S_T^2}(\sigma_{22} + \sigma_{33})^2 + \frac{1}{S_T^2}(\sigma_{23}^2 - \sigma_{22}\sigma_{33}) + \frac{1}{S^2}(\sigma_{12}^2 + \sigma_{13}^2) = 1$$

where

X_t, X_c, Y_t and Y_c are described above

S = Shear strength, the allowable value of σ_{12} and σ_{13}

S_T = Transverse shear strength, the allowable value of σ_{23}

As can be seen from the above equations, the Hashin failure criteria are capable of predicting individual modes of in-plane failure for composite plies. For compression fibre failure, the Hashin failure criterion is similar to the maximum stress criterion. However, to predict tensile fibre failure, the Hashin criterion includes a shear term. In cases where the shear stress is small compared to the tensile longitudinal stress, the Hashin failure criterion and the maximum stress criterion give similar results. However, when the shear stress is large, the Hashin failure criterion is much more conservative than the maximum stress criterion.

Similarly, the Hashin matrix failure criterion defines matrix compressive and tensile failure. The matrix criteria also account for the effect of the shear component which is more significant in the case of matrix failure compared to fibre failure. However it was suggested by Echaabi et al. (1996) that this damage model was relatively less accurate in predicting matrix dominated failure. The uncertainty of the Hashin criterion for matrix failure was also reported by Paris (2001) who suggested the use of the Puck matrix failure criteria as proposed by Kopp et al. (1996) and Kroll et al. (1997). In his study, Paris (2001) suggested that the Hashin matrix criterion is safer to use for materials which have $S_T < S$ (where S = Transverse shear strength, the allowable value of shear stress σ_{12} and σ_{13}) because it gives conservative results under such condition. However, for materials with $S_T > S$ the results may be non-conservative.

The Hashin failure criteria are capable of considering individual failure modes separately; however, no interactions between failure modes are defined. The maximum stress and Hashin failure criteria exemplify the majority of the available failure criteria, where either separate equations are used to define different failure modes (including 3D failure modes such as delamination) or semi-empirical equations were developed to define overall failure.

2.3 Damage progression

Progressive failure analysis is a modelling approach used to simulate composite failure behaviour. This approach is well suited for modelling bearing failure as bearing failure is a progressive phenomenon where the material gradually loses strength and stiffness due to increasing damage. The main aim of a progressive failure analysis approach is to reduce the material stiffness properties (directionally) as the damage occurs in the model. Several different techniques are employed to define the property degradation laws. The most simple property degradation law can be defined as the knock-down approach, in which the material stiffness is reduced by a certain percentage of initial stiffness once damage has occurred. As an example, if fibre damage occurs in the tensile direction, then the tensile stiffness of the composite in the fibre direction can be reduced by a certain value. The stiffness is not reduced any further than a predetermined value (Labeas et al. 2008). This approach has some major limitations:

- This can lead to numerical instability in the FE model.
- This can lead to significant mesh sensitivity issues in the FE model.

Another more practical approach is to define a post damage-initiation degradation law as described by De Vries (2001) and Linde et al. (2004). The real behaviour is still difficult to capture, as the degradation of material properties is affected by a large number of parameters. This approach is less sensitive to the mesh size compared to the knock-down approach. Capabilities in the solver (Abaqus User Manual 2010) provides a bilinear damage initiation and progression behaviour, in which the non-damaged material stiffness and strength determine the initial material response. Once the damage initiated, it is assumed that the material properties reduce linearly until total material collapse. To alleviate the problem of mesh sensitivity during material softening, Abaqus uses a characteristic length in the formulation so that the constitutive law is expressed as a stress-displacement relation. The problem of numerical instability can also be alleviated by not reducing the stiffness to zero after total material collapse as suggested by McCarthy et al. (2005).

2.4 Cohesive zone modelling

As discussed earlier the fracture process in composite laminates is quite complex, involving both intralaminar damage mechanisms (eg. matrix cracking, fibre fracture) and interlaminar damage (delamination). Without the delamination failure mode, the predictive capabilities of progressive failure analysis remain limited. The majority of models currently

available in literature are capable of predicting intralaminar and interlaminar failure individually. Several different techniques have been used to predict delamination, including Virtual Crack Closure Technique (VCCT), cohesive zone modelling and special delamination failure criteria. In this project delamination is considered important due to its significance emphasised by several authors mentioned earlier. After considering several techniques it was decided to use cohesive zone modelling to predict delamination. The cohesive zone modelling was selected over VCCT and delamination criteria because of the following reasons:

- Care must be taken in selecting the element size at the crack tip when using VCCT to simulate delamination. Raju (1988) has shown that the individual components of the energy release rate do not converge when the ratio of the size of delamination tip element to the ply thickness decreased.
- An initial delamination must be defined to use the VCCT approach, which defeats the purpose of predicting the occurrence of delamination.
- Cohesive zone modelling combines a stress based formulation with fracture mechanics based formulation to predict the initiation and progression of delamination.
- Cohesive zone modelling is capable of capturing non-self similar crack growth, which is a very important quality to model composite failure as pointed out by de Moura et al. (2000).
- It is difficult to experimentally determine the properties required to model delamination using delamination failure criteria.

In Abaqus, cohesive zone modelling can be implemented using cohesive elements or cohesive surface definitions. To accurately simulate the interlaminar cracking process an appropriate constitutive equation for the cohesive elements/surface is required. The constitutive equation for the interface are phenomenological mechanical relations between the tractions and interfacial separations such that, with increasing interfacial separation, the tractions across the interface reach a maximum, decrease and vanish when complete decohesion occurs. The following different constitutive equations are available for defining the traction-separation law as described by Needleman (1987), Xu et al. (1987), Needleman (1999) and Crisfield et al. (1997):

- Linear elastic-perfectly plastic equation
- Linear elastic-linear softening equation (or Bi-linear equation, most common)

- Linear elastic-progressive softening equation
- Linear elastic-regressive softening equation

An accurate prediction of the length of the cohesive zone ahead of a crack tip is fundamental for the correct simulation of delamination in composite materials under both quasi-static and fatigue loading. To ensure correct dissipation of energy during delamination propagation, several cohesive finite elements (up to 3 or 4) have to span the cohesive zone (Turon et al. 2008). The length of the cohesive zone depends on:

- Material properties
- Geometry/size of the structure
- Loading mode

For a typical carbon/epoxy or glass/epoxy composite material, the length of the cohesive zone is smaller than one or two millimetres (Turon et al. 2007). The requirement of a cohesive zone length can sometimes lead to a very fine mesh and hamper the computational efficiency of the model. An alternative approach to smaller element size in the cohesive zone is to reduce the strength τ_3^0 and τ_{shear}^0 such that the length of the cohesive zone increases to cover at least three elements. The propagation of an existing delamination can be considered to be driven by the energy release rate, which is calculated more accurately when the damage zone is elongated. This approach reduces the cost of the simulations. It is recommended that mode I and mode II strengths must be reduced by the same factor in mixed mode loading. If the pure mode interface strengths are lowered by a different factor, the shape of the initiation surface changes and, therefore, the results of the simulation become inaccurate, specially if the mode ratio changes during the simulation (Turon et al. 2007). Reduction of interfacial strength may accurately predict delamination growth; however, it can also lead to changes in stress distribution around the crack tip. Therefore, it should be used with caution.

2.5 Conclusion

A detailed literature review of current experimental and modelling techniques has been presented. The presented literature survey showed that the majority of the available work on the effect of bolt torque and clearance is related to straight shank bolts. Very limited literature is present on the effects of bolt torque, clearance and countersunk depth to thickness ratio for countersunk composite bolted joints. Significant efforts have been made on linear modelling of the composite bolted joints. This has showed that the

presence of countersink alters the stress and strain field around the hole. However, the majority of the current non-linear analytical work involved writing a user subroutine for composite failure analysis, and therefore is not useful without the access to the codes. The literature review also highlighted the advanced modelling techniques available in current finite element software which can be used to model the behaviour of bolted composite joints.

In the current work, the effects of bolt torque, clearance and countersunk depth to thickness ratio on the behaviour of countersunk joints are investigated. The through-thickness damage profile of the joint is also characterised against the tested parameters. Finite element modelling is used to further investigate the effects of the tested parameters on the stress distribution, initiation and progression of damage in single lap joints. Interlaminar and intralaminar damage approaches are combined to predict the failure behaviour of bolted composite joints. In this respect, the present work provides an insight in the area of mechanically fastened joints where there is significant need of detailed investigation.

3 EXPERIMENT METHODS

An experimental investigation was conducted on the effects of bolt torque, clearance and countersunk depth to thickness ratio on single lap countersunk bolted joints. This chapter describes the pre-testing preparations, testing procedure and microscopy analysis conducted on the joints.

3.1 Testing preparations

A plain weave prepreg carbon fibre/epoxy (T300/970) plies with a nominal thickness of 0.22 mm were used. The lay-up was symmetric and quasi-isotropic with alternate plies at an angle of 0^o and 45^o. Depending upon the thickness of the laminate a total of 14 plies (3.08 mm) and 16 (3.52 mm) plies were used. The manufacturer recommended procedure was used for laminate manufacturing. Table 3-1 shows the variables tested in the experimental regime. A straight shank hole laminate was tested under bearing and a range of countersunk single lap joints were tested at different bolt torque (BT), clearance (CL) and countersunk depth to thickness (HT) ratio levels. The bolt torque was varied from 0 Nm to 4.206 Nm. The maximum shear-off torque for selected nut assembly was in the range of 4.5 Nm - 5.6 Nm (HI-LOK standard 1979) (Hi-Lok). The selected torque values were 0%, 41% and 83% of maximum average shear off torque. A calibrated torque wrench was used to provide a consistent torque without reaching the shear-off value as this has a large variable range. Similarly, clearance was varied from 0 to 440 µm. Except for the neat fit joint, it was decided to test clearance beyond the current aerospace recommendation of 1% of bolt diameter (McCarthy et al. 2005). The selected values were 5% and 9% of bolt diameter respectively. The countersunk depth to thickness ratio was varied from 0.56 to 0.76. ASTM D5961 suggests a reasonable range of countersunk depth to thickness ratio to be between 0 – 0.7. An average value of ~0.5 is currently used in practice. In the current work it was decided to test the values close to the extreme and beyond the suggested range. A detailed summary of the tested specimen is provided in Table 3-1.

To use the Hi-Lok fastening system additional attachments were designed which required recalibration of the torque wrench. The hole clearance was created using a standard metal drill bit to increase the diameter of only the straight shank region of the hole. The quality of the hole was improved using a special sanding tool. The dimensions of single lap joints are shown in Table 3-2 and Figure 3-1. The dimensions of bearing specimens

are shown in Figure 3-2. A detailed description of specimen dimensions, laminate manufacturing and joint preparation including hole over-sizing, torque wrench calibration etc. is provided in Appendix I.

Table 3-1 Specimen Details

	Bolt torque (N m)	Clearance (μm)	HT	Number of specimens
Bearing	n/a	n/a	n/a	4
BT1	0 (finger tight)	0	0.56	3
BT2	2.103	0	0.56	3
BT3	4.206	0	0.56	3
CL1	2.103	0	0.56	3
CL2	2.103	240	0.56	3
CL3	2.103	440	0.56	3
HT2	2.103	0	0.56	3
HT1	2.103	0	0.64	3
HT3	2.103	0	0.76	3

Table 3-2 Dimensions of single lap joint (mm)

Tests	*L*	*t*	*w*	*e*	*D* (Bolt)	*A*	*OL*	Plies	*HT*	*SLT*	*SLB*
BT	152.4	3.52	31.75	31.75	4.76	9.56	63.5	16	0.56	5	7
CL	152.4	3.52	31.75	31.75	4.76	9.56	63.5	16	0.56	5	7
HT1	152.4	3.08	31.75	31.75	4.76	9.56	63.5	14	0.64	5	7
HT2	152.4	3.52	31.75	31.75	4.76	9.56	63.5	16	0.56	5	7
HT3	152.4	3.52	31.75	31.75	6.35	12.71	63.5	16	0.76	5	7

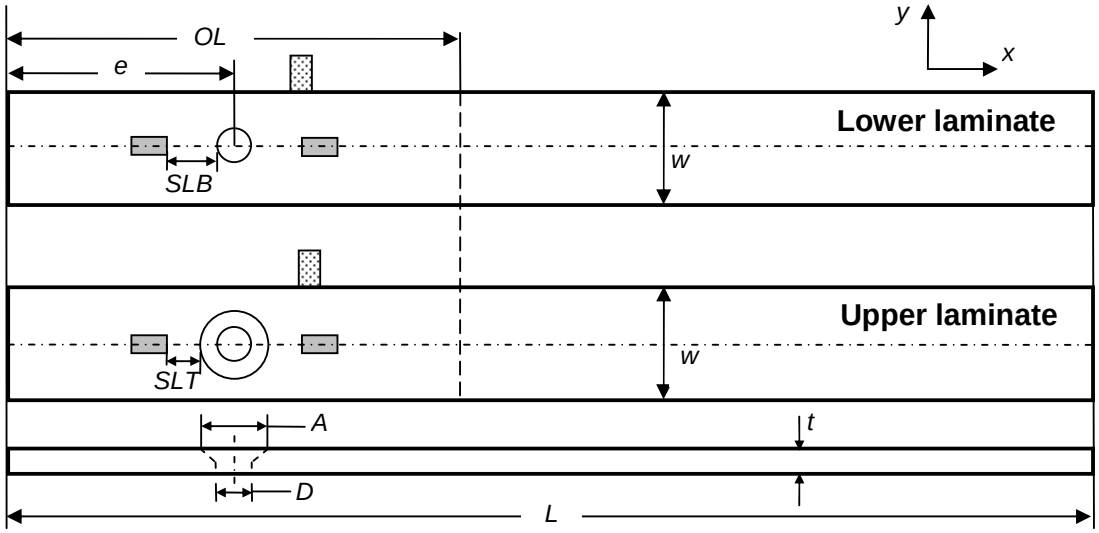

Figure 3-1 Single lap joint geometry

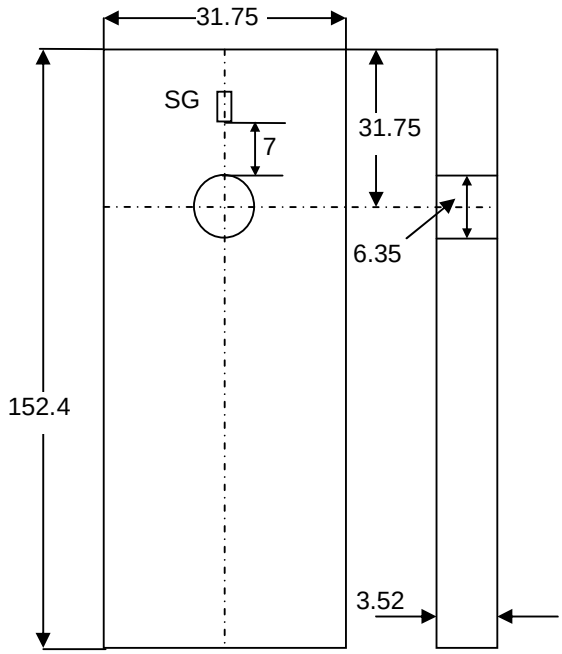

Figure 3-2 Filled hole specimen dimensions (mm)

3.2 Test setup

The tests were conducted on an MTS®- 810 Material test system with a maximum load capacity of 100 kN. An MTS® extensometer was used to record the displacement of the specimens. The tests were conducted in displacement control, with a loading rate of 0.5 mm/min. The test data acquisition was done at the rate of four data points per second from the test machine and extensometer and at the rate of one data point per second from the strain gauges (SGs). Both the bearing test and countersunk single lap joints were tested using the same setup. As bearing failure is a progressive non-catastrophic damage, tests were stopped after a drop in the load was noted in the load-displacement curve together with significant visible bending and increased crackling noise.

Prior to assembling the joint, tabs were attached to each joint member. The tabs were used to attach an extensometer to the joint. The extensometer was used because the displacement value from the machine grips included machine compliance which could lead to erroneous results. The extensometer tabs for the single lap joint were placed 12 mm apart as shown in Figure 3-3. The extensometer was modified so that it could be attached to the tabs. The modified extensometer is shown in Figure 3-4.

The strain gauges were attached after the joints were assembled to minimise the chance of damaging the strain gauge during joint assembly. For the case of the bearing test all

the specimens were strain gauged, however, only one specimen of each single lap joint configuration was strain gauged.

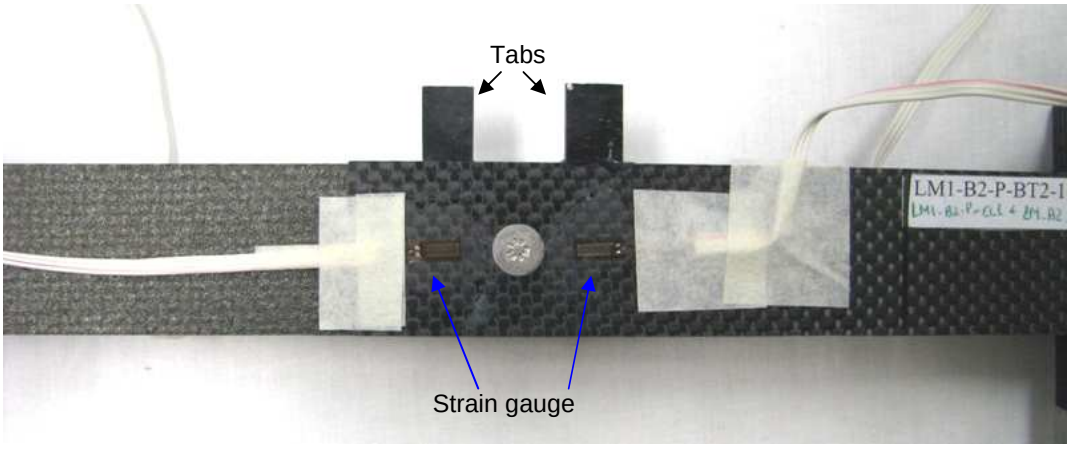

Figure 3-3 Assembled single lap joint

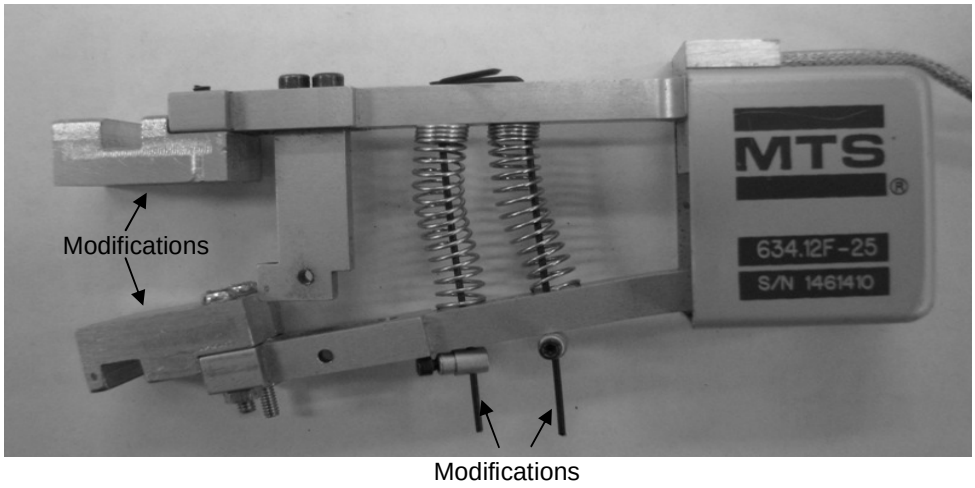

Figure 3-4 Modified extensometer

The complete experimental setup for the bearing test together with a simplified schematic is shown in Figure 3-5. The test fixture and the bolt used for the bearing test were manufactured from high strength steel. The bolt was finger tightened providing no lateral constraint to the fixture. There was no lateral support provided by the test fixture to the bearing specimen. The extensometer was secured to the test fixture at one end and to the extensometer tab at other end, as shown in Figure 3-6. Four specimens were tested for the bearing test. Three specimens were loaded up to ultimate failure load (UFL), however one specimen was loaded up to the initiation of non-linearity.

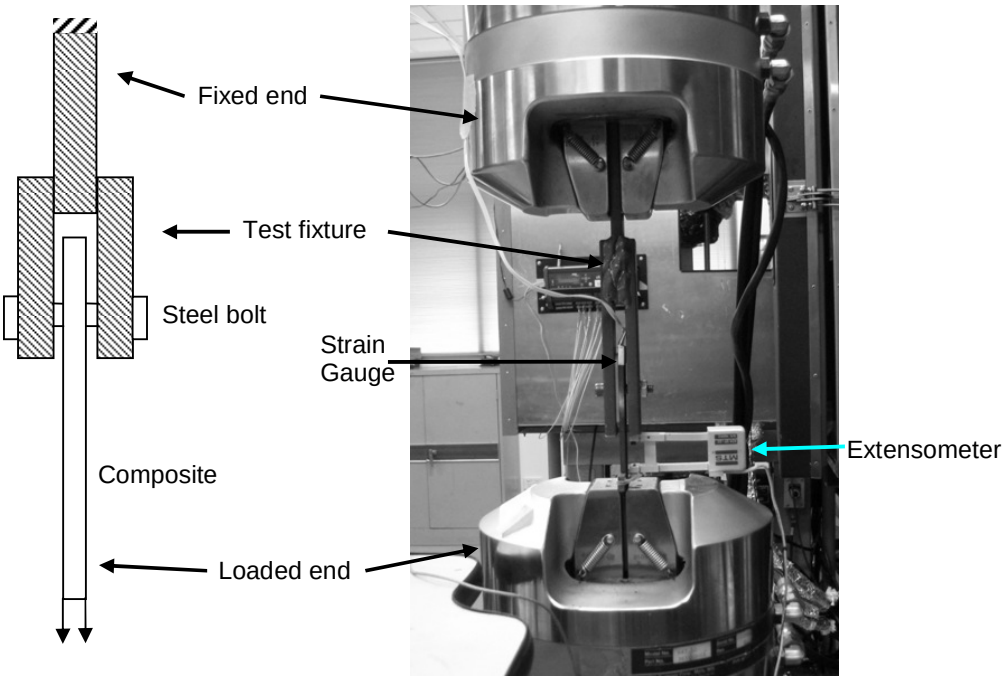

Figure 3-5 Experimental setup for bearing test

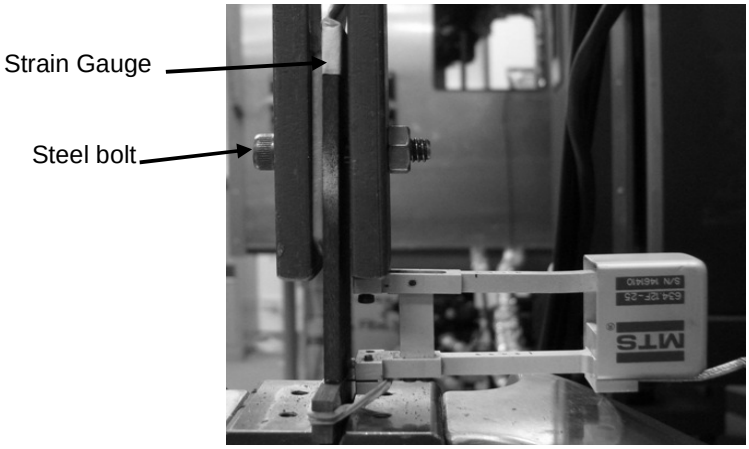

Figure 3-6 Extensometer attachment for bearing test

The complete experimental setup for the single lap joint is shown in Figure 3-7. Figure 3-8 shows the extensometer attachment and the location of the SG for the single lap test. No lateral support was used in the experiments. The extensometer was attached very close to the hole to reduce the effect of bending on the extensometer reading. All the tests had the same setup where the end of the countersunk laminate was pulled in tension and the end of the bottom laminate was fixed. Three specimens were tested for each joint configuration as shown in Table 3-1. All the specimens were loaded to maximum failure load.

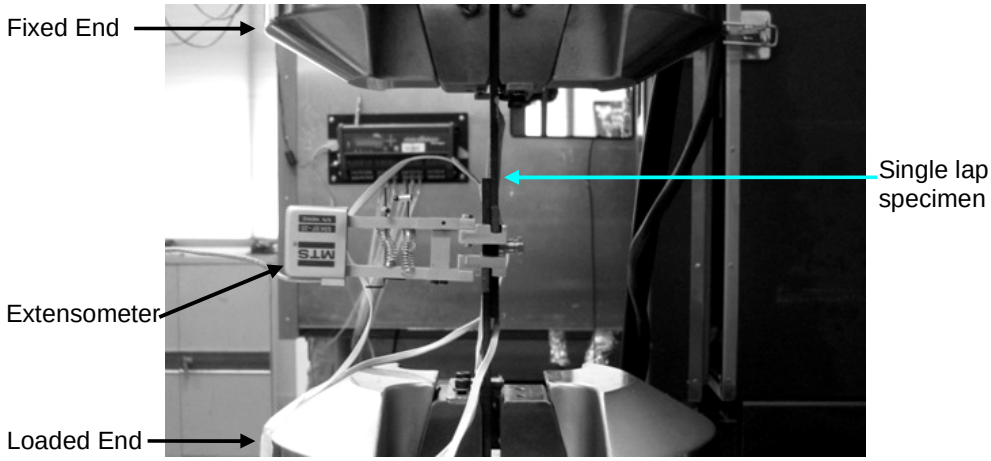

Figure 3-7 Single lap test set up

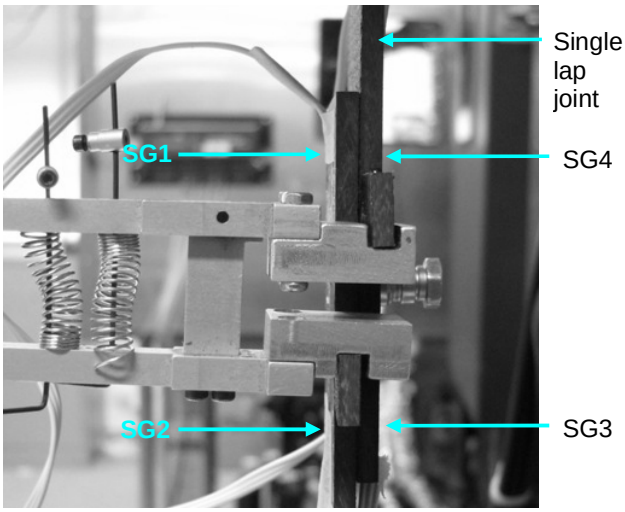

Figure 3-8 Extensometer attachment and strain gauges for single lap joint

3.3 Microscopy

Destructive microscopy was used to perform the damage analysis. For bearing specimens, two samples were selected for post test damage analysis. For single lap tests one specimen per test was evaluated using microscopy. Two sections at 45^{o} and 0^{o} to the applied load were analysed. The sections are shown in Figure 3-9. Figure 3-9 also shows the cylindrical coordinate system used to plot radial and tangential stresses around the circumference of the hole. The sections at 0^{o} and 45^{o} provide the progression of damage along the perimeter of the hole together with the through-thickness progression of damage. For the single lap joint, bearing occurred on opposite sides of the hole for the upper and lower laminates. Therefore to account for this the sections were cut from

diametrically opposite sides as shown in Figure 3-10. This procedure allowed an inspection of the most damaged region of the single lap joint.

A micrograph of the undamaged hole edge of a bearing and single lap sample is shown in Figure 3-11. In the case of the single lap joint, the bottom surface of the upper laminate and the top surface of the lower laminate were in contact and formed the shear plane of the joint. The micrographs were taken at 5X magnification using a Leica optical microscope.

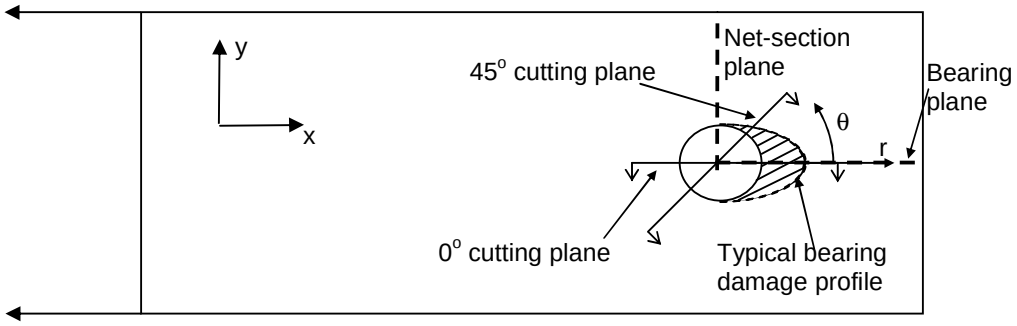

Figure 3-9 Sections for post processing

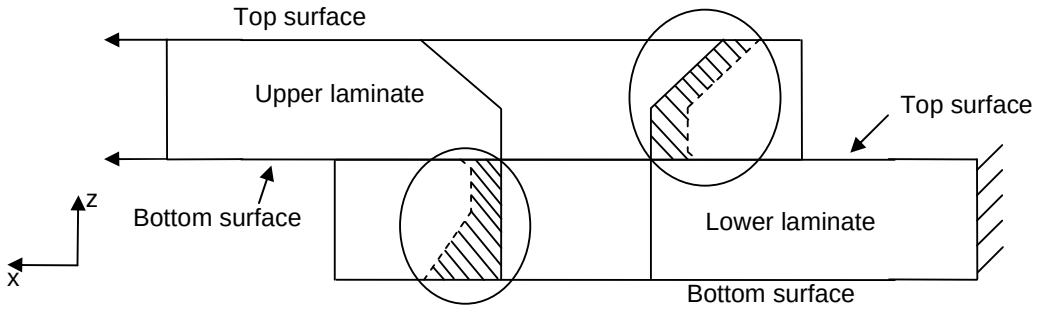

Figure 3-10 Inspected regions of single lap specimens

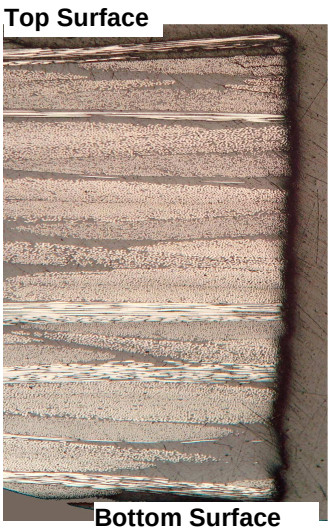

a) Lower laminate/Bearing specimen

b) Upper laminate

Figure 3-11 Undamaged laminates

3.4 Conclusion

An experimental investigation was conducted on the effects of bolt torque, clearance and countersunk depth to thickness ratio on the behaviour of single lap composite joints. The tests were conducted based on ASTM D5961. Destructive microscopy was used to analyse the through-thickness damage profile of the joints.

4 EXPERIMENT RESULTS

In this chapter, experimental results of the tested joint configurations are discussed. Micrographs of through-thickness damage profile are also discussed to characterise the effect of various parameters on the damage profile. A summary of major conclusions is provided at the end of the chapter.

4.1 Bearing Test

The major failure mode in the bearing test was the bearing of the specimen. No net tension, shear out or bending failure was noticed during the testing. The test was repeated on four different specimens, out of which three were loaded beyond the linear region and one specimen was loaded up to the initiation of non-linearity, as shown in Table 4-1. The purpose of loading specimen 4 up to the initiation of non-linearity was to gain insight into the progression of bearing failure in the specimen. As shown in Table 4-1 specimens 2 and 4 were selected for sectioning and microscopy. The method described in ASTM D953 was used to determine the bearing load (BL). However, during testing the deformation of the hole was not recorded, therefore the extensometer displacement was used to determine the bearing load. ASTM D953 suggests 4% hole diameter to be used as the critical value to determine bearing load as shown in Figure 4-1. The average bearing load for the bearing tests was estimated to be approximately 9.14 kN.

In the case of CT_FL_1 laminate there were two maximum failure loads as shown in Figure 4-1. For the purpose of this work the first maximum load was used as the ultimate failure load (UFL). This was due to the fact that the second maximum load occurred after the strain gauge was damaged due to extensive bearing failure. The composite was assumed to have failed in bearing if the hole elongation was more than 15% of the hole diameter (Johnson et al. 2007). In the case of the second maximum load the hole elongation was significantly larger than 15%. The difference between first and second maximum loads was approximately 2.3%, which can be considered negligible. In all the load-displacement curves the load was plotted against the displacement value determined using the extensometer. The load-displacement behaviour for all the specimens is shown in Figure 4-2. The initial no load region in the load-displacement curve can be due to a mismatch between the hole and bolt diameters, initial adjustment of the machine and initial adjustment of the extensometer. The linear behaviour of all the specimens was very similar. The first non-linearity load compared very well for all the specimens. The

maximum difference between the first non-linearity load was approximately 5%. The response after the first non-linearity load was not as comparable as the linear response. Specimen 1 and 3 showed very similar behaviour, however specimen 2 showed higher stiffness in the non-linear regime compared to the other specimens. The ultimate failure load had approximately 5.4% variation between all the tested specimens.

Table 4-1 Bearing test results

Specimens	Loading regime	FNL load (kN)	BL (kN)	UFL (kN)	Sectioning
CT_FL_1	Ultimate failure	9.67	9.05	13.03	N/A
CT_FL_2	Ultimate failure	9.69	9.7	12.36	✓
CT_FL_3	Ultimate failure	9.41	8.6	12.91	N/A
CT_LL_4	First non-linearity load	9.88	9.2		✓
Average		9.66	9.14	12.77	

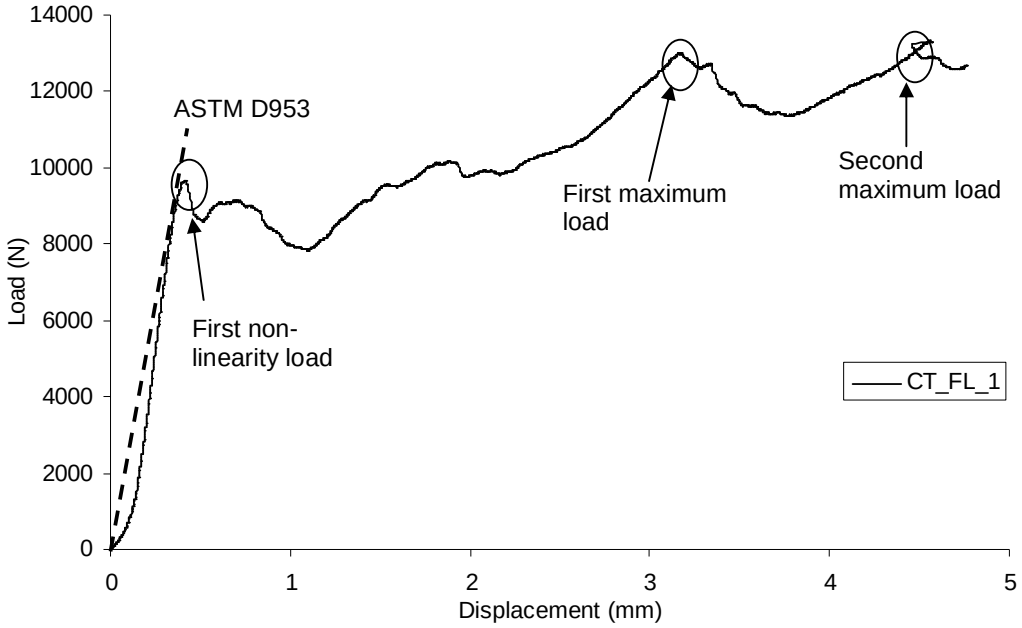

Figure 4-1 Load-displacement curve of specimen 1 under bearing

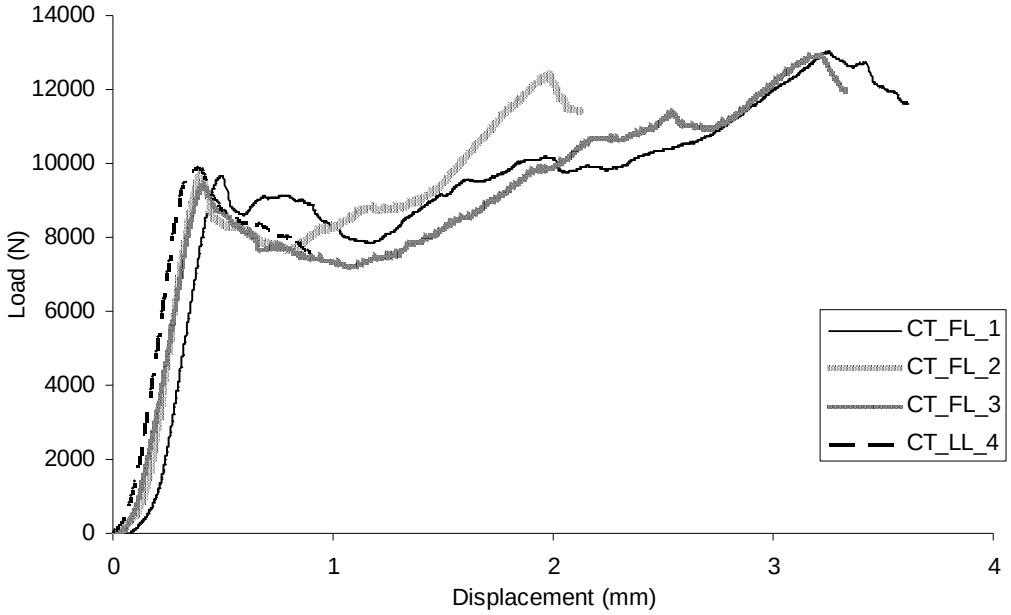

Figure 4-2 Load-displacement curves for bearing test

The strain gauge was located 7 mm from the hole edge in the compression region. The strain initially had a linear behaviour until the first non-linearity load. However, due to the occurrence of damage, the stress was redistributed in the material leading to relaxation which is clearly visible in Figure 4-3. Figure 4-4 shows the strain distribution for the bearing test specimens. It can be seen in Figure 4-4 that the maximum strain occurred at the ultimate failure load of the specimen.

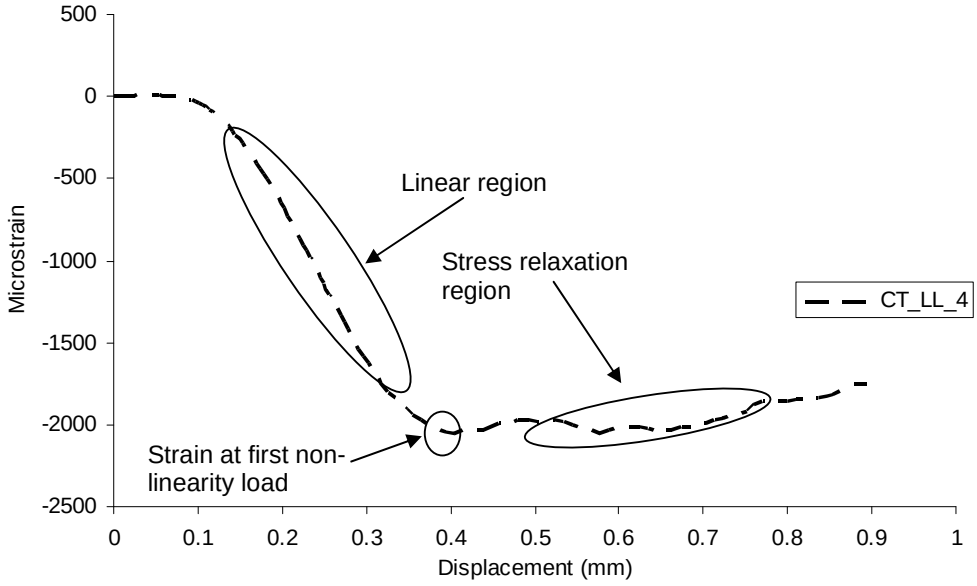

Figure 4-3 Strain data for specimen loaded up to the linear load

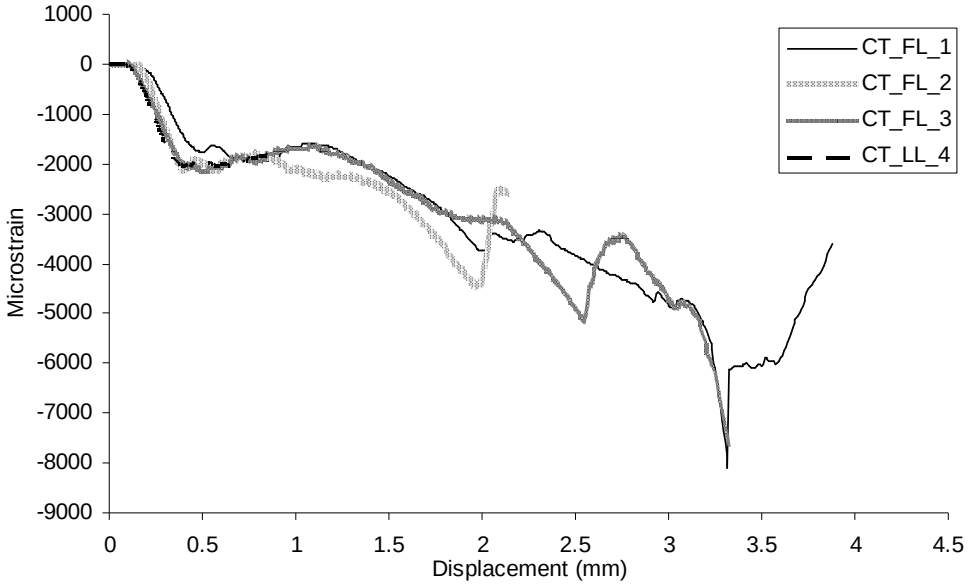

Figure 4-4 Strain data for bearing test

The micrographs of the specimen loaded to the first non-linearity are shown in Figure 4-5. From Figure 4-5 it can be seen that the damage increased significantly from 45^o to 0^o cutting planes. In the 45^o cutting plane some edge damage was recorded close to the top surface of the laminate. The 45^o section also showed formation of interlaminar and intralaminar shear cracks as described previously in the literature review. Some delamination could also be seen close to the top and bottom layer of the laminate. This could have occurred due to composite fraying under the bearing load leading to delamination of the layers close to the top and bottom surfaces. The 0^o cutting plane showed similar damage to the 45^o cutting plane, however the extent of damage was more with clearly visible shear crack bands and the damage extended further from the edge of the hole.

a) Damage at 45^o cutting plane

b) Damage at 0^o cutting plane

Figure 4-5 Damaged edge for specimen loaded up to linear load

The damage in the specimen loaded until ultimate failure load is shown in Figure 4-6. Figure 4-6a clearly shows the classical fraying associated with bearing damage. The same damage mechanisms as reported for the specimen loaded up to the first non-linearity load were seen for fully loaded specimens. The 45^o cutting plane also showed significant loss of material and loss of the hole edge. Similarly for the 0^o cutting plane, the damage mechanisms were the same as listed above, however, the amount of damage seemed to be less. The amount of delamination visible in the fully loaded specimens reduced. This was due to the fact that the 0^o cutting plane suffered extensive material and edge loss due to bearing and also during sectioning. This reduced the amount of visible through-thickness damage in the section.

Compared to the specimen loaded up to the first non-linearity load, the fully loaded specimen experienced significantly larger amounts of damage. The fraying associated with bearing was visible only in the fully loaded specimen. The fully loaded specimen also experienced extensive material and hole edge loss, which was not visible in the specimen loaded up to the first non-linearity load.

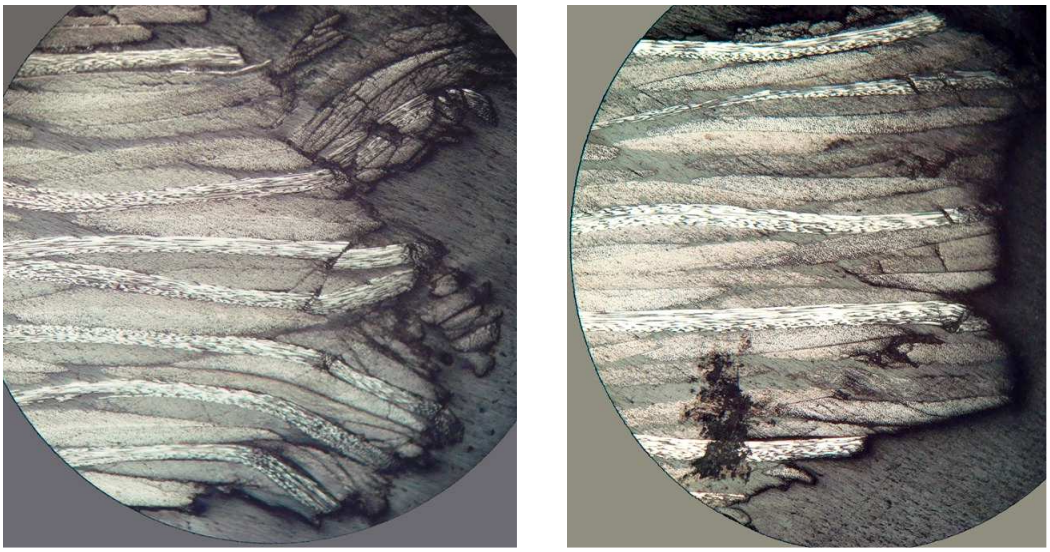

a) Damage at 45^{o} cutting plane b) Damage at 0^{o} cutting plane

Figure 4-6 Damaged edge for specimen loaded up to ultimate load

From the above analysis the following conclusions can be drawn:

- The amount of damage reduced along the edge of the hole as the angle moved away from 0^{o}.
- The damage mechanisms which constituted bearing failure were:
    - Interlaminar and intralaminar shear cracks comprising of:
        - Fibre kinking
        - Fibre matrix shear
        - Matrix compression
- Delamination was not a major failure mode. It can be considered as a consequence of shear cracks.
- The amount of damage significantly increased from the first non-linearity load to the ultimate failure load.
- The first non-linearity load was caused by the initiation of the damage mechanisms constituting bearing failure. Once initiated, the damage led to complete crushing of the edge material, which provided resistance to further crushing leading to an increase in the load-carrying capacity until ultimate failure occurred. Beyond ultimate failure, this cycle of crushing and resistance repeated until loading was stopped, however, there was not much increase in the ultimate failure load. This phenomenon was visible in Figure 4-1.

4.2 Effects of bolt torque

Three different bolt torques as shown in Table 3-1 were used to characterise the effects of bolt torque on the behaviour of the single lap joint. The selected bolt torque range covered the practical range of bolt torques, applicable to the industry. To achieve zero Nm torque, the nut was finger tightened. The load-displacement behaviour of BT1 joints is shown in Figure 4-7. It can be seen that all three repetitions were very close to each other. The coefficients of variation were 0.53% for average ultimate failure load and 4% for average bearing load (BL).

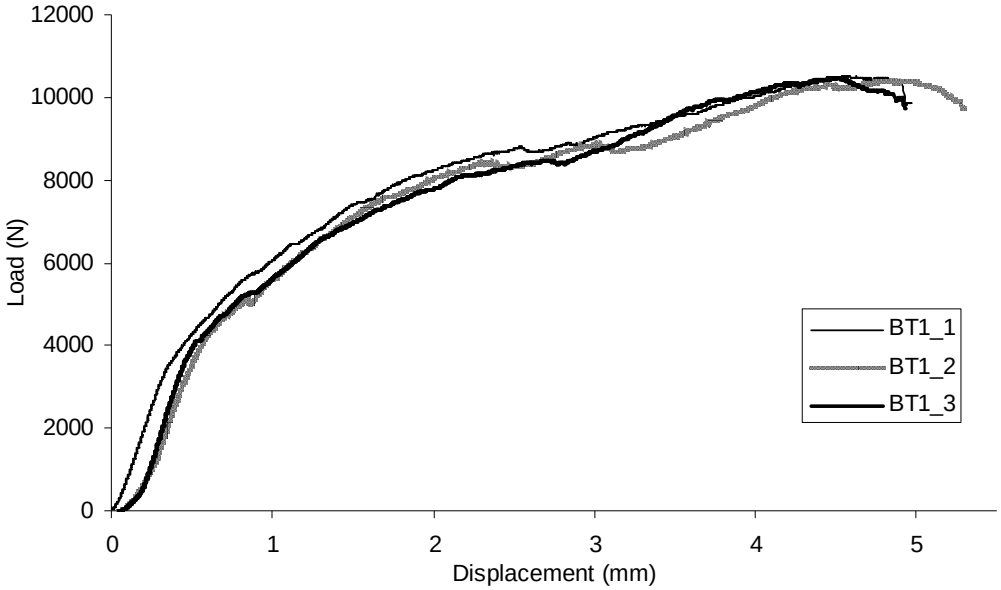

Figure 4-7 Load-displacement behaviour for joints with 0 Nm torque

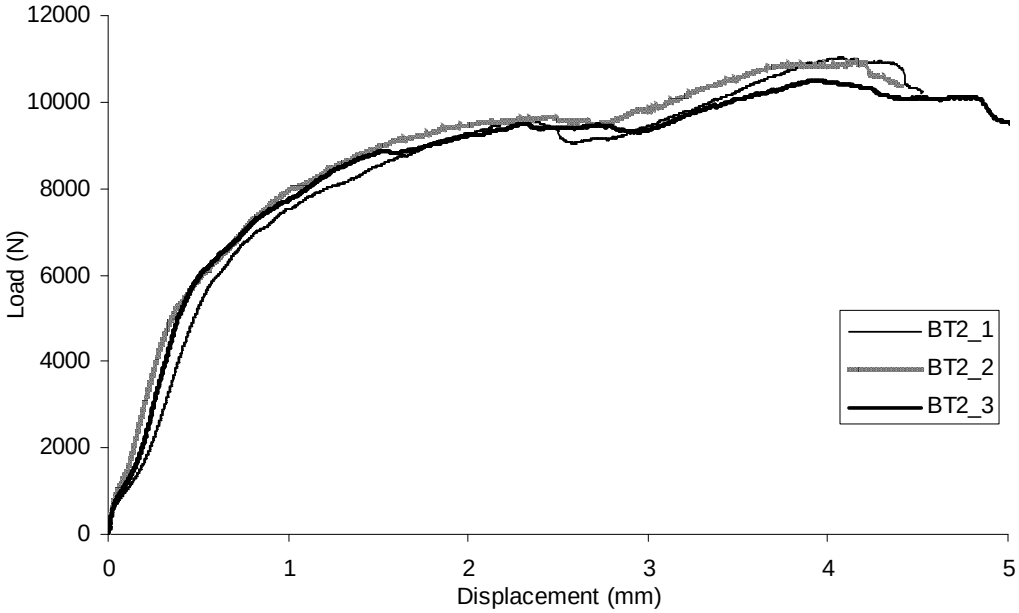

Figure 4-8 Load-displacement behaviour for joints with 2.103 Nm torque

The load-displacement curves for BT2 are shown in Figure 4-8. In this case the coefficients of variation were 2.6% for average ultimate failure load and 9.8% for average bearing load. Similarly for the case of BT3 shown in Figure 4-9, the coefficients of variation were 0.54% for average ultimate failure load and 5.4% for average bearing load.

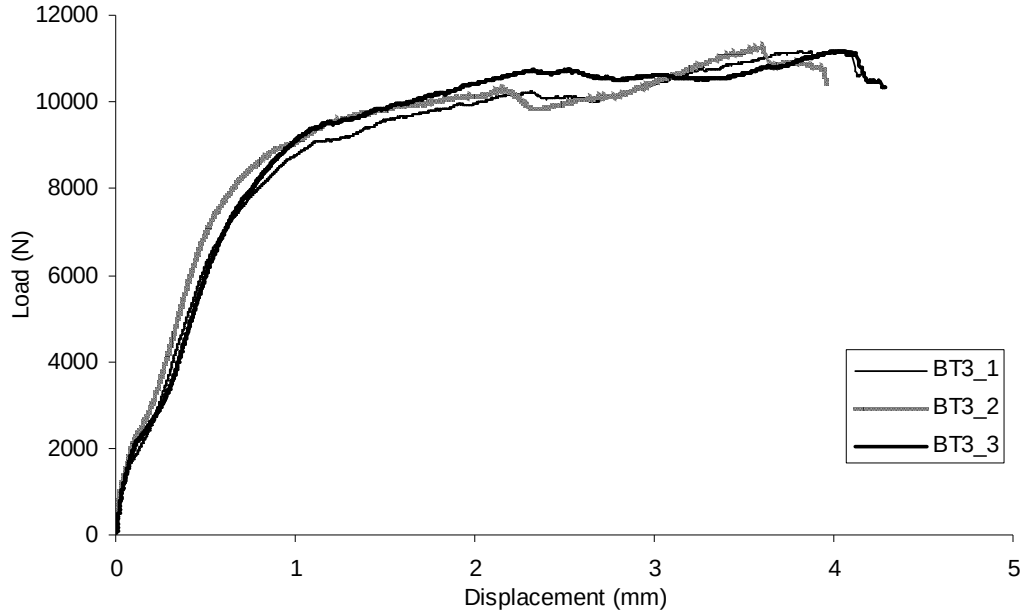

Figure 4-9 Load-displacement behaviour for joints with 4.206 Nm torque

Figure 4-10 shows the effects of bolt torque on the load-displacement behaviour. A representative curve for each bolt torque was used to compare the results. The figure clearly shows that as the bolt torque was increased the ultimate failure load increased and the failure displacement (FD) reduced. It can be seen in the figure that there was a transverse shift in the load-displacement curve. Another noticeable difference was the delay in the reduction of the load-carrying capacity after the maximum load was reached. For the case of BT1 the maximum load occurred at 4.57 mm (approx.) and the significant reduction in the load-carrying capacity was noticed at 4.90 mm (approx.). This reduced to 4.15 mm (approx.) and 4.20 mm (approx.) for the case of BT2, however, in the case of BT3 the reduction was almost immediate. A slight change in initial slope can be seen in Figure 4-8 and Figure 4-9. This is due to the effects of frictional forces. It is easier to explain these effects using an example of joints with clearance, therefore, an explanation is provided in the next section.

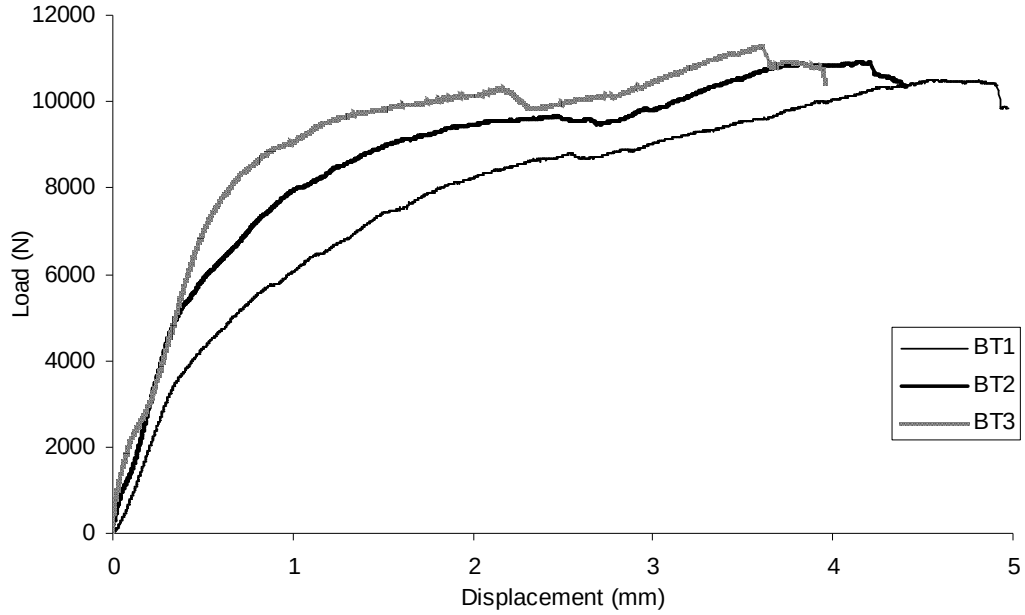

Figure 4-10 Effects of variation of bolt torque

From Table 4-2 it can be seen that changing the bolt torque from 0 to 4.206 Nm led to approximately 7.2% improvement in the load-carrying capacity of the joint. Despite a significant increase in bolt torque the improvement in ultimate failure load was not very significant. A significant increase in bearing load with increased bolt torque could be seen in Table 4-2. The initial application of the torque led to significant improvement in bearing load, however, the subsequent increase in the torque value led to slight reduction in the value of bearing load. The difference was minor and can be considered as negligible. The effects of bolt torque on ultimate failure load and bearing load can be seen from Figure 4-11 and Figure 4-12 respectively. The figures also show the average shear off torque value for the selected fasteners. The load was normalised based on the values of the BT1 joint. The insensitivity of ultimate failure load towards bolt torque was also reported by other authors such as Khashaba et al. (2005) and Sun et al. (2002). Khashaba et al. (2005) showed similar maximum percentage (approximately 6%) improvement in ultimate failure load for the double lap joint under the same bolt torque range. Cooper et al. (1995) also showed that increasing bolt torque has limited improvement in failure load for a given *e/d* and *w/d*.

Table 4-2 Summary of bolt torque results

Experiment	Ultimate failure load (avg.), kN	Bearing load, kN	% Δ Ultimate failure load from BT1	% Δ Bearing load from BT1
BT1	10.46	2.39	0	0
BT2	10.82	3.18	3.38	33.14
BT3	11.21	3.08	7.16	29.07

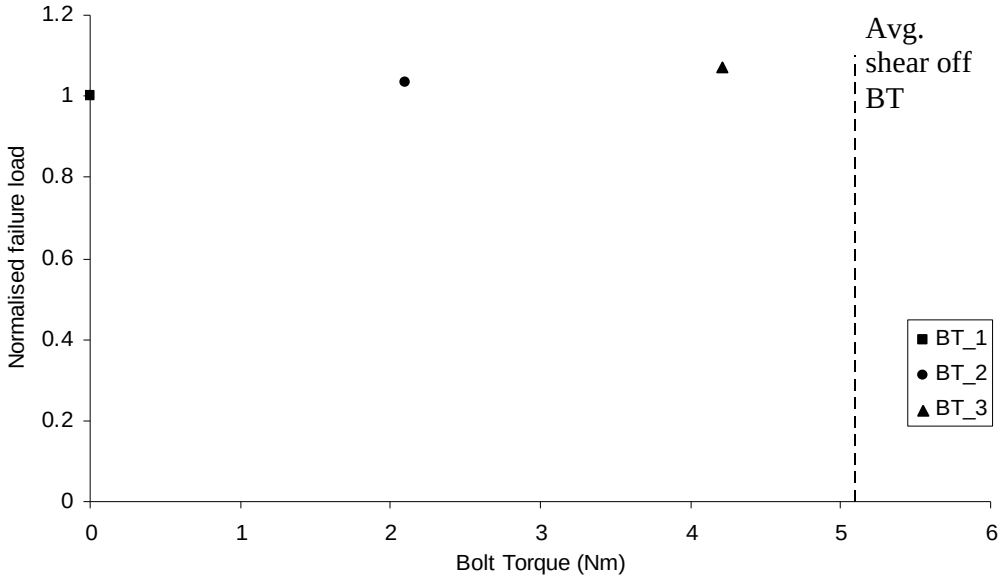

Figure 4-11 Effect of bolt torque on ultimate failure load

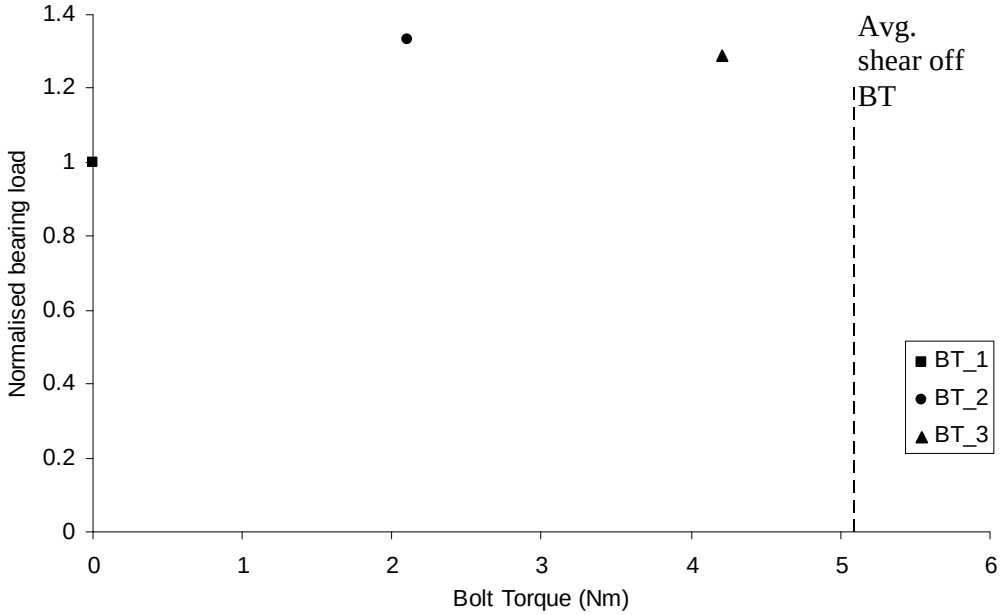

Figure 4-12 Effect of bolt torque on bearing load

To better understand the effects of variation in bolt torque, microscopy analysis was performed on the single lap joint specimens after the specimens were tested. As for the case of bearing samples, 0^o and 45^o sections were used as the cutting planes. A comparison of damage profiles for BT1 joint and bearing specimen highlighted the effects of the countersunk geometry on the damage profile. Comparison of Figure 4-13 with Figure 4-6 shows that the presence of countersunk led to an inclined damage in the upper laminate. It also promoted delamination at the start of countersunk region. The effects of single lap configuration on the damage profile cannot be neglected. However, the highlighted issues were considered to be a consequence of countersunk geometry.

The damage profiles for all the three bolt torques are shown in Figure 4-13 to Figure 4-15. From Figure 4-13 classical fraying associated with bearing is clearly visible. It was also very clear that the top and the bottom half of the upper laminate separated at the location where the countersunk region started. Therefore, delamination occurred in the high stress region. This delamination was termed as Primary delamination. In the countersunk region, a damage fault line could be seen. The fault line was inclined to the vertical and almost parallel to the countersunk edge. Close to the top surface, another delamination seen behind the angular fault line was termed Secondary delamination because it was a secondary effect of through-thickness shear cracking. The straight region of the upper laminate experienced similar failure mechanisms as described for the bearing specimen. A through-thickness crack travelled from the bottom of the laminate to the start of countersunk region.

By applying 2.103 Nm of torque, significant changes in the failure behaviour can be noted from Figure 4-14. The most obvious observation was that the fraying of the countersunk region disappeared and was replaced by bulging out at the top layer. The separation at the start of the countersunk region was suppressed, though the delamination was still present. The damage in the countersunk region was again inclined at an angle to the vertical and parallel to the countersunk edge. Similar to the BT1 joint damage, another secondary delamination close to the top surface was noticed. However, this time the delaminated layer was different to the BT1 specimen. The straight part of the upper laminate did not experience much damage. The majority of the damage was close to the bottom surface of the upper laminate. The major damage mechanism noted in the straight region was through-thickness shear cracking.

As the bolt torque was increased up to 4.206 Nm, the damage was restricted to the edge of the hole as seen in Figure 4-15. Similar to the BT2 specimen, significant bulging was seen at the top surface. The countersunk edge was less damaged compared to joints with 0 Nm and 2.103 Nm torque. However, it can be seen that internally the laminate experienced significant damage in the form of interlaminar and intralaminar shear cracks. As in the previous cases the damage was parallel to the countersunk region. Delamination was initiated in the region where the countersunk started, however, it did not separate as in the case of joint with 0 Nm torque. This delamination transformed into a through-thickness crack leading to more damage. Other delaminations close to the top surface were secondary delaminations as previously discussed.

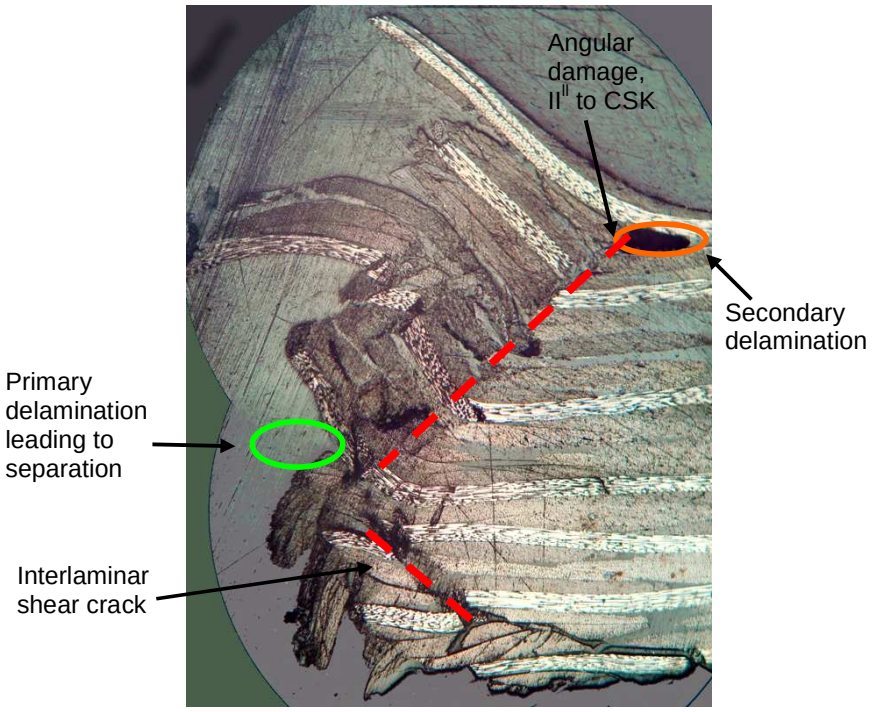

Figure 4-13 Damaged upper laminate at 0^o section for joints with 0 Nm bolt torque

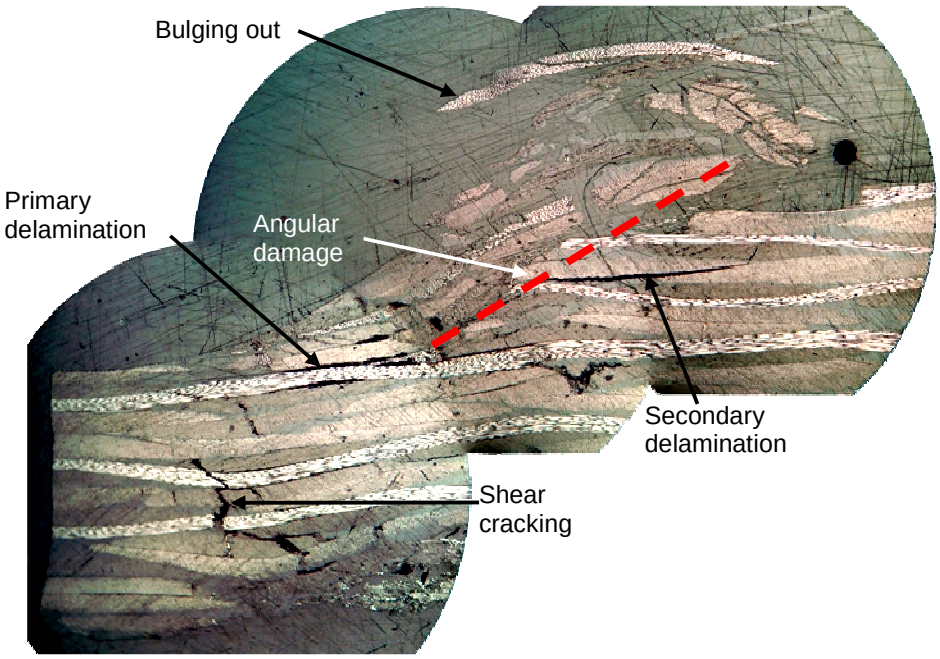

Figure 4-14 Damaged upper laminate at 0^o section for joints with 2.103 Nm bolt torque

For BT1 and BT2 specimens, the upper laminate 45^o sections were damaged during the sectioning process, leading to no results for this section. The 45^o section for the BT3 specimen is provided in Figure 4-16. This provided an indication of how the damage progressed around the hole. The comparison between Figure 4-15 and Figure 4-16 shows that the damage profiles at both angles were similar. The 0^o section experienced much more damage compared to the 45^o section. It is also important to note that no primary delamination was seen in the case of the 45^o section. The secondary delamination was still present close to the top surface of the laminate. The damage fault line was still inclined to the vertical and the countersunk hole edge did not experience any damage, however the bottom section of the straight hole edge was damaged similar to the 0^o section.

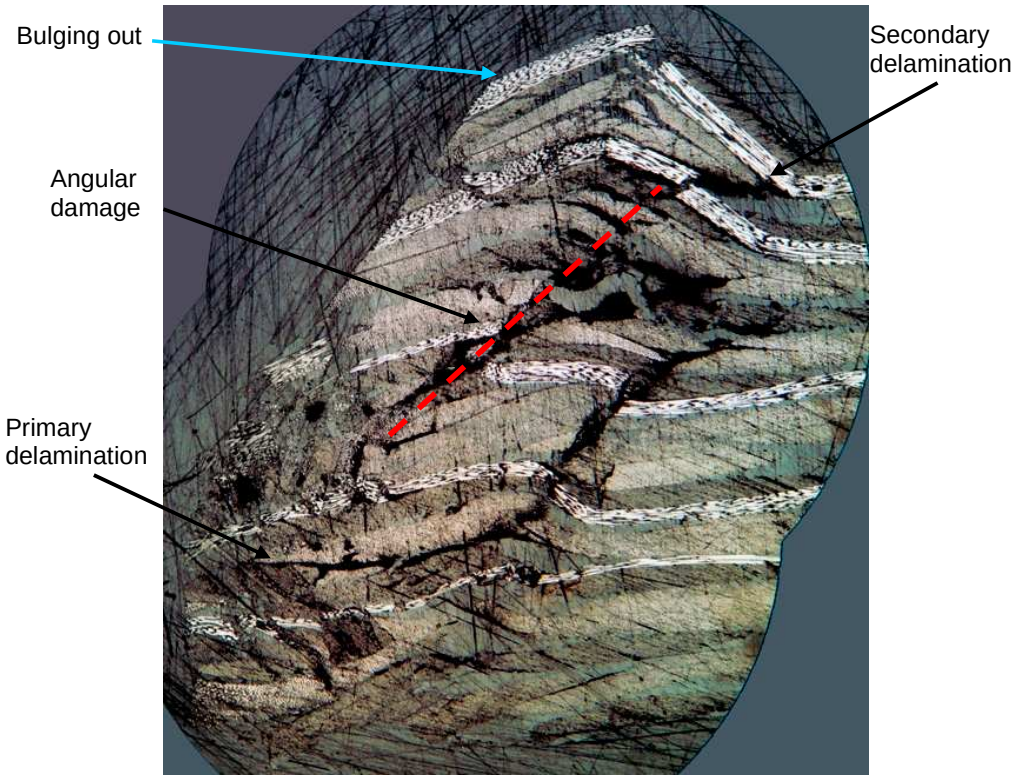

Figure 4-15 Damaged upper laminate at 0^{o} section for joints with 4.206 Nm bolt torque

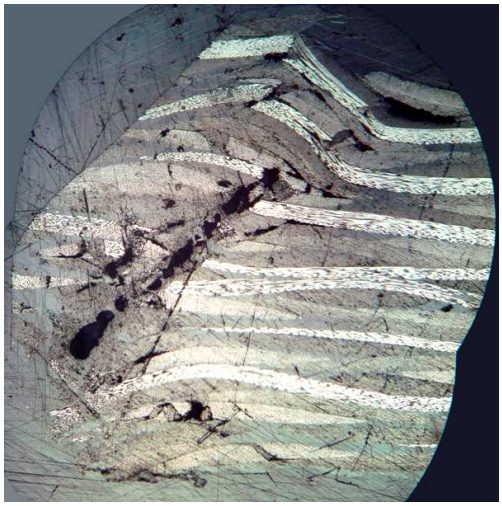

Figure 4-16 Damaged upper laminate at 45^{o} section for joints with 4.206 Nm bolt torque

The lower laminate of the joint as described in Figure 3-10 did not contain any countersunk region, therefore the top surface of the laminate was the surface in contact with the lower surface of the upper laminate. During specimen preparations the 0^{o} section for the joint with finger tight bolt were sectioned incorrectly leading to no results for this section. The damage in the 0^{o} section for the joint with 2.103 Nm torque is shown in Figure 4-17. In spite of the straight hole, the damage in the laminate was divided in two

parts: straight damage region (close to the top surface) and angular damage region (close to the bottom surface). The damage mechanisms of the upper and lower laminates were similar. The damage of the lower laminate comprised of shear cracking, secondary delamination and bulging. However, the lower laminate did not contain any primary delamination for the case of the BT2 joint. The secondary delamination occurred close to the bottom surface and was a result of laminate bulging and angular damage. The edge of the hole did not experience much damage.

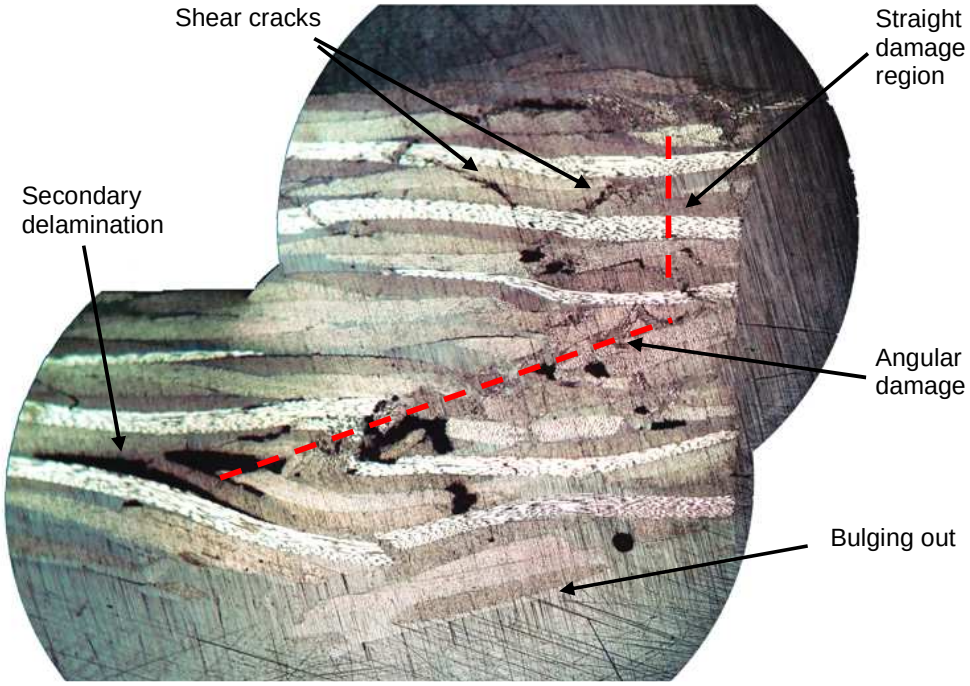

Figure 4-17 Damaged lower laminate at 0^o section for joints with 2.103 Nm bolt torque

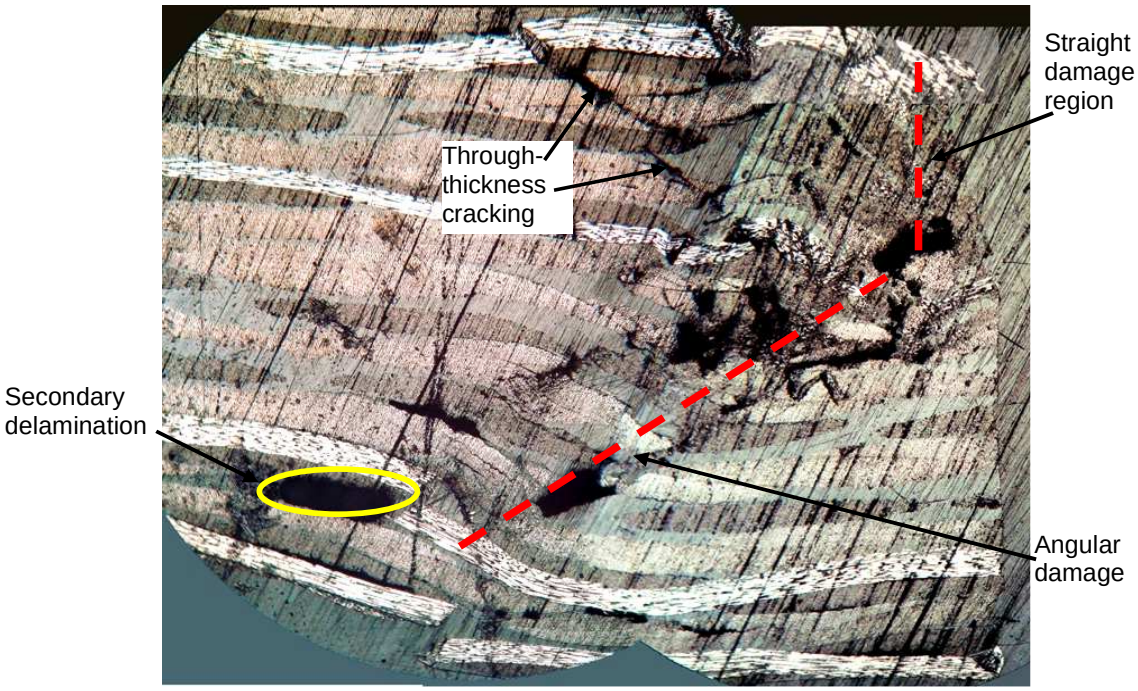

Figure 4-18 Damaged lower laminate at 0^{o} section for joints with 4.206 Nm bolt torque

For the case of the joint with 4.206 Nm torque, the failure profile was similar to the joint with half the torque. The damage was divided in two parts: straight and angular damage. Again no primary delamination was noted for the lower laminate of the BT3 joint. It can be seen that the amount of damage increased compared to the joint with 2.103 Nm torque and the bulging out of the bottom surface became almost insignificant. The damage in the angular band was more severe, leading to multiple secondary delaminations and significant crushing. The straight damage region in the case of the BT3 laminate contained higher crushing damage compared to the BT2 laminate. The damage in the 45^{o} sections are shown in Figure 4-19. For all the 45^{o} sections, the amount of damage reduced compared to the 0^{o} sections. However, all the 45^{o} sections showed material loss in the straight damage region. The material loss can be due to sectioning. The angular damage bands had the similar inclination for all the laminates. All the laminates showed secondary delamination in the fourth or fifth layer from the bottom. No significant bulging was seen at the 45^{o} sections. All the other damage mechanisms present in 0^{o} sections were also visible in the 45^{o} sections.

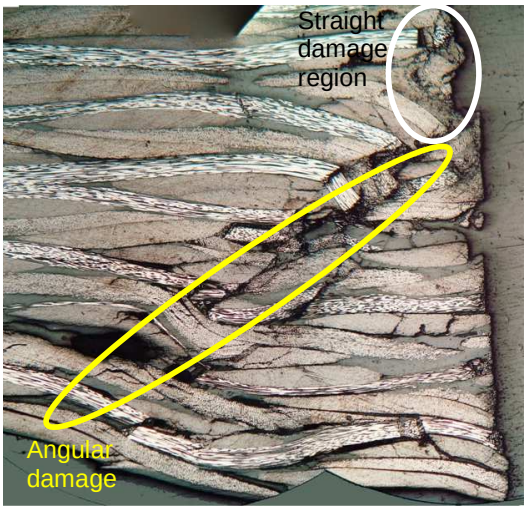

a) LM1_B2_BT1_B

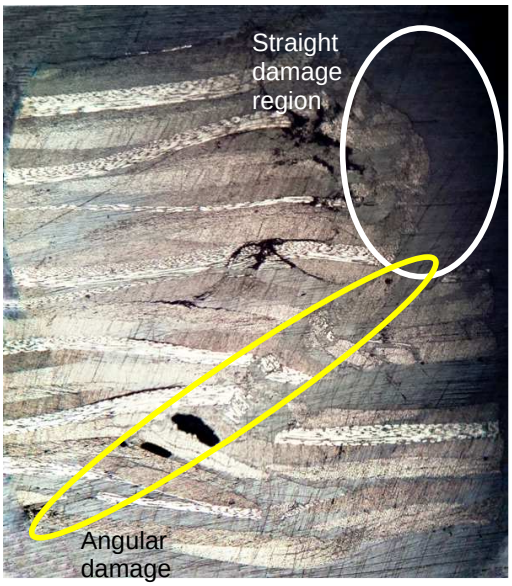

b) LM1_B2_BT2_B

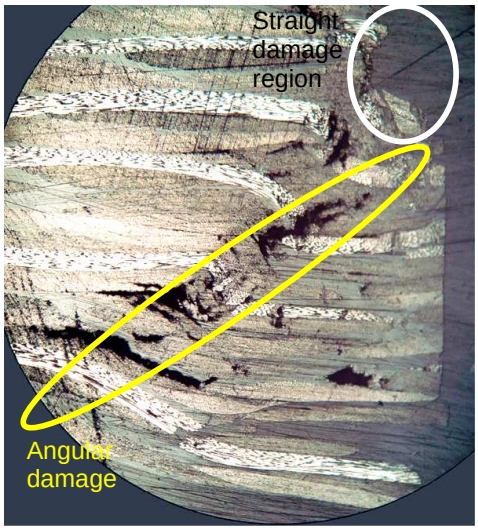

c) LM1_B2_BT3_B

Figure 4-19 Damaged lower laminates at 45^{o} section

The above analysis of failure behaviour for a single lap joint under the effect of bolt torque was used to define a damage profile for this type of joint. The effects of variation in bolt torque on damage profile of a composite single lap joint under tensile loading are shown in Figure 4-20. The given schematic can be used as a guide to show the overall behaviour, however, it is not to scale.

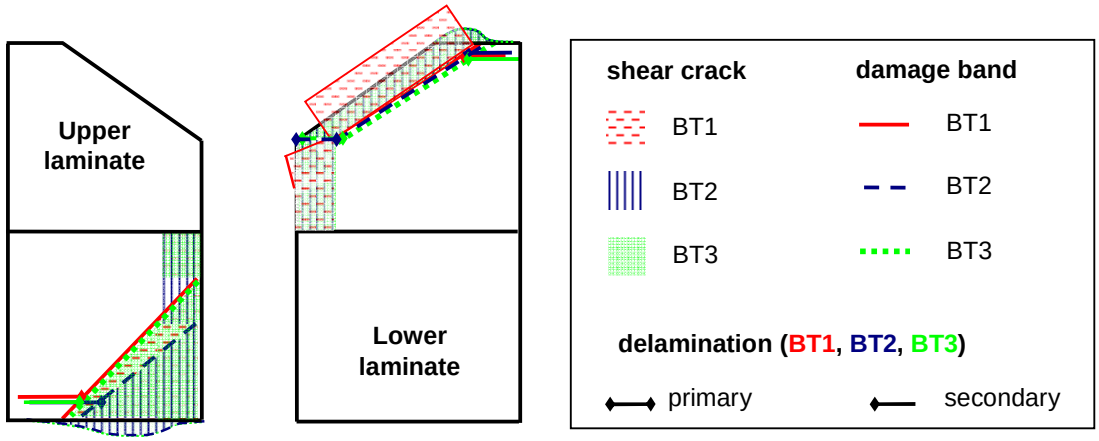

Figure 4-20 Effects of bolt torque on the damage profile of upper and lower laminates at 0^o

The following important conclusions can be drawn from the above analysis:

- The through-thickness damage for both upper and lower laminates was divided in two parts:
  - Angular damage
  - Straight damage
- The primary delamination was only present in the upper laminate close to the start of the countersunk region.
- The secondary delaminations were present close to the free surfaces of the joint (i.e. top surface of the upper laminate and bottom surface of the lower laminate).
- All the damage mechanisms listed in the bearing test results were applicable for the case of the single lap joint test, which includes interlaminar and intralaminar shear cracks.
- The damage reduced in the circumferential direction away from the 0^o cutting plane.
- For the range of bolt torques tested, the inclination of the angular fault line for both upper and lower laminates did not change significantly with a change in the bolt torque.
- No primary delamination was seen for the 45^o sections of the upper laminate. This showed that the delamination was only prevalent close to 0^o sections.
- There was no primary delamination reported for the lower laminate. However, all the sections of the lower laminate experienced secondary delamination.
- The effects of bolt torque on the behaviour of the joint were:
  - The ultimate failure load increased slightly with an increase in bolt torque.

- The bearing load initially increased significantly for a torque of 2.103 Nm, but was unaffected by further increase of torque up to 4.206 Nm.
- The extent of bearing damage reduced with an increase in bolt torque.
- As the torque was increased the fraying of the laminate was converted to bulging out of the top surfaces of the upper laminate.
- The complete separation of layers visible in the finger tight joint was suppressed by the application of bolt torque.
- The application of bolt torque did not prevent the occurrence of the delamination at the start of the countersunk region.
- An increase in bolt torque led to an increase in the density of through-thickness damage in the laminate.

4.3 Effects of clearance

Three different clearances as shown in Table 3-1 were used to characterise the effects of clearance. The present study examined the tolerance levels beyond the current industry practice to establish the response of a single lap joint. Figure 4-21 shows the general arrangement of the laminate with clearance. As described in the Appendix I, the clearance was created by increasing the diameter of the straight shank section of the hole, while, the diameter of the countersunk region was not changed. As shown in Figure 4-21, a change in the diameter of the straight shank also affected the contact condition in the countersunk region. Due to this change it was difficult to ensure that the bolt was perfectly in the middle of the hole. This misalignment affected the initial response of the single lap joint.

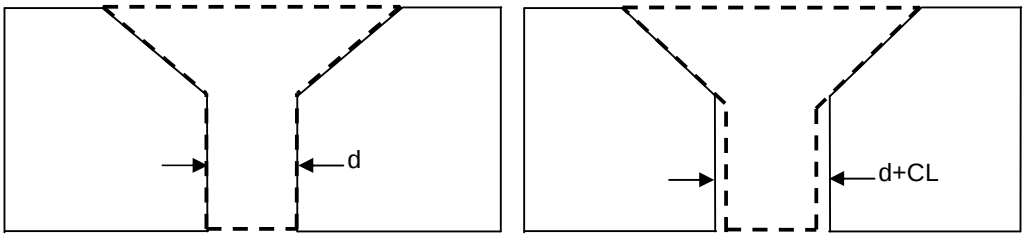

Figure 4-21 Clearance for countersunk joint

The presence of clearance led to a lag in the initial load-displacement behaviour of the joint as pointed out by McCarthy et al. (2005) and Kelly et al. (2004). If the bolt was perfectly aligned in the middle of the hole, the lag would be equal to the clearance. The joint with no clearance (neat fit) was same as the BT2 joint. Therefore the results shown in

the previous section for the BT2 joint were used as the response of the CL1 specimen. The response of the joint with 220 µm clearance is shown in Figure 4-22. The figure clearly shows the initial lag in load carried by the joint due to the presence of clearance. Once the clearance was traversed the specimen started to carry load until final failure occurred as shown in the Figure 4-22. The coefficients of variation were 1.9% for average ultimate failure load and 4.2% for average bearing load.

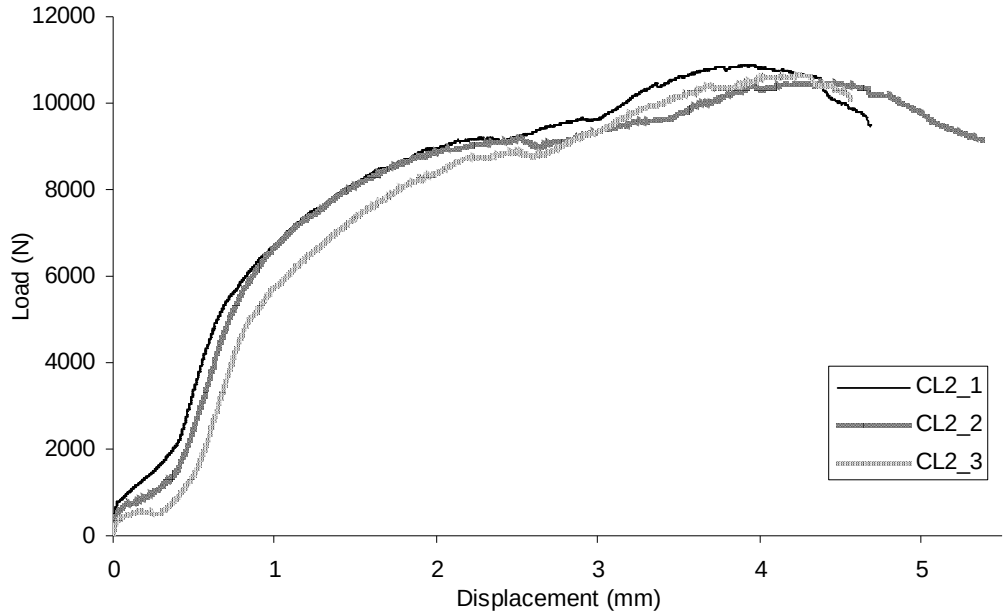

Figure 4-22 Load-displacement behaviour for joints with 220 µm clearance

Figure 4-23 shows that the initial lag in load-carrying ability was higher for the case of the CL3 joint compared to the CL2 joint. The coefficients of variation were 1.6% for average ultimate failure load and 10.6% for average bearing load. The misalignment of the bolt during assembly can be easily seen in Figure 4-22 and Figure 4-23. The difference in the initial lag between specimens 1 to 3 shown in both the figures was due to difference in the initial location of the bolt relative to the hole edge. This had a slight effect on the load-displacement behaviour of the joint.

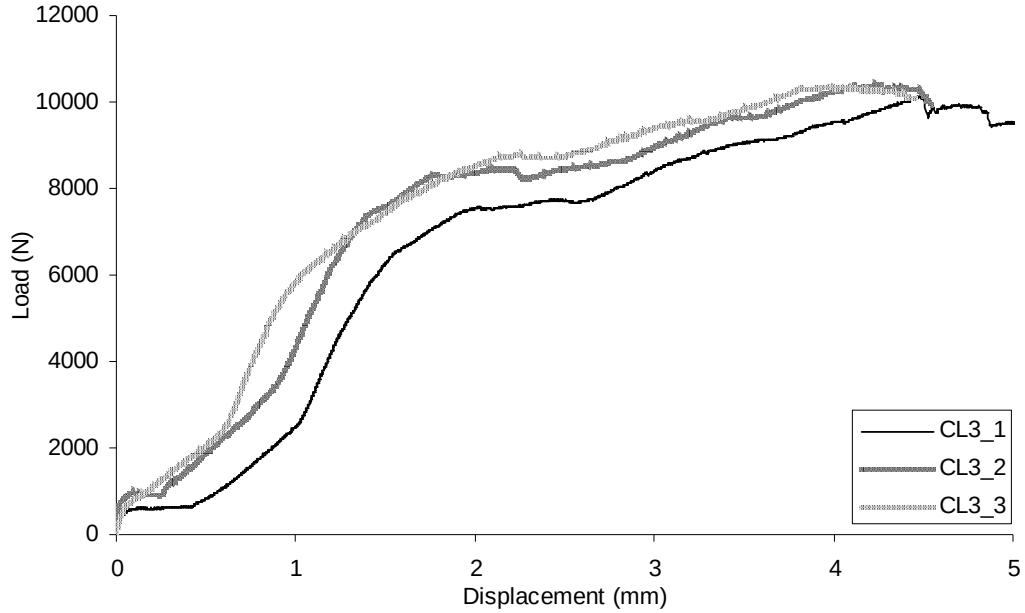

Figure 4-23 Load-displacement behaviour for joints with 440 µm clearance

The presence of clearance highlighted the two different initial stiffnesses of the joint which were also seen in the joint with no clearance. The first stiffness (Stiffness1) was due to static frictional force whereas the second (Stiffness2) was due to initial contact between the bolt and laminate as shown in Figure 4-24. The figure shows that stiffness1 was higher than stiffness2. Once the static friction was overcome, the laminate travelled the initial clearance. During this phase the load was resisted by dynamic friction and this phase appears as a region of almost no change in load with an increase in displacement as shown in Figure 4-24. Once the surface of the bolt and the edge of the hole came into contact the load was transferred from the laminate to the bolt and vice versa and the joint carried load with some changes in the stiffness (due to damage) until ultimate failure.

The effects of clearance on the load-displacement behaviour are shown in Figure 4-25. Similar to bolt torque joint analysis a representative curve from each clearance joint was plotted in Figure 4-25. It can be seen that as the clearance between the bolt and hole increased the ultimate failure load and bearing load reduced and failure displacement increased. A lateral shift in the load-displacement curve can be noted from the plot. It can be seen in Figure 4-25 that the initial stiffness of the joint was affected by the presence of the clearance. Similar to the findings of McCarthy et al. (2005), the stiffness of the joint reduced as the clearance was increased. Except for the initial lag in the load-carrying

ability, the load-displacement profile for the joint with clearance was very similar to the joint without clearance.

Table 4-3 shows that the ultimate failure load and bearing load reduced due to the presence of clearance. The clearance of 440 μm led to a reduction of 4.73% in ultimate failure load and an increase of 4.86% in failure displacement. A reduction of approximately 17% of bearing load was reported for the joint with 220 μm clearance. The reduction in bearing load for the joint with double that clearance was approximately 22% which was not very significant compared to the effects of CL2. This showed that an increase from 220 μm to 440 μm had limited effect on bearing load. Figure 4-26 and Figure 4-27 show the effect of clearance on ultimate failure load and bearing load respectively. The load was normalised based on the value of CL1 joint. The figures also marked the location of current allowable clearance for the aerospace industry.

Very little literature was available for comparison with results of countersunk bolted joints with clearance. The work done by McCarthy et al. (2002) and Kelly et al. (2004) on countersunk and protruded double lap joints respectively also suggested that the ultimate strength of the joint was not significantly affected by the presence of clearance. Extensive research on the effects of clearance in pin connections conducted by many authors such as Hyer et al. (1987), Eriksson (1986) and Naik et al. (1985) suggested that the clearance had significant effect on the strength and stiffness of a pin joint. As only minor effects were noticed in this study, it could be concluded that the presence of bolt torque may have reduced the adverse effects of the clearance. The effect of clearance can be more critical in a multi-fastened joint, where clearance in each fastener can significantly affect the overall behaviour of the joint.

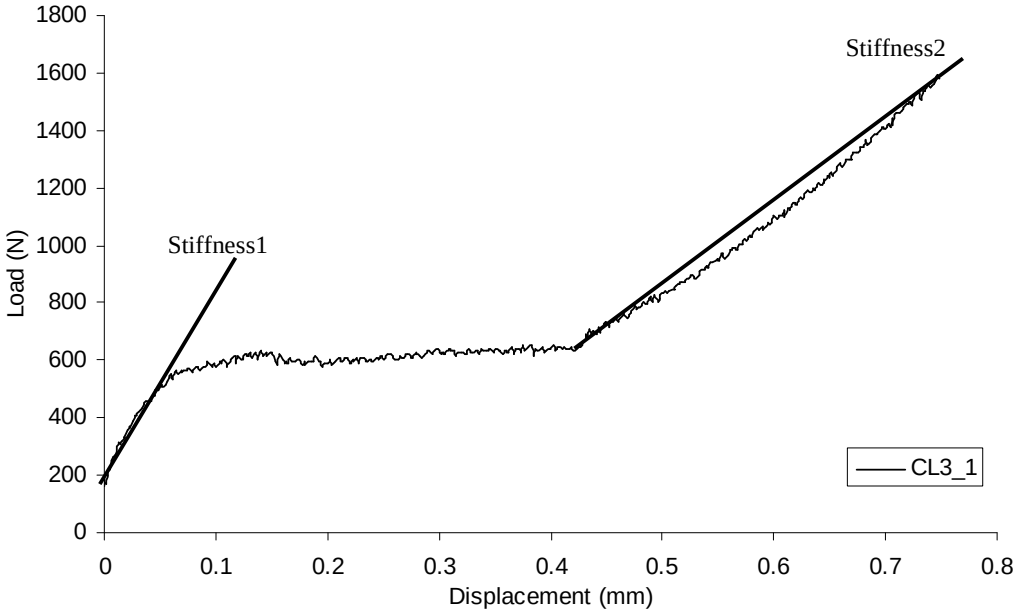

Figure 4-24 Change in stiffness during initial loading

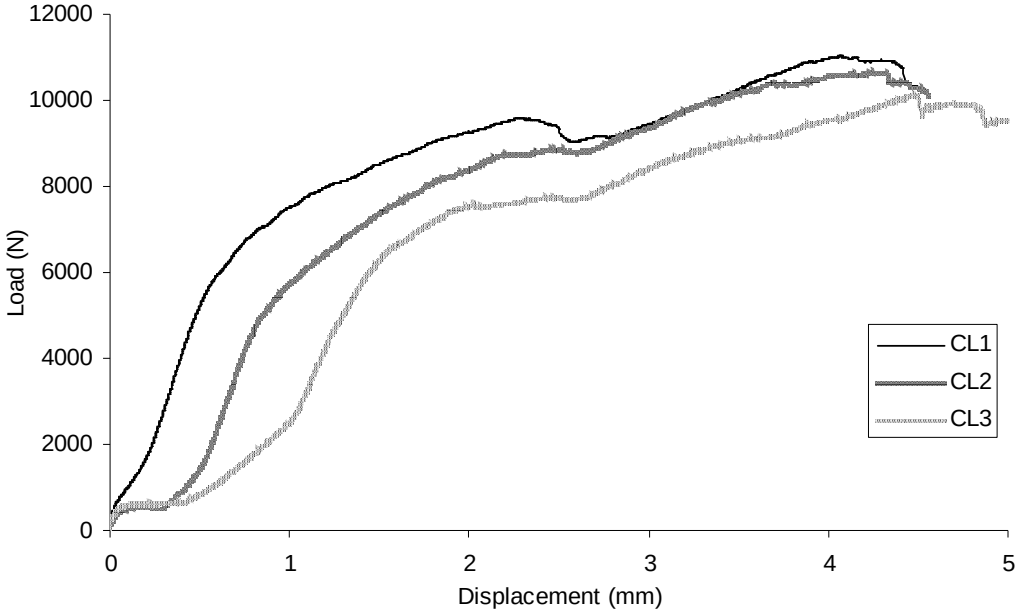

Figure 4-25 Effect of variation of clearance

Table 4-3 Summary of clearance results

Experiment	Ultimate failure load (avg.), kN	Bearing load (kN)	% Δ Ultimate failure load from CL1	% Δ Bearing load from CL1
BT2/CL1	10.82	3.18	0	0
CL2	10.66	2.64	1.43	17.03
CL3	10.31	2.47	4.73	22.19

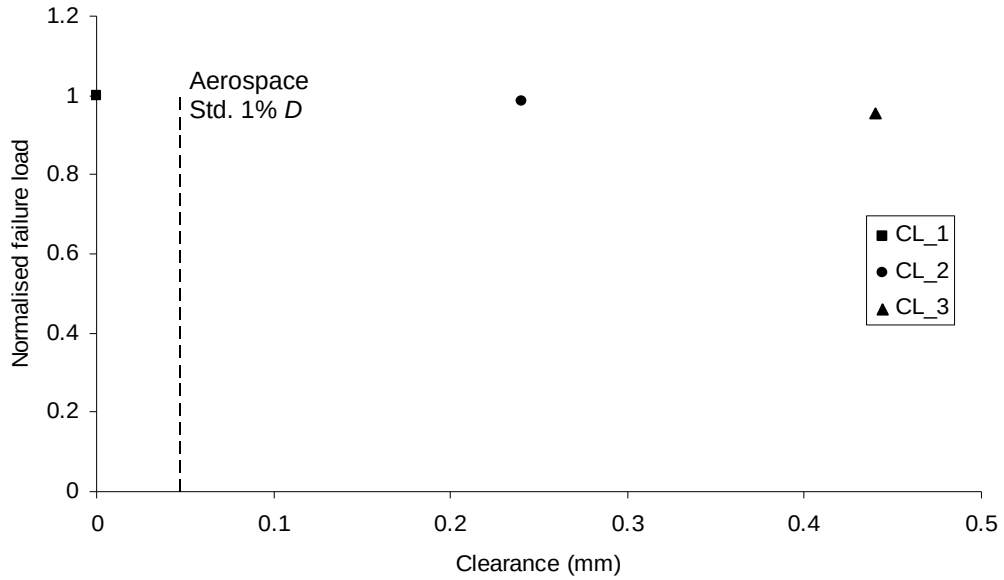

Figure 4-26 Effects of clearance on the ultimate failure load

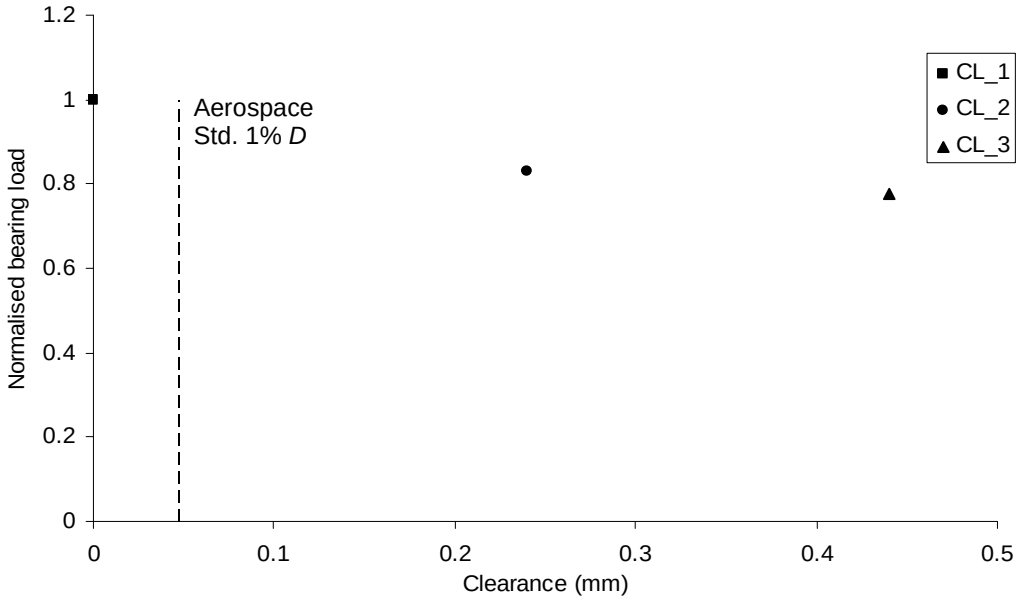

Figure 4-27 Effects of clearance on bearing load

Similar to bolt torque specimens, the clearance specimens were examined using destructive microscopy. The angular sections and inspected region described for the bolt torque specimens were also used for the clearance specimens. As the results of BT2/CL1 specimen were provided in the previous section, this section will only show the results of CL2 and CL3 specimens. The 0^o section view of the upper laminate for CL2 specimen is shown in Figure 4-28. It can be seen in the figure that due to the presence of

clearance the laminate experienced two angular damage bands in the countersunk region. The first band led to initiation of detachment of the countersunk region from the laminate. The second damage band was similar to the damage bands seen in the bolt torque samples. If the loading was continued further it is believed that the countersunk region would have detached from the laminate at the first damage band due to significant failure. Compared to the neat fit specimen the laminate also showed significant damage to the straight shank region. Excessive crushing was seen in the straight shank region. Other damage mechanisms such as secondary delamination, interlaminar and intralaminar shear cracks were present in the laminate. No primary delamination was seen in the failed specimen. There were no signs that suggested primary delamination was present before the significant damage to the countersunk or straight shank region. This showed that the presence of clearance reduced the chance of the occurrence of primary delamination in the countersunk laminate.

The damage profile of the joint with 440 μm clearance as shown in Figure 4-29 was similar to the damage profile of the joint with 220 μm clearance as shown in Figure 4-28. The difference in the degree of damage between the two laminates was due to the fact that for the CL3 joint the ultimate failure load was smaller compared to the CL2 joint, leading to less bearing damage of the laminate and therefore less overall damage. This can be seen in the photo of the top view of the upper laminates taken after dismantling the joint and before sectioning as shown in Figure 4-30. The amount of bearing damage experienced by the joint with 220 μm clearance at failure was significantly more than the joint with 440 μm clearance and this was the cause of higher through-thickness damage shown in micrographs of the CL2 laminate. From Figure 4-29 it can be seen that the two angular damage bands were parallel to each other and similar to the no clearance specimens the bands were parallel to the countersunk region. A large number of secondary delaminations were seen emanating after the damage bands. Similar to the CL2 specimen, no delamination was seen at the start of the countersunk region. Significant damage and complete material loss of the straight shank region can be seen in the figure. The straight shank region close to the bottom surface of the upper laminate experienced extensive damage because the clearance led to very high stresses in this region as the joint was loaded as demonstrated later in finite element analysis section.

The loading sequence due to the presence of clearance is shown in Figure 4-31. Figure 4-31a shows the loading and boundary condition (BC) on the joint before the load was

applied. Figure 4-31b shows the initial stage of loading where due to clearance the upper laminate slides over the lower laminate until the straight shank of the bolt contacts the hole edge of the lower laminate. As the load was increased beyond this point the bolt starts to rotate and the upper laminates slides to contact the countersunk and straight shank region of the bolt. Once this contact was established a high stress region was developed close to the bottom surface of the upper laminate and top surface of the lower laminate. This high stress concentration region shown in Figure 4-31c led to significant damage in the straight shank region visible in the micrographs.

The 45^o section of the CL2 laminate is shown in Figure 4-32. The figure shows significant damage in the countersunk and straight shank regions. The damage mechanisms noticed at 0^o section were also present at 45^o section, however the amount of damage was less. This shows that the amount of damage reduced from the 0^o to the 45^o section. The reduction in damage at 45^o could also be due to the reduction in the contact region between bolt and hole surface caused by the presence of the clearance.

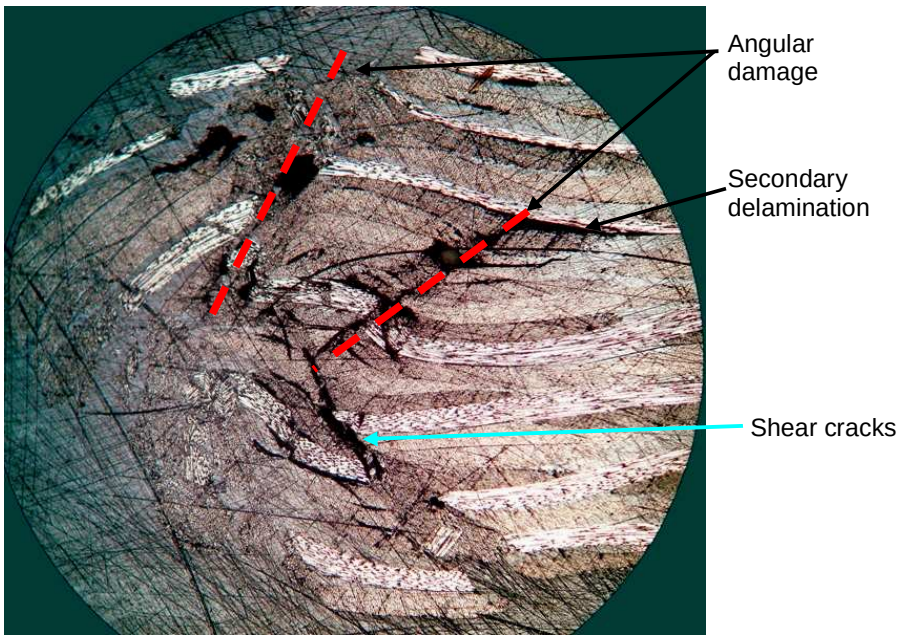

Figure 4-28 Damaged upper laminate at 0^o section for joints with 220 μm clearance

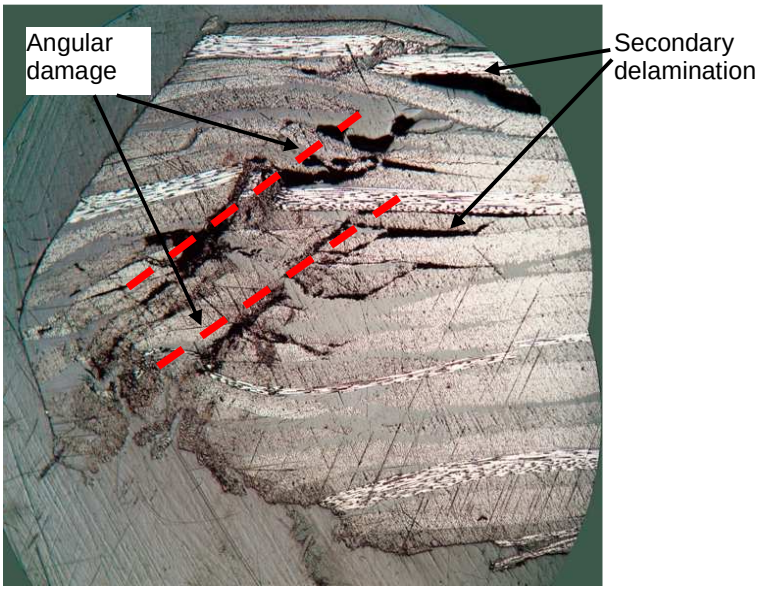

Figure 4-29 Damaged upper laminate at 0^o section for joints with 440 μm clearance

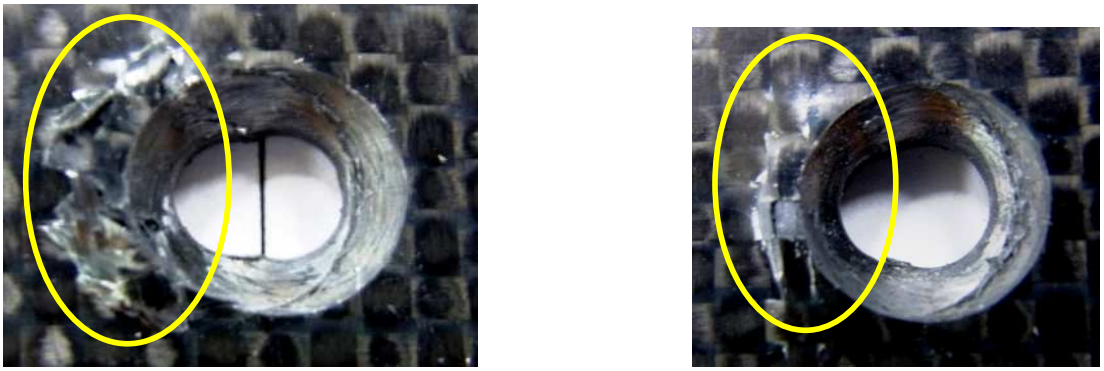

a) Joint with 220 μm clearance

b) Joint with 440 μm clearance

Figure 4-30 Bearing damage (circled) in clearance laminates after testing

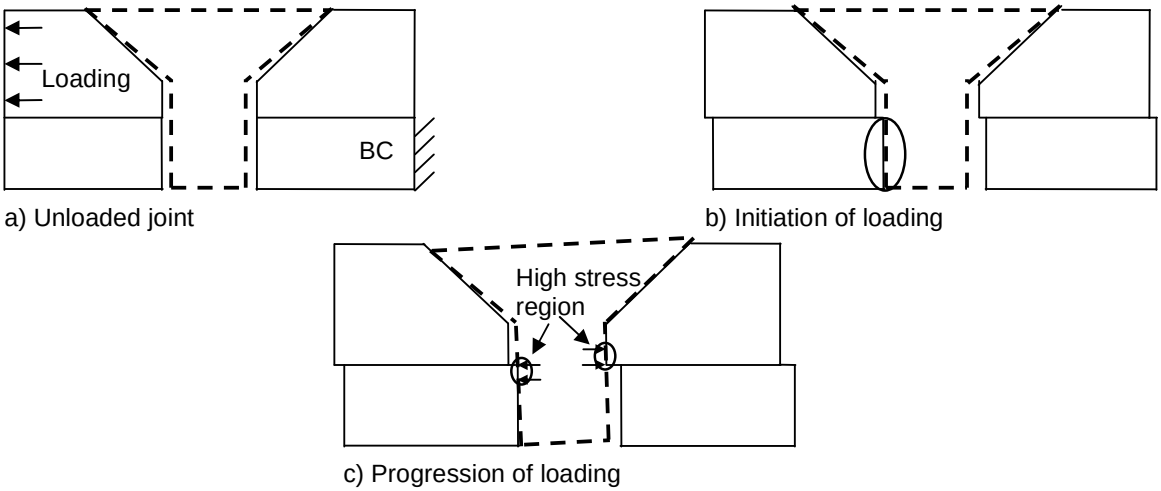

a) Unloaded joint

b) Initiation of loading

c) Progression of loading

Figure 4-31 Loading sequence due to clearance

The lower laminate also experienced high stresses close to the top surface as shown in Figure 4-31. The effects of the high stress concentration region can be seen in Figure 4-33. The top half of the lower laminate experienced more damage compared to the bottom half. The damage of the bottom half was similar to the damage shown for the neat fit specimen. However, the extensive crushing and second angular damage band which occurred in the joint with 220 µm clearance was not present in the neat fit joint. The angular damage bands were approximately perpendicular to each other. The presence of the second angular band also showed that the clearance had significant effect on the stress distribution through the thickness of the laminate. Again no primary delamination was noticed in the laminate, though secondary delaminations were present.

The damage for the joint with 440 µm clearance was very similar to the joint with half the clearance. The major difference was in the angle of the second angular band and the damage to the layers close to the top surface. This can be seen in Figure 4-34. For the joint with 440 µm clearance the angle of the second angular band was steeper and the amount of damage was less compared to the joint with half the clearance. However, the damage bands were almost perpendicular to each other as was the case for the joint with 220 µm clearance. The other common damage mechanisms were present and have been highlighted in Figure 4-34.

The damage for the 45^{o} sections is shown in Figure 4-35. The damage profile for CL2 specimen was similar to the 0^{o} section, however, the amount of damage reduced. For the CL3 specimen, the amount of damage significantly reduced and damage could be seen in the bottom layers of the specimen. This could be due to the fact that the clearance of 440 µm significantly reduced the contact region between the bolt and the hole leading to much localised damage in the specimen. This shows that the clearance affected the distribution of the damage along the circumference of the hole. The effects of changing clearance on the failure profile of the upper and lower laminate are provided in Figure 4-36.

Figure 4-32 Damaged upper laminate at 45^{o} section for joints with 220 μm clearance

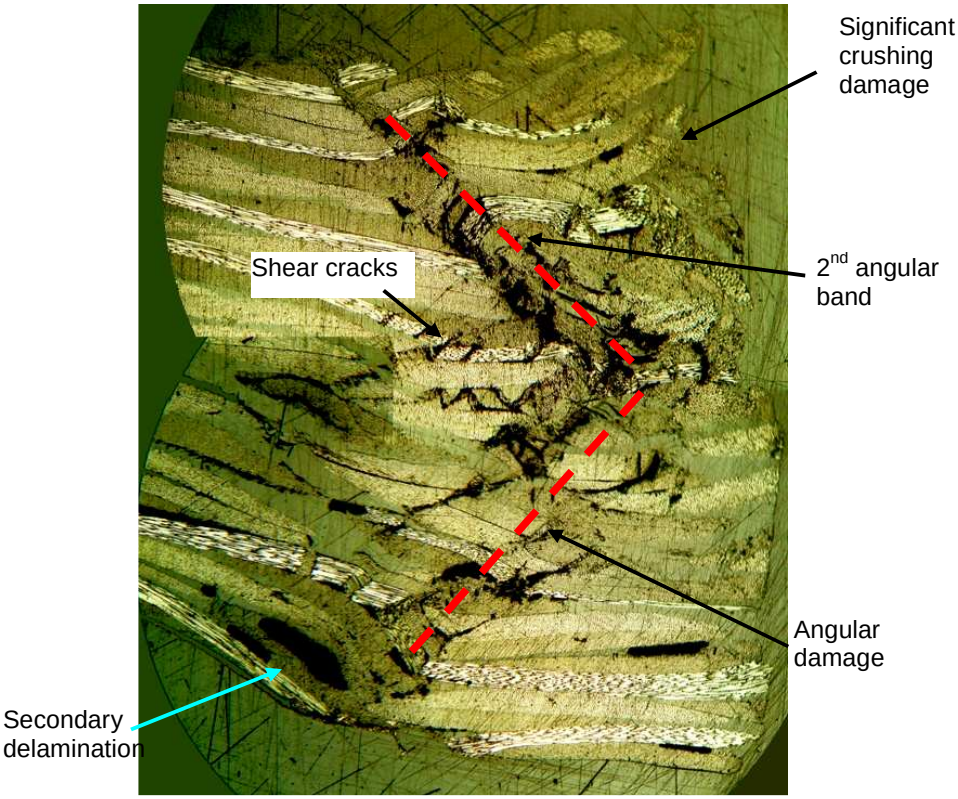

Figure 4-33 Damaged lower laminate at 0^{o} section for joints with 220 μm clearance

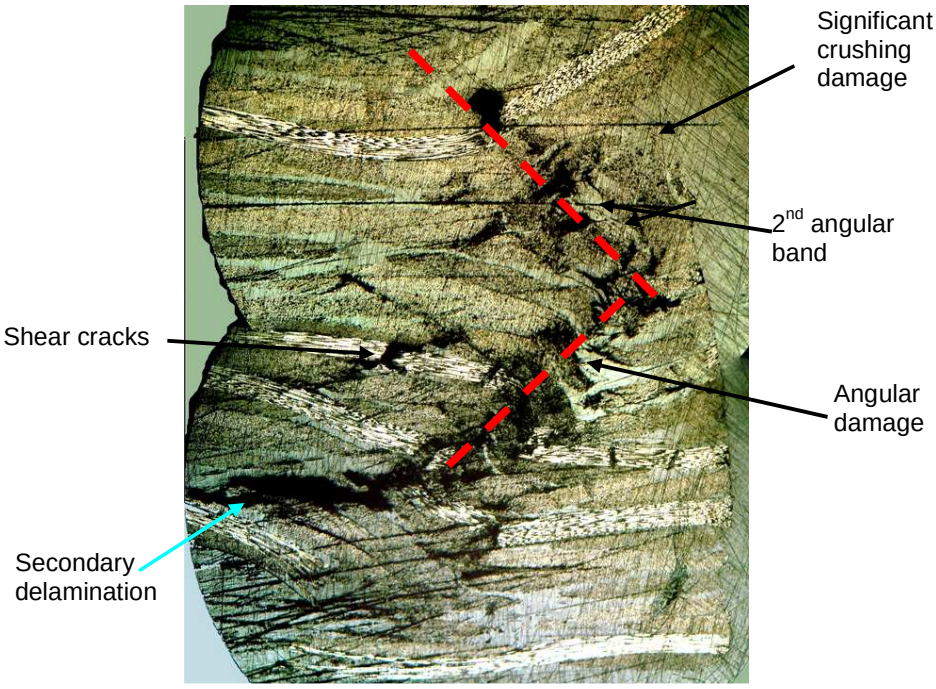

Figure 4-34 Damaged lower laminate at 0° section for joints with 440 µm clearance

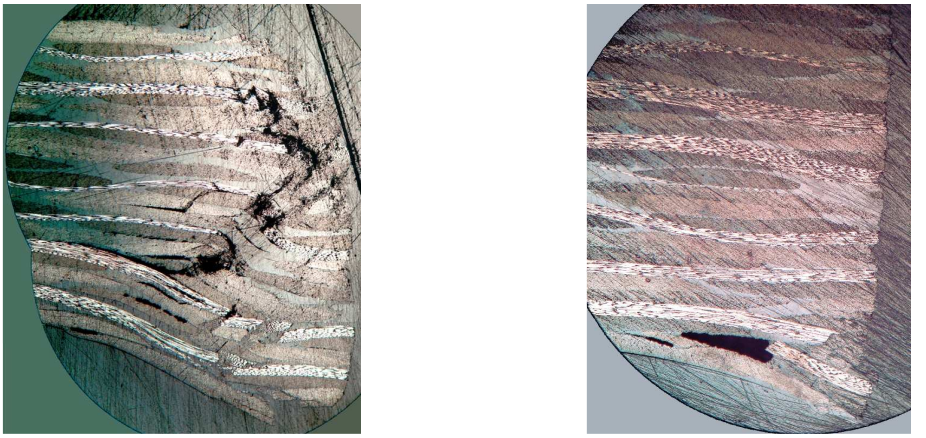

a) Joints with 220 µm clearance

b) Joints with 440 µm clearance

Figure 4-35 Damaged lower laminate at 45° section

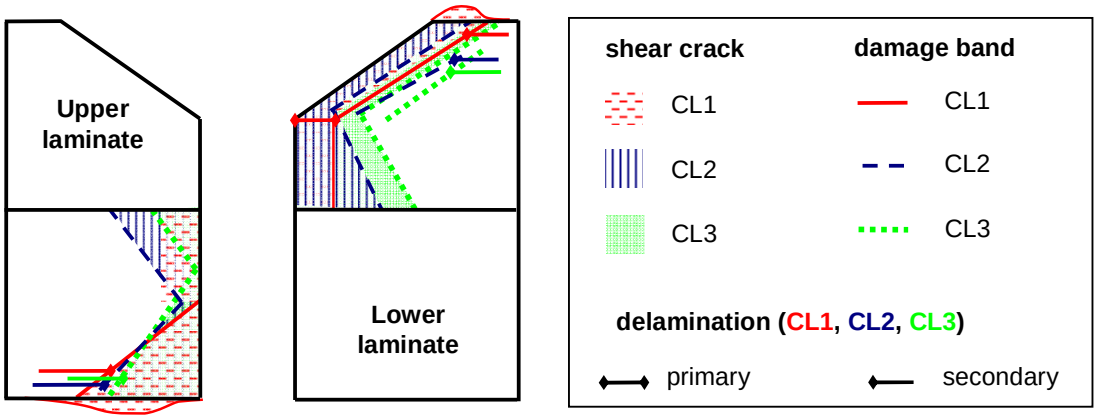

Figure 4-36 Effects of clearance on the damage profile of upper and lower laminates at 0°

The following important conclusions can be drawn from the above analysis:

- No primary delamination was noticed in any of the joints with clearance.
- The secondary delamination was close to the top surface of the upper laminate and bottom surface of the lower laminate.
- All the shear cracking damage mechanisms listed in the bearing test results were applicable for the case of single lap joint with clearance.
- The effects of clearance on the behaviour of the joint are as follows:
    - As the clearance increased the ultimate failure load reduced slightly.
    - The intensity of bearing damage reduced with an increase in clearance.
    - An increase in clearance from 0 µm to 220 µm significantly reduced bearing load, however, further increase to 440 µm had marginal effect on the bearing load.
    - As the clearance increased the contact region between the bolt and hole reduced causing localised damage and change in damage distribution along the circumference of the hole.
    - As the clearance was increased the single lap joint experienced higher bending.
    - Due to clearance the upper laminate experienced two different parallel angular damage bands.
    - The lower laminate also experienced two different angular damage bands. However, in this case the damage bands were almost perpendicular to each other.

4.4 Effects of countersunk depth to thickness ratio

Three values of countersunk depth to thickness ratio as listed in Table 3-1 were tested to understand their effect on the behaviour of the single lap joint. The final value exceeded the recommended range (ASTM D5961) of countersunk depth to thickness ratio to understand and document the behaviour of the joint under extreme cases. The countersunk depth to thickness ratio of 0.64 was achieved by varying the thickness of the laminate and keeping the bolt diameter constant. However, to achieve a countersunk depth to thickness ratio of 0.76 it was decided to change the bolt keeping the laminate thickness the same as the laminate would have become very thin leading to thickness related effects to dominate the results. The bolt was changed from being 3/16” diameter to 1/4” diameter bolt.

The results of HT2 (0.56) joint are same as the results of the BT2 specimen, therefore these results are not repeated in this section. The load-displacement curves for the joint with countersunk depth to thickness ratio of 0.64 are shown in Figure 4-37. For HT1_1 specimen, the test was stopped and started again because the strain gauge data acquisition system did not collect data initially. This led to the second initial curves visible for HT1_1 specimen. The load-displacement curves showed good agreement for all three samples. The coefficients of variation were 0.43% for average ultimate failure load and 9.5% for average bearing load. The final failure mode of this joint was bearing, however, an increased amount of bending was noted during testing.

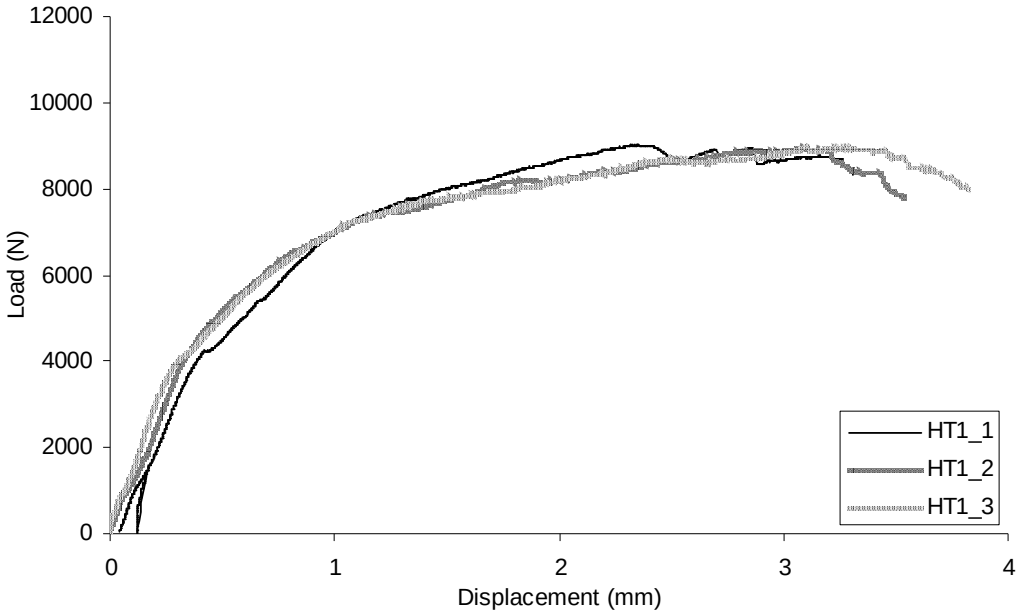

Figure 4-37 Load-displacement behaviour for joints with countersunk depth to thickness ratio of 0.64

The joint with countersunk depth to thickness ratio of 0.76 loaded in tension experienced significant bending, and failed catastrophically in bending rather than in bearing. Out of the three specimens tested, two specimens (HT3_1 and HT3_3) failed by bending failure of the upper laminate and HT3_2 specimen failed due to bending failure of the lower laminate. The difference in the failed laminate led to different ultimate failure load for the joints as shown in Figure 4-38. The load-displacement behaviour of each joint was very similar, however the ultimate failure load for HT3_2 was slightly higher than other joints. As the failure was catastrophic the value of load and displacement after the ultimate

failure load are of no significance, therefore the full plot is not displayed. The profile of the load-displacement curve for this joint was very different from all the other tested joints.

The change in failure mode clearly signifies the importance of the countersunk depth to thickness ratio in achieving bearing failure. Even though the joint with countersunk depth to thickness ratio of 0.64 experienced significant bending during loading, the final failure was bearing. The coefficients of variation were 4.1% for average ultimate failure load and 33.3% for average bearing load. Due to a larger variation in the bearing load for HT3_2 specimen, the coefficient of variation was higher compared to other tests. The average bearing load without the contribution of HT3_2 joint was used for any further comparison. The effects of varying the countersunk depth to thickness ratio on the stress-displacement behaviour of the joint are shown in Figure 4-39. To compare the results from different joints, stress instead of load was plotted against displacement. The acting load was divided by the product of hole diameter and laminate thickness to calculate the stress, i.e.

$$\text{Stress} = \frac{\text{Load}}{(\text{Hole diameter}) \times (\text{Laminate thickness})}$$

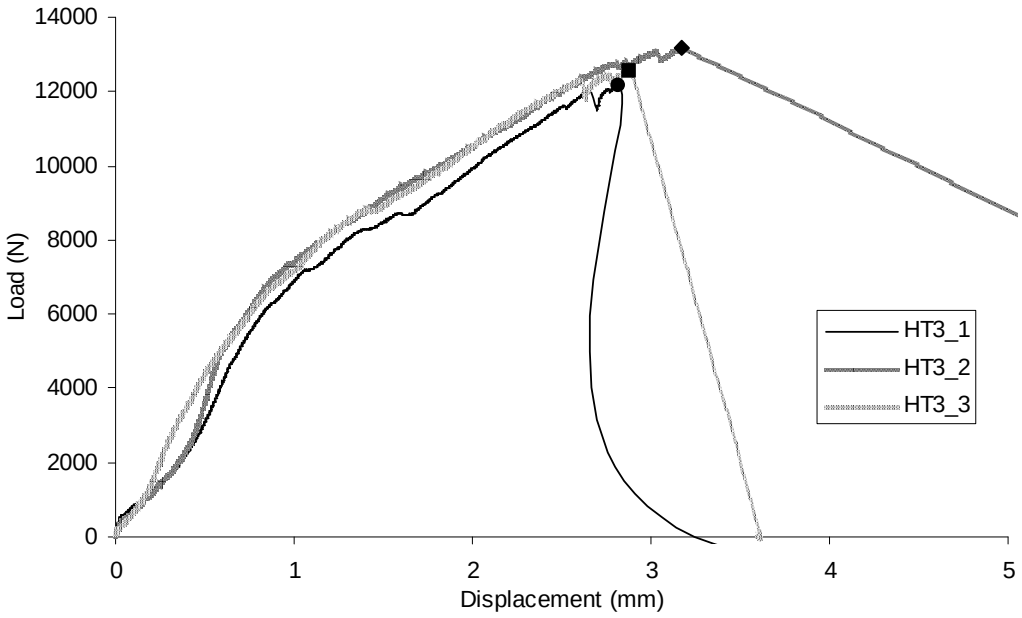

Figure 4-38 Load-displacement behaviour for joints with countersunk depth to thickness ratio of 0.76

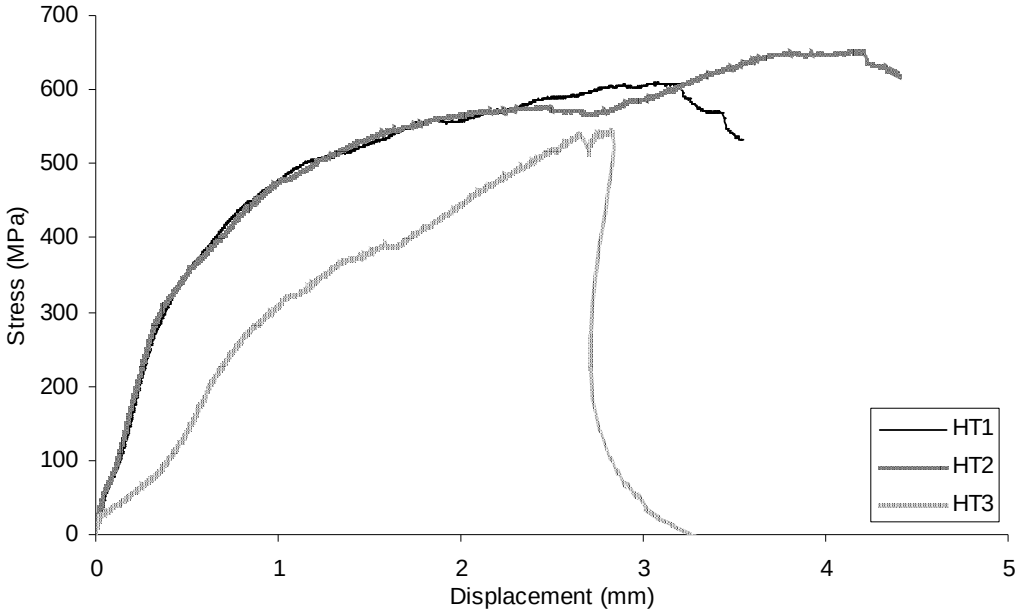

Figure 4-39 Effects of variation of countersunk depth to thickness ratio

From Figure 4-39 it can be seen that as the countersunk depth to thickness ratio increased from 0.56 to 0.64 the ultimate failure stress reduced. The stress-displacement curve had a similar profile for the joints with countersunk depth to thickness ratio of 0.56 and 0.64, however the joint with countersunk depth to thickness ratio of 0.76 showed significantly different profile. The comparison of results for various configurations of countersunk depth to thickness ratio is shown in Table 4-4. The table shows the results for ultimate failure stress (UFS) and bearing stress (BS) to normalise the effects of change in geometry. The results of HT3 joint cannot be directly compared with other countersunk depth to thickness ratio joints as the final failure mode was different. It can be seen in the table that as the countersunk depth to thickness ratio increased the ultimate failure stress of the joint reduced. The bearing stress was not significantly affected by increased countersunk depth to thickness ratio for the specimens with bearing failure. This variation is shown in Figure 4-40 and Figure 4-41. Similar to previous analyses the stress was normalised based on the stress of HT2 joint. The figures also mark the upper limit of countersunk depth to thickness ratio as suggested by ASTM D9561. Very limited work has been reported on the effects of countersunk depth to thickness ratio on the performance of single lap composite bolted joints. Garrett (1986) compared results of countersunk depth to thickness ratio 0.52, 0.8 and 1.0 (i.e. knife edge). Strength reduction of 16.4% and 34.3% for 80% and 100% countersunk laminates respectively were reported by the author.

Table 4-4 Comparison of countersunk depth to thickness ratio

Experiment	Bearing stress (avg.), (N/mm^2)	Ultimate failure stress (avg.), N/mm^2	% Δ Bearing stress from HT2	% Δ Ultimate failure stress from HT2
HT2	189.8	645.77	0	0
HT1	191.7	612.52	-1	5.15
HT3	107.4	564.60	43.4	12.57

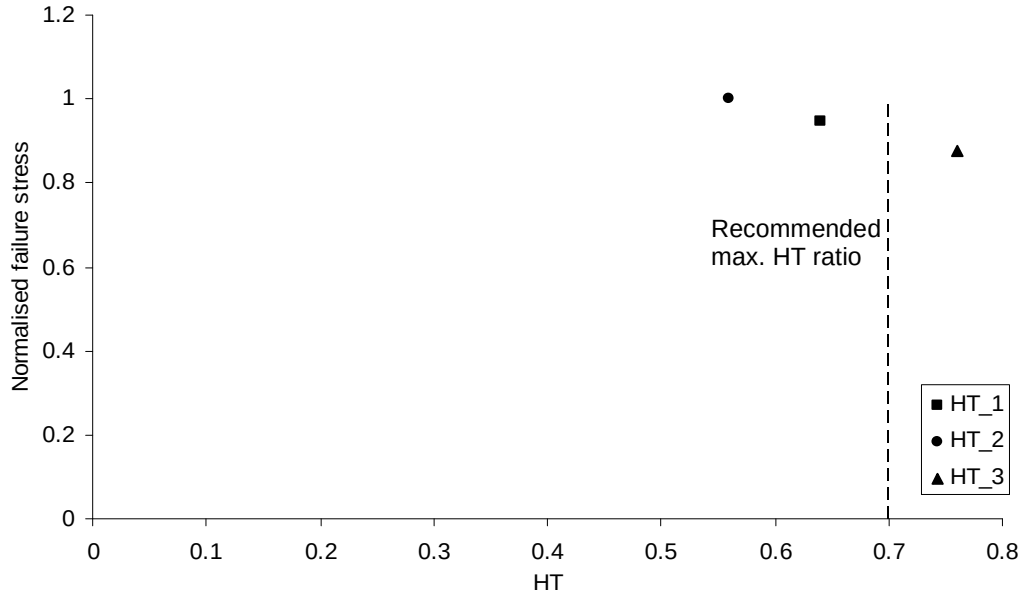

Figure 4-40 Effects of countersunk depth to thickness ratio on ultimate failure stress

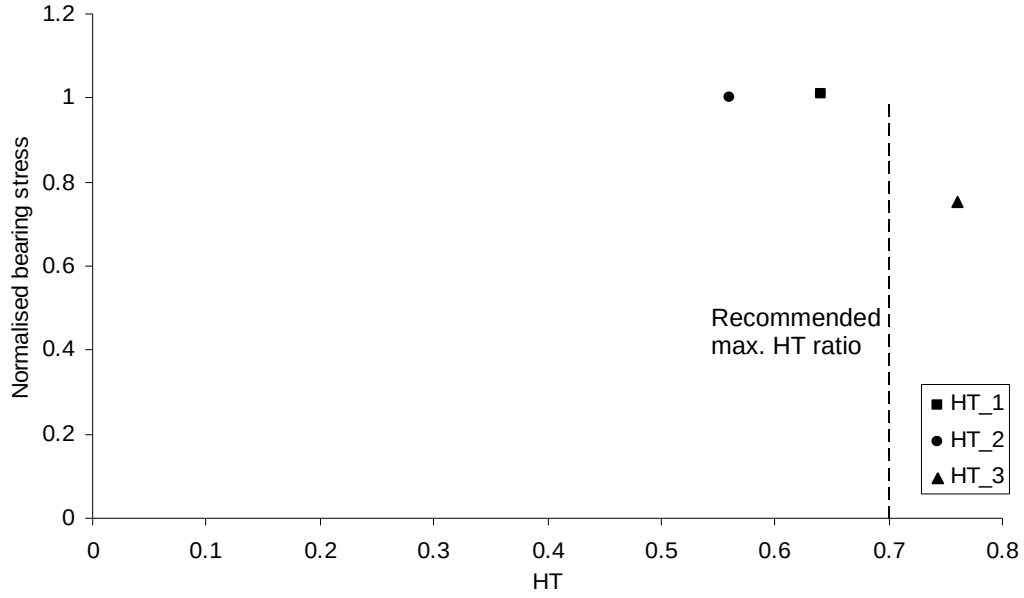

Figure 4-41 Effects of countersunk depth to thickness ratio on bearing stress

The damaged specimens were analysed using destructive microscopy to determine the through-thickness failure profile. The undamaged sections of upper laminate for HT1 and HT3 joint are shown in Figure 4-42. As previously mentioned, the thickness and the number of layers for the HT1 specimen was less than HT3 and HT2 specimen. The inspection region of the single lap joint was the same as used for bolt torque and clearance specimens.

The through-thickness damage in the upper laminate of the joint with countersunk depth to thickness ratio of 0.64 at the 0^o section is shown in Figure 4-43. Similar to the bolt torque specimens a single angular band was present in the countersunk region. Other damage mechanisms were also present as highlighted in the figure, though the primary delamination could not be seen. The change in countersunk depth to thickness ratio affected the through-thickness stress distribution which may have prevented the occurrence of the primary delamination. This can be due to increased contribution of bending stress and reduced bearing in the laminate. The combined effect of bending and bearing stress also led to higher damage at the bottom layers of the upper laminate and reduced through-thickness damage in the straight shank region. The straight shank region of the joint with countersunk depth to thickness ratio of 0.56 did not experience any edge damage and only suffered internal damage as visible in Figure 4-14. The secondary delamination was again prevalent in the layers close to the top surface of the laminate. The countersunk edge did not experience any damage in the upper laminate of the joint with countersunk depth to thickness ratio of 0.64. The countersunk edge in the joint with countersunk depth to thickness ratio of 0.56, experienced significant damage together with bulging out of the top surface.

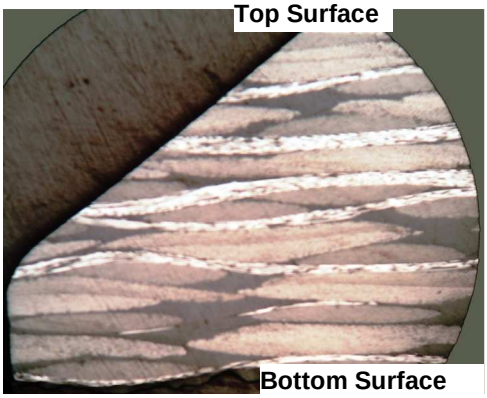

a) Upper laminate, HT1

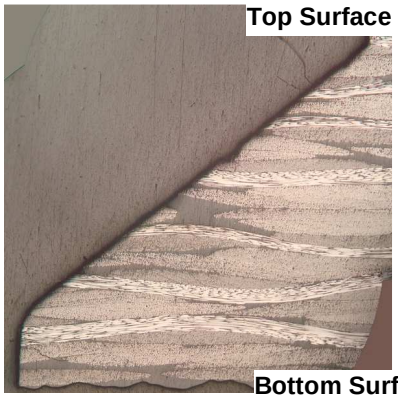

b) Upper laminate, HT3

Figure 4-42 Undamaged upper laminates

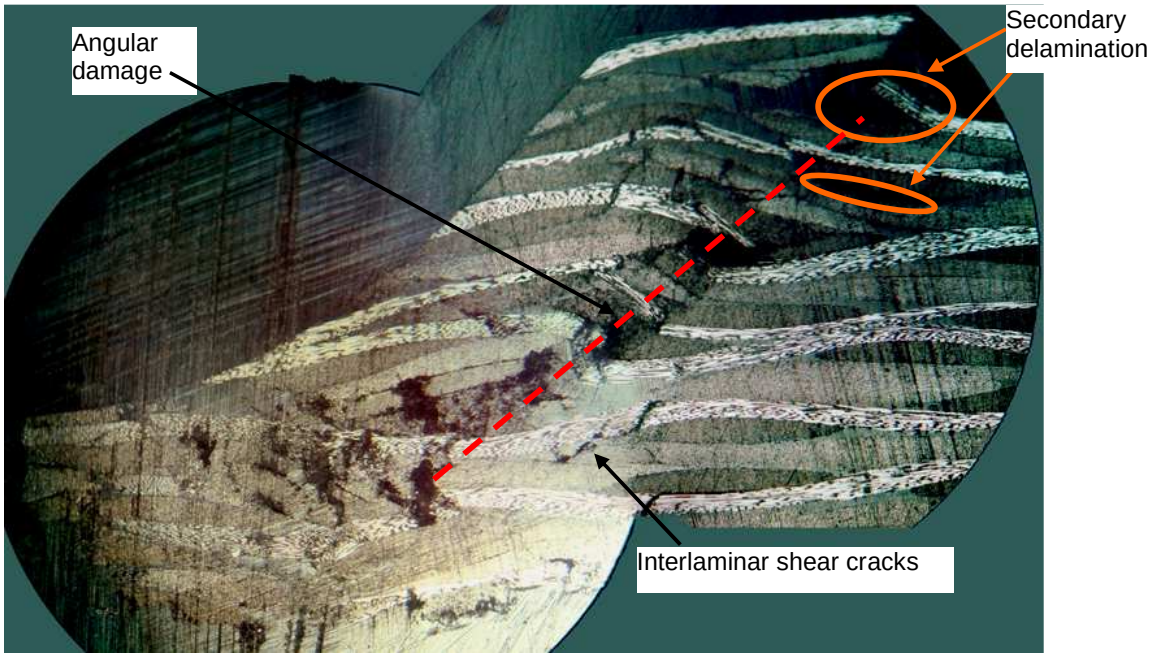

Figure 4-43 Damaged upper laminate at 0^o section for joints with countersunk depth to thickness ratio of 0.64

The damage for the joint with countersunk depth to thickness ratio of 0.76 at the 0^o section is shown in Figure 4-44. Figure 4-44a shows the complete specimen at 5X magnification. It can be seen in the figure that the laminate did not experience much damage except in the straight shank region. The damaged region highlighted in Figure 4-44a is shown in Figure 4-44b at 10X magnification. The laminate experienced significant damage and material loss in the straight shank region. The damage extended to the interior of the laminate starting from the hole edge. The countersunk region did not have any significant damage except some fibre kinking and breaking. No damage to the countersunk edge was seen in the laminate. This specimen did not have any angular band, secondary delamination or primary delamination. This was due to the fact that before the laminate could experience any of these failure mechanisms, bending led to catastrophic failure of the laminate as shown in Figure 4-45. This showed that angular damage band and secondary delamination occurred at a later stage during loading. It can be seen that the damage at the countersunk hole initiated approximately at ±90^o from the loading direction. The final failure mode resembles net section failure but because the laminate failed in bending it is termed as bending failure.

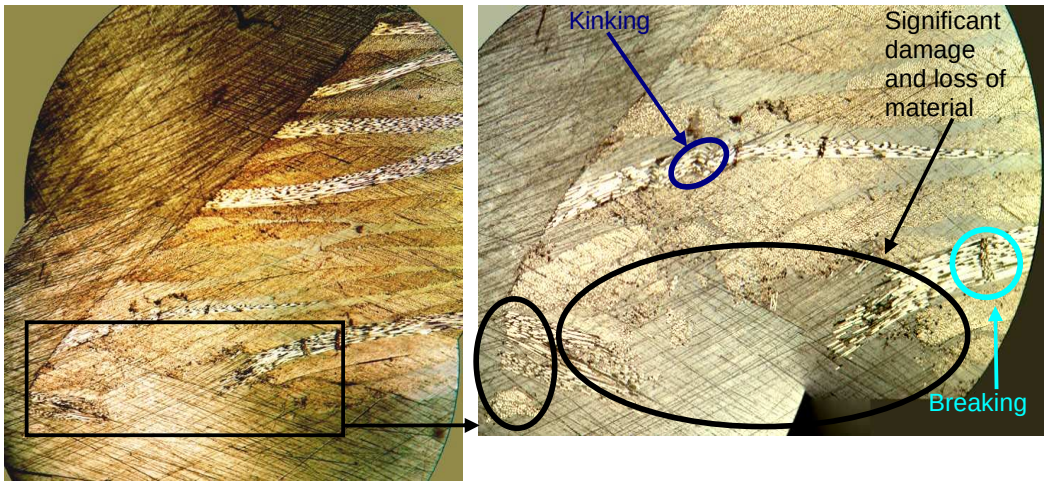

a) 5X complete HT3 upper laminate b) 10X damaged region HT3 upper laminate

Figure 4-44 Damaged upper laminate at 0^{o} section for joints with countersunk depth to thickness ratio of 0.76

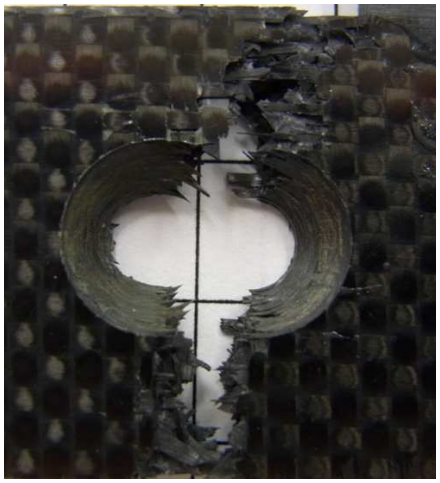

Figure 4-45 Top view of bending failure in upper laminate for joints with countersunk depth to thickness ratio of 0.76

The damage in the lower laminate for the joint with countersunk depth to thickness ratio of 0.76 is shown in Figure 4-46. It can be seen that the straight damage covered more through-thickness region compared to BT2/HT2 specimen shown in Figure 4-17. The edge damage also significantly increased. Again no primary delamination can be seen, though the laminate experienced significant secondary delamination, shear cracking and crushing. The circumferential distribution of damage can be seen in the 45^{o} sections shown in Figure 4-47. Compared to the 0^{o} section the amount of damage in the 45^{o} section for the HT3 specimen has reduced. Higher material loss can be seen for the bottom layers of the lower laminate. This can be due to the sectioning process. All the

damage mechanisms reported for the 0^o section were also present in the 45^o section. The damage for the joint with countersunk depth to thickness ratio of 0.64 was very similar to the joint with countersunk depth to thickness ratio of 0.56, however, the straight damage covered more through-thickness region of HT1 specimen compared to BT2/HT2 specimen. The change in countersunk depth to thickness ratio also affected the bending characteristics of the joint and the failure mode. From the above analysis a damage profile for countersunk depth to thickness ratio specimen can be defined. A schematic showing the effects of changing countersunk depth to thickness ratio on the damage profile of the upper and lower laminate can be seen in Figure 4-48. The profile was only applicable to the specimens that failed in bearing mode.

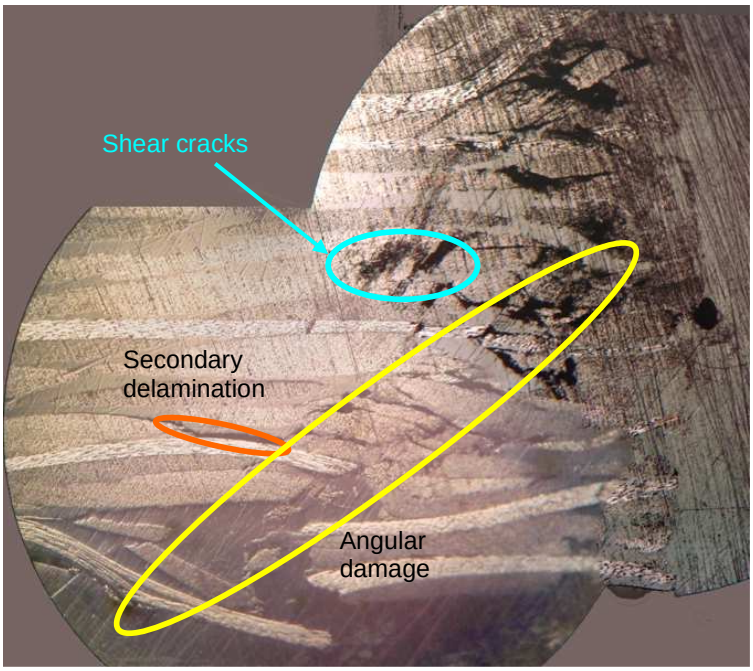

Figure 4-46 Damaged lower laminate at 0^o section for joints with countersunk depth to thickness ratio of 0.76

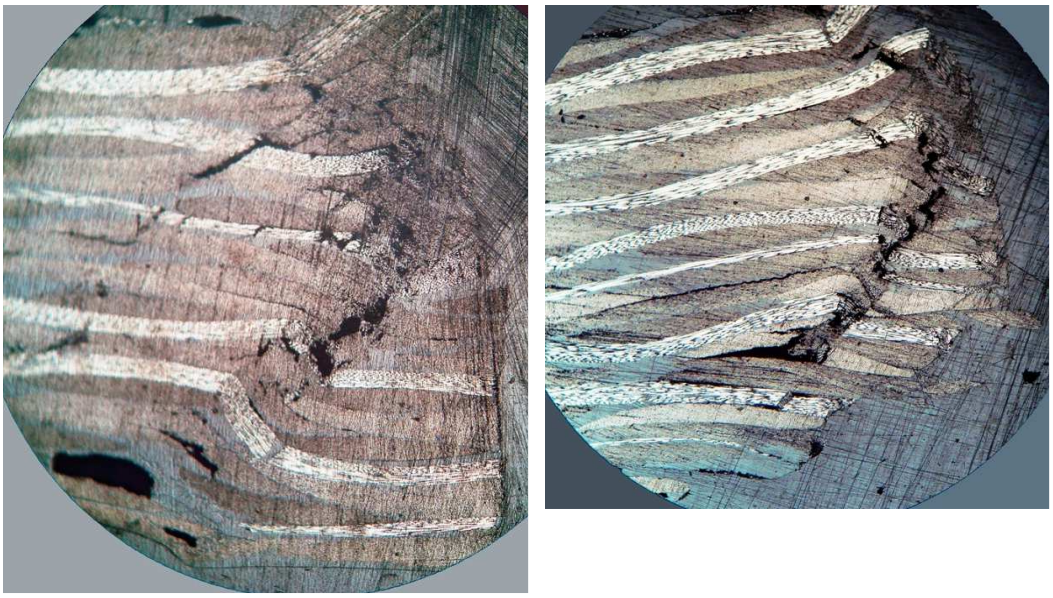

a) LM2_B3_HT1_B b) LM1_B1_HT3_B

Figure 4-47 Damaged lower laminate at 45^o section

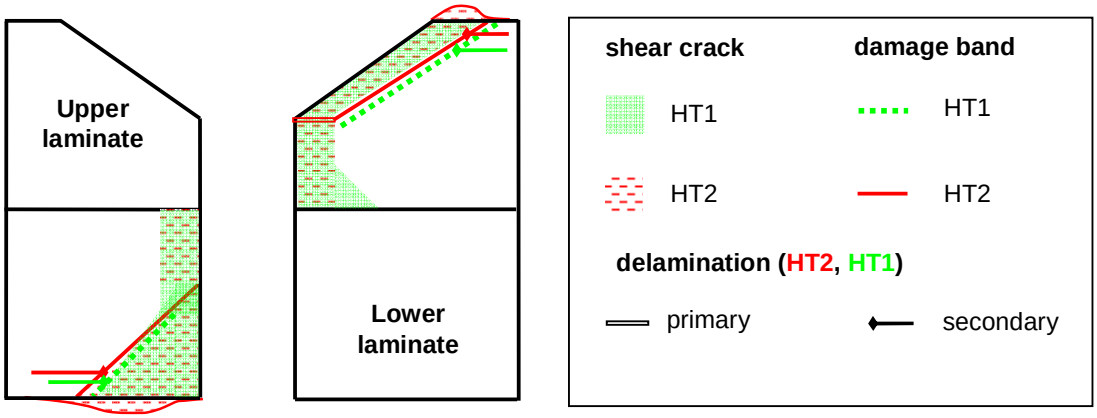

Figure 4-48 Effects of countersunk depth to thickness ratio on the damage profile of upper and lower laminate at 0^o

The following important conclusions can be drawn from the above analysis:

- No primary delamination was noticed for the joints with countersunk depth to thickness ratio of 0.64 and 0.76.
- The secondary delamination was reported close to the top surface of the upper laminate and bottom surface of the lower laminate.
- The damage reduced around the hole circumference from 0^o to 45^o.
- The through-thickness damage for both upper and lower laminate of the specimen that failed in bearing can be divided in two parts:
    - Angular damage

    - Straight damage
- For the specimen that failed in bending the damage in upper laminate does not follow the profile shown in Figure 4-48.
- The effects of increased countersunk depth to thickness ratio on the behaviour of the joint are
    - The ultimate failure stress reduced slightly with an increase in countersunk depth to thickness ratio for joint failed in bearing.
    - The bearing stress did not change with an increase in countersunk depth to thickness ratio for joint failed in bearing.
    - The increase in countersunk depth to thickness ratio reduced the amount of bearing occurring in the laminate and increased the amount of bending in the joint.
    - An excessive increase in countersunk depth to thickness ratio changed the final failure mode from bearing to bending failure.
    - Due to an increase in countersunk depth to thickness ratio the damage in the straight shank region of the upper laminate was increased.
    - The straight damage region in the lower laminate increased up to the middle of the laminate for the case of the joint with countersunk depth to thickness ratio of 0.76.

4.5 Conclusion

The experimental analysis of the effects of bolt torque, clearance and countersunk depth to thickness ratio on the behaviour of the single lap joint was discussed in detail. The microscopy analysis of the failed specimen provided detailed knowledge of the failure profile and failure mechanisms experienced in different specimens. The following major conclusions can be drawn from the above analysis:

- An increased bolt torque led to significant increase in bearing load and minor increase in ultimate failure load.
- The presence of bolt torque constrained the laminate in the thickness direction, leading to restricted delamination growth rather than complete separation of the layers.
- An increased clearance led to marginal reduction in ultimate failure load and significant reduction in bearing load.

- An increased clearance led to variation in through-thickness stress distribution, therefore significant variation in through-thickness damage profile of the upper and lower laminate.
- For countersunk depth to thickness ratio of 0.76, the final failure mode changed from bearing to bending.
- Only bolt torque joints showed occurrence of primary delamination in the upper laminate, and no primary delamination was noted for lower laminates.
- The through-thickness damage profile for all the joints can be divided in two sections:
    - Angular damage
    - Straight damage (bolt torque, countersunk depth to thickness joints) or second angular damage (clearance joints)
- An increase in bolt torque, clearance and countersunk depth to thickness ratio led to reduction in the bearing damage of the laminates.
- The secondary delamination and angular damage band do not lead to initial damage as they occur at significantly higher load. Initial damage consists of fibre compressive failure, matrix failure, etc.

5 NUMERICAL ANALYSIS METHODOLOGY

An analysis methodology was developed for capturing the behaviour of the bolted joints and is discussed in this chapter.

5.1 Solver

Generally, explicit analysis is used for dynamic problems that cover a short analysis time and typically involve large non-linearity, such as crash or impact problems. However, it can also be used to model quasi-static problems that have significant non-linearity, where the standard implicit analysis technique can become inefficient. Initial attempts to use standard non-linear implicit analysis (Abaqus/Standard 6.9) to predict the joint behaviour in this work were unsuccessful due to the complex contact conditions and progressive failure behaviour leading requiring very small time increments. Several attempts were made to improve the implicit analysis through the use of parameters such as contact controls, stabilisation and other damping factors. However, suitable and convergent behaviour could not be achieved, particularly in comparison with the experimental progressive failure results.

As a result, the explicit non-linear analysis solver Abaqus/Explicit 6.9 was chosen for the numerical analysis methodology. Modelling of a quasi-static test using explicit analysis required estimation of the correct time period using frequency analysis and introduced hourglass controls and mass scaling in the model. These aspects are detailed further in subsequent sections.

5.2 Element type

The current FE software provided different types of elements which can be used to model composite materials. Two-dimensional shells, continuum shells and three-dimensional solid elements can be used to define composite materials in FE modelling. In all the elements three different approaches can be used to model composite laminates:

- Stacked approach
- Layered approach
- Mixed approach

In the stacked approach each layer of composite is modelled using one element. This would lead to the most detailed through-thickness modelling of the composite laminate. In

the layered approach a single through-thickness element contains all the layers of the composite. In the mixed approach the number of through-thickness elements is not the same as the number of layers in the composite. The number of through-thickness elements is defined by the user and each through-thickness element contains multiple layers, leading to an intermediate modelling philosophy. An example of different modelling approaches for modelling a four layered composite laminate is shown in Figure 5-1.

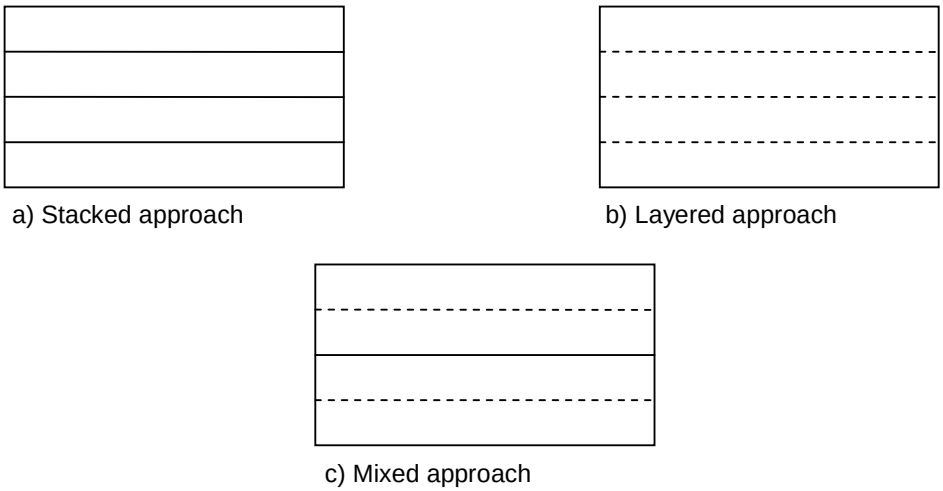

Figure 5-1 Modelling approaches for composite laminate

The mixed modelling approach was used in this project. This approach provided a good combination of detailed and efficient modelling. The software used interpolation at various integration points to determine the properties of several layers in the mixed and layered approach.

The selection of elements to be used was based on the balance of required and available capabilities. Three major elements were available in Abaqus as discussed below:

3D solid elements — The library of solid elements in Abaqus contains first- and second-order iso-parametric elements. The first-order elements are the 4-node quadrilateral for plane and axisymmetric analysis and the 8-node brick for three-dimensional cases. The library of second-order iso-parametric elements includes “serendipity” elements: the 8-node quadrilateral and the 20-node brick, and a “full Lagrange” element, the 27-node (variable number of nodes) brick. The term “serendipity”

refers to the interpolation, which is based on corner and mid-side nodes only. In contrast, the full Lagrange interpolation uses product forms of the one-dimensional Lagrange polynomials to provide the two- or three-dimensional interpolation functions.

The three-dimensional brick elements can also be used for the analysis of laminated composite solids. Several layers of different material, in different orientations, can be specified in each solid element. These elements use the same interpolation functions as the homogeneous elements, but the integration takes the variation of material properties in the stacking direction into account. However, three dimensional elements cannot be used with composite failure model available in Abaqus.

Shell elements

The general-purpose elements provide robust and accurate solutions in all loading conditions for thin and thick shell problems. Thickness change as a function of in-plane deformation is allowed in their formulation. They do not suffer from transverse shear locking, nor do they have any unconstrained hourglass modes. With the exception of the small-strain elements, all of these elements consider finite membrane strains.

Composite shell sections are composed of layers made of different materials in different orientations. Shell sections integrated during analysis allow the cross-sectional behaviour to be calculated by numerical integration through the shell thickness. Any number of material points can be defined through the thickness, and the material response can vary from point to point. The composite shell element (Continuum and ordinary) is capable of accounting for full composite failure analysis based on composite failure model provided in Abaqus.

Continuum shell elements

Continuum shell elements discretize an entire three-dimensional body. The thickness is determined from the element nodal geometry. Continuum shell elements have only displacement degrees of freedom. From a modelling point of view continuum shell

elements look like three-dimensional continuum solids, but their kinematic and constitutive behaviour is similar to conventional shell elements.

To select the element for this project Table 5-1 was used. The comparison between the three element types available in Abaqus showed that Continuum shell elements were the best available choice. The major factors in the selection were the availability of composite failure and use of cohesive contact for predicting delamination. The continuum shell had all the capabilities except 3D stresses. It would be ideal if 3D solid elements could have the composite failure capabilities, however, the lack of it (in Abaqus version 6.9) led to the selection of continuum elements. Three-dimensional brick elements were used to model the nut and bolt. As the bolt-nut assembly was assumed to be rigid, the choice of element did not affect the results.

Table 5-1 Element selection table

Capabilities	2D shell	Continuum shell	3D solid
3D Geometry	N.A.	Yes	Yes
3D stress state	N.A.	N.A.	Yes
Layered element	Yes	Yes	Yes
CSK contact surface	N.A.	Yes	Yes
Composite failure	Yes	Yes	N.A.
Cohesive contact	N.A.	Yes	Yes
Computational efficiency	Yes	Yes	N.A.
Selected element	N.A.	Yes	N.A.

5.3 Composite failure model

This section provides a description of the model for in-plane failure of fibre-reinforced composites provided in Abaqus. The failure model is capable of predicting the onset and progression of in-plane composite damage. The model requires three major components:

- Elastic behaviour
- Damage initiation
- Damage evolution

The elastic stiffness properties of the composite define the undamaged properties required for the failure model. For damage initiation, the Hashin failure criteria detailed previously in section 2.2.3 are used. These criteria define four in-plane damage modes: fibre and matrix failure in tension and compression.

For damage evolution, each damage mode has a fracture toughness defined. This fracture toughness is used to control a linear degradation of selected terms in the stiffness matrix, which corresponds to damage in each mode. This linear degradation is defined based on a stress-displacement relationship, such that by the time the stiffness properties have been degraded to zero, the energy per area dissipated corresponds to the fracture toughness associated with that damage mode. In this way, the failure model is not mesh-sensitive, which would be the case if the stiffness properties were instantaneously set to zero upon detection of failure (Lapczyk and Hurtado 2007). A detailed description on the determination of the material properties is provided in the next section.

5.4 Material properties

Raju et al. (1992) reviewed various models used to determine mechanical properties of fabric composites. In general, the analytical models can be classified as elementary, Classical Laminate Plate Theory (CLPT) and numerical models. The elementary models are based on strength of materials and many of them have been widely used despite being the simplest. An example of an elementary model is to model each fabric layer as two unidirectional plies. This was used in the current project to model the plain weave fabric ply. This approach led to twice the number of UD plies compared to the original fabric plies, i.e. the laminates with 14 and 16 fabric plies were modelled with 28 and 32 UD plies respectively. The modelling approach was based on the available composite failure models in current version of Abaqus. The available composite failure model is only applicable to UD plies. As such, each fabric ply was split into two UD plies for modelling purposes. The unidirectional material properties of the ply were determined using the procedure explained by Chamis (1987). The micromechanical model was based on the following assumptions:

1. The fibres are
    - Perfectly aligned without any undulation and damage.
    - Linearly elastic
    - Regularly spaced
    - Homogeneous
    - Orthotropic
2. The matrix is
    - Homogeneous
    - Linearly elastic
    - Isotropic

3. The composite is
    - Linearly elastic
    - Homogeneous
    - Without voids

The fibre and matrix properties provided by Chamis (1987), listed in Table 5-2, were used to determine the ply properties.

Table 5-2 Fibre and matrix properties

Property	Value
V_f	0.62
V_m	0.38
E_{f11}	32 Msi
E_{f22}	2 Msi
E_m	0.5 Msi
G_{f12}	1.3 Msi
G_{f23}	0.7 Msi
ν_{f12}	0.2
ν_m	0.35
S_{fT}	350 ksi
S_{fC}	300 ksi
S_m	15 ksi
S_{mC}	35 ksi
S_{mS}	13 ksi
G_m	0.185 Msi

Table 5-3 shows the micro-mechanics equations (Chamis, 1987) and the calculated values from an initial set of properties for the representative UD plies.

Table 5-3 Calculated initial material properties of UD plies

Property	Equation	Calculated
E_{11} (GPa)	$E_{11} = V_f E_{f11} + V_m E_m$	138
E_{22} (GPa)	$E_{22} = \frac{E_m}{1-\sqrt{V_f}\left(1-E_m/E_{f22}\right)}$	8.42
G_{12} (GPa)	$G_{12} = \frac{G_m}{1-\sqrt{V_f}\left(1-G_m/G_{f12}\right)}$, $G_m = \frac{E_m}{2(1+\nu_m)}$	3.93
G_{13} (GPa)	$G_{13} = G_{12}$	3.93
G_{23} (GPa)	$G_{23} = \frac{G_m}{1-\sqrt{V_f}\left(1-G_m/G_{f23}\right)}$	3.03
ν_{12}	$\nu_{12} = V_f \nu_{f12} + V_m \nu_m$	0.257
ν_{23}	$\nu_{23} = \frac{E_{f22}}{2G_{23}} - 1$	0.387
S_{11T} (MPa)	$S_{11T} = V_f S_{fT}$	1496
S_{11C} (MPa)	$S_{11C} = 10S_{12S} + 2.5S_{mT}$	1026
S_{22T} (MPa)	$S_{22T} = \left[1-\left(\sqrt{V_f}-V_f\right)\left(1-E_m/E_{f22}\right)\right]S_{mT}$	90
S_{22C} (MPa)	$S_{22C} = \left[1-\left(\sqrt{V_f}-V_f\right)\left(1-E_m/E_{f22}\right)\right]S_{mC}$	211
S_{12S} (MPa)	$S_{12S} = \left[1-\left(\sqrt{V_f}-V_f\right)\left(1-G_m/G_{f12}\right)\right]S_{mS}$	77
S_{13} (MPa)	$S_{13} = \left[1-\left(\sqrt{V_f}-V_f\right)\left(1-G_m/G_{f12}\right)\right]S_{mS}$	77
S_{23} (MPa)	$S_{23} = \left[\frac{1-\sqrt{V_f}\left(1-G_m/G_{f23}\right)}{1-V_f\left(1-G_m/G_{f23}\right)}\right]S_{mS}$	69

The assumptions were valid for UD plies, however, to model woven fabric as two UD layers some of the assumptions become invalid. The fibres were not perfectly straight and follow the weave pattern of the fabric. Similarly, voids were not totally avoidable during the

manufacturing process. A 2% void content provided a good approximation of the material properties (Chamis, 1987). It was therefore important to account for these irregularities in the derivation procedure. To reduce the error in the calculated material properties, the initial load displacement response of the bearing experiments was used to determine the strength and stiffness properties. Only the initial response was used because during the initial stages, there was a linear relationship between various parameters. The bearing results were used because it did not involve any bending and bolt tilting as is the case for single lap joints. The resulted variation in the response of bearing model due to change in the material properties can be seen from Figure 5-2, where Prop1 were the original calculated properties and Prop2 were the benchmarked properties based on the results of bearing test. It can be seen that Prop2 provides a similar initial response compared to experimental results. The final calibrated material properties for the UD plies can be seen from Table 5-4. These properties were used for all the single lap joint models.

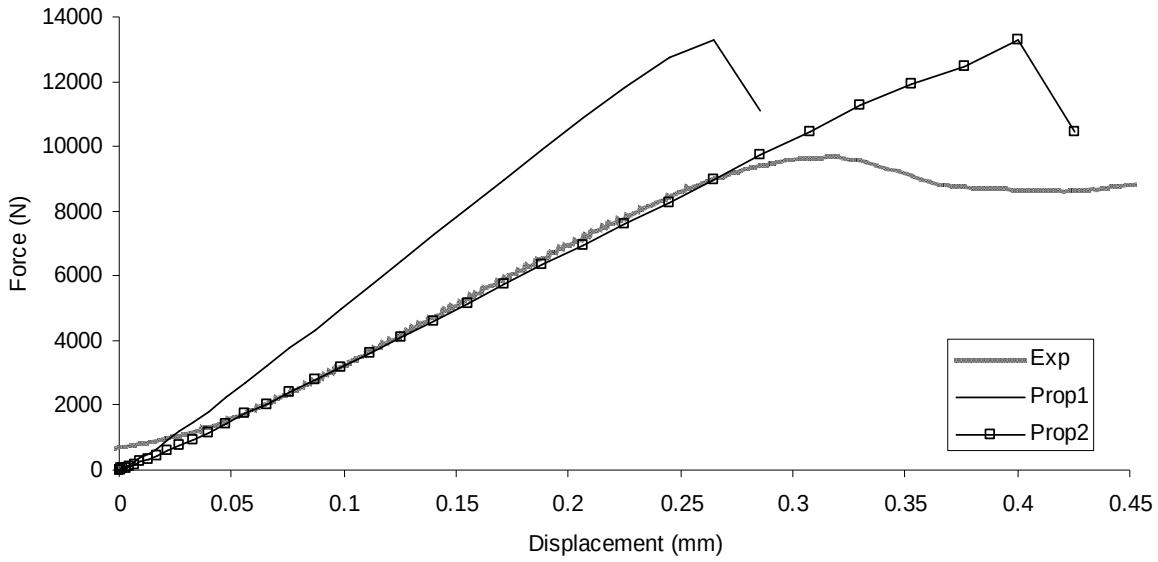

Figure 5-2 Variation of initial properties

Table 5-4 Material properties of UD plies

Property	Value
E_{11}	84.7 GPa
E_{22}	5.22 GPa
G_{12}	2.41 GPa
G_{13}	2.41 GPa
G_{23}	1.88 GPa
ν_{12}	0.3
ν_{23}	0.387
S_{11T}	1009 MPa
S_{11C}	865 MPa
S_{22T}	81 MPa
S_{22C}	188 MPa
S_{12S}	69 MPa
S_{13}	69 MPa
S_{23}	62 MPa
ρ	1.6 g/cm^3

The determination of fibre and matrix failure toughness values for compressive and tensile failure mode is very difficult as there is no set standard for calculating these values (Pinho et al. 2006). Several different methods to determine the fracture toughness values are available in the literature as pointed out by Harris et al. (1986), Cowley et al. (1997), Soutis et al. (2000) and Pinho et al. (2006):

- Compact tension (CT)
- Compact compression (CC)
- End notch flexural (ENF)
- Double-edge notched tension (DENT)
- Centre cracked tension (CCT)

However, the major limitation with all the above listed tests was that none of them had bearing failure as the major failure mode governing the fracture toughness of the laminate. As discussed previously bearing failure was the main failure mode for the tests

conducted in the current study. Harris et al. (1986) reported that the different methods led to different values of fracture energy for same laminate. This suggests that the major phenomenon which governs the failure of the specimen is important to determine the correct energy values of the laminate. Other investigators who utilized several specimen types (Reedy 1980; Shih et al. 1981) concluded that the modes of fracture and the fracture energy varied considerably with specimen configuration.

A detailed investigation of laminates failed by fibre micro-buckling was conducted by Soutis et al. (2000). The author showed that compressive failure of unidirectional and multidirectional carbon fibre-epoxy laminates was controlled by fibre micro-buckling. However, the methodology developed by Soutis et al. (2000) only applied to kink band formation and propagation for fibre failure tangential to the hole. It also did not account for other failure mechanisms in bearing failure mode. Pinho et al. (2006) used CT and CC specimen to determine the fracture toughness in tensile and compressive fibre failure modes. The microscopy failure phenomenon pointed out by Pinho et al. (2006) was close to the failure phenomenon noted in the microscopy analysis of the specimens. However, the developed approach did not account for delamination, interaction between matrix cracking and fibre dominated failure modes. The interaction between the fibre and matrix failure modes was important phenomenon for bearing failure as it led to shear cracks seen in the microscopy analysis.

The bearing test was used to calibrate the values of fibre failure fracture toughness as the effect of matrix failure fracture toughness was assumed to be negligible. Due to the close resemblance to bearing failure mode, values determined by Pinho et al. (2006) were used as the starting values in the FE investigation. In Abaqus the composite failure is defined by the stress-displacement based continuum law as shown in Figure 5-3. The positive slope of the stress-displacement curve prior to damage initiation corresponds to linear elastic material behaviour; the negative slope after damage initiation is achieved by evolution of the respective damage variables (Abaqus User Manual 2010). The area under the curve is defined as the fracture toughness of the respective damage mode. A comparison was made between the original, 20% reduced and 30% reduced fracture toughness values. The 30% reduced values provided the best approximations of experimental results, therefore these values were used. A load-displacement plot comparing the results between the three sets of values is provided in Figure 5-4. The final values used in all the models are provided in Table 5-5.

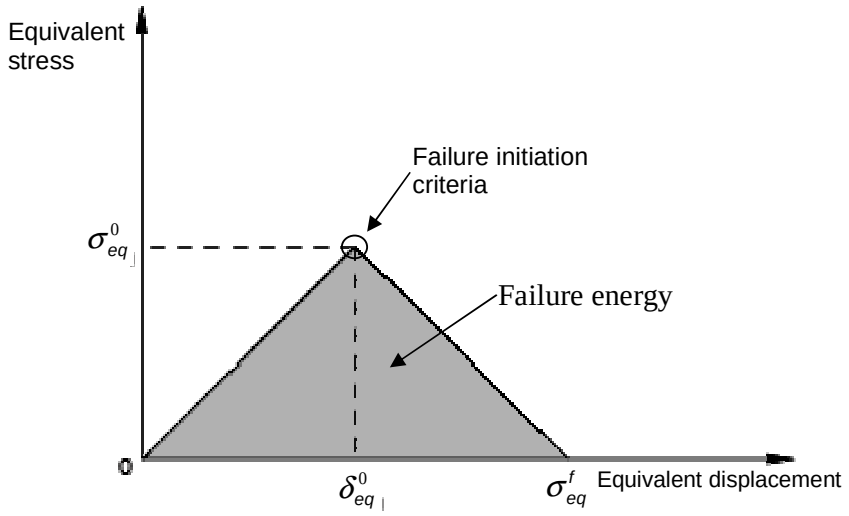

Figure 5-3 Stress-displacement relation for composite failure model (Abaqus User Manual 2010)

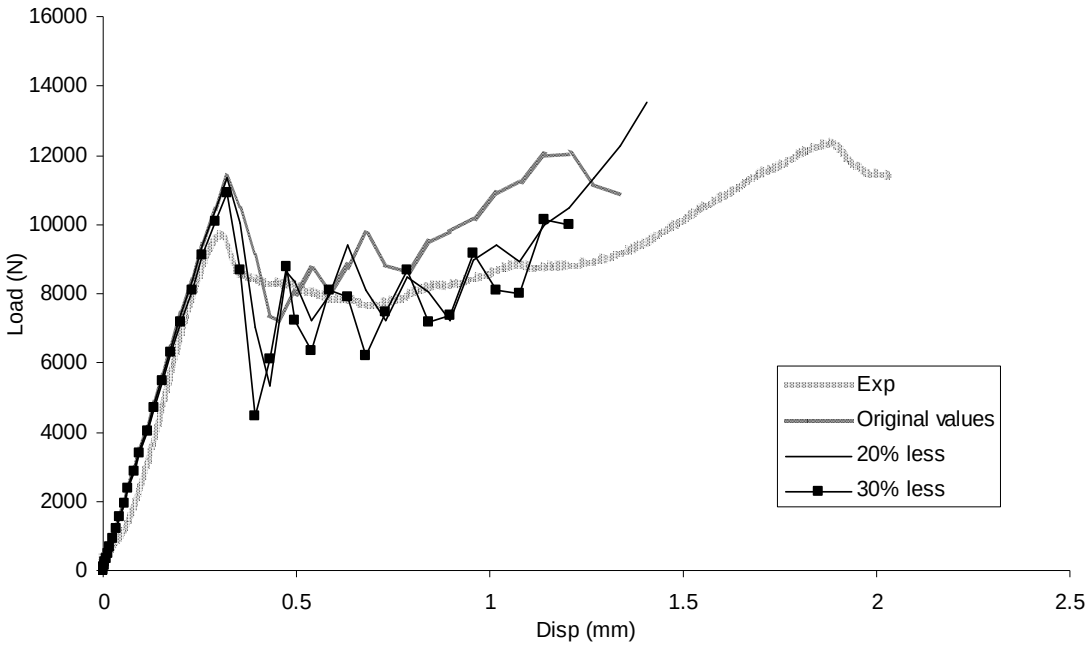

Figure 5-4 Load-displacement curves for different fibre failure fracture toughness values

Table 5-5 In-plane failure fracture toughness values

Property	Value (N/mm)	
	Original	Final
G_{Ft}	91	64
G_{Fc}	79	55
G_{Mt}	0.15	0.15
G_{Mc}	0.45	0.45

5.5 Cohesive modelling

The modelling of the cohesive behaviour can be performed using either cohesive elements or a cohesive surface. In this project zero thickness cohesive elements were used to model delamination. It can be seen in the experimental investigation that the primary delamination only occurred in the region where the countersunk and straight shank region met. It was decided to only model the primary delamination in this project, therefore only one cohesive element layer was added to the previously used models.

The formulation of the cohesive elements was based on the Cohesive Zone Modelling (CZM) approach. The cohesive zone modelling approach is one of the most commonly used tools to investigate interfacial fracture as highlighted by Turon et al. (2007). The major assumption of the cohesive zone modelling approach is that a cohesive zone develops near the crack tip. The continuum fields governing the bulk deformations was linked to micro-structural failure mechanisms through cohesive zone modelling. Therefore the properties of the bulk material, crack initiation condition and the crack propagation function characterise a cohesive zone modelling approach. The traction-separation law governing the behaviour of cohesive elements assumes linear elastic response up to the initiation of damage and a linear, exponential or tabular response to predict the progression of the damage. An example of bi-linear and linear-exponential traction-separation law is shown in Figure 5-5.

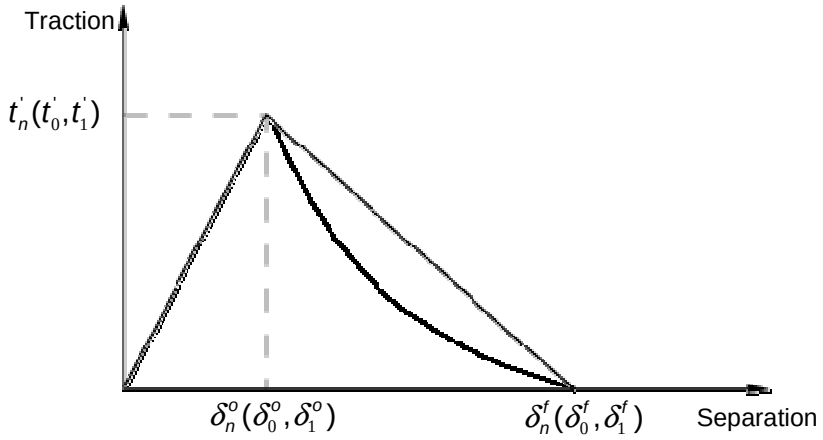

Figure 5-5 Traction-separation law for cohesive elements, (Abaqus User Manual 2010)

From Figure 5-5, it can be seen that the three properties required to define the traction-separation law were: the initial stiffness, damage initiation criteria and critical strain energy release rate (G_c) i.e. the area under the traction-separation curve. Several guidelines have

been proposed to determine the stiffness of the interface. Daudeville et al. (1995) used the thickness and the elastic modulus of the interface to calculate the stiffness. Due to very small interface thickness (order of 10^{-5} m) the obtained stiffness was very high. Zou et al. (2002), based on their own experience, proposed a value for the interface stiffness between 10^4 to 10^7 times the value of the interfacial strength per unit length. Camanho et al. (2003) used 10^6 N/mm to accurately predict the behaviour of carbon/epoxy specimens. Similarly, Kim (2010) provided an accurate prediction of delamination in an impact scenario using approximately 10^6 N/mm as the interfacial stiffness. Based on the analysis of Camanho et al. (2003) and Kim (2010) the value of 10^6 N/mm was used as the stiffness of the cohesive elements. As stated by Turon et al. (2007) it is important to make sure that the cohesive contribution to the compliance was significantly small compared to the volumetric constitutive relation. If this was not achieved a stiff connection between two neighbouring layers before delamination initiation could not be assured.

To accurately predict delamination using cohesive elements, it was important to have a minimum number of elements in the cohesive zone. In the current work it was decided to have three elements in the cohesive zone, based on the work of Falk et al. (2001) and Dávila et al. (2001). In typical carbon/epoxy or glass/epoxy composite materials, the length of the cohesive zone is smaller than one or two millimetres (Turon et al. 2007). Therefore to have three elements in the cohesive zone the mesh size in the delamination direction would be approximately 0.33 mm. The current mesh size was approximately 0.99 mm, therefore it would be required to have a mesh three times denser than the current mesh. This would significantly increase the time required to run the analysis. Another approach which can be used to have three elements in the cohesive zone is to increase the length of the cohesive zone. Alfano et al. (2001) observed that variations of the maximum interfacial strength did not have a strong influence on the predicted results, but that lowering the interfacial strength could improve the convergence rate of the solution. The reduction in interfacial strength led to an increase in the length of the cohesive zone i.e. more elements fall in the cohesive zone. This provided an accurate representation of the fracture process ahead of the crack tip, however, the stress distribution in the regions near the crack tip may be altered. The equation provided by Turon et al. (2007) was used to determine the modified interfacial strength.

$$\overline{\tau^0} = \sqrt{\frac{9\pi E G_C}{32 N_e^0 l_e}}$$

where

$\overline{\tau^0}$ = Modified interfacial strength

E = Transverse Young's modulus of the composite

G_C = Strain energy release rate for the given mode

N_e^0 = Number of elements in the cohesive zone

l_e = Length of the element in the delamination direction

Based on the above equation the interfacial strength for mode I, mode II and mode III were calculated to be 20 MPa, 40 MPa and 40 MPa respectively. To calculate the strengths, the strain energy release rate for mode I, mode II and mode III were taken to be 0.258 N/mm, 1.08 N/mm and 1.08 N/mm respectively as reported by Kim (2010).

5.6 Contact

The contact between fastener and composite laminate, bolt and nut and between upper and lower laminates in a single lap joint was defined using contact properties. It was important to correctly represent the contact behaviour to achieve an accurate FE model. The inclusion of contact definition in the model significantly increased the complexity of the model. It also led to increased simulation time and convergence difficulties. Therefore it was important to determine the best way to implement contact conditions in the FE model without severely limiting its application. The following paragraphs describe how contact was included in the FE models, based on the knowledge gained by literature survey. A detailed description of contact theories can be found in the Abaqus User Manual (2010).

The contact regions for the bearing model are shown in Figure 5-6. The contact definition for this model only involved modelling bolt to composite contact. However, the contact regions for the single lap joint were not as straightforward as shown in Figure 5-7. The following contact regions were defined for the single lap joint:

- Upper laminate and bolt contact
    - Upper laminate and bolt countersunk contact region
    - Upper laminate and bolt straight contact region
- Upper and lower laminate contact

- Lower laminate and bolt contact
- Lower laminate and nut contact
- Nut and bolt contact (not shown in the figure)

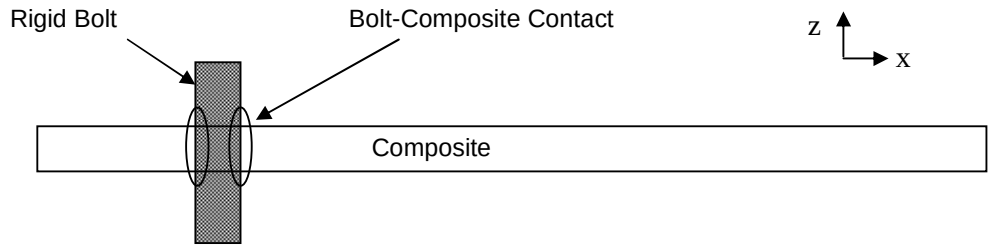

Figure 5-6 Contact region for bearing model, (Chishti et al. 2010)

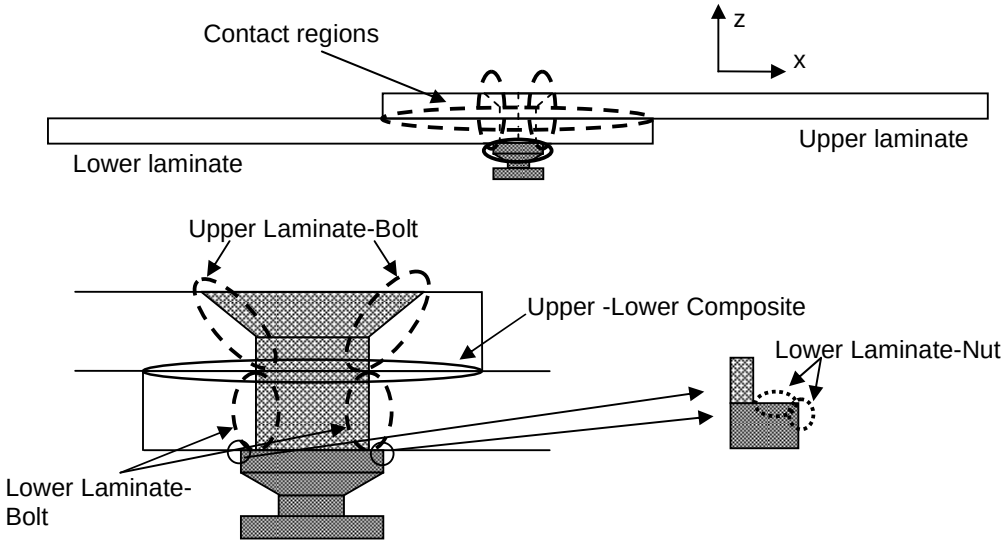

Figure 5-7 Contact region for single lap model, (Chishti et al. 2010)

The detailed description of nut-bolt contact region is provided in the bolt torque section. The contact surfaces of the composite laminates were based on the underlying nodes rather than the elements. This was necessary because the underlying element experienced failure (Abaqus User Manual 2010).

5.6.1 Friction

Friction was modelled between bolt-laminate contact, nut-laminate contact and laminate-laminate contact. Both bearing and single lap joints experienced significant damage before final failure, therefore contact forces provided a significant contribution to the failure progression and load distribution. The presence of bolt torque also implied that the friction could not be ignored in this contact definition as suggested by Thoppul et al. (2009) and Oh et al. (1997). The friction between the contacting bodies was defined using a coefficient of friction. Several different values for coefficient of friction were used in the

literature as shown by Presson et al. (1998), Viisoreanu et al. (1998), Kelly et al. (2004) and Xiao et al. (2000). However, the most widely used value of coefficient of friction, 0.2, was selected for the analysis (Tserpes et al. 2001).

5.7 Bolt torque

Bolt torque can be applied using several different methods including:

- Bolt movement
- Using anisotropic thermal expansion
- Using Abaqus in-built capability

The in-built capability of Abaqus version 6.9 was only applicable for analysis with implicit solver Abaqus/Standard, therefore it could not be used for the present work. The use of anisotropic thermal expansion coefficient required the use of an instrumented bolt to determine the coefficient of thermal expansion (Ireman, 1998). The simplest approach to apply bolt torque was by displacing the bolt. This process required the bolt and nut to be meshed as separate entities and multiple steps to apply the torque.

In the initial step, the contact between the bolt outer surface and the nut inner surface together with all the other contacts discussed above were established. The initial contact between bolt and nut was a non-frictional contact. This allowed the bolt to slide in the nut without any frictional force and prevented it from penetrating the nut. Once the contacts were established the bolt was pushed in the required displacement to apply the torque. In the second step the nut and bolt were glued together. To achieve such contact condition, Abaqus provided a rough friction and no separation contact option. In the third step, the joint was fixed only at the nut and bolt to remove any residual stresses from previous steps. In the fourth and the final step the correct BCs were applied and the structure was loaded. An illustration of the above description together with the BCs can be seen in Figure 5-8. The BCs used in the steps replicate how the joint was assembled. The displacement used to replicate the applied bolt torque can be seen in Table 5-6. The displacement was calculated based on the applied torque, bolt diameter and torque coefficient as described by Budynas et al. (1989).

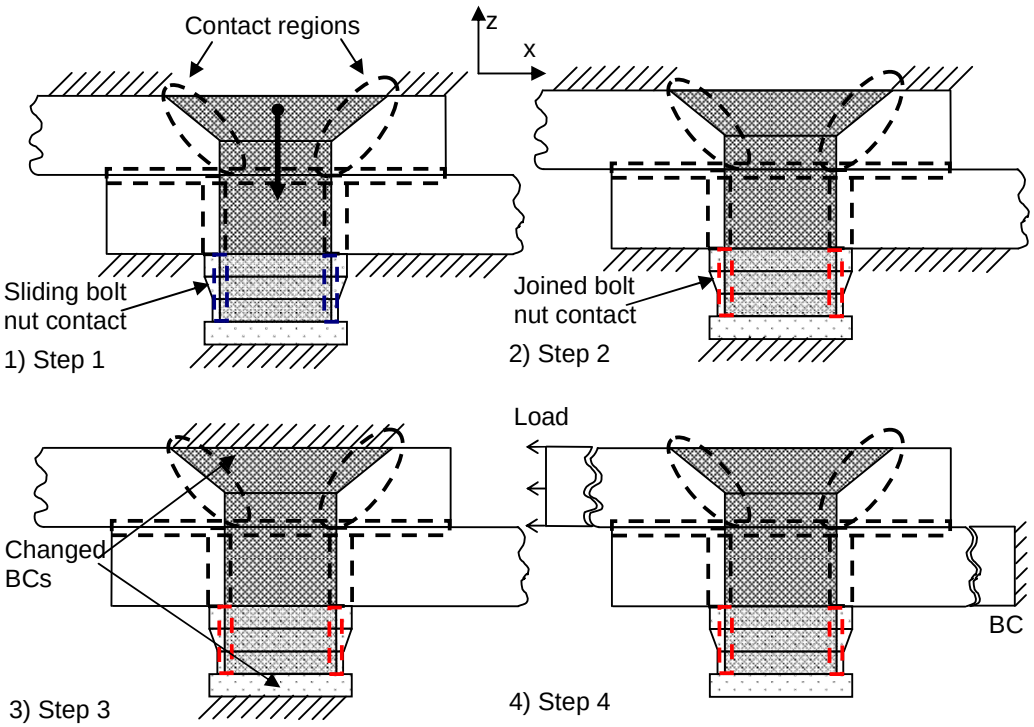

Figure 5-8 Steps to apply bolt torque

Table 5-6 Bolt torque displacement

Simulation	BT (Nm)	Displacement (mm)
BT1	0.0	0.00
BT2	2.103	0.0081
BT3	4.206	0.0162

5.8 Mesh density

The density of the mesh in a model can severely affect the results of an analysis. It was important to determine the optimum mesh density distribution which provided efficient and accurate results. It is not necessary to have the same mesh size for the whole model and model size can be significantly reduced by selectively distributing the finer mesh in the most critical regions. The single lap laminate was divided in three regions of varied density. This was necessary as it was important to have a smooth transition between different mesh density regions. The in-plane mesh density distribution of the single lap laminate is shown in Figure 5-9. The region close to the hole had the highest mesh density (D1). The transition mesh density (D2) was used between the highest mesh density (D1) and the lowest mesh density (D3) region. This provided a smooth transition of mesh from fine to coarse significantly reducing the adverse effect on the final results.

The D3 mesh region was far away from the high stress region therefore it did not significantly affect the results.

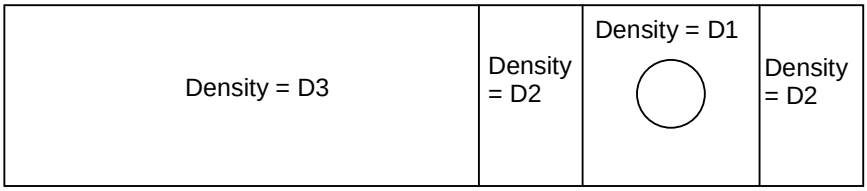

Figure 5-9 Different in-plane mesh density regions for bearing and single lap joint laminate

The results of three different in-plane mesh densities were compared to determine the effect of mesh density on the final results. The different mesh densities are shown in Figure 5-10. The mesh size for the region D1 is shown in Figure 5-11. The comparison of different model characteristics is provided in Table 5-7. It can be seen in Table 5-7 that an increase in the mesh density led to reduction and convergence of the maximum failure load. The difference between the maximum load of model 2 and model 3 was approximately 1.63%, however, the model size was increased by almost four times and the simulation time also increased by approximately four times. This showed that the mesh density in model 2 provided accurate results without being too computationally expensive. It was decided to use the M2 mesh to model the bearing and single lap countersunk composite joints. A detailed description of element distribution in the M2 mesh is provided in Figure 5-12.

The M2 mesh only provided a planar distribution of the mesh density. The through-thickness element density was mainly affected by the depth of the countersunk. For modelling joints with variable countersunk depth to thickness ratio and clearance four elements through the thickness (two for countersunk and two for straight shank region) were used to model the upper laminate. For the bolt torque models two elements through the thickness (one for countersunk and one for straight shank region) were used to model the upper laminate. Through-thickness mesh density did not affect the results. However, it can lead to early termination of simulation as shown in Figure 5-13. Two elements through-thickness were used in mesh 1 and four elements through-thickness were used in mesh 2. The number of through-thickness elements was selected to minimise the computational expense. The lower laminate for all the joints had four elements through the thickness.

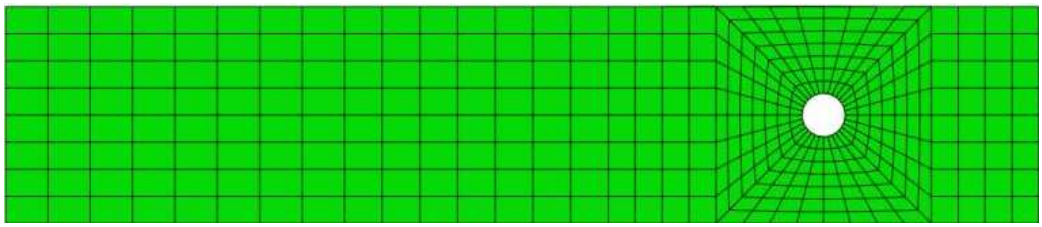

a) Coarse Mesh, M1

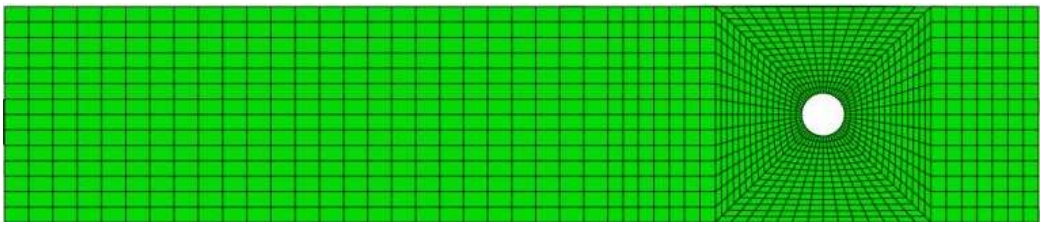

b) Fine Mesh, M2

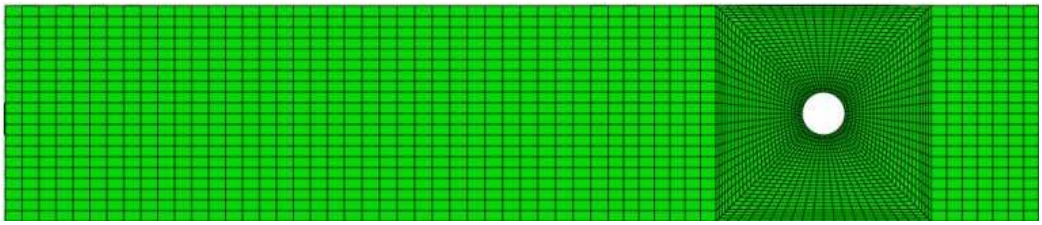

c) Finest Mesh, M3

Figure 5-10 Different mesh densities for bearing and single lap joint laminate

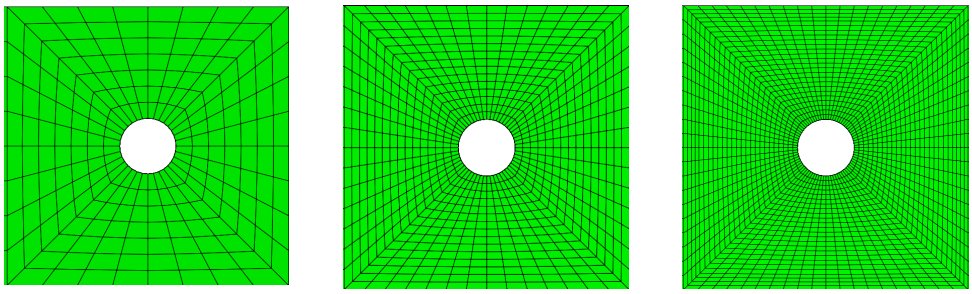

M1 M2 M3

Figure 5-11 Mesh density close to the hole (D1)

Table 5-7 Mesh density comparison table

Models	Mesh density	Model size (Mb)	Simulation time (Hrs)	Maximum force (kN)	% Difference
Model 1	M1	39.6	1.33	13.65	0
Model 2	M2	107.4	4.43	11.67	14.50
Model 3	M3	443.1	13.00	11.48	15.90

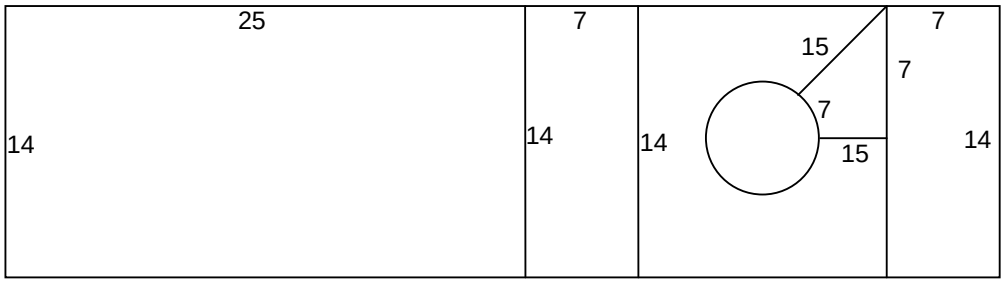

Figure 5-12 Number of elements for mesh density M2

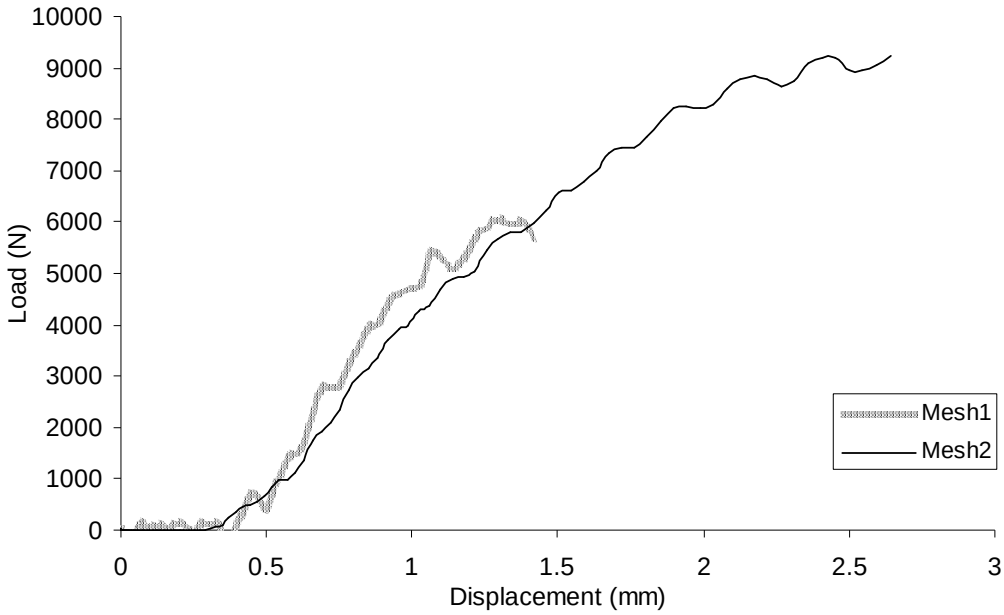

Figure 5-13 Effect of through-thickness mesh density on CL3 joint

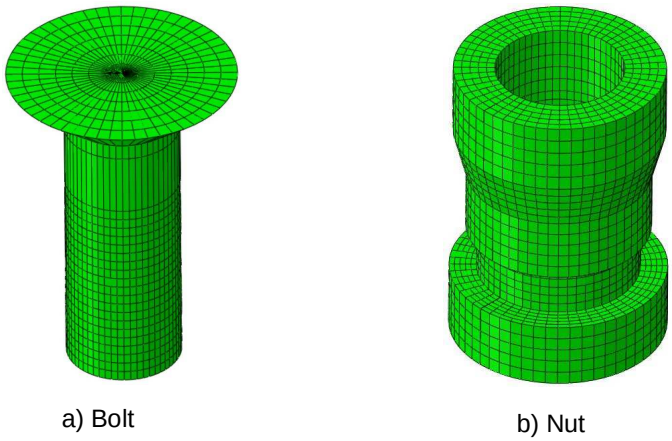

Figure 5-14 Isometric view of bolt and nut mesh

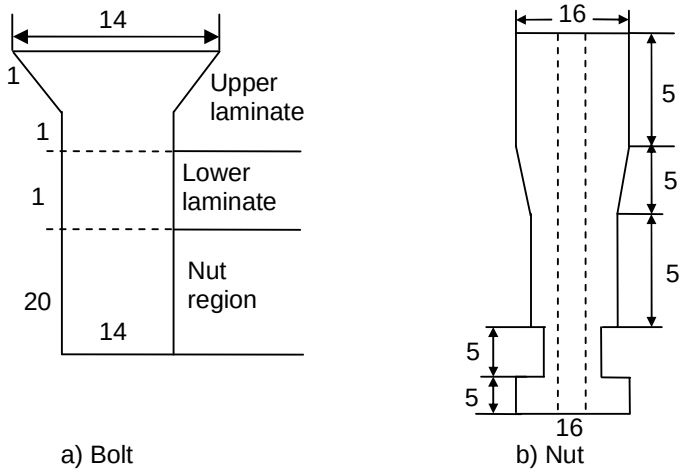

Figure 5-15 Number of elements for bolt and nut

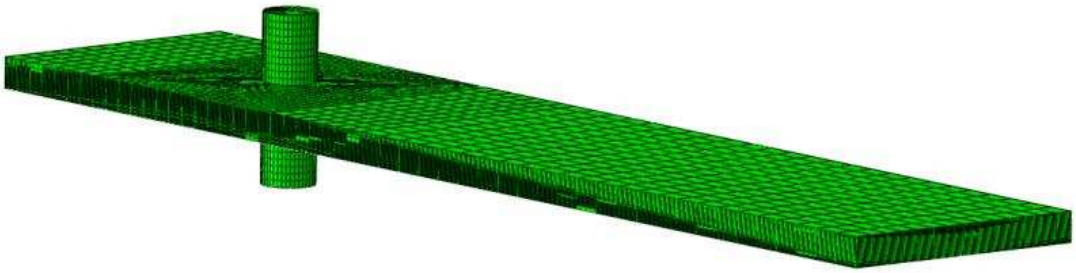

Figure 5-16 Bearing model

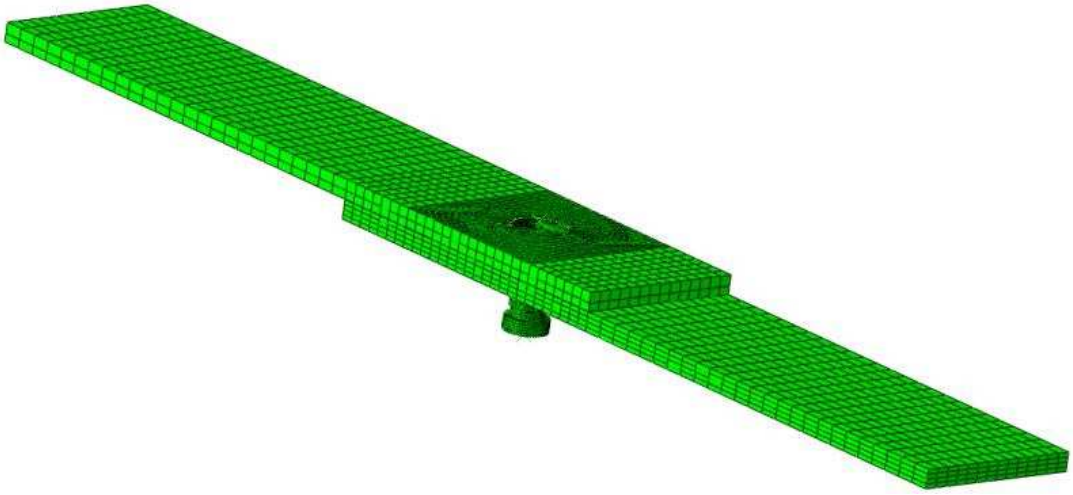

Figure 5-17 Single lap model

During the testing it was noticed that the fasteners did not experience any damage (during both bearing and single lap tests), therefore it was decided to define them as rigid bodies during analysis. The rigid body did not affect the simulation time and results, therefore any practical mesh size could be used to define the rigid body. It was decided to use a mesh density coarser than the density of the laminate as the fasteners acted as “Master” in the

contact definition. The mesh can be seen in Figure 5-14. The number of circumferential elements was same as the laminate hole. A description of the number of elements in the bolt and nut cross-section is provided in Figure 5-15. An example of an assembled model for bearing and single lap simulation can be seen in Figure 5-16 and Figure 5-17 respectively.

5.9 Mass scaling

To achieve an economical solution in static analyses, it is often useful to increase the mass of the model artificially (mass scaling). This allows for faster time increments, but can lead to a reduction in accuracy. A fixed mass scaling factor was used in the project, i.e. the mass was scaled by the same factor once at the beginning of the simulation. The factor was determined using a bearing model and was also used in single lap analysis. The mass scaling was performed only on the composite laminates for both bearing and single lap analysis. To determine the suitable mass scaling factor, simulation time, kinetic energy and internal energy were compared for different values of the scaling factor. The factor which resulted in quickest analysis with least effect on the above listed variables compared to the non-mass scaled model (MS0) was used for further analysis.

The variation of internal energy during simulation is shown in Figure 5-18. The internal energy for all the models was the same, which showed that the mass scaling did not affect the internal energy of the model. The major impact of mass scaling was on the kinetic energy of the model as shown in Figure 5-19. It can be seen that an increase in the MS factor increased the kinetic energy of the model. The kinetic energy (inertia effect) affected the accuracy of the quasi-static solution, therefore it was important have an optimal balance between speed and accuracy to achieve an efficient solution. It can be seen that the MS2 factor had a kinetic energy distribution similar to MS0 and also reduced simulation time significantly as shown in Table 5-8. Based on these results, the mass scaling factor MS2 was used in all the models.

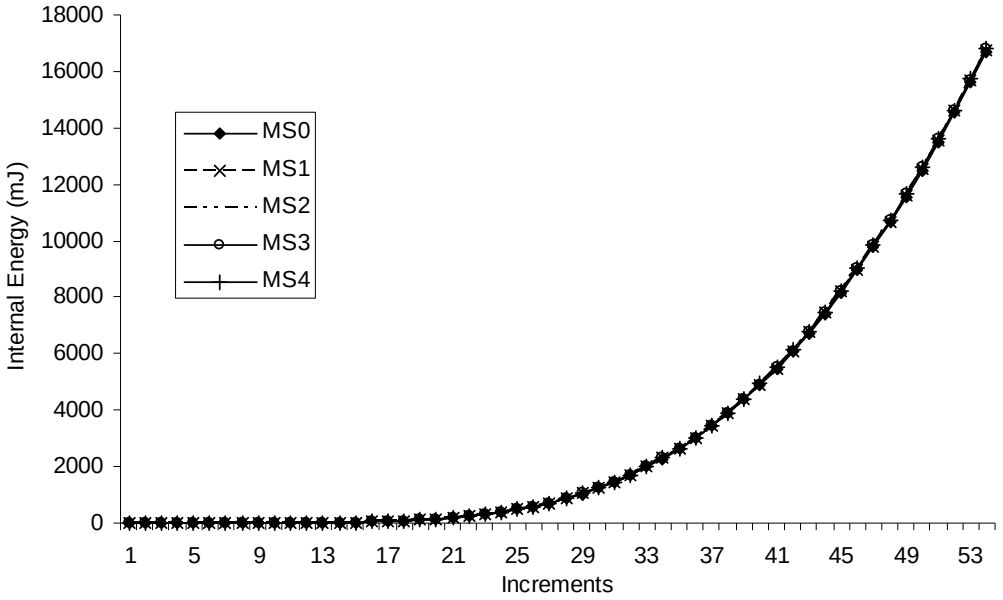

Figure 5-18 Effects of variation of MS factor on Internal energy

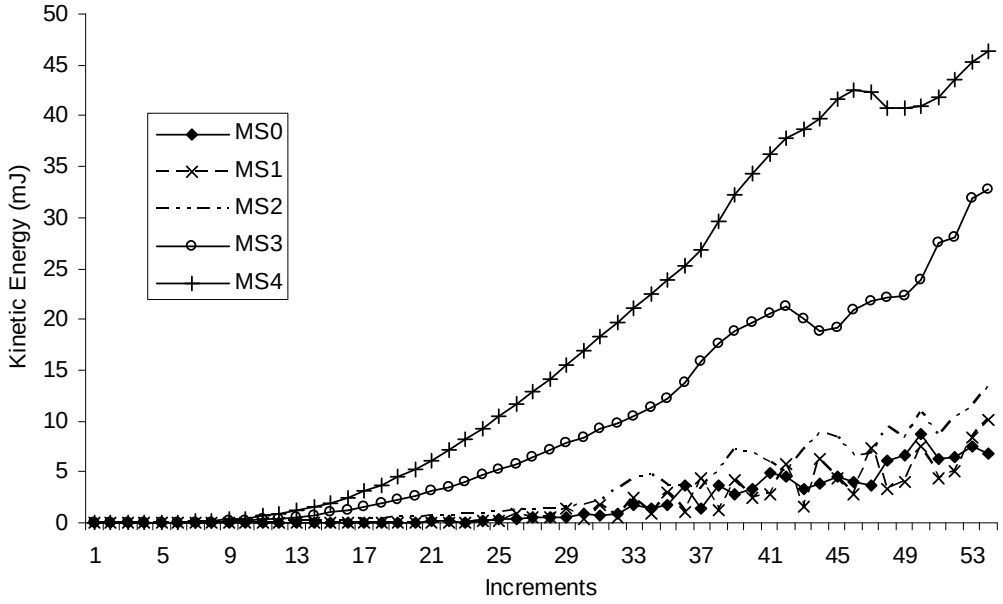

Figure 5-19 Effects of variation of MS factor on Kinetic energy

Table 5-8 Mass scaling comparison

Mass scaling	MS factor	Simulation time (Hrs)	Selected model
MS0	0	89.25	N/A
MS1	10	57.23	N/A
MS2	100	11.6	Yes
MS3	500	6.93	N/A
MS4	1000	5.5	NA

5.10 Hourglass control

Reduced integration elements were used in the model to increase the speed of the simulation. The use of reduced integration elements may lead to hourglass modes during loading. Excitation of these modes may lead to severe mesh distortion, with no stresses resisting the deformation. Hourglass controls attempt to minimise these problems without introducing excessive constraints on the element's physical response. A linear combination of viscous and stiffness hourglass control (i.e. “combined” hourglass stiffness) with all default settings was used in all the models (Abaqus User Manual 2010).

5.11 Maximum Damage Index

The maximum damage index (MD) defines the amount of damage an element undergoes before it can be declared as a failed element. The value of MD can range from 0 (no damage) to 1 (100% damage). The default values for continuum shell were 1.0 for the case of element deletion and 0.99 for all the other cases (Abaqus User Manual 2010). However, it is possible to apply a user-defined value for maximum degradation. The use of user-defined MD promotes stability as the failed element would not have zero stiffness, which is a major cause of numerical instability as pointed out by several authors (Padhi et al. 2002; McCarthy et al. 2005). A parametric study was conducted to determine the optimum value of MD. The Figure 5-20 shows the variation of the load-displacement curve for different values of MD. It can be seen that the values of 0.90 and 0.96 made the model too stiff after failure initiation. The final model with value of 0.985 captured the damage progression quite well. The value of 0.985 was selected for all the models.

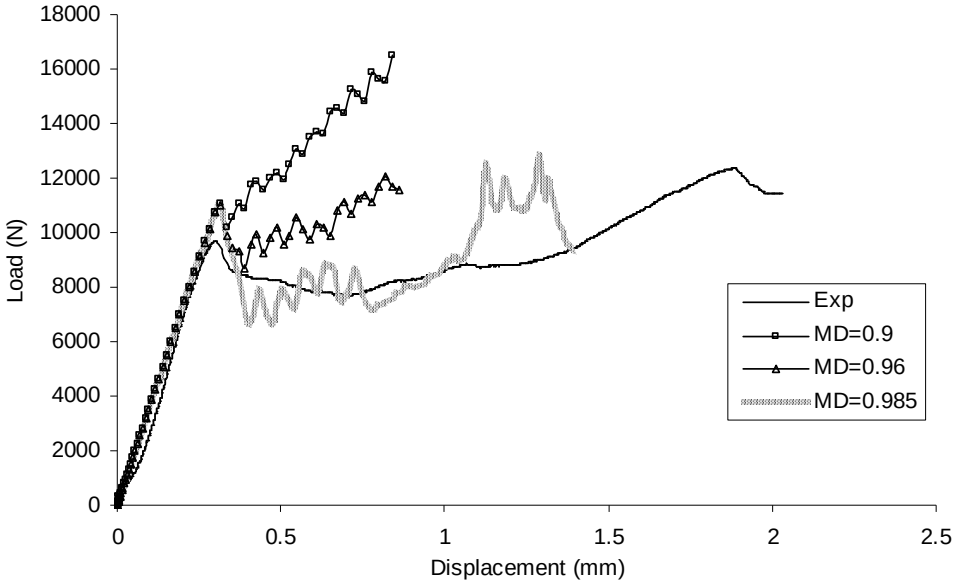

Figure 5-20 Variation of maximum damage index

5.12 Boundary conditions

The BCs and loading used to model bearing and single lap joint are shown in Figure 5-21 and Figure 5-22 respectively (Chishti et al. 2010). The length of the loaded region was the same as the grip length of the testing machine. The grip was displaced in the longitudinal direction to apply the load. The transverse and the vertical motions were restricted in the loaded region. For the bearing test the rig did not provide any lateral support; therefore, it was not modelled and a simple pin was used in place of the bolt. The ends of the pin were restricted in all the directions. For the single lap joint the end of the bottom laminate was fixed in all direction. The load was applied using displacement boundary condition.

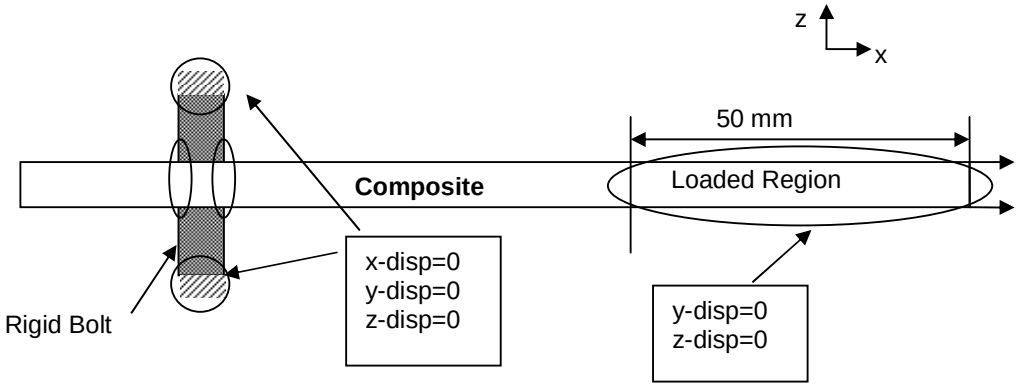

Figure 5-21 Bearing test boundary conditions

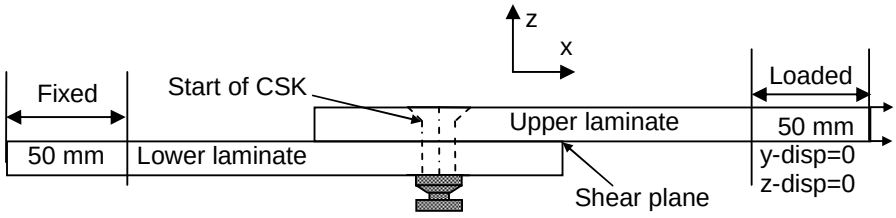

Figure 5-22 Single lap joint boundary conditions

5.13 Conclusion

A modelling methodology was developed to countersunk composite bolted joints. The developed methodology used the capabilities of the currently available finite element software to model progressive composite damage, frictional contact, application of bolt torque and other features of composite single lap bolted countersunk joints.

6 NUMERICAL ANALYSIS RESULTS

This section provides a detailed analysis of the finite element results. A comparison with experimental results is provided together with further detailed investigation of finite element results. The layer-wise results shown in the chapter were created using the in-built capability of Abaqus/Viewer to show results for each layer even if the layer is not explicitly modelled.

6.1 Experimental comparison

In this section, a comparison between experimental and FE results is provided. This section establishes the accuracy and applicability of the developed modelling approach. Table 6-1 provides a comparison for all the developed models. The HT3FE model represents a special case of HT3 joint as discussed later. The clearance and countersunk depth to thickness ratio models terminated early due to excessive element distortion. Table 6-1 compares the load at 2 mm displacement for these models. The displacement of 2 mm was selected because it was the maximum displaced reached by all the models and it was located in the non-linear region of the load-displacement curve.

It can be seen that all the models predicted ultimate failure load or load at 2 mm displacement quite well. The prediction of bearing load was not as accurate. The bearing load for bearing and BT1 joints was predicted reasonably well. However, for all the other models that failed in bearing, the bearing load was underestimated. The model was not able to capture the fully developed stiffness of the joint which led to difference in bearing load results.

The comparison between FE and experimental results of the BT2 joint is shown in Figure 6-1. The fully developed joint stiffness was under predicted by 24% which was similar to the difference noted for bearing load in the BT2 joint. A similar phenomenon was noted for all the joints. However, the overall load-displacement behaviour of the joint was captured very well. The comparison of experimental and FE load-displacement curve for bearing simulation is shown in Figure 6-2. The model was able capture the load-displacement behaviour reasonably well. However, it was not able to capture the complete non-linear behaviour of the joint.

Table 6-1 Experiment and FE comparison

	Experimental		Finite Element		% Diff. UFL / Load at 2 mm	% Diff. BL
	UFL / Load at 2 mm (kN)	BL (kN)	UFL / Load at 2 mm (kN)	BL (kN)		
Bearing	12.77	9.14	12.79	10	0.17	9.44
BT1=0	10.46	2.39	10.31	2.1	1.47	12.13
BT2=2.1	10.82	3.18	11.16	2.4	-3.18	24.53
BT3=4.2	11.21	3.08	11.33	2.4	-1.03	22.1
CL1=0	9.47	3.18	10.3	2.4	-8.7	24.53
CL2=240	8.38	2.64	8.94	1.8	-6.75	31.82
CL3=440	7.55	2.47	8.22	1.8	-9	27
HT2=0.56	9.47	3.18	10.3	2.4	-8.7	24.53
HT1=0.64	8.20	2.81	9.32	2.1	-13.61	25.3
HT3=0.76	10.53	2.4	11.03	3.0	-4.78	-25
HT3FE=0.75	N/A	N/A	7.5	1.7	N/A	N/A

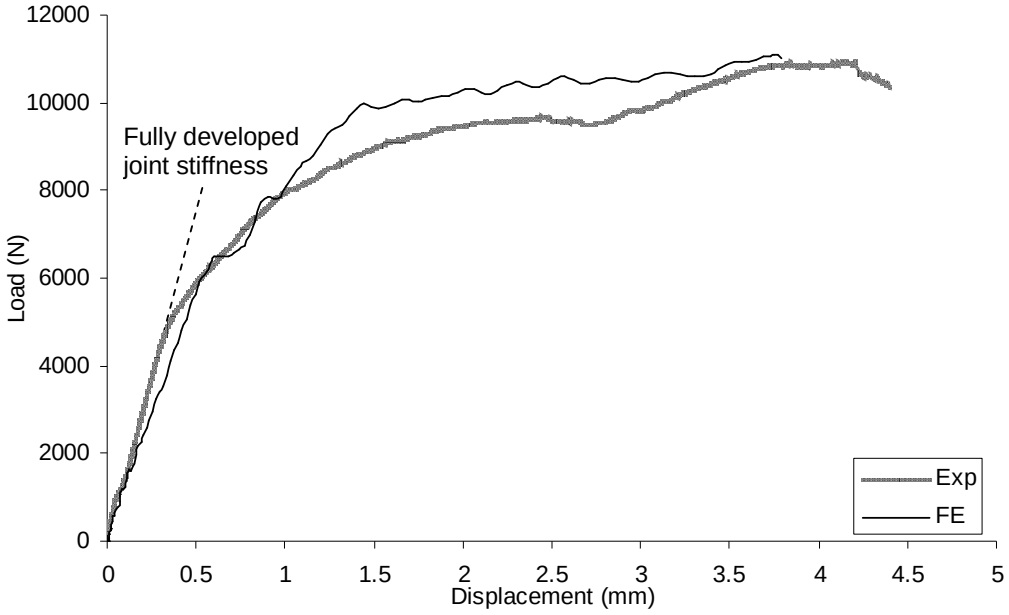

Figure 6-1 Load-displacement result for joint with 2.103 Nm bolt torque

Figure 6-2 Load-displacement results of bearing joint

A comparison of load-displacement behaviour for CL2 and HT1 joint is shown in Figure 6-3 and Figure 6-4 respectively. The results of CL2 analysis showed a delay in load-carrying capacity of the joint. The response of the FE results was very similar to the experimental analysis. As previously stated the FE analysis stopped before the ultimate failure load could be achieved. The model of HT1 joint under- and over-estimated some sections of the load-displacement curve. Similar to the BT2 joint the FE model over-estimated the stiffness in the non-linear region for HT1 joint.

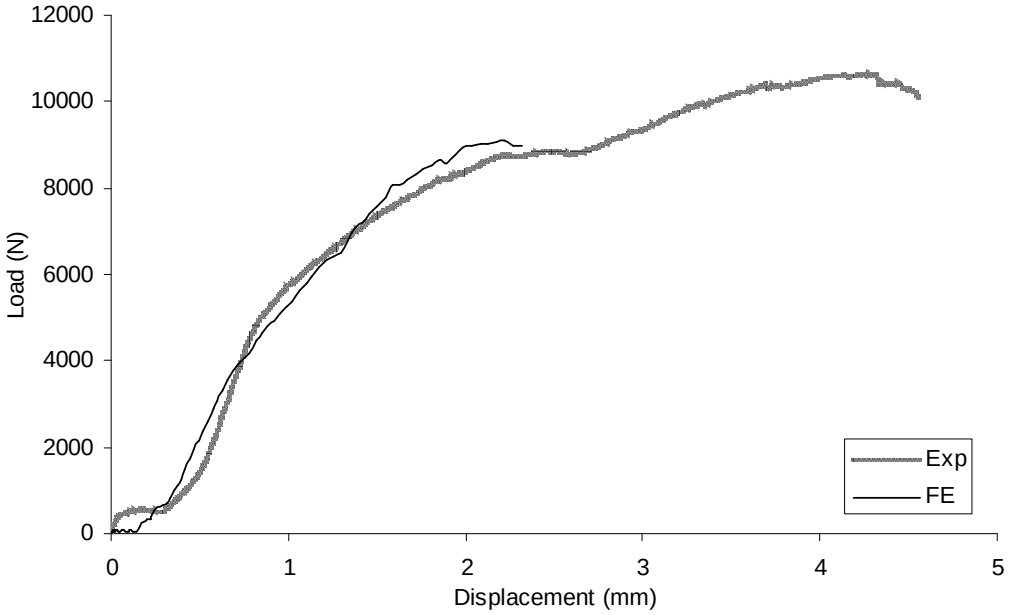

Figure 6-3 Load-displacement result for joint with 220 μm clearance

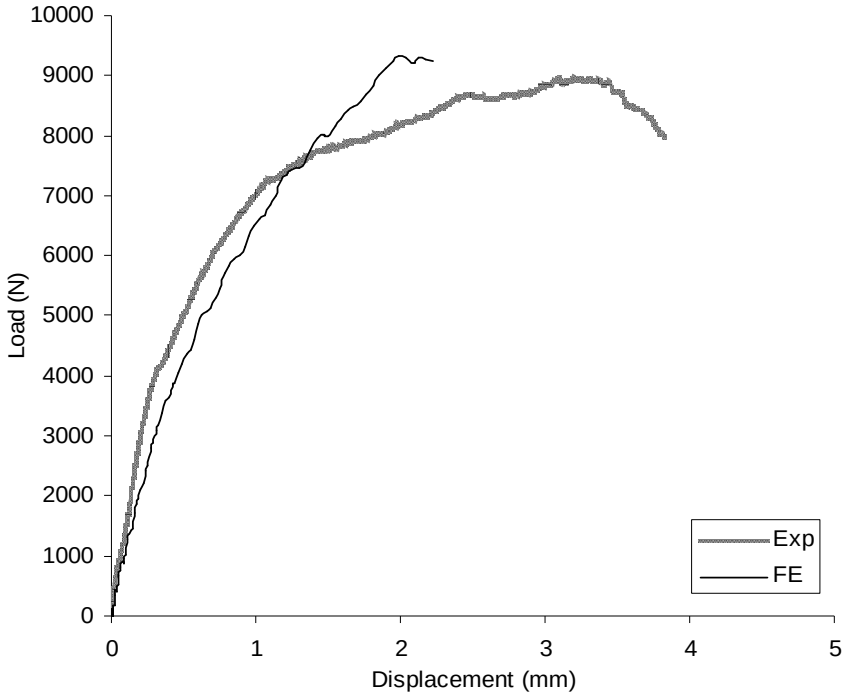

Figure 6-4 Load-displacement result for joint with countersunk depth to thickness ratio of 0.64

The through-thickness damage distribution was compared to the experimental micrographs. In the current study undeformed shapes were used when the results of experiments were compared with FE to reduce the ambiguity caused by deformed elements. In the figures the red colour indicates complete failure of the structure and dark

blue or white colour indicate no failure. Any colour in between shows progression of the damage. This scale was applicable to all the FE images showing damage, and is shown in Figure 6-5. Figure 6-6 shows the damage at 45^{o} cutting plane for first non-linearity load. The FE results showed fibre compressive (FC) failure only. The fibre compressive failure mode was considered to be the most critical failure mode for the current study, therefore was used for all the comparative analyses. The FE model predicted experimental results quite well as not much fibre failure was reported in experimental results at this stage.

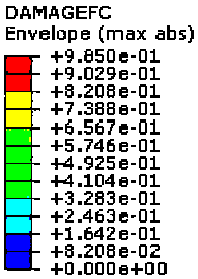

Figure 6-5 Scale for damage plots

The damage for the same load at zero degree cutting plane is shown in Figure 6-7. Compared to 45^{o} cutting plane the damage at 0^{o} cutting plane has increased in both extent and severity. The figure also showed that the top and the bottom layers experienced more damage compared to middle layers. The FE model predicted this phenomenon quite well. The boxes in Figure 6-7 show the extent of damage in both experimental and FE results. The FE model only showed fibre compressive damage, this led to slightly different extent of damage compared to experimental results.

The fibre compressive damage in BT1 laminate is compared with experimental results in Figure 6-8. The figure shows two different ways to plot fibre compressive failure. In part b) damage in each layer is plotted separately, whereas in part c) an “envelope” approach is used to plot the damage. The envelop approach over-predicts the damage as it plots the maximum damage index in each element through the thickness. However, the profile and extent of damage was captured well by the envelop damage plotting approach. A similar comparison for fibre compressive damage in the lower laminate of BT1 joint is shown in Figure 6-9. The damage profile of other joint configurations was captured accurately by the FE model. The results are discussed in the following sections and the envelop approach is used in any further comparison. The analysis showed that the FE model is capable of predicting the behaviour and damage profile (through-thickness and extent) of bearing and single lap joint accurately.

Figure 6-6 Damage at 45^{o} cutting plane at first non-linear load (See Figure 6-5 for damage scale)

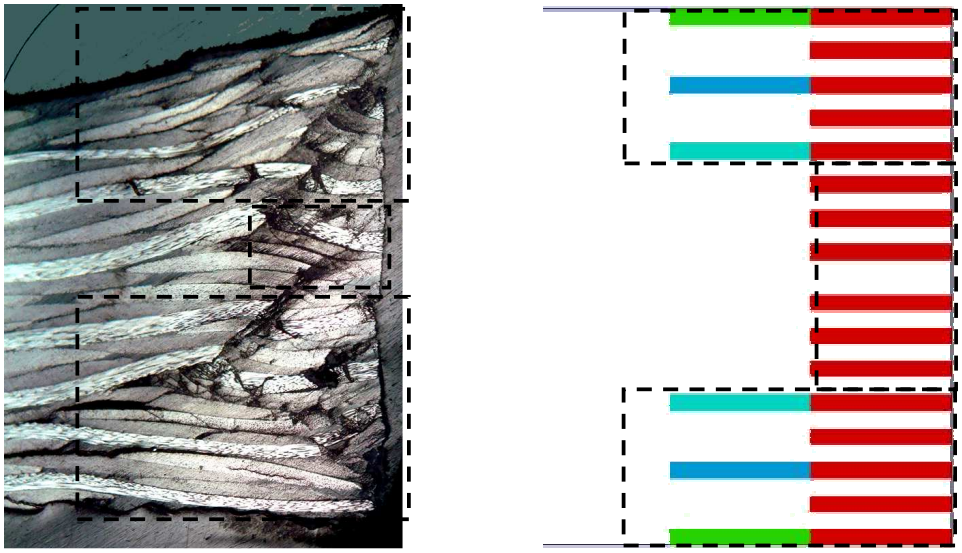

Figure 6-7 Damaged at 0^{o} cutting plane at first non-linear load (See Figure 6-5 for damage scale)

a) BT1 Experiment

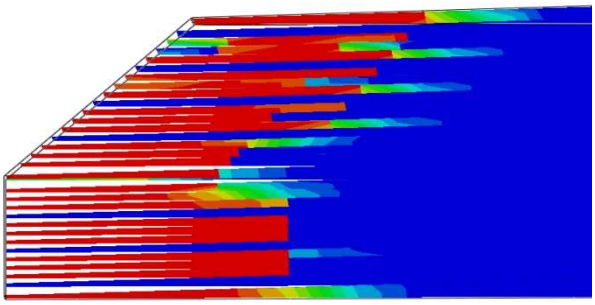

b) BT1 FE

c) BT1 FE envelope

Figure 6-8 Fibre compressive damage in upper laminate of joint with 0 Nm bolt torque at 0^o cutting plane (See Figure 6-5 for damage scale)

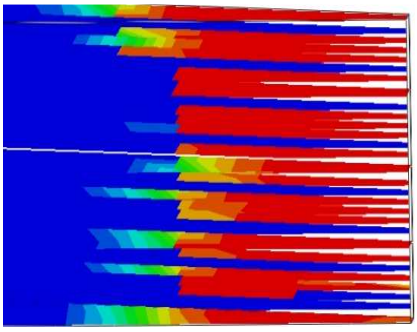

a) BT1 FE

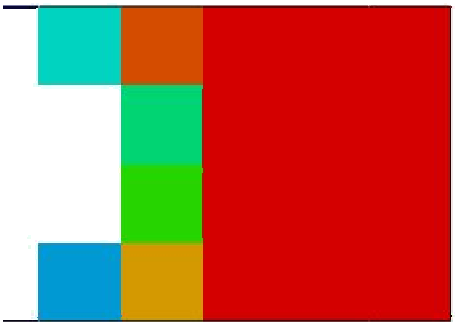

b) BT1 FE envelope

Figure 6-9 Fibre compressive damage in lower laminate of joint with 0 Nm bolt torque at 0^o cutting plane (See Figure 6-5 for damage scale)

The accuracy of the models was also monitored using various energy outputs. Figure 6-10 shows the variation of internal energy (ALLIE), hourglass energy (ALLAE), kinetic

energy (ALLKE), work done due to mass scaling (ALLMW) and viscous damping energy (ALLVD) for the BT1 joint. The ALLIE was plotted on the right hand y-axis of the plot to show the distribution of the other energies. It can be seen that all the energies were with in 10% of ALLIE. Plots similar to Figure 6-10 were obtained for all the simulations, however, they will not be shown here.

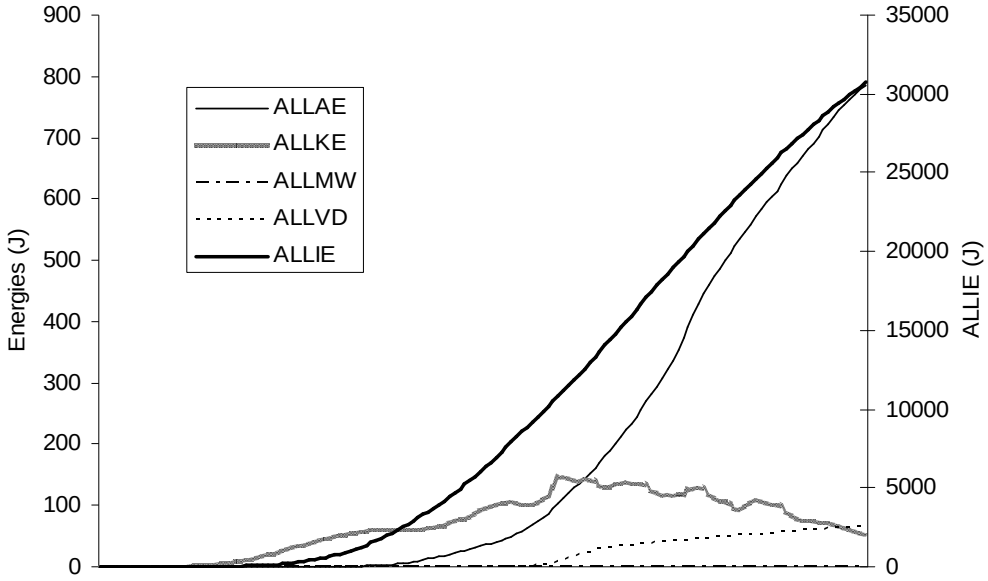

Figure 6-10 Energy variation for joint with 0 Nm bolt torque

6.2 Effect of Countersunk

This section discusses the effects of the countersink on stress distribution and damage in a single lap joint. The effects of countersunk can be understood by analysing the results of the BT1 joint. Figure 6-11 shows the location used to plot the distribution of stress concentration factor around the hole in single lap joints. Figure 6-12 shows the circumferential distribution of radial stress (σ_R) for bearing joint (at the symmetric plane) and single lap joint (at shear plane (shr pln) and at the start of countersunk) in 0^o plies normalised using the maximum radial stress in the bearing laminate (σ_{bmax}). The figure shows that at the shear plane of the single lap joint the maximum radial stress was 40% higher than the bearing joint. The presence of the countersunk led to 67% increase in the maximum radial stress in the single lap joint compared to the bearing joint. This showed that both the single lap joint and countersunk geometry led to significant increase in the radial stress of the laminate. The cylindrical coordinate system used to plot the stress concentration factor is shown in Figure 3-9 together with the location of bearing and net section planes.

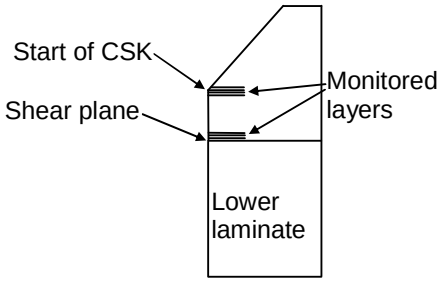

Figure 6-11 Layers used for stress concentration factor distribution

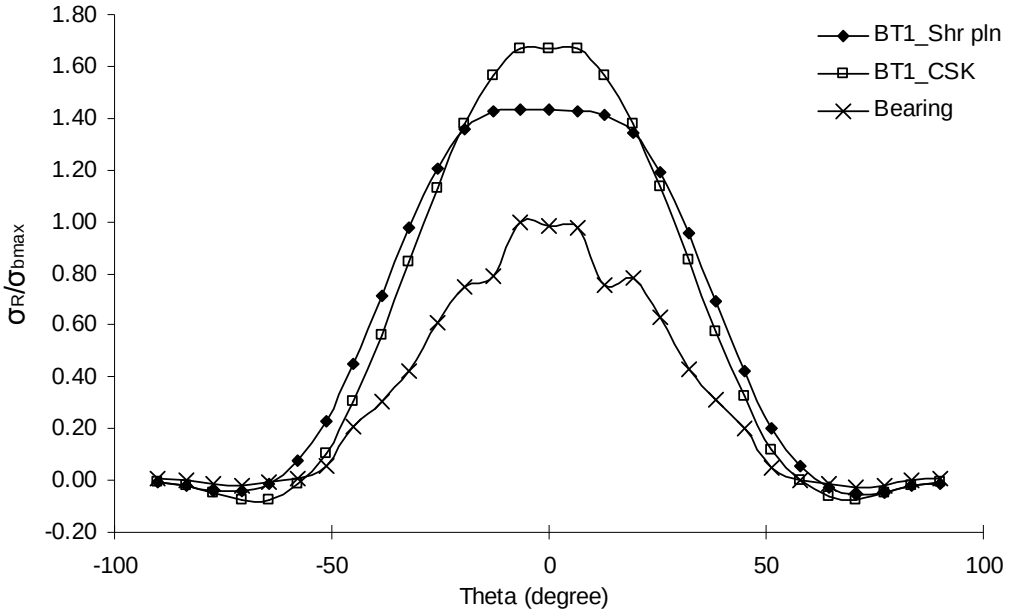

Figure 6-12 Effect of countersunk on radial stress concentration factor in upper laminate at ~1.5 kN

A high element density model with full 3D elements was developed for linear stress analysis of the single lap joint. The distribution of σ_{33} and σ_{13} through the thickness of countersunk laminate is shown in Figure 6-13 and Figure 6-14 respectively. Similar to radial stresses it can be seen that high through-thickness stresses existed at the start of countersunk region. The presence of the countersunk also affected the initiation of damage through the thickness. Damage initiation and progression in 0^o plies through the thickness of the bearing joint and upper laminate of the single lap joint is shown in Figure 6-15. Layers 1 and 13 were in the straight shank region of the upper laminate. Layer 1 was located at the shear plane of the joint. Similarly, layers 20 and 32 (top surface) were located in the countersunk region of the upper laminate. The damage index was plotted versus normalised displacement with respect to the total displacement. The displacement of the hole edge for the bearing model and the relative displacement between upper and

lower laminates were used to plot the results. As the final displacements for the bearing and single lap joints were different, normalising the displacement simplified the comparison of damage progression in both the joints.

The damage in the countersunk region was significantly delayed compared to the straight shank region. The damage in 0^o plies of the bearing joints initiated and progressed together. The damage in the straight shank region of upper laminate initiated slightly earlier than the bearing laminate, however, the difference was negligible. The progression of damage was similar to the bearing joint. However, the presence of the countersunk led to a delay in initiation and progression of damage as shown in Figure 6-15. The intensity and the extent of damage were also affected by the presence of the countersunk. The damage progression at 2 mm displacement in various layers is shown in Figure 6-16, and is described in detail in the next section. From this analysis it can be seen that the presence of countersunk had a significant effect on the majority of the joint parameters.

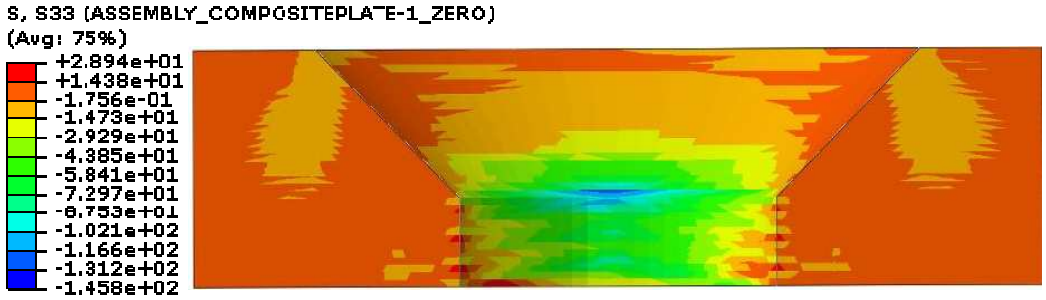

Figure 6-13 Distribution of σ_{33} (MPa) in the countersunk laminate

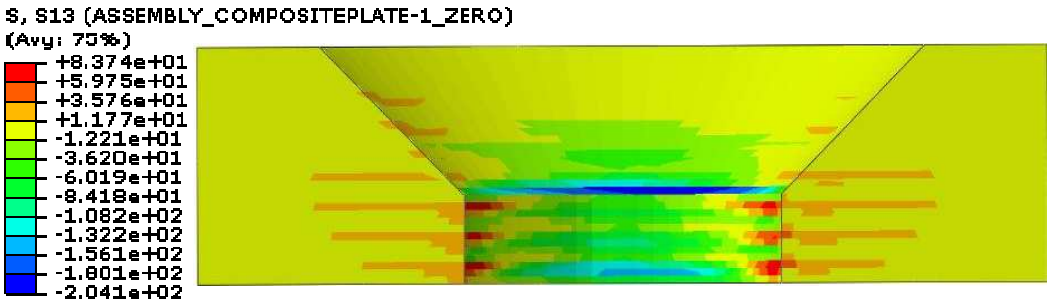

Figure 6-14 Distribution of σ_{13} (MPa) in the countersunk laminate

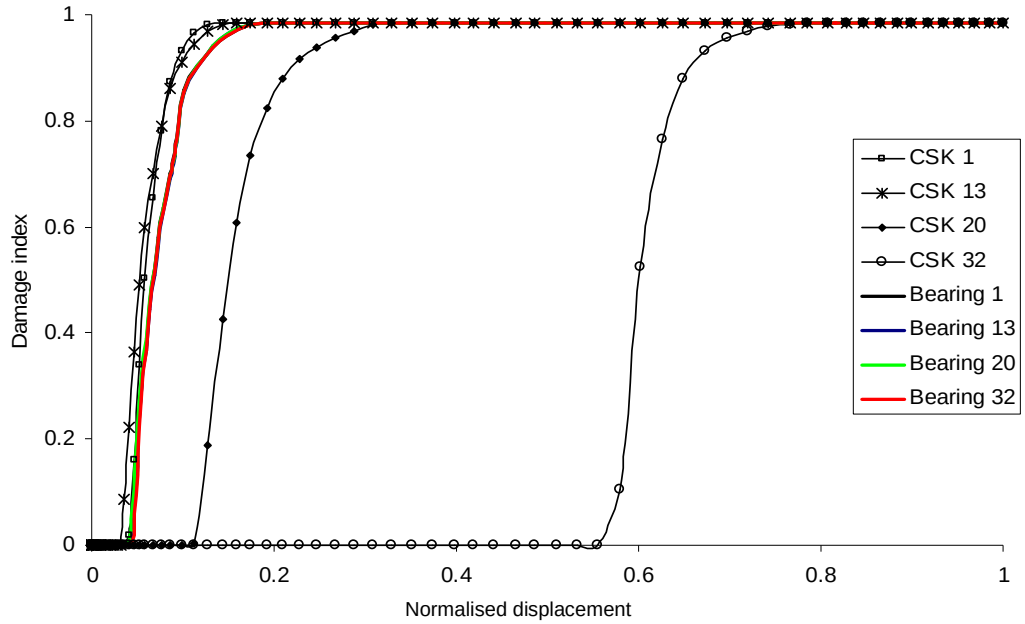

Figure 6-15 Damage progression at selected ply locations in bearing and single lap joint

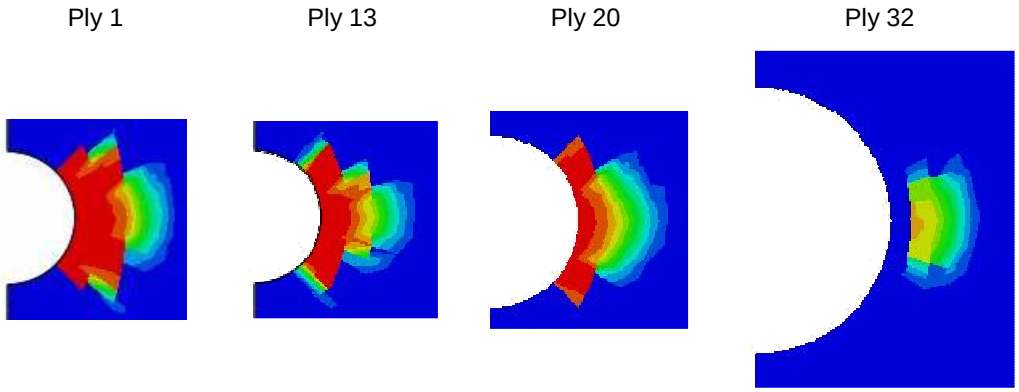

Figure 6-16 Damage progression for upper laminate of joint with 0 Nm bolt torque (See Figure 6-5 for damage scale)

6.3 Effects of clearance

The following section discusses the results of clearance joint analyses. The load-displacement behaviour of the clearance joint is shown in Figure 6-17. In a similar way to experimental results, the FE models showed a delay in load-carrying capacity due to clearance. An increased clearance from 0 µm to 440 µm led to reduction in the fully developed joint stiffness as seen in experimental results. The contact area for the bolt is shown in Figure 6-18. The black region shows the area in contact. It can be seen that as clearance was increased the contact area reduced. For clearance of 220 µm and 440 µm a reduction of 7.2% and 8.8% respectively was noticed as shown in Figure 6-18. This

shows that reduced contact area is not directly proportional to clearance for countersunk joints.

The reduced contact area led to high localised stresses as shown in Figure 6-19. The stress concentration factor was calculated using the local stresses at the hole normalised by the bearing stress at 1.5 kN applied load. The stress concentration factor increased almost three times for joints with 220 µm and 440 µm clearance. The distribution of radial stress concentration factor for both the joints was similar due to only marginal reduction (-1.6%) in contact area for the joint with 440 µm clearance compared to the joint with 220 µm clearance. Other stress plots are provided in Appendix II.

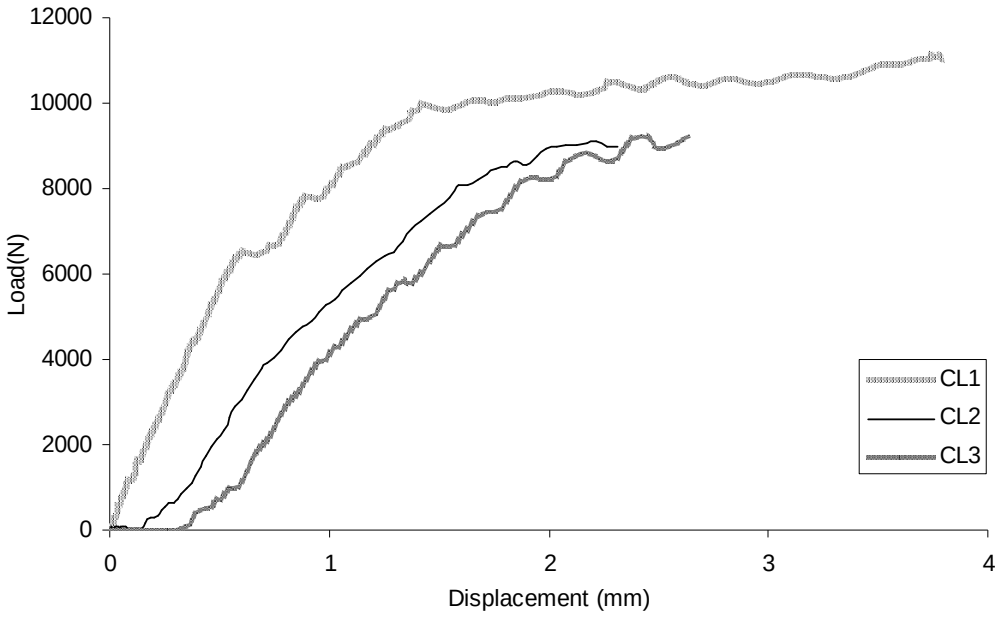

Figure 6-17 Effects of variation of clearance

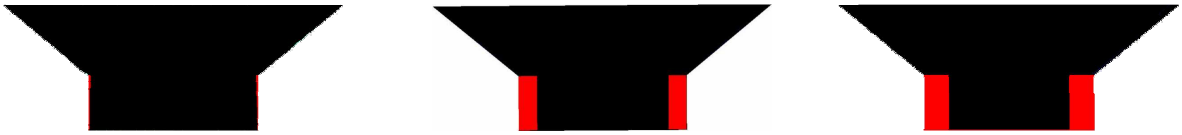

a) CL1 (0%) b) CL2 (-7.2%) c) CL3 (-8.8%)

Figure 6-18 Effects of clearance on fully developed contact area

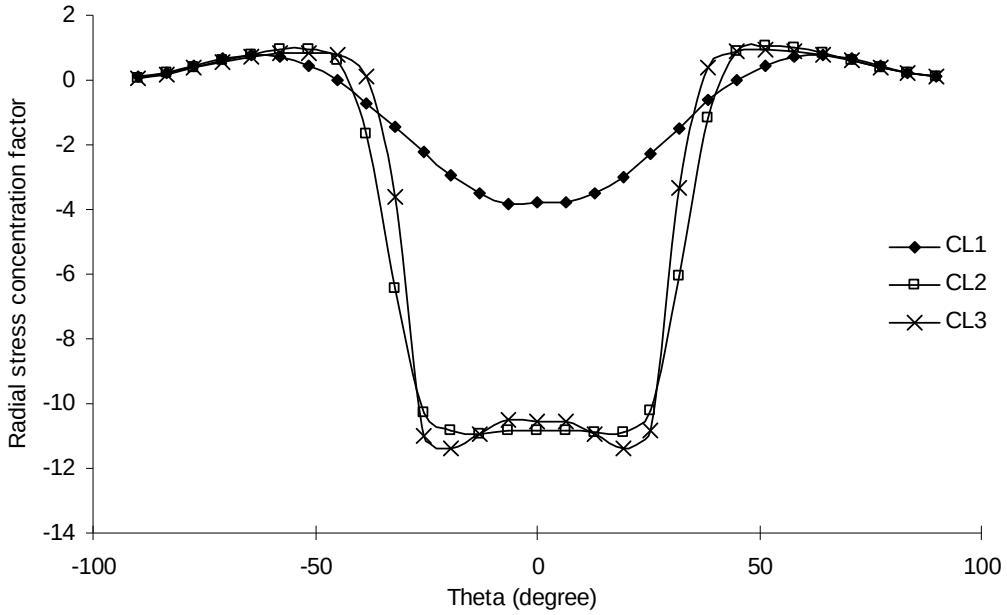

Figure 6-19 Effect of clearance on radial stress concentration factor at shear plane (0^o ply) in upper laminates at ~1.5 kN

The presented results are taken at 2 mm displacement of the joint; therefore, they cannot be directly compared with experimental micrographs. The through-thickness fibre compressive damage progression for the upper and lower laminate at the intersection of the bearing plane and hole edge in 0^o plies is shown in Figure 6-20. Layer 1 marked the location of the joint shear plane and layer 32 showed the location of top surface in the upper laminate. Layer 32 in the lower laminate marked the location of shear plane of the joint. The dashed line shows the start of the countersunk region. An increase in clearance also affected the damage initiation and progression through the thickness of the laminate. This is significant because it shows that clearance can lead to internal damage in the joint even when a neat fit joint is not expected to contain any damage. It can be seen that an increased clearance led to fibre compressive damage in the plies close to the shear plane at the bearing load in upper and lower laminate. This was not seen for the neat fit joint. The presence of clearance also led to no fibre compressive damage in ply 32 (top surface of upper laminate). The bottom and top layers of the lower laminates did not suffer any failure until 2 mm displacement. It was expected that these layers would fail close to ultimate failure load as seen in the neat fit joints.

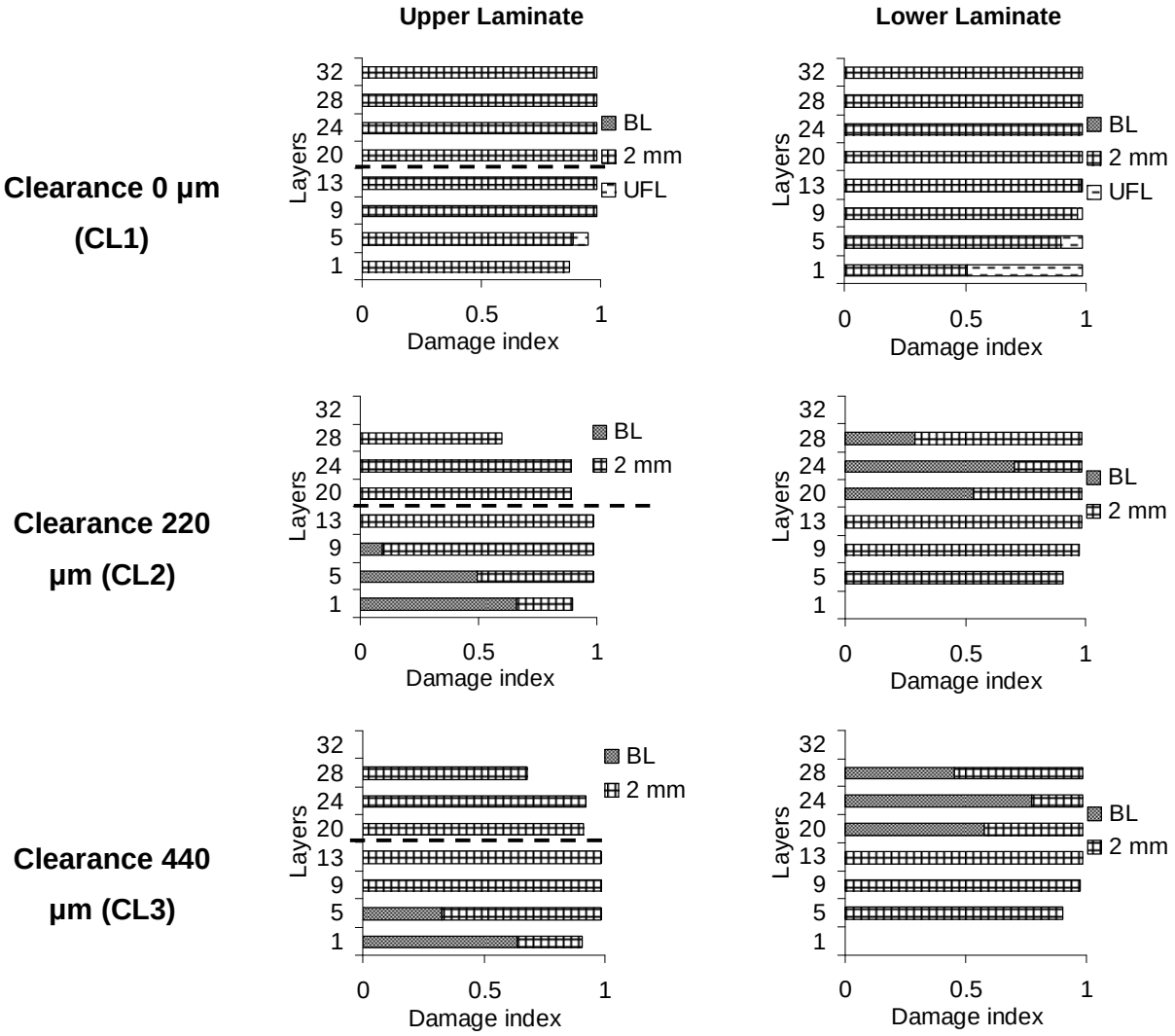

Figure 6-20 Effect of clearance on through-thickness fibre compressive damage progression at the hole edge

The severity and extent of fibre compressive failure at bearing load can be seen in Figure 6-21. The joint with no clearance did not experience any fibre compressive failure at bearing load. The joint with 220 µm clearance experienced most failure at bearing load. The extent and intensity of fibre compressive failure in the lower laminate was similar for joints with 220 µm and 440 µm clearance. Similarly, a comparison of failure profiles at 2 mm displacement is shown in Figure 6-22. The joints with 220 µm and 440 µm clearances showed significant variation in the damage profile compared to the neat fit joint. The extent of damage was higher for the neat fit joint. The model confirmed the finding of the experimental analysis that the overall bearing damage reduced for joints with clearance. The amount of damage reduced for CL3 (440 µm) joint compared to CL2 (220 µm) joint as seen in experiments.

The circumferential distribution of fibre compressive damage in selected 0^o plies is shown in Figure 6-23. The dashed line marks the location of the start of countersunk region. An increase in clearance led to reduction of damage in the circumferential direction all through the thickness of both upper and lower laminates. The top layer of the upper laminate did not experience failure at 2 mm displacement. The severity of the damage in the upper laminate reduced as clearance increased. Similarly for the lower laminate as the clearance increased the intensity and extent of the damage reduced. The highest damage was located at the shear plane for the upper laminate.

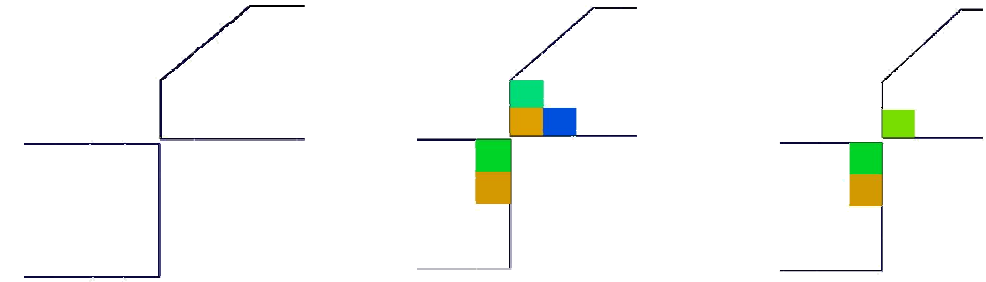

a) CL1 b) CL2 c) CL3

Figure 6-21 Effect of clearance on through-thickness fibre compressive damage at bearing load at 0^o cutting plane (See Figure 6-5 for damage scale)

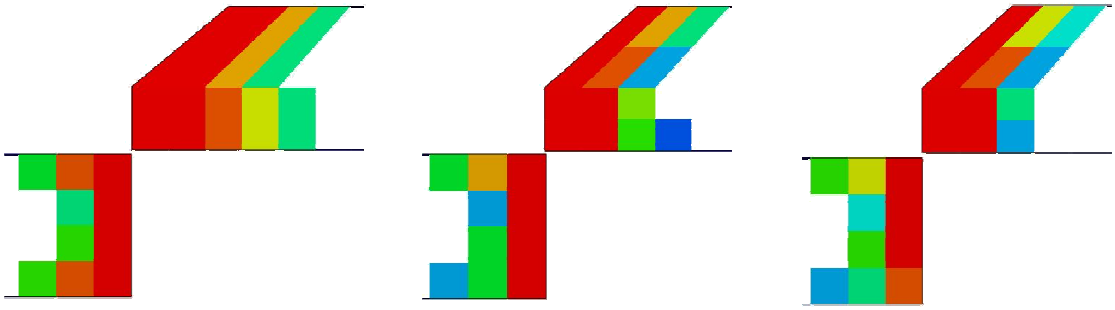

a) CL1 b) CL2 c) CL3

Figure 6-22 Effect of clearance on through-thickness fibre compressive damage at 2 mm at 0^o cutting plane (See Figure 6-5 for damage scale)

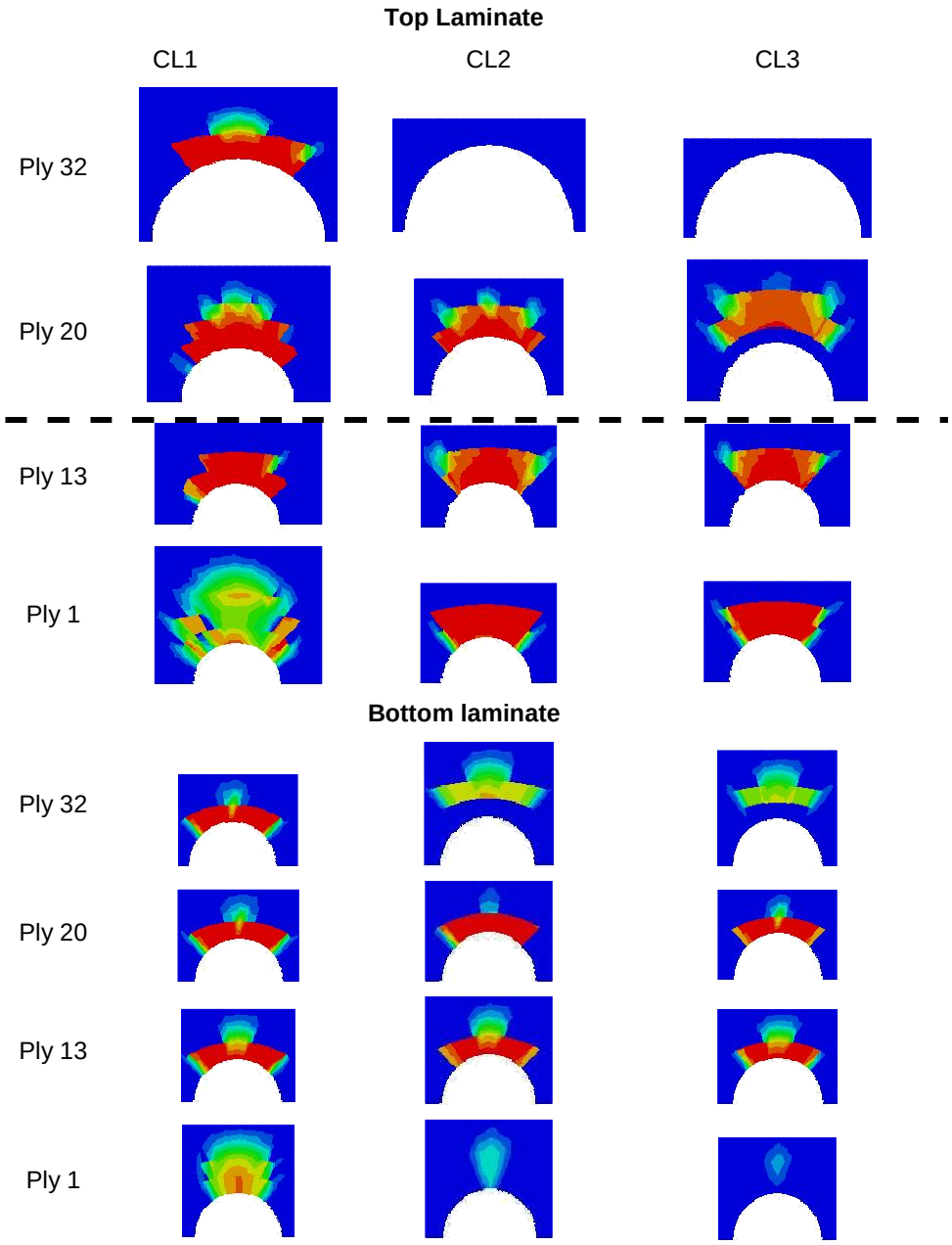

Figure 6-23 Effect of clearance on fibre compressive damage at 2 mm in 0^o plies (See Figure 6-5 for damage scale)

6.3.1 Conclusion

The bolt-hole clearance joint analysis provided detailed results of damage initiation and progression in the laminates. The model did not reach ultimate failure load for two joints with clearance, however, it accurately captured the load-displacement behaviour of the joint. The reduced contact led to less circumferential distribution of damage around the hole and higher stress concentration in the contact region. The through-thickness damage

initiated earlier due to bolt-hole clearance (i.e. at bearing load), however, the outer surface layers did not damage initially. The model also showed that the intensity of damage in the circumferential direction reduced with an increase in bolt-hole clearance.

6.4 Effects of countersunk depth to thickness ratio

To compare the results of joints with different countersunk depth to thickness ratio it was decided to model the joint with countersunk depth to thickness ratio of 0.76 with the same bolt as used for HT1 (0.64) and HT2 (0.56) analysis. This analysis was termed "HT3FE" (0.76). The laminate had $(0/90/+45/-45)_{3S}$ lay-up sequence. The laminate thickness was 2.64 mm and the depth of the countersunk was 1.98 mm. Due to different bolt and laminate thickness, HT3FE results cannot be compared with experimental HT3 analysis.

The load-displacement curves for the countersunk depth to thickness ratio joints are shown in Figure 6-24. The analysis of the joint with countersunk depth to thickness ratio of 0.64 stopped before reaching ultimate failure load due to excessive element distortion. The HT3FE model ran successfully and was externally terminated because an increase in load was not expected if the analysis continued any further. It can be seen that as the countersunk depth to thickness ratio was increased the maximum load was reduced. The initial stiffness of the joint was also reduced. The failure mode could change if the countersunk depth to thickness ratio was increased beyond the recommended limit of 0.7 as was observed in the experimental HT3 analysis.

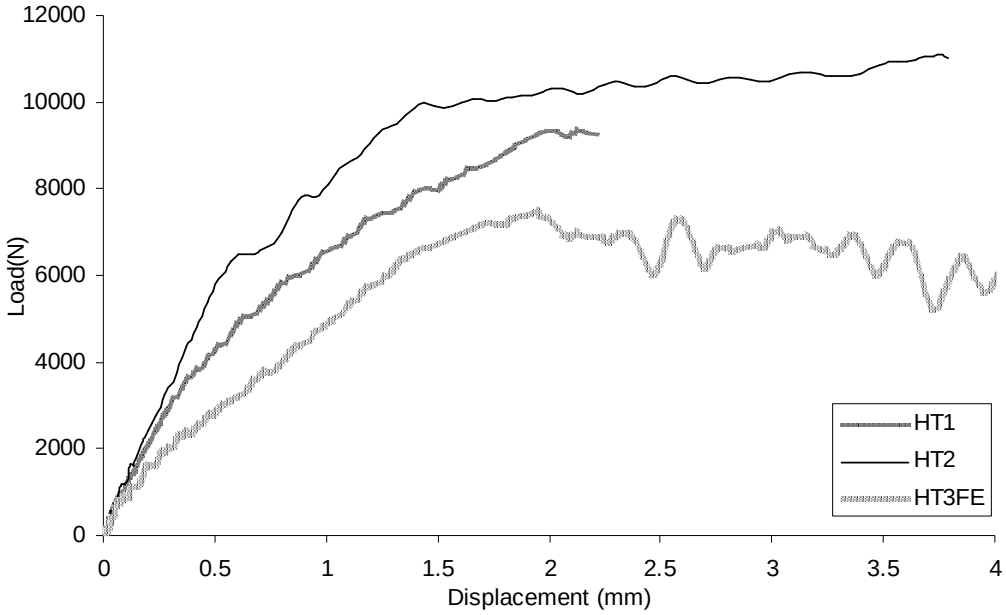

Figure 6-24 Effect of variation of clearance

The model for the joint with countersunk depth to thickness ratio of 0.76 also experienced significantly higher bending compared to the other two joints. The comparison using the region with D1 mesh at 2 mm longitudinal displacement is shown in Figure 6-25. Similar to the experimental results, the figure shows that an increase in countersunk depth to thickness ratio led to higher bending in the joints. The maximum relative displacement between the upper and lower laminate of HT2, HT1 and HT3FE joints were 1.88 mm, 2.12 mm and 2.38 mm respectively. The relative displacement for HT1 and HT3FE joints showed an increase of approximately 13% and 21% respectively compared to the HT2 joint. This clearly showed that the HT3FE model experienced severe bending compared to HT2 model.

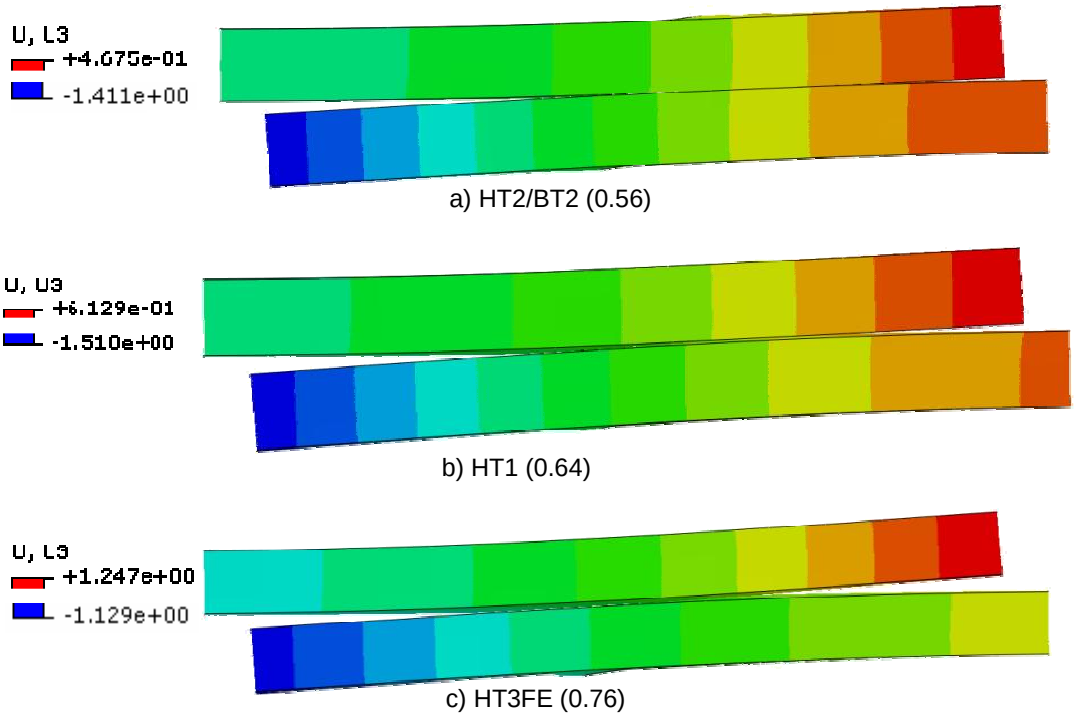

a) HT2/BT2 (0.56)

b) HT1 (0.64)

c) HT3FE (0.76)

Figure 6-25 Through-thickness displacement of various joints at 2 mm displacement

Figure 6-26 shows the fibre tensile failure progression in the bottom ply of the upper laminate at the intersection of hole edge and net-section plane. The damage index was plotted for one element at the edge of the hole as shown in the Figure 6-26. The fibre tensile failure was plotted because the bending of the joint manifested itself as tensile load in the bottom layer of the upper laminate. It can be seen that as the countersunk depth to thickness ratio was increased from 0.56 (HT2) to 0.64 (HT1), the damage index at 2 mm displacement increased from 0.4 to 0.5 respectively. A significant jump in the damage index can be seen for the joint with countersunk depth to thickness ratio of 0.76, which

reached a damage index value close to 0.9 at 2 mm displacement. Another important feature to note is that the net section plane did not experience total failure in the joint with countersunk depth to thickness ratio 0.56; however, in the joint with countersunk depth to thickness ratio 0.76 the net section plane experienced total failure. This showed that as the countersunk depth to thickness ratio was increased the joint experienced increased bending (seen in Figure 6-25) leading to failure in net tension region as seen in the experiments. Therefore, the finite element model was able to capture the bending phenomena in the joint. However, the amount of bending in the finite element model was less than the experimental results. This could be due to the use of linear elements in modelling the composite laminate. As highlighted by Ireman (1998), linear elements are much stiffer in bending compared to actual joint behaviour.

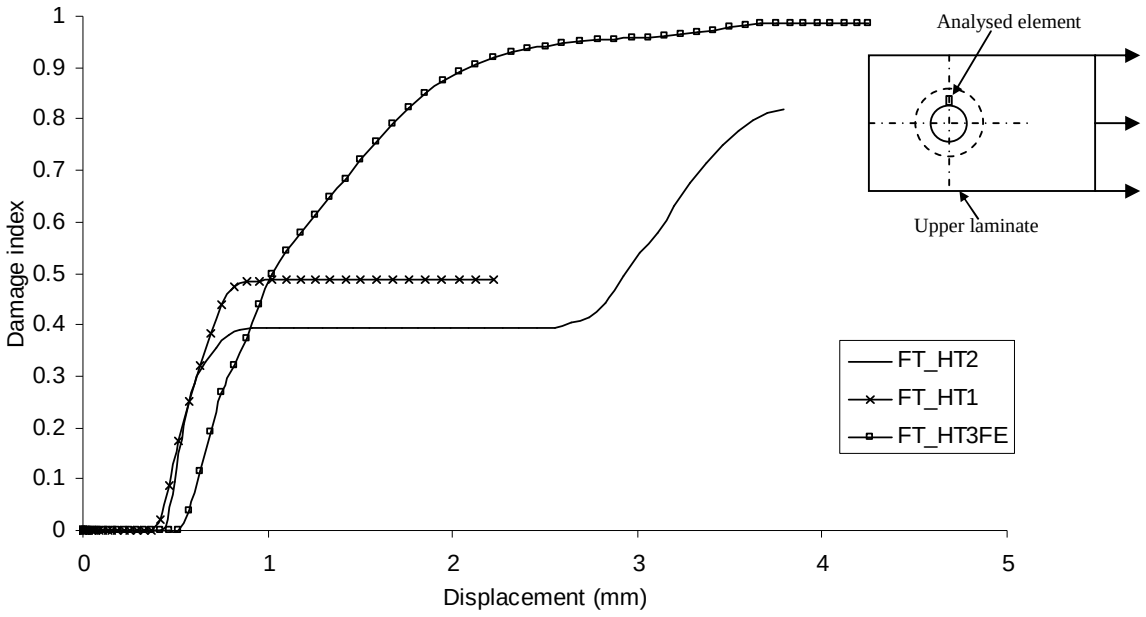

Figure 6-26 Fibre tensile failure progression in the bottom ply of the upper laminate at the net section plane

The stress concentration factor at the shear plane of the upper laminate had a profile similar to the CL2 joint around the hole (Compare Figure 6-19 and Figure 6-27). The calculation of stress concentration factor was the same as used previously in clearance joint analysis. The high stress concentration factor led to early damage in 0^o plies at the bearing plane. The HT3 results are not shown due to the different failure mode. Other stress plots are provided in Appendix II.

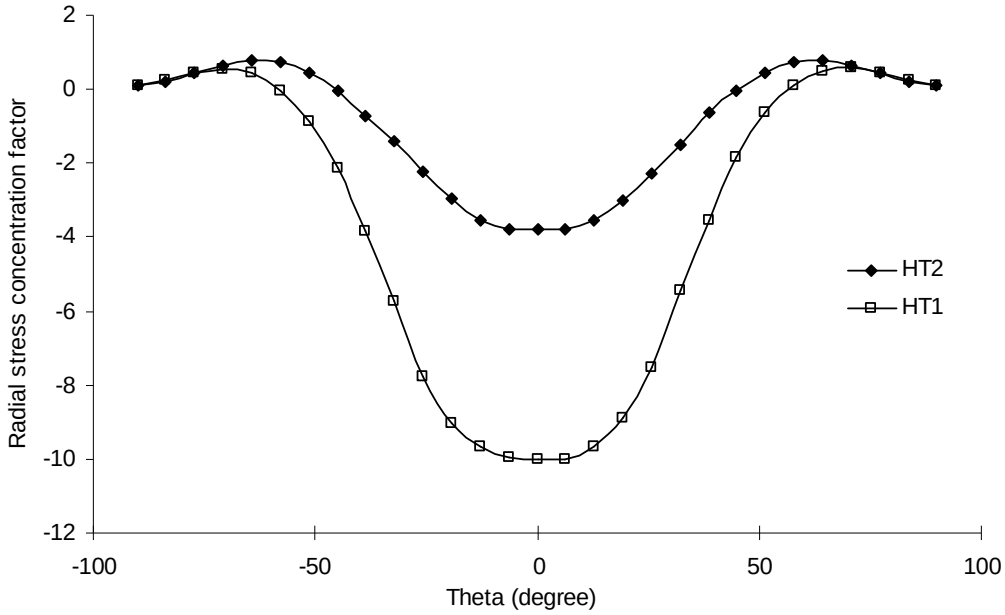

Figure 6-27 Effect of countersunk depth to thickness ratio on radial stress concentration factor at shear plane (0^o ply) in upper laminates at ~1.5 kN

The through-thickness fibre compressive damage in the 0^o plies at the intersection of bearing plane and hole edge is shown in Figure 6-28. The comparison between the upper laminate of the joints with countersunk depth to thickness ratio of 0.56 and 0.64 showed that for HT1 (0.64) joint fibre compressive damage started at bearing load. The plies located at the shear plane of the joint failed first. Similarly in the lower laminate the ply close to the shear plane damaged in fibre compressive failure at bearing load for the joint with countersunk depth to thickness ratio of 0.64. The lower laminate of HT3FE (0.76) joint showed a significantly different damage distribution through the thickness of the joint. It can be seen that the layers close to the shear plane did not experience failure, however, the layers away from the shear plane failed at both bearing load and ultimate failure load. This again suggests an increasing contribution of secondary bending to the failure of the joint. A high compressive stress occurred in the outer plies of the lower laminate due to outward bending promoting compressive failure in the outer plies.

The through-thickness damage profile and internal extent of fibre compressive damage in 0^o plies for all countersunk depth to thickness ratio joints can be seen in Figure 6-29. An increase in countersunk depth to thickness ratio led to early fibre compressive failure in the plies at the shear plane of the joint. In a similar way to experimental results, the shear plane of the HT1 joint experienced extensive failure as can be seen in Figure 6-30. The

plies away from the shear plane had less damage compared to the plies at the shear plane for the HT1 joint. However the damage in the countersunk region in the HT1 upper laminate was less compared to the HT2 upper laminate. This showed that a change in countersunk depth to thickness ratio significantly affected the damage initiation and damage progression of the joint. The HT3FE model showed failure of the outer plies. As explained previously this occurred due to extensive bending. Compared to HT2 (0.56) and HT1 (0.64) joint, the fibre compressive failure significantly reduced in the HT3FE (0.76) joint.

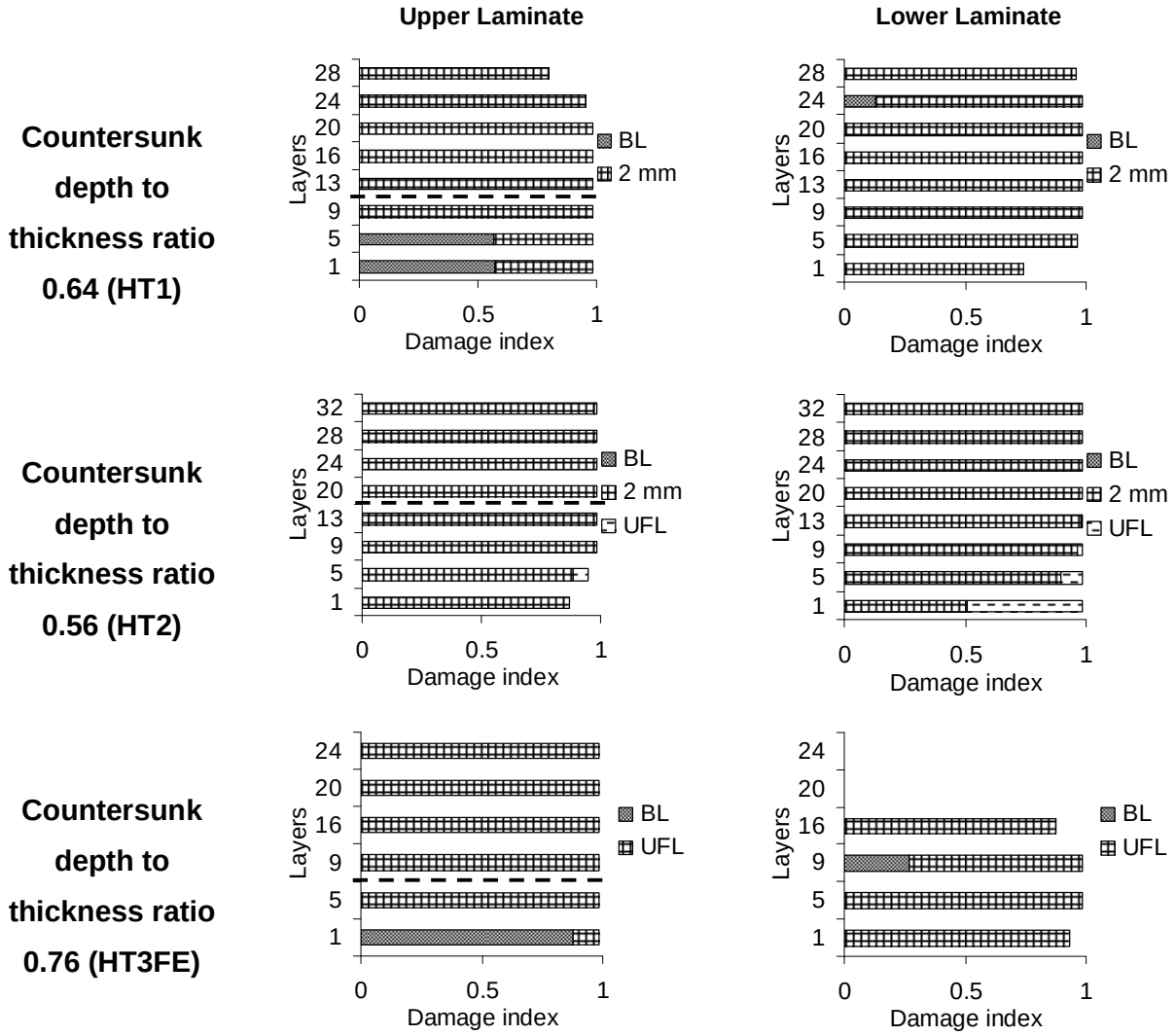

Figure 6-28 Effect of countersunk depth to thickness ratio on through-thickness fibre compressive damage progression

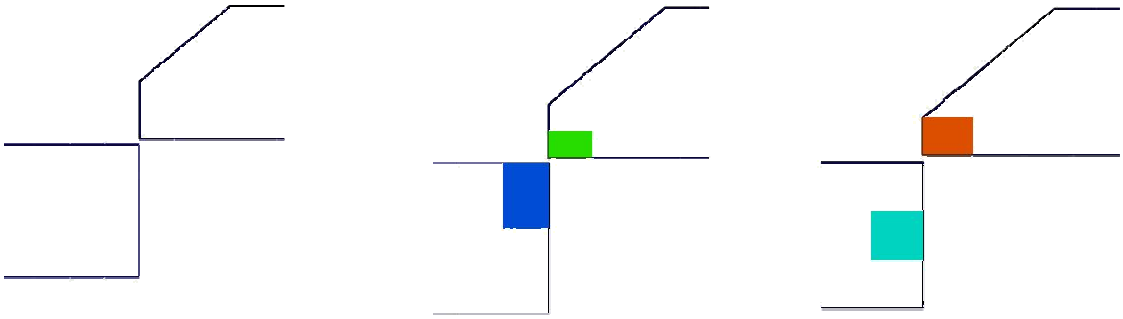

a) HT2 b) HT1 c) HT3FE

Figure 6-29 Effect of countersunk depth to thickness ratio on through-thickness fibre compressive damage at bearing load at 0^o cutting plane (See Figure 6-5 for damage scale)

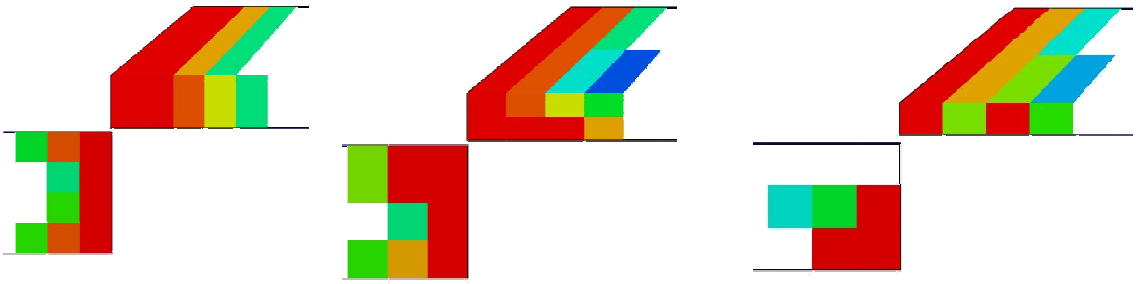

a) HT2 b) HT1 c) HT3FE

Figure 6-30 Effect of countersunk depth to thickness ratio on through-thickness fibre compressive damage at 2 mm at 0^o cutting plane (See Figure 6-5 for damage scale)

The through-thickness progression of damage is shown in Figure 6-31. As the countersunk depth to thickness ratio was increased from 0.56 to 0.64 the intensity of damage at the shear plane increased. The damage reduced away from the shear plane. The outer plies of the joints with countersunk depth to thickness ratio of 0.56 and 0.64 were damaged, however, the plies in HT2 (0.56) joint had more bearing damage compared to plies in HT1 (0.64) joint. The circumferential extent of the damage was not significantly affected except at the shear plane where plies in the HT2 (0.56) joint were damaged more than the HT1 (0.64) joint. In the joint with countersunk depth to thickness ratio of 0.76, the damage was significantly different compared to HT1 (0.64) and HT2 (0.56) joints. This was due to the different final failure mode of the joints. The shear plane still experienced damage; however, the extent of damage was less compared to the HT2 and HT1 joints. The fibre compressive damage significantly reduced for the topmost layer of the upper laminate. The outermost layer of the lower laminate showed much more damage compared to the HT2 and HT1 joints due to excessive bending.

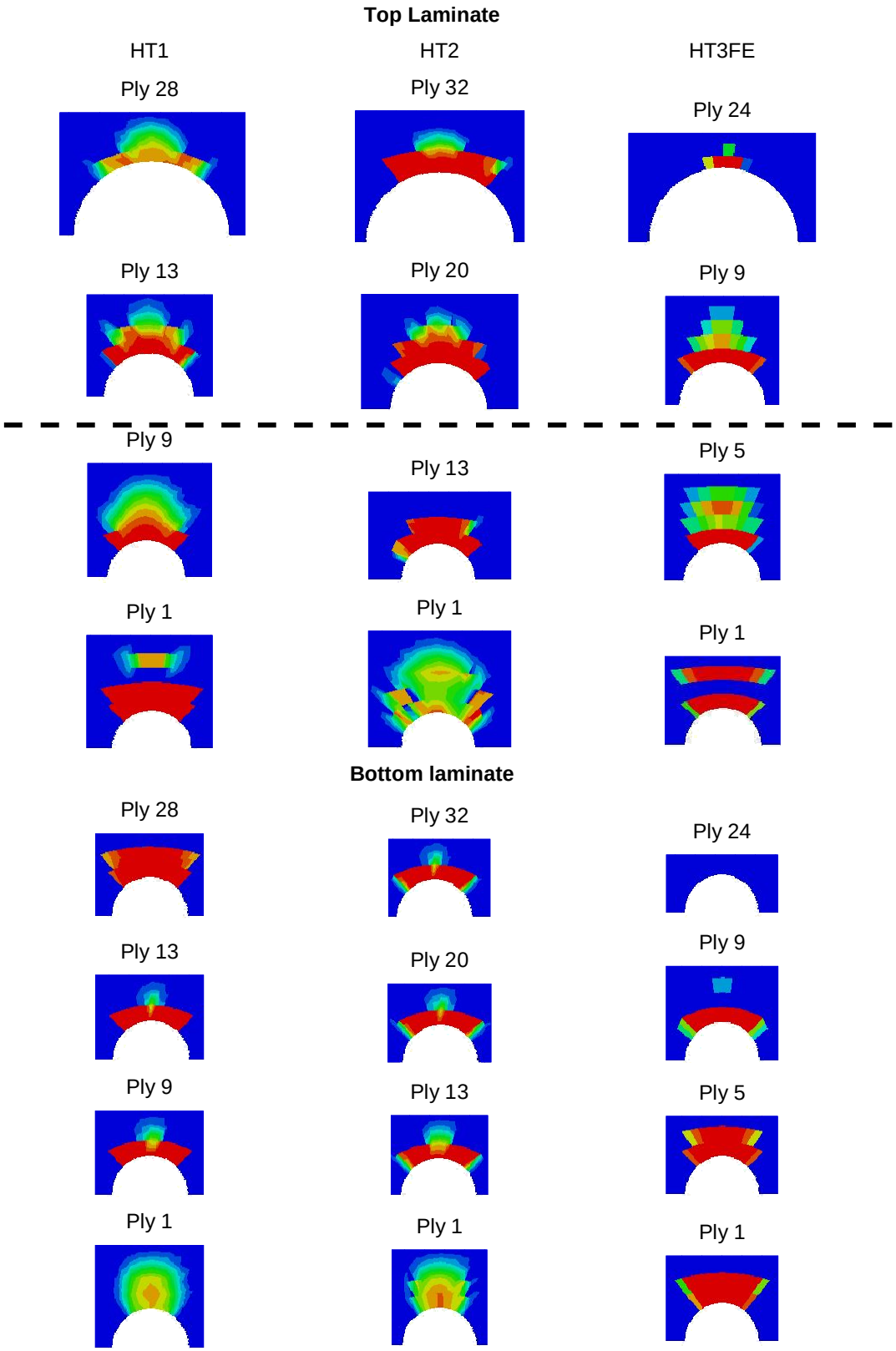

Figure 6-31 Effect of countersunk depth to thickness ratio on fibre compressive damage at 2 mm in 0^o plies (See Figure 6-5 for damage scale)

6.4.1 Conclusion

In summary, countersunk depth to thickness ratio had a severe effect on ultimate failure load and bearing load as it led to a change in the final failure mode from bearing to a combination of bearing and bending failure for the HT3FE (0.76) joint. The radial stress concentration in HT1 (0.64) joint was similar to CL2 (220 μm) joint. A higher countersunk depth to thickness ratio led to early damage initiation in the laminate. It also led to higher damage at the plies close to the shear plane of the joint. The developed approach predicted a combination of bearing and bending failure with increased contribution of bending failure for the joint with countersunk depth to thickness ratio of 0.76.

6.5 Effects of bolt torque

The FE analysis was used to investigate the effects of bolt torque on the damage progression and damage distribution in a single lap joint. The effect of bolt torque on FE load-displacement curve can be seen in Figure 6-32. Similar to the experimental results, the initial stiffness of the load-displacement curve showed slight variation with increased bolt torque. The results of joints with bolt torque of 2.103 Nm and 4.206 Nm only had small variations. This could be due to the lack of through-thickness behaviour of continuum elements and the approach used to apply bolt torque.

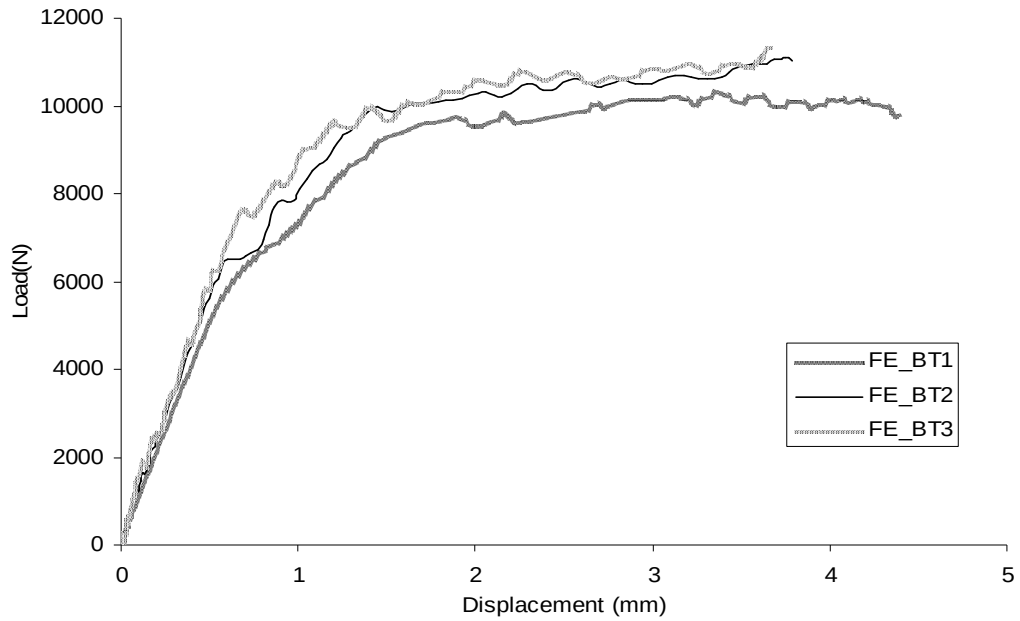

Figure 6-32 Effects of variation of bolt torque

The through-thickness fibre compressive damage progression for the upper and lower laminate at the intersection of the bearing plane and hole edge in 0^o plies is shown in Figure 6-33. No damage was seen in the joint at the bearing load. An increased bolt torque led to more damage in the upper laminate and less damage in the lower laminate at 2 mm displacement. The outer layers in the lower laminate (1 and 5) damaged at a later stage of loading with an increase in bolt torque. This could be a consequence of the approach used to apply the bolt torque.

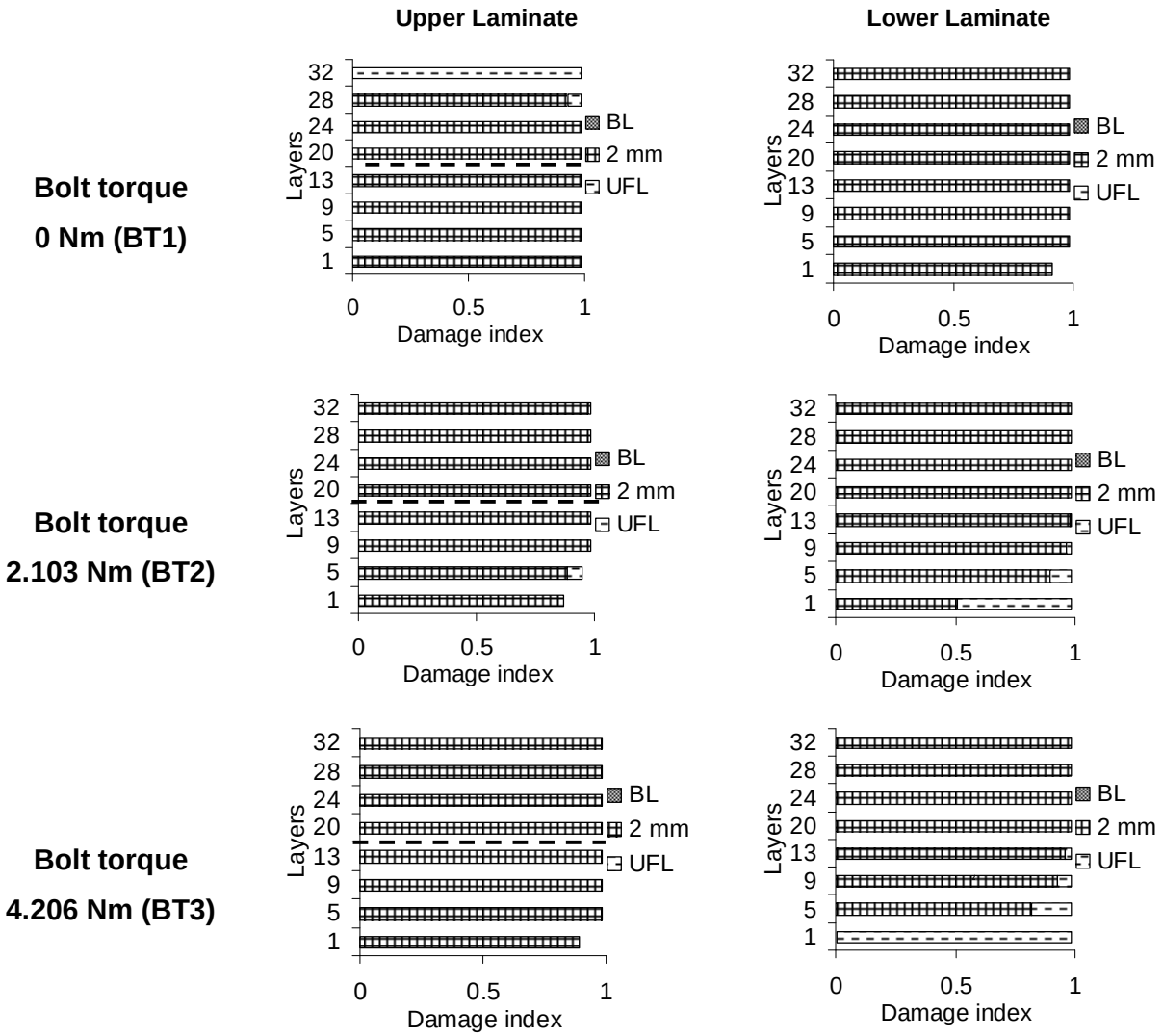

Figure 6-33 Effects of bolt torque on fibre compressive damage progression at the hole edge in 0^o direction

The radial extent of fibre compressive damage in the through-thickness direction at 2 mm displacement and ultimate failure load is shown in Figure 6-34 and Figure 6-35 respectively. It can be seen that the damage had a similar profile but different extent and

intensity for each bolt torque. After the initial increase of bolt torque to 2.103 Nm, further increase up to 4.206 Nm did not significantly affect the damage profile. The amount of through-thickness damage in the upper laminate increased with an increase in bolt torque as seen in the experimental analysis.

The progression of fibre compressive damage at various plies in the laminate is shown in Figure 6-36. The dashed line marks the location of start of countersunk region. A large section of the hole at the shear plane failed under fibre compressive failure at 2 mm displacement. The figure shows that as the bolt torque increased the damage at the shear plane in the upper laminate increased. The intensity and extent of damage in both circumferential and radial directions reduced for the plies away from the shear plane. The damage in the bottom laminate did not seem be affected significantly by the bolt torque except at the shear plane, where the damage slightly reduced with an increase in bolt torque.

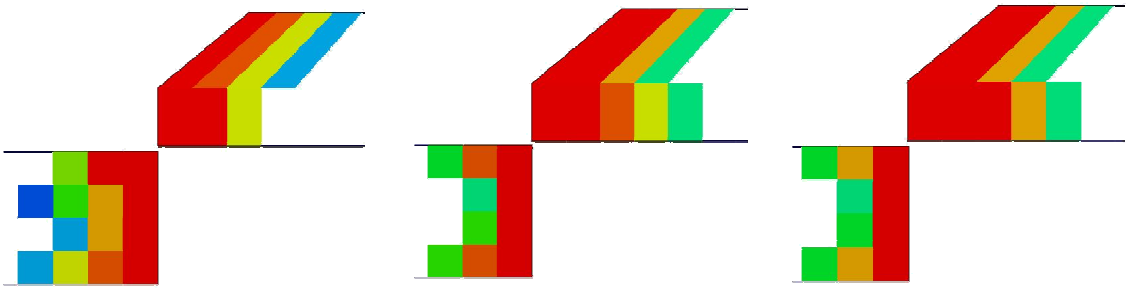

Figure 6-34 Effects of bolt torque on through-thickness fibre compressive damage at 2 mm at 0^o cutting plane (See Figure 6-5 for damage scale)

Figure 6-35 Effects of bolt torque on through-thickness fibre compressive damage at ultimate failure load at 0^o cutting plane (See Figure 6-5 for damage scale)

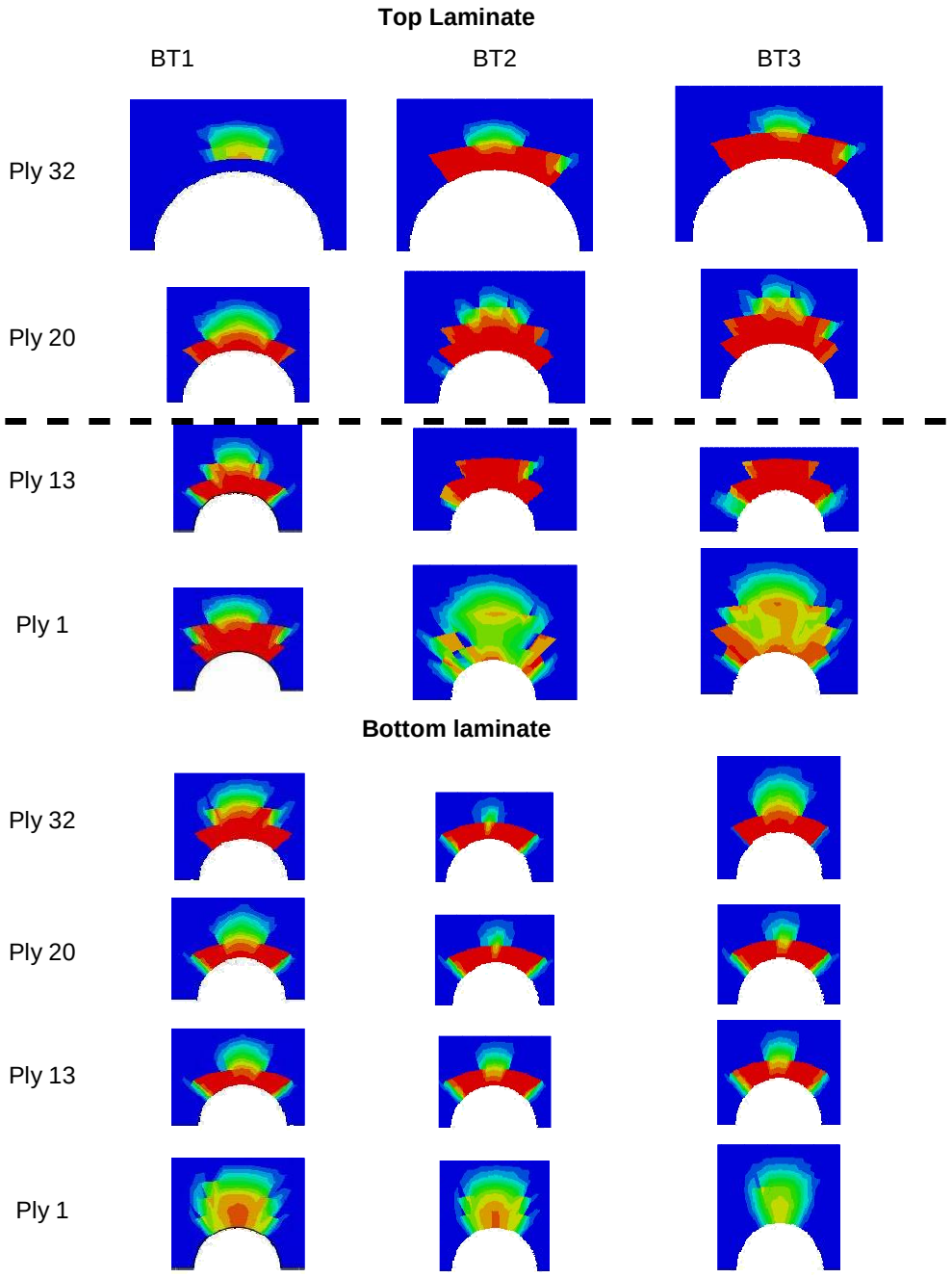

Figure 6-36 Effects of bolt torque on fibre compressive damage at 2 mm in 0^o plies (See Figure 6-5 for damage scale)

6.5.1 Conclusion

In summary the finite element analysis showed that an increase in bolt torque led to marginal increase in ultimate failure load and significant increase in bearing load, which agreed with the experimental results. The initial stiffness of the joint increased with an increase in bolt torque. Furthermore, the finite element analysis showed that an increase

in bolt torque led to higher damage at the shear plane and increased damage through the thickness of the laminate. An increased bolt torque led to early damage of the top ply in the upper laminate. The circumferential extent of damage reduced in the layers away from the shear plane.

6.6 Models with cohesive elements

The experimental analysis showed primary delamination was only present in the bolt torque joints. In this study an attempt was made to model only the primary delamination. As previously explained cohesive elements were used to model delamination between the countersunk and straight shank region of the upper laminate. The load-displacement curve for the model with delamination (BT1_Delam) is shown in Figure 6-37 together with the previous FE model and experimental results. The linear load-displacement behaviour of the joint was similar to the previous FE model. Major differences in load-displacement behaviour occurred after the initiation of the non-linear region. The significant drop in the load-carrying capacity was due to a combination of extensive fibre failure along the straight shank region and initiation of delamination. Figure 6-38 shows the fibre compressive damage in the edge elements in the straight shank of the hole at an increment before the significant load drop in the load-displacement curve. It can be seen that the majority of the layers in the straight shank had more than 80% damage, which led to reduction in load-carrying capability seen in Figure 6-37.

The progression of delamination and fibre compressive failure in an element located at the hole edge at the bearing plane in layer 13 (0^o layer in the straight shank region close to countersunk) and layer 15 (first layer in the countersunk region) can be seen in Figure 6-39 together with load-displacement curve. The fibre compressive failure and delamination failure initiated at approximately the same time, however, initial fibre failure progressed much faster than delamination. An early delamination initiation could occur due to stress singularity at the start of countersunk as pointed by McCarthy et al. (2005), Ericson et al. (1984) and Agarwal (2006). The error can be reduced by modelling the curvature (see Figure 3-11) at the start of the countersunk. Despite the early initiation, the load-displacement response was not significantly affected by the delamination.

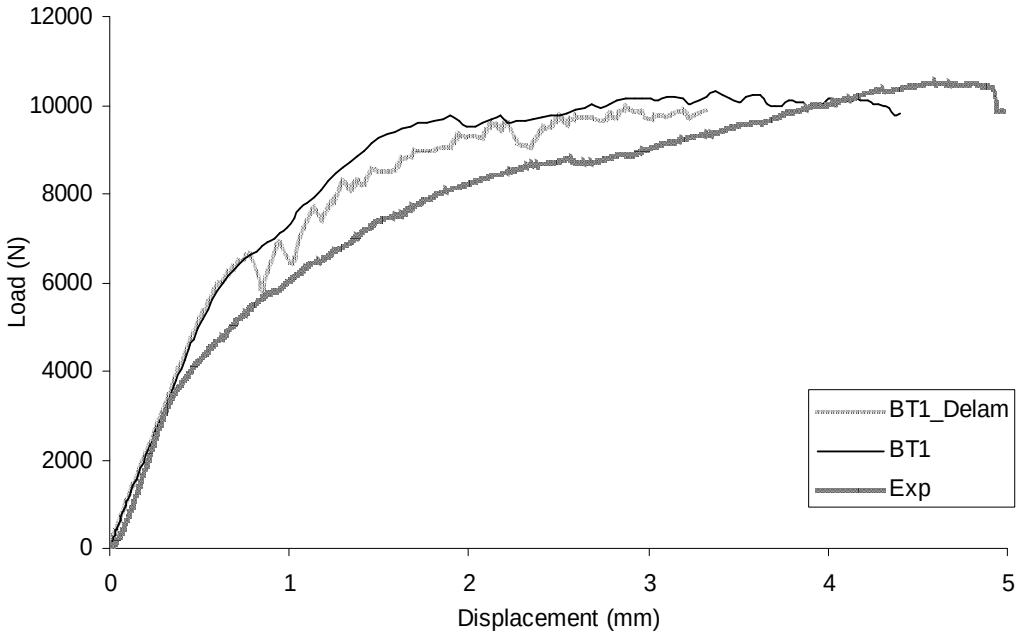

Figure 6-37 Load-displacement behaviour of joint with 0 Nm bolt torque

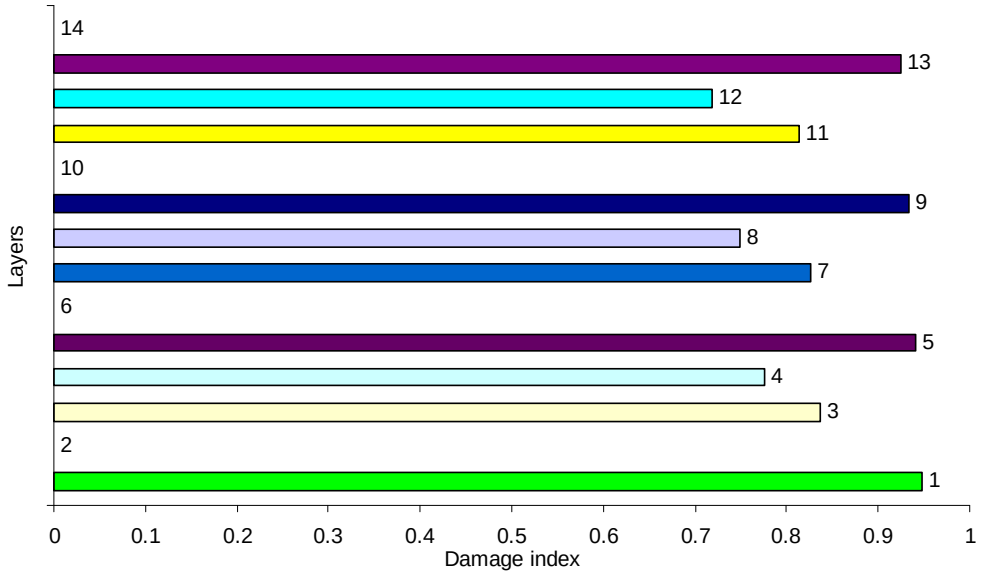

Figure 6-38 Fibre compressive damage in straight shank region just before significant load drop

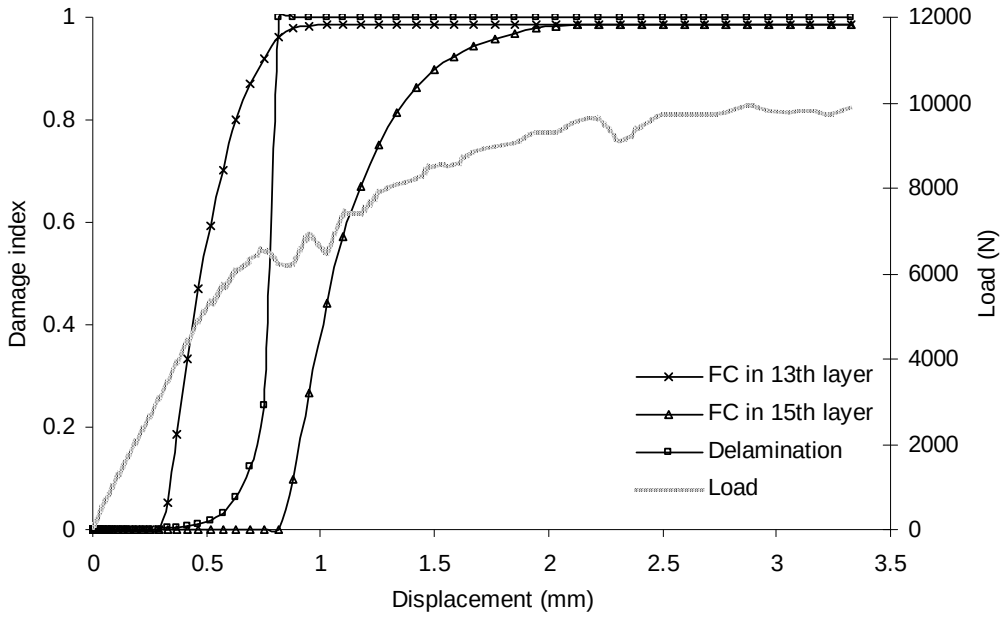

Figure 6-39 Delamination and damage index for finite element model with delamination

6.7 Conclusions

A detailed FE investigation on the effects of bolt torque, clearance and countersunk depth to thickness ratio agreed with the experimental results. The following major conclusions can be drawn from the above analysis:

- The start of countersunk experiences higher stress concentration than straight-sided hole.
- The plies in the countersunk region failed later compared to plies in the straight-sided hole.
- Increasing bolt torque reduces the peak of bearing stress between bolt and fastener hole.
- Increasing bolt torque delays the initiation of damage.
- An increased hole clearance reduces the contact area which in turn leads to significantly higher stress concentration factor at the hole edge.
- Hole clearance triggers early damage initiation and reduces the extent of damage in the upper and lower laminates.
- As countersunk depth to thickness ratio increases, the secondary bending increases, as does the stress concentration.
- Similar to hole clearance, higher countersunk depth to thickness ratio causes early damage initiation in the upper and lower laminates.

- Computational simulation reveals that delamination does not effect on the behaviour of the joint in an significant way. However, further investigation is required to verify this finding.

7 DISCUSSION

The following sections provide a detailed discussion of the adopted modelling methodology together with suggestions to improve the current approach.

7.1 Material properties

The use of two UD plies to represent woven fabric required definition of unidirectional properties for the plies. The use of micromechanical equations to calculate the material properties showed promising results, however, this approach has certain limitations. The approach is not capable of accounting for the fibre undulation in a ply. External loading on the laminate may lead to microscopy moment in the ply due to undulation in the fibres. However, the effect of the moment is considered negligible. The transverse behaviour of a single UD ply is also different compared to a woven ply. Despite of the limitations, the modelling approach was capable of capturing the overall joint behaviour and progression of damage within the laminate.

7.2 Modelling parameters

The coefficient of friction was selected based on detailed literature review as previously discussed. The selected value was the most widely accepted friction coefficient, however, it has been highlighted in the literature that changing the coefficient of friction could lead to variation in results. The friction coefficient between the upper and lower laminate would have the biggest impact on the results as it was the largest contact surface area. Mould release, surface contaminants and surface preparation may lead to wide variations in friction coefficients.

The combined approach of using continuum shell elements which lack through-thickness behaviour and application of bolt torque using through-thickness displacement could have resulted in the inability of the model to capture the fully developed joint stiffness, leading to some significantly different values for bearing load. The bolt displacement was calculated based on available literature, however, it does not account for the friction between the bolt and hole surface and the contribution of the composite laminate during the tightening process. Variation in thread geometry can also significantly affect the applied torque. The research showed that this approach may have limited applicability, particularly for initial stiffness predictions. The use of thermal expansion coefficient

together with experimentally determined bolt extension using instrumented bolt could provide a better approximation.

The parameters such as hourglass coefficient, mass scaling factor and maximum degradation factor were determined using parametric studies. These modelling parameters are affected by the selected modelling approach. The use of different material, element type, contact definition etc. would require determination of new values of these parameters to accurately model the behaviour. As shown previously, careful selection of these parameters can lead to efficient and accurate modelling approach.

7.3 Damage modelling

The Abaqus composite failure model was used to predict the progressive damage in the joint. The failure model was capable of predicting in-plane damage in the laminate. The microscopy analysis of the experimental specimens showed that together with in-plane damage, the laminates also experienced through-thickness damage in the form of interlaminar shear cracks. The model lacked the capability of capturing the interlaminar shear cracks as the failure model could only account for in-plane damage. However, the accumulation of in-plane damage in various plies of the laminate captured the overall failure behaviour of the joint. The analysis suggested a need for full three-dimensional damage model capable of accounting for complicated damage phenomena such as shear cracks. To be able to accurately capture the real composite failure behaviour, the new model should be able to predict the initiation and progression of shear cracks within and between each ply of the laminate.

7.4 Failure energies

Failure in fastened composite joints loaded in shear is by the initiation and growth of bearing damage which as previously described includes interlaminar and intralaminar shear cracks and delamination. The failure was governed by failure modes such as fibre kinking, matrix compression and fibre matrix shear. The experimental determination of the fracture toughness associated with these failure modes is important for material characterisation and for numerical modelling. Currently, there are no standards to determine these properties (Pinho et al. 2006). As previously mentioned various methods are used to determine fracture toughness of composite laminates. Harris et al. (1986) showed that the fracture toughness results of centre cracked tension and double edge notched tension tests were dependent on the thickness of the specimen. Specimen

configuration also significantly affected the results (Shih et al. 1981; Reedy 1980). The majority of the current tests determine the tensile fracture toughness and only two tests (compact compression and centre notched compression) can be used for calculating the compressive fracture toughness. The compact compression and centre notched compression test uses open hole specimens therefore the actual bearing failure would not be replicated during the test. As explained in the material properties section, the inability to replicate the actual failure phenomena could lead to inaccurate fracture energy calculations.

It can be summarised that the tensile and compressive fracture toughness are affected by several parameters such as the test used to determine the fracture toughness, lay-up of the laminate, thickness of the laminate and governing failure modes among others. Therefore the facture energy associated with bearing damage would depend upon composite lay-up, thickness and material. This means it would need re-characterisation for different laminates. To reduce the effect of different test set-ups on the facture toughness, the use of filled hole tension specimen to calculate bearing fracture toughness has been proposed.

The use of filled hole bearing specimen to determine the compressive failure energy showed promise in the initial study. The filled hole test accurately captured the nature of bearing failure. Further research should be conducted on characterising the compressive failure energy using bearing test. The characterisation should focus on identifying the failure energy of the unidirectional ply using suitable data reduction techniques, before application with multi-directional laminates. The developed approach should account for fibre damage and fibre-matrix damage interaction to accurately capture the bearing failure behaviour. The current approaches cannot account for interaction of different failure modes.

7.5 Delamination

The delamination failure was modelled using cohesive elements. The linear behaviour of the model with delamination was similar to the model without delamination. The non-linear behaviour was marginally affected by the presence of delamination. The singular stresses at the edge of the hole and continuum shell elements could have influenced delamination model. The lack of through-thickness behaviour in continuum shell elements can lead to erroneous modelling of delamination.

The sharp edge at the start of countersink could also have influenced the results. The real countersunk holes as shown in the experimental micrographs had curved region at the start of countersink which is a standard industry practice. Modelling of the curvature at the start of countersunk may lead to better approximation of delamination. The approach used for modelling delamination seemed promising as it was able to capture the underlining behaviour, however further detailed analysis is required to accurately model delamination behaviour.

7.6 Early termination

All the models terminated due to excessive element distortion. This numerical instability occurred due to significant distortion of the composite elements. It was observed that excessive distortion led to negative element volume. This led to incomplete non-linear analysis which was not capable of predicting the ultimate failure load of the joint. However, the final failure load predicted using the finite element models was on average within 12% of the experimentally predicted ultimate failure load. The inability to predict ultimate failure load restricts the applicability of the developed modelling approach, despite of the fact that ultimate failure is not as critical for the design process.

The research showed that the longevity of the analysis can be improved by increasing the number of through-thickness elements in the composite laminate. However, only limited numbers of elements were increased to provide a compromise between longevity and computational efficiency. Other methods of increasing longevity such as modifying element controls, solution controls etc. can also be used.

8 CONCLUSIONS AND RECOMMENDATIONS

This section provides detailed conclusions from experimental and finite element investigations, followed by suggested future work at the end of the section.

8.1 Conclusions

The experimental investigation and finite element computation show that the load-carrying capacity of joints fastened using countersunk bolts is affected by a number of design parameters, including bolt torque, hole clearance and countersunk depth to thickness ratio. A new method to determine the compression fracture energy using bearing failure has been proposed. In addition, the following conclusions can be drawn from the detailed experimental and finite element investigation:

- The damage mechanisms that constituted bearing failure are interlaminar and intralaminar shear cracks comprising of fibre kinking, fibre matrix shear and matrix compression.
- The through-thickness damage profile for all the joints can be divided in two sections:
  - Angular damage
  - Straight damage (bolt torque, countersunk depth to thickness joints) or Second angular damage (clearance joints)
- The countersunk fasteners cause higher stress concentration than straight-shank fasteners.
- Increasing bolt torque:
  - Lowers maximum radial stress or bearing stress, contributing to higher ultimate failure load.
  - Delays damage initiation in the plies close to laminate surface.
  - Reduces complete ply separation at the start of countersink compared to joints with zero bolt torque.
- Increasing hole clearance:
  - Reduces contact area and significantly increases hoop stresses at the hole edge.
  - Slightly reduces ultimate failure load but significantly reduces bearing load.
  - Significantly varies through-thickness stress distribution and as such the through-thickness damage profile of the upper and lower laminate.

    - Causes an early initiation and reduced circumferential extent of damage in the upper and lower laminate.
    - Restricts delamination at the start of countersunk region.
- Increasing countersunk depth to thickness ratio:
    - Lowers ultimate failure load.
    - Causes significant secondary bending and high hoop stresses around the bolt hole.
    - Changes the failure mode from bearing to catastrophic bending failure for joints with countersunk depth to thickness ratio equal or greater than 0.76.
    - Restricts delamination at the upper region of the countersink.
- Primary delamination does not significantly contribute to the failure of the single lap joints. However, further investigation is required to confirm this finding.
- Secondary delamination and angular damage bands do not lead to initial failure as they occur at significantly higher loads.

8.2 Future work

The following points highlighted in the study require further investigation:

- A more accurate and realistic composite failure model is needed capable of accounting for complicated phenomena such as shear cracks as well as modelling woven fabric composites.
- An accurate and efficient modelling of delamination needs further investigation.
- The present study analysed single bolted joint. It is important to understand the effect of tested parameters on multi-bolt countersunk joint. It has been reported that for protruding head bolts, hole clearance affects the load transfer mechanism in multi-bolt joint (McCarthy 2005). There is a need to understand this effect for multi-row countersunk bolted joints.
- The effect of tested parameters on hybrid composite joints should also be studied as hybrid joints are becoming important in aerospace industry.
- There is a need to apply composite failure criteria to three-dimensional solid elements which may provide better through-thickness stress distribution.
- The version of Abaqus used in the analysis did not have damage model for fabric composite materials. A fabric composite failure model would lead to better prediction capabilities.

- The approach used for determining the failure energies in bearing seemed promising. It should be investigated further to develop it in a testing standard.
- Attempt should be made to improve the analysis by using higher order elements and use of arc-length method to set up the non-linear solver.

REFERENCES

Abaqus® 6.9 Documentation. 2010, Providence, RI, USA: Dassault Systèmes Simulia Corporation, Rhode Island, USA.

Agarwal, B D, Broutman, L J and Chandrashekhara, K, 2006, 'Analysis of Laminated Composites', In: *Analysis and Performance of Fibre Composite*, John Wiley and Sons, New Jersey, USA, pp. 213-281.

Agarwal, B D, Broutman, L J and Chandrashekhara, K, 2006, 'Analysis of Laminated Plates and Beams', In: *Analysis and Performance of Fibre Composite*, John Wiley and Sons, New Jersey, USA, pp. 282-323.

AIAA, *AIAA aerospace design engineers guide*, 2003, American institute of Aeronautics and Astronautics Inc., Virginia, USA

Alfano, G and Crisfield, M A, 2001, 'Finite element interface models for the delamination analysis of laminated composites: mechanical and computational issues', *International Journal for Numerical Methods in Engineering*, vol. 72, no. 2, pp. 111-170.

Aronsson, C G, 1993, 'Strength of carbon/epoxy laminates with countersunk hole', *Composite Structures*, vol. 24, pp. 283-289.

Baker, A, Dutton, S and Kelly D, 'Joining of Composite Structures', In: *Composite Materials for Aircraft Structures,* 2004, American Institute of Aeronautics and Astronautics, Inc., Virginia, USA, pp. 289-368.

Basso, N, Chishti, M, Bayandor, J, Thomson, R and Bisagni C, 2006, 'Investigation of adhesively bonded composite structure joints', in *26th International Council of the Aeronautical Sciences*, Anchorage Alaska, USA, 14-19 September.

Bhargava, A, Shivakumar, K N, 2007, 'Three-dimensional tensile stress concentration in countersunk rivet holes', *The Aeronautical Journal*, vol. 111, pp. 777-786.

Black, J B and Hart-Smith, L J, Douglas, 1987, Paper 7765, *32nd international SAMPE Symposium and Exhibition*, Anaheim, California, 6-9 April, p. 360,.

Bruhn, E.F, *Analysis and design of flight vehicle structures*, 1973, Tri-state offset company, USA.

Budynas, R G, Nisbett, J K and Shigley, J E, 1989, *Shigley's mechanical engineering design*, 5th edition, McGraw-Hill: New York, USA.

Camanho, P P and Matthews, F L, 1997, 'Stress analysis and strength prediction of mechanically fastened joints in FRP: a review', *Composites Part A*, vol. 28, pp. 529-547.

Camanho, P P and Matthews, F L, 1999, 'A progressive damage model for mechanically fastened joints in composite laminates', *Journal of Composite Materials*, vol. 33, pp. 2248-2280.

Camanho, P P, Bowron, S and Mathews, F L, 1998, 'Failure mechanisms in bolted CFRP', *Journal of Reinforced Plastic Composites*, vol. 43, no. 3, pp. 195-216.

Camanho, P P, Dávila, C G and Ambur, D R, 2001, *Numerical Simulation of Delamination Growth in Composite Materials*, NASA Technical report TP-2001-211041, National Aeronautics and Space Administration, Virginia, USA.

Camanho, P P, Dávila, C G and de Moura, M F, 2003, 'Numerical simulation of mixed-mode progressive delamination in composite materials', *Journal of Composite Materials*, vol. 37, no. 16, pp. 1415-1438.

Chamis, C C, 1987. 'Simplified composite micromechanics equations for mechanical, thermal, and moisture-related properties', In: Weeton, J.W., Peters, D.M. and Thomas, K.L. Editors, 1987. *Engineers' Guide to Composite Materials*, American Society for Metals, Metals Park, Ohio, USA, pp. 8–24 (Section 3).

Chang, F K, Scott R A, Springer G, 1982, 'Strength of mechanically fastened composite joints', *Journal of Composite Materials*, vol. 16, no. 6, pp. 470-494.

Chishti, M, Wang, C H, Thomson, R and Orifici, A C, 2010, 'Progressive damage in single lap countersunk composite joints', in *9th World Congress on Computational Mechanics*, Sydney, Australia, 19-23 July.

Classical Laminate Theory, 2010, Efunda, Inc., Californa, USA, viewed on 10th March, 2010, Available from: <http://www.efunda.com/formulae/solid_mechanics/composites/comp_laminate.cfm >.

Collings, T A, 1977, 'The strength of bolted joints in multi-directional CFRP laminates', *Composites*, vol. 8, pp. 43-54.

Composite Material, *Chapter-3 Micromechanics of composite material,* viewed on 02 August 2010, Available from: <http://www.ncat.edu/~ccmradm/Dr%20homepage/meen613/chapter3.pdf>.

Cooper, C and Turvey , J, 1995, 'Effects of joint geometry and bolt torque on the structural performance of single bolt tension joints in pultruded GRP sheet material', *Composite Structures*, vol. 32, pp. 217-226.

Cowley, K D, and Beaumont, P W R, 1997, 'The interlaminar and intralaminar fracture toughness of carbon-fibre/polymer composites: the effect of temperature', *Composites Science and Technology*, vol. 57, pp. 1433-1444.

Crisfield, M A, Hellweg H B, and Davies G A O, 1997, 'Failure analysis of composite structures using interface elements', in *NAFEMS Conference on Application of Finite Elements to Composite Materials*, London, UK, 10 May.

Daniel, I M, and Ishai, O, 2006, *Engineering Mechanics of Composite Materials*, 2nd edition, Oxford University Press, New York, USA.

Daudeville, L, Allix, O and Ladeveze P, 1995, 'Delamination analysis by damage mechanics, some applications', *Composite Engineering*, vol. 5, no. 1, pp. 17-24.

Dávila, C G, Camanho, P P, and de Moura, M F, 2001, 'Mixed-Mode decohesion elements for analyses of progressive delamination', in *42nd AIAA/ASME/ASCE/AHS/ASC Structural Dynamics and Materials Conference*, Seattle, USA, 16-19 April.

de Moura, M F, Gonçalves, J P, Marques, A T and Castro, P T, 2000, 'Prediction of compressive strength of carbon-epoxy laminates containing delamination by using a mixed-mode damage model', *Composite Structures*, vol. 50, pp. 151-157.

De Vries, T J, 2001, *Blunt and Sharp Notch Behaviour of Glare Laminates*, PhD thesis, Delft University Press, The Netherlands.

DiNicola, A J and Fantle, S L, 1993, 'Bearing strength of clearance fit fastener holes in toughened graphite/epoxy laminates', *Composite Materials: Testing and Design*, vol. 11, pp. 220-237, ASTM STP 1206, American Society for Testing and Materials, Pennsylvania, USA.

Echaabi, J, Trochu, F and Gauvin, R, 1996, 'Review of failure criteria of fibrous composite materials', *Polymer Composites*, vol. 17, no. 6, pp. 786-798.

Ekh, J and Schön J, 2006, 'Load transfer in multirow, single shear, composite-to-aluminium lap joints', *Composites Science and Technology*, vol. 66, pp. 875-885.

Ericson, K, Persson, M, Carlsson, L and Gustavsson, A, 1984, 'On the prediction of the initiation of delamination in a [0/90]S laminate with a circular hole', *Journal of Composite Materials*, vol. 18, pp. 495-506.

Eriksson, L I, 1986, 'Contact stresses in bolted joints of composite laminates', *Composite Structures*, vol. 6, no. 1, pp. 57-75.

Falk, M L, Needleman, A and Rice, J R, 2001, 'A critical evaluation of cohesive zone models of dynamic fracture', *Journal of Physics IV*, vol. 11, pp. 543-550.

Flabel, Jean-Claude, Practical stress analysis for design engineers, 1997, Lake city publication company, Idaho, USA

Garrett, R A, 'Effect of defects on aircraft composite structures', MD Report, McDonnell Aircraft Company, Missouri, USA.

Garrett, R A, 1986, 'Effect of manufacturing defects and service-induced damage on the strength of aircraft composite structures', in *Composite Materials: Testing and Design (Seventh Conference)*, ASTM STP 893, American Society for Testing and Materials, Philadelphia, USA.

Ghezzo, F, Giannini, G, Cesari, F, and Caligiana G, 2008, 'Numerical and cxperimental analysis of the interaction between two notches in carbon fibre laminates', *Composites Science and Technology*, vol. 68, pp. 1057-1072.

Harris, C E and Morris, D H, 1986, 'A comparison of the fracture behaviour of thick laminated composites utilizing compact tension, three-point bend, and center-cracked tension specimens', *Fracture Mechanics*, vol. 17, pp. 124-135.

Hart-Smith, L J, 1978, 'Mechanically-fastened joints for advanced composites – Phenomenological considerations and simple analyses', in *4th Conference on Fibrous Composites in Structural Design*, San Diego, California, 14-17 November, Douglas paper 6748A.

Hashin, Z and Rotem, A, 1973, 'A fatigue failure criterion for fibre reinforced materials', *Journal of Composite Materials,* vol. 7, pp. 448-464.

Hashin, Z, 1980, Failure criteria for unidirectional fibre composites, *Journal of Applied Mechanics*, vol. 47, pp. 329-334.

HI-LOK Standards, 1979, Standards committee for HI-LOK products, Fairchild fasteners, California, USA.

Hyer, M W, Klang, E C, and Cooper, D E, 1987, 'The effects of pin elasticity, clearance and friction on the stresses in a pin-loaded orthotropic plate', *Journal of Composite Materials*, vol. 21, no. 3, pp. 190-206.

Ireman, T, 1998, 'Three-dimensional stress analysis of bolted single-lap composite joints', *Composite Structures*, vol. 43, pp. 195-216.

Ireman, T, Ranvik, T and Eriksson, I, 2000, 'On damage development in mechanically fastened composite laminates', *Composite Structures*, vol. 49, pp. 151-171.

Johnson, S W, and Treasurer, P J, 2007, 'Ply ,modifications to alter damage initiation and progression in laminates containing circular holes', in *16th International Conference on Composite Materials*, Kyoto, Japan, 8-13 July.

Kelly, G and Hallström, S, 2004, 'Bearing strength of carbon fibre/epoxy laminates: effects of bolt-hole clearance', *Composites Part B*, vol. 35, pp. 331-343.

Khashaba, U A, Sallam, H E M, Al-Shorbagy, A E and Seif, M A, 2005, 'Effect of washer size and tightening torque on the performance of bolted joints in composite structures', *Composite Structures,* vol. 73, pp. 310-317.

Kim, M, 2010, *Impact resistance of composite scarf joints under load*, MEng thesis, RMIT University, Melbourne, Australia.

Kopp, J and Michaeli, W, 1996, 'Dimensioning of thick laminates using new IFF strength criteria and some experiments for their verification', in *Proceedings of the ESA ESTEC Conference*, pp. 305–312.

Kretsis, G and Matthews, F L, 1985, 'The strength of bolted joints in glass fiber/epoxy laminates', *Composites*, vol. 16, pp. 92-105.

Kroll, L and Hufenbach, W, 1997, 'Physically based failure criterion for dimensioning of thick-walled laminates, *Applied Composite Materials,* vol. 4, pp. 321–332.

Labeas, G, Belesis, S and Stamatelos D, 2008, 'Interaction of damage failure and post-buckling behaviour of composite plates with cut-outs by progressive damage modelling', *Composites Part B*, vol. 39, pp. 304-315.

Lapczyk, I, and Hurtado, J A, 2007, 'Progressive damage modeling in fiber-reinforced materials', *Composites Part A*, vol. 38, pp. 2333-2341.

Linde, P, Pleitner, J, De Boer, H, and Carmone, C, 2004, 'Modelling and simulation of fibre metal laminates', *in Abaqus Users' Conference*, Massachusetts, USA, June.

Matthews, F L, Kilty, P F and Godwin, E W, 1982, 'Load-carrying joints in fibre reinforced plastics', *Plastic and Rubber Process and Applications*, vol. 2, pp. 19-25.

McCarthy, C T and McCarthy, M A, 2005, 'Three-dimensional finite element analysis of single-bolt, single-lap composite bolted joint Part II-effects of bolt-hole clearance', *Composite Structures*, vol. 71, pp. 159-175.

McCarthy, C T, McCarthy, M A, and Lawlor, V P, 2005, 'Progressive damage analysis of multi-bolt composite joints with variable bolt-hole clearances', *Composites Part B*, vol. 36, pp. 209-305.

McCarthy, M A, Lawlor, V P, Stanley, W F and McCarthy, C T, 2002, 'Bolt-hole clearance effects and strength criteria in single-bolt, single-lap, composite bolted joints', *Composites Science and Technology*, vol. 62, pp. 1415-1431.

McCarthy, M A, McCarthy, C T, Lawlor, V P, Stanley, W F, 2005, 'Three-dimensional finite element analysis of single-bolt, single lap composite bolted joints: Part I – model development and validation', *Composite Structures*, vol. 71, pp. 140-158.

MIL-HDBK-17, Composite Materials Handbook, 2002, US Department of Defense, Pennsylvania, USA

MIL-HDBK-60, Threaded Fasteners – Tightening to Proper Tension (Torque), 1990, US Department of Defense, Pennsylvania, USA .

Naik, R A and Crews, J H, 1985, 'Stress analysis method for a clearance-fit bolt under bearing condition', *AIAA Journal*, vol. 24, pp. 1348-1353.

Needleman, A, 1987, 'A continuum model for void nucleation by inclusion debonding', *Journal of Applied Mechanics*, vol. 54, pp. 525-531.

Needleman, A, 1999, 'An analysis of intersonic crack growth under shear loading', *Journal of Applied Mechanics*, vol. 66, pp. 847-857.

Nelson, W D, Bunin, B L and Hart-Smith, L J, 1981, *Critical Joints in Large Composite Aircraft Structure*, NASA report, NASA-CR-3710, National Aeronautics and Space Administration, Virginia, USA.

Nuismer, R J and Tan, S C, 1988, 'Constitutive relations of a cracked composite lamina', *Journal of Composite Materials*, vol. 22, pp. 306-321.

Oh, J H, Kim, Y G and Lee, D G, 1997, 'Optimum bolted joints for hybrid composite materials', *Composite Structures*, vol. 38, no. 1-4, pp. 329-341.

Orifici, A C, Herzberg, I and Thomson, R S, 2008, 'Review of methodologies for composite material modelling incorporating failure', *Composite Structures*, vol. 86, pp. 194-210..

Padhi, G S, McCarthy, M A and McCarthy, C T, 2002, 'BOLJAT – BOLJAT-A tool for designing composite bolted joints using three-dimensional finite element analysis', *Composites Part A,* vol. 33, no. 11, pp.1573-1584.

Papanikos, P, Tserpes, K I, Labeas, G, and Pantelakis, Sp, 2005, 'Progressive damage modelling of bonded composite repairs', *Theoretical and Applied Fracture Mechanics*, vol. 43, pp. 189-198.

Paris, F, 2001, *A Study of Failure Criteria of Fibrous Composite Materials*, NASA Technical report CR-2001-210661, National Aeronautics and Space Administration, Virginia, USA.

Petrossian, Z, and Wisnom, M R, 1998, Prediction of delamination initiation and growth from discontinuous plies using interface elements, *Composites Part A,* vol. 29, pp. 503–515.

Pinho, S T, Robinson, P and Iannucci, L, 2006, 'Fracture toughness of the tensile and compressive fibre failure modes in laminated composites', *Composites Science and Technology*, vol. 66, no. 13, pp. 2069-2079.

Presson, E, Madenci, E and Eriksson, I, 1998, 'Delamination initiation of laminates with pin-loaded holes', *Theoretical and Applied Fracture Mechanics*, vol. 30, pp. 87-101.

Puck, A and Schürmann H, 1998, 'Failure analysis of FRP laminates by means of physically based phenomenological models, *Composites Science and Technology*, vol. 58, pp. 1045-1067.

Puck, A and Schürmann H, 2002, ‘Failure analysis of FRP laminates by means of physically based phenomenological models, *Composites Science and Technology*, vol. 62, pp. 1633-1662.

Puck, A, 1969, ‘Calculating the strength of glass fibre plastic laminates under combined load’, *Kunststoffe*, vol. 59, no. 11, pp. 780-787.

Raju, I S, Crews, J H, and Aminpour, M A, 1988, ‘Convergence of strain energy release rate components for edge-delaminated composite laminates’, *Engineering Fracture Mechanics*, vol. 30, no. 3, pp. 383-396.

Raju, I S, Foye, R L, and Avva, V S, 1992, 'A review of analytical methods for fabric and textile composites', in JN Reddy & AV Krishna Murthy, editors, *Composite Structures - Testing, Analysis and Design*, Springer – Verlag, New York, USA.

Reedy, E D Jr, ‘On the specimen dependence of unidirectional boron/aluminum fracture toughness’, *Journal of Composite Material Supplement*, vol. 14, pp.118-131.

Rinderknecht, S and Kroplin, B, 1994, ‘Calculation of Delamination Growth with Fracture and Damage Mechanics’, in Hughes T J R, Oñate, E, and, Zienkiewicz, O C, editors, *Recent Developments in Finite Element Analysis*, CIMNE, Barcelona, Spain.

Roskam, J, *Airplane design, Part III: Layout design of cockpit, fuselage wing and empennage: cutaways and inboard profiles,* 1986, Roskam aviation and engineering corporation, Kansas, USA.

Shih, T T and Logsdon, W A, 1981, ‘Fracture behavior of thick-section graphite/epoxy composite’, in *Fracture Mechanics: Thirteenth Conference*, ASTM STP 743, American Society for Testing and Materials, Philadelphia, USA.

Shivakumar, K N and Newman, J C Jr, 1992, *Stress Concentrations for Straight-shank and Countersunk Holes in Plates Subjected to Tension, Bending and Pin Loading,* NASA Technical paper 3192, National Aeronautics and Space Administration, Virginia, USA.

Soni, S R, 1983, ‘A comparative study of failure envelopes in composite laminates’, *Journal of Reinforced Plastics and Composites*, vol. 2, pp. 34-42.

Soutis, C and Curtis, P T, 2000, ‘A method for predicting the fracture toughness of CFRP laminates failing by fibre microbuckling’, *Composites Part A*, vol. 31, pp. 733-740.

Soutis, C, Fleck, N A and Smith, P A, 1991, ‘Failure prediction technique for compression loaded carbon fibre-epoxy laminate with open holes’, *Journal of Composite Materials*, vol. 25, pp. 1476-1498.

Standard test method for bearing response of polymer matrix composite laminates, ASTM D5961, 2007, American Society for Testing and Materials, Pennsylvania, USA.

Standard test method for bearing strength of plastics, ASTM D953, 2002, American Society for Testing and Materials, Pennsylvania, USA.

Starikov, R and Schön, J, 2001, 'Quasi-static behaviour of composite joints with countersunk composite and metal fasteners', *Composites Part B*, vol. 32, pp. 401-411.

Stockdale, J H and Matthews, F L, 1976, 'The effect of clamping pressure on bolt bearing loads in glass fibre-reinforced plastics', *Composites*, pp. 34-38.

Sun, H T, Chang, F K, and Qing, X, 2002, 'The response of composite joints with bolt clamping loads, Part II Model verification', *Journal of Composite Materials*, vol. 36, pp. 69-92.

Tan, S C and Nuismer, R J, 1989, 'A theory for progressive matrix cracking in composite laminates', *Journal of Composite Materials*, vol. 23, pp. 1029-1047.

Tan, S C and Perez, J, 1993, 'Progressive failure of laminated composites with a hole under compressive loading', *Journal of Reinforced Plastics*, vol. 12, pp. 1043-1057.

Tan, S C, 1991, 'Progressive failure for composite laminates containing openings', *Journal of Composite Materials*, vol. 25, pp. 556-577.

Thoppul, S D, Finegan, J and Gibson, R F, 2009, 'Mechanics of mechanically fastened joints in polymer-matrix composite structures – A review', *Composites Science and Technology*, vol 69, pp. 301-329.

Tserpes, K I, Papanikos, P and Kermanidis, Th., 2001, 'A three – dimensional progressive damage model for bolted joints in composite laminates subjected to tensile loading', *Fatigue and Fracture of Engineering Materials and Structures*, vol. 24, pp. 663-675.

Turon, A, Costa, J, Camanho, P P and Maimí, P, 2008, *Mechanical Response of Composites*, Springer, New York, USA.

Turon, A, Dávila, C G, Camanho, P P and Costa J, 2007, 'An engineering solution for mesh size effects in the simulation of delamination using cohesive zone models', *Engineering Fracture Mechanics*, vol. 74, pp. 1665-1682.

Viisoreanu, A and Wadolkowski, K, 1998, 'Particularities of single shear pin joints modelling for MSC/NASTRAN', available from: <www.mscsoftware.com/support/library/conf/amuc98/p03898.pdf>.

Wang H S, Hung, C L and Chang F K, 1996, 'Bearing failure of bolted composite joints. Part I: Experimental characterisation', *Journal of Composite Materials*, vol. 30, pp. 1284-1313.

Whitworth, H A, Othieno, M and Barton, O, 2003, 'Failure analysis of composite pin loaded joints', *Composite Structures*, vol. 59, pp. 261-266.

Xiao Y, Ishikawa T, ‘An experimental investigation of the bearing failure mechanisms in bolted composite joints’, 2001, in *13th International Conference on Composite Materials (ICCM-13)*, Beijing, China, 25-29 June, Paper ID1559, CD-ROM.

Xiao, Y, Wang, W, Takao, Y and Ishikawa, T, 2000, ‘The effective friction coefficient of a laminate composite, and analysis of pin-loaded plates’, *Journal of Composite Materials*, vol. 34, pp. 69-87.

Xu, X P, and Needleman, A, 1987, ‘Numerical simulations of fast crack growth in brittle solids’, *Journal of Mechanics and Physics of Solids*, vol. 32, no. 9, pp. 1397-1434.

Yamada, S E, 1978, ‘Analysis of laminate strength and its distribution’, *Journal of Composite Materials*, vol. 12, pp. 275-284.

Zou, Z, Reid, S R, Li, S and Soden, P D, 2002, ‘Modelling interlaminar and intralaminar damage in filament wound pipes under quasi-static indentation’, *Journal of Composite Materials*, vol. 36, pp. 477-499.

APPENDIX I.

This section describes the specimen manufacturing, hole preparations, torque wrench calibration.

I. Specimen Details

The design of bearing and single lap joint specimens was based on ASTM standard D5961. The critical geometric restrictions were the same for both bearing and single lap joint specimens and were shown in Table 2-1.A plain weave fabric carbon/epoxy material system was used for laminate manufacturing. A quasi-isotropic lay-up was used for both single lap and bearing specimens. The single lap test regime utilised two different Hi-Lok® fastening systems. A structural steel bolt was used for bearing testing. To reduce the ambiguity in identification of specimens, a labelling system was developed to identify the major characteristic of both single lap and bearing specimens. The labelling system identifies the following parameters of the specimens:

- Laminate Lay-up/ Thickness
- Bolt Type
- Testing Parameter
    1. Bolt Torque
    2. Clearance
    3. Countersunk depth to thickness ratio

The specimens for bearing tests were manufactured using a quasi-isotropic lay-up of $[(0/45)_4]_S$. The labelling system was divided into three different parts describing the following:

1. CT = Bearing test
2. FL = Specimen loaded to failure

    OR

    LL = Specimen loaded to the onset of non-linearity
3. 1, 2, 3 etc. = Specimen number

Therefore a specimen labelled CT_FL_1 was the first bearing hole test specimen loaded to ultimate failure. Similarly a single lap joint specimen labelling system describes the following variables:

1. Different laminates
    - LM1 = 16 Ply (3.52 mm) laminate with $[0/45/0/45/0/45/0/45]_S$
    - LM2 = 14 Ply (3.08 mm) laminate with $[0/45/0/45/0/45/0]_S$

2. Different bolt/nut assemblies
    - B1 = HL-13-8-5/HL86-8
    - B2 = HL-13-6-5/HL86-6PB6
    - B3 = HL-13-6-4/HL86-6PB6
3. Test Variables
    - Bolt Torque
        1. BT1 = Finger Tight (assumed to be 0 Nm)
        2. BT2 = 2.103 Nm
        3. BT3 = 4.206 Nm
    - Over size/Clearance
        1. CL1 = Neat fit/Smallest Clearance (~ 0 µm)
        2. CL2 = 240 µm
        3. CL3 = 440 µm
    - Countersunk depth to thickness ratio
        1. HT1 = 0.64
        2. HT2 = 0.56
        3. HT3 = 0.76
4. Specimen number = 1, 2, 3, etc.
5. Upper and lower laminate of the joint
        a. A = Upper laminate, i.e. laminate with countersunk hole
        b. B = Lower laminate, i.e. laminate with straight shank hole

For example the first 3.52 mm upper laminate of a single lap joint with finger tight bolt will have “LM1_B2_BT1_A_1” code.

The geometry of the bearing test specimen can be seen in Figure I - 1. The figure also shows the location of strain gauge (SG) and extensometer tab attachment. For single lap joint specimens the SGs on the upper and lower laminate were vertically aligned. The geometry of single lap laminates can be seen in Figure I - 2. The geometry of the bolt and nut is shown in Figure I - 3. The dimensions of the single lap joint are provided in Table I - 1. The dimensions of the bolts and nuts used in single lap tests are provided in Table I - 2 and Table I - 3 respectively. The assembled joint in Figure I - 4 shows the extensometer tab location together with SG numbering.

Table I - 1 Dimensions of single lap joint (mm)

Tests	*L*	*t*	*w*	*e*	*D* (Bolt)	*A*	*OL*	Plies	*HT*	*SLT*	*SLB*
BT	152.4	3.52	31.75	31.75	4.76	9.56	63.5	16	0.56	5	7
CL	152.4	3.52	31.75	31.75	4.76	9.56	63.5	16	0.56	5	7
HT1	152.4	3.08	31.75	31.75	4.76	9.56	63.5	14	0.64	5	7
HT2	152.4	3.52	31.75	31.75	4.76	9.56	63.5	16	0.56	5	7
HT3	152.4	3.52	31.75	31.75	6.35	12.71	63.5	16	0.76	5	7

Table I - 2 Bolt dimensions (mm)

Bolt	*A*	*Z*	*H*	*D*	*MG*
HL13-6-4	9.56	0.38	1.99	4.76	6.35
HL13-6-5	9.56	0.38	1.99	4.76	7.94
HL13-8-5	12.71	0.38	2.69	6.35	7.94

Table I - 3 Nut dimensions (mm)

Nut	*C*	*E*	*F*	*G*	*I*	*J*	*K*	*L*	*M*
HL8-6PB6	7.8	2.72	1.9	2.38	1.84	2.55	6.75	5.96	7.91
HL86-8	10.5	2.85	3.0	2.8	1.92	3.3	8.64	7.8	8.6

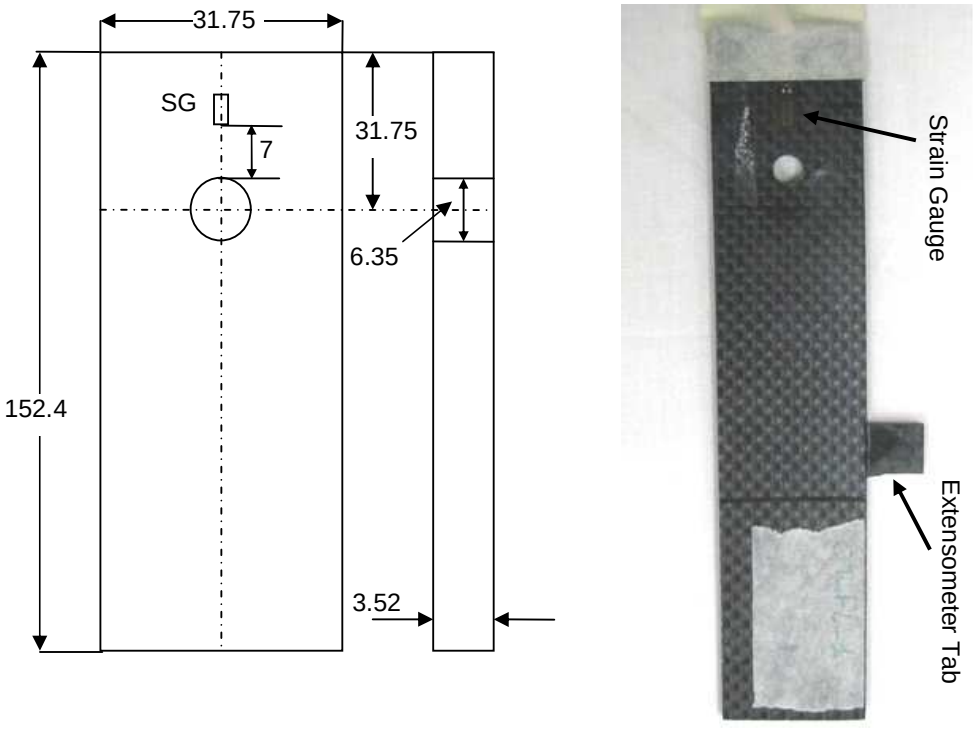

Figure I - 1 Filled hole specimen dimensions (mm)

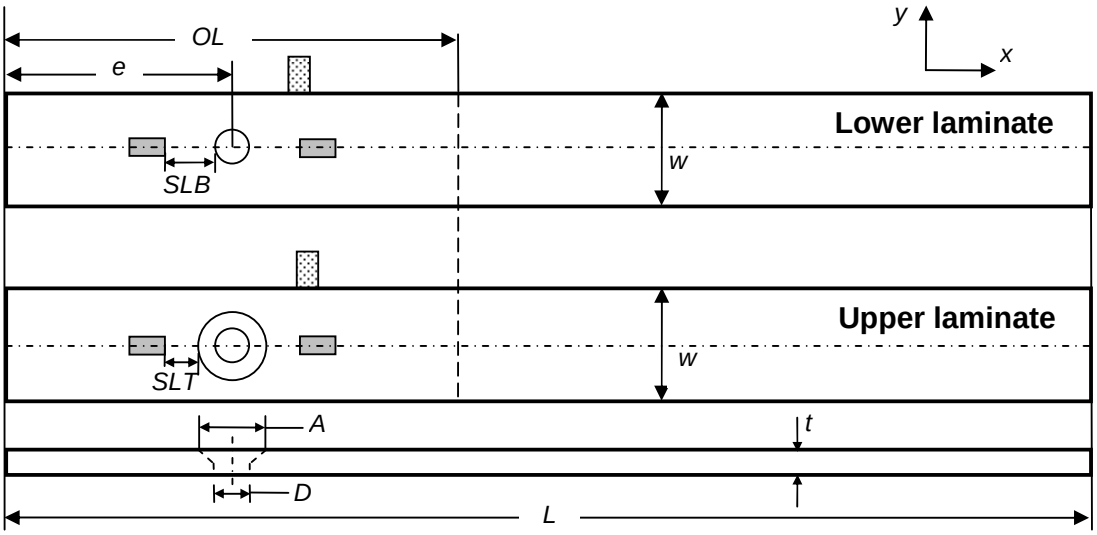

Figure I - 2 Single lap joint geometry

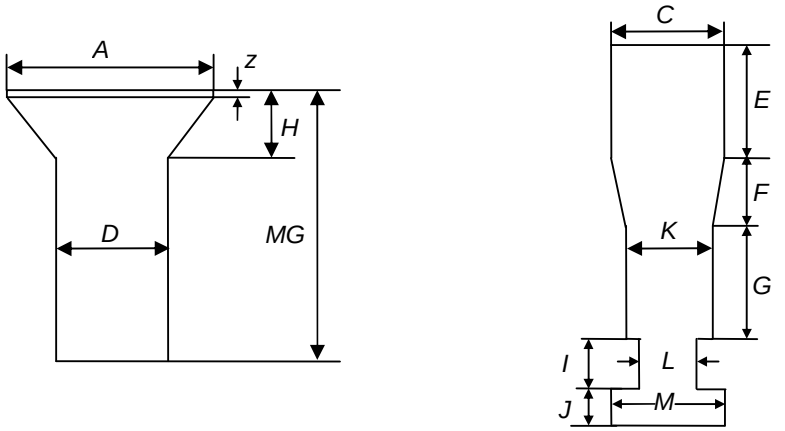

a) Bolt *b) Nut*

Figure I - 3 Bolt and nut geometry

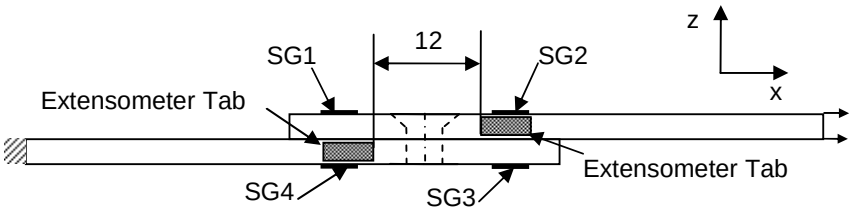

Figure I - 4 Strain gauge numbering and extensometer tab location (mm)

Table I - 4 shows the test matrix used in the experimental program. A total of 21 single lap and 4 bearing specimens were tested.

Table I - 4 Test Matrix

Testing the effect of BT					
		BT1	BT2	BT3	Laminate thickness (mm)
Fastener	HL13-6-5	3	3	3	3.52
Testing the effect of CL					
		CL1	CL2	CL3	Laminate Thickness (mm)
Fastener	HL13-6-5	3	3	3	3.52
Testing the effect of HT					
		HT1	HT2	HT3	Laminate thickness (mm)
	HL13-8-5			3	3.52
	HL13-6-4	3			3.08
Fastener	HL13-6-5		3		3.52

To best utilise the available material, it was decided to use a panel size of 350 mm x 350 mm. Each panel consists of 8 plies across the width and 2 plies along the length. A 20 mm run-off along all the edges and 5 mm gap between plies was assumed to have good quality specimen and to account for cutting tool respectively. The details of panel layout and cutting plan are shown in Figure I - 5 and Figure I - 6 respectively. The material required to manufacture the laminates can be calculated as follows:

Across the width = 20 + 8(32+5) + 20

= 336 mm

Along the length = 20 + 2(152.4) +5 + 20

= 349.8 mm

Total number of panels

= Number of plies per joint specimen x total number of joint specimen / (number of joint specimen per panel)

= (16 x 21 / 8)

= 42 panels

Number of 0/90 panels = 21

Number of +45/-45 panels = 21

Total material required = Length x width

= 6.75*1.2

= 8.1 m^2

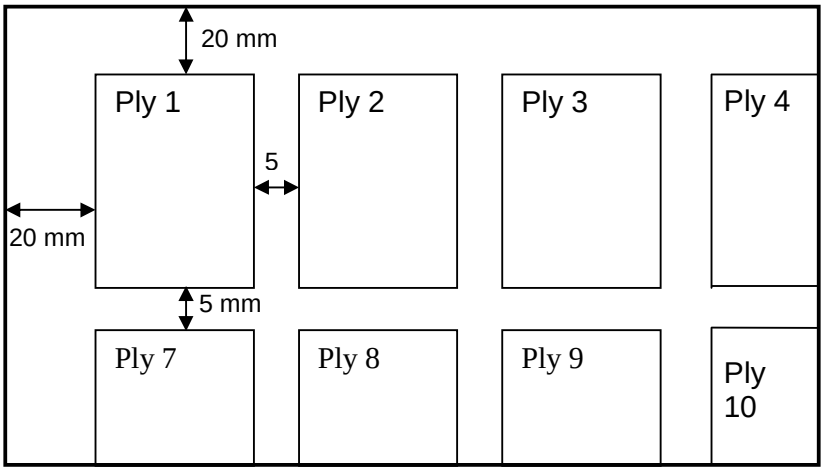

Figure I - 5 Detailed layout of a panel

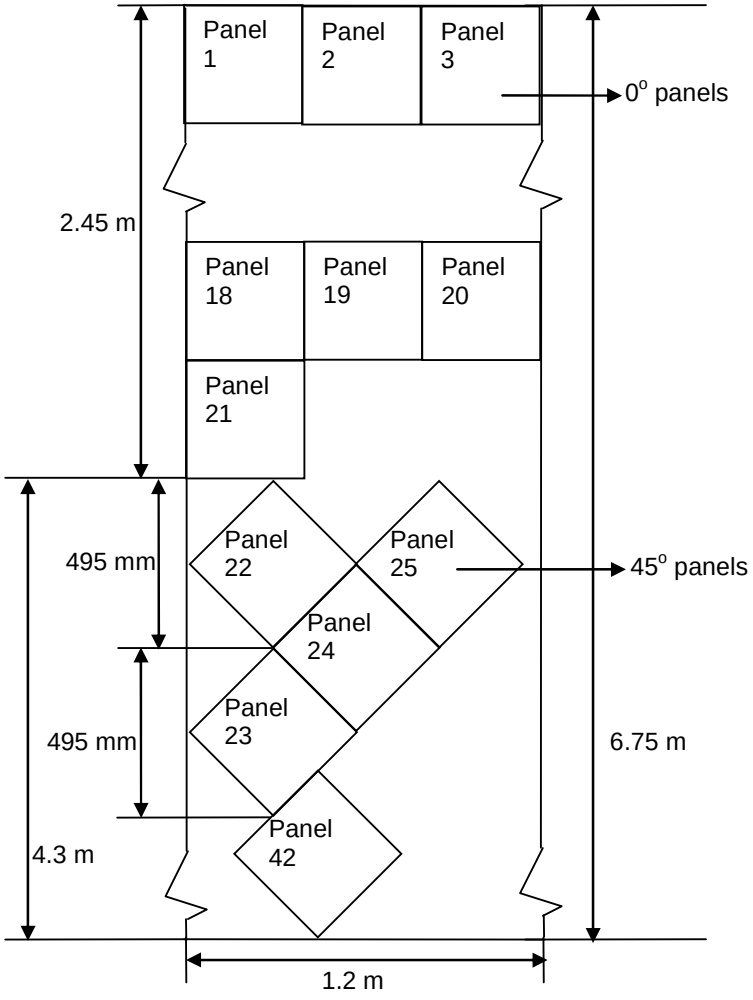

Figure I - 6 Panel cutting plan

II. Specimen Manufacturing

This section describes laminate manufacturing, specimen preparations (hole drilling, strain gauge attachment, torque wrench calibration and creating clearance holes) and final joint assembly.

I.I.I. Laminate manufacturing

The composite panels were manufactured using a vacuum bagging processes. To minimise the chances of air entrapment a roller was used at every layer and the lay-up was debulked after every fourth ply as shown in Figure I - 7. The debulking was done for approximately 2-3 minutes. The debulking also improved the interlaminar cohesion during the curing process. After the lay-up the laminate was cured in an autoclave using a vacuum bagging process. A thick aluminium plate was used as tool on which the laminates were cured. The quality of the laminate surface was determined by the tool; therefore it was important to ensure high quality of tool surface. Before the laminate was placed on the tool, a release film was placed on the tool surface. This film ensured an easy release of the laminate from the tool and prevented any contamination of the metal surface by the resin of the pre-preg material. It was important to ensure the release film did not have any contaminant and was perfectly straight so that contaminants or wrinkles on the film were not imprinted on the surface of the laminate.

The prepared laminate was placed on the top of the release film. A peel ply was used to provide a smooth surface finish. Another layer of release film was placed on the top of the laminate or the peel ply. A layer of breather cloth was placed on the top of the second release film. The breather cloth is a thick felt-like cloth that provided a continuous air path for pulling the air from the bag as well as a cushion which prevented air from being trapped. It also allowed the extra resin to bleed out during the curing process. A vacuum bag was then placed on the top of the breather cloth and the bag was sealed using a sealant tape. Before the vacuum bag was sealed the vacuum port was placed slightly away from the panels to prevent any damage to the panels. A schematic of the vacuum bagging process prior to curing is shown in Figure I - 8. The laminate was cured in an autoclave using the curing cycle shown in Figure I - 9.

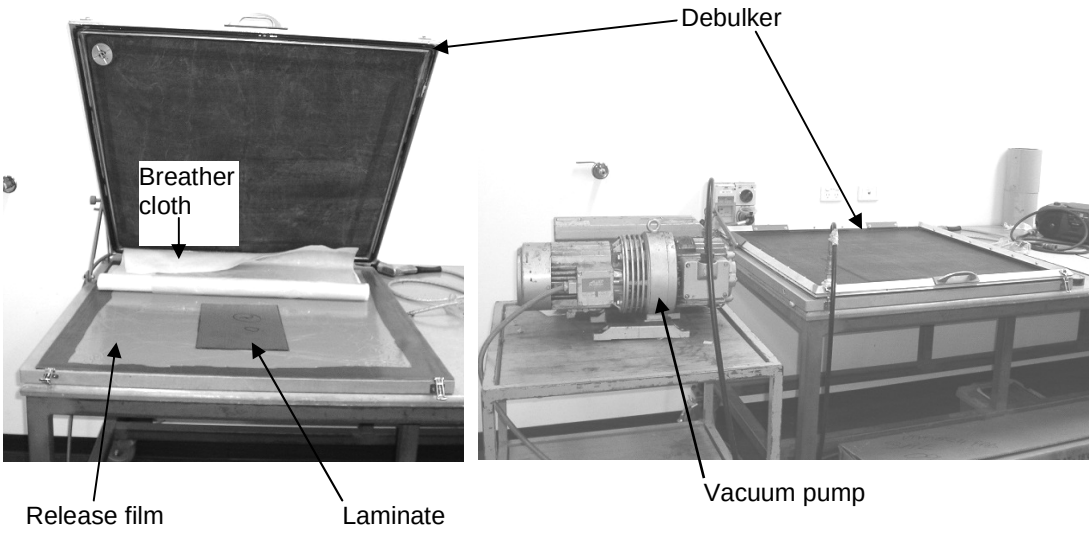

Figure I - 7 Debulking of the laminate

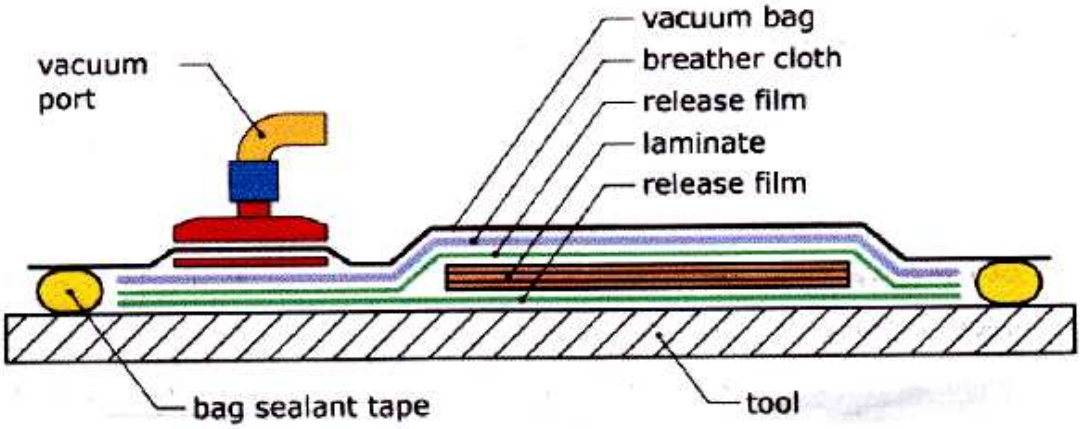

Figure I - 8 Vacuum bagging (Basso 2006)

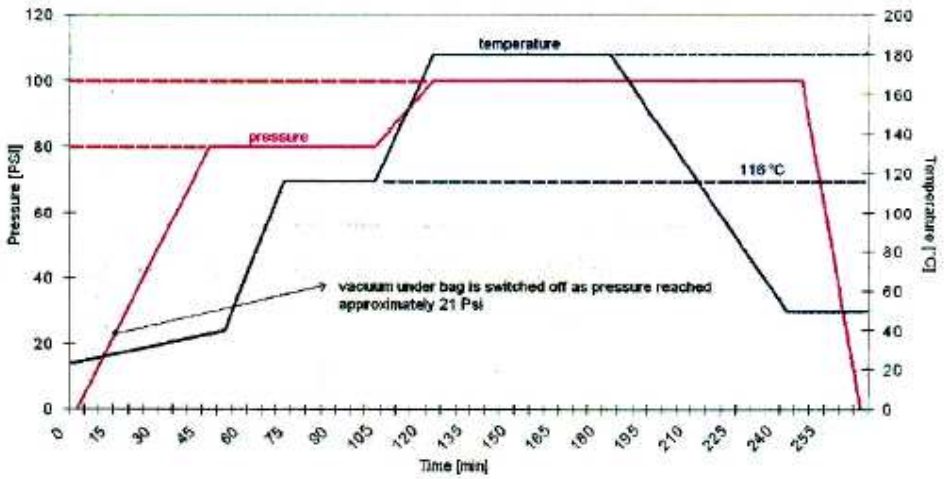

Figure I - 9 Autoclave curing cycle (Basso 2006)

After all the specimens were labelled, holes were drilled at the specified location. The holes were drilling in the following sequence:

- Straight shank hole
- Countersinking
- Over sizing

A simple hole drilling rig shown in Figure I - 10 was designed to achieve high quality holes. The laminate was fixed between the holding plates to stop any lateral movement while drilling and it was pushed down during drilling to stop any vertical motion. The rig was fixed to the drilling machine to provide accurate, repeatable hole location. The base plate also prevented any fibre fraying, delamination and splintering which could occur at the exit layer of the specimen if adequate support was not provided.

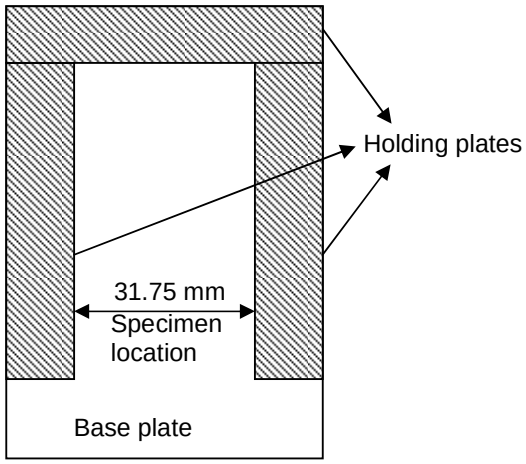

Figure I - 10 Drilling Rig (Top view)

The standard 100^{o} countersunk was created using tools specifically designed to drill composites. The depth of countersunk was adjusted such that the bolt head was perfectly aligned with the laminate surface. The clearance was created after countersinking. This was done to prevent misalignment of the countersunk due to clearance between the hole and countersinking tool guide. As can be seen in Figure I - 11, if the hole was not over sized the edges of the hole provide a guide to countersunk tool which prevented any lateral movement producing high quality countersunk holes. However, the lateral movement would occur if the hole was over sized before countersinking.

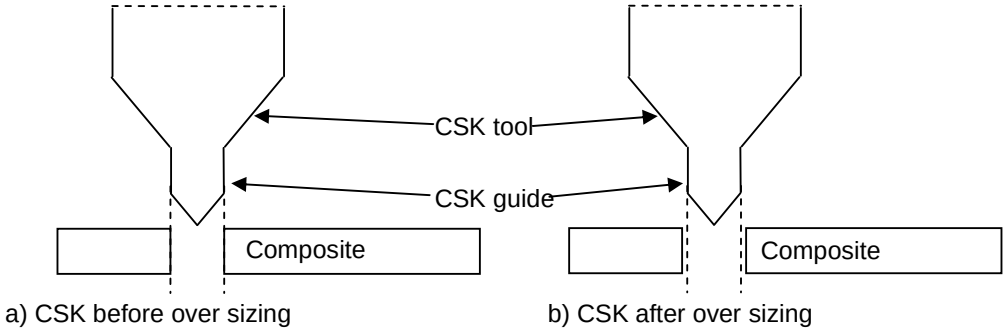

Figure I - 11 Effect of over sizing on CSK tool

I.I.II. Over sized hole

After countersunk holes were drilled, clearance specimens were over sized using high quality standard metal drill bits. The drill bits were not specially designed to be used on composites therefore a hole quality check was performed to determine if these drill bits could be used. To check the quality of the over sized hole, a microscopy comparison between the edge of the over sized hole and the edge of the non-over sized hole (drilled using special diamond tip drill bits) was done. As can be seen in Figure I - 12, the non-over sized hole edge was of high quality, as it had almost smooth edge compared to the uneven edge of untreated over sized hole.

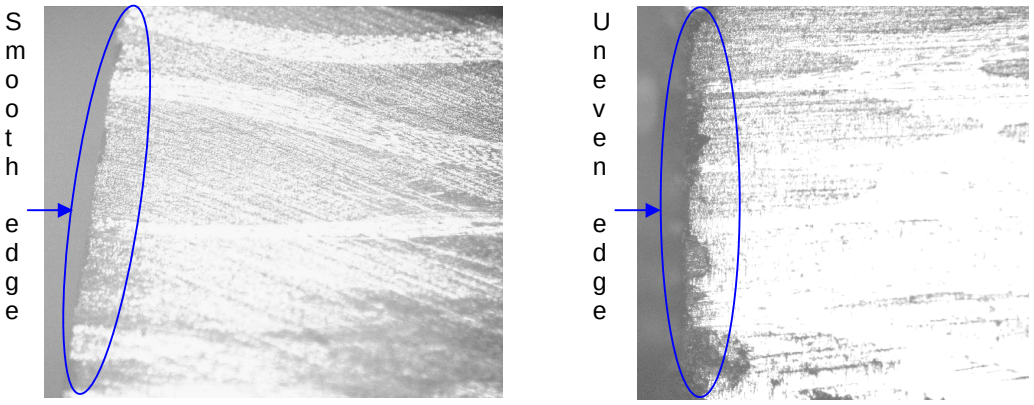

Figure I - 12 Untreated over sized edge comparison

The untreated state of the over sized hole was not acceptable for aerospace applications as the edge had several potential sites for micro crack initiation due to stress concentration in uneven regions. It was decided to sand the edge of over sized holes to remove the unevenness. The sanded edge was termed as the “treated edge”. The process of sanding removed the features that would lead to stress concentration and

crack initiation at the edge. The treated and non-over sized hole edges are compared in Figure I - 13. The over sized treated edge was smoother than the non-over sized edge.

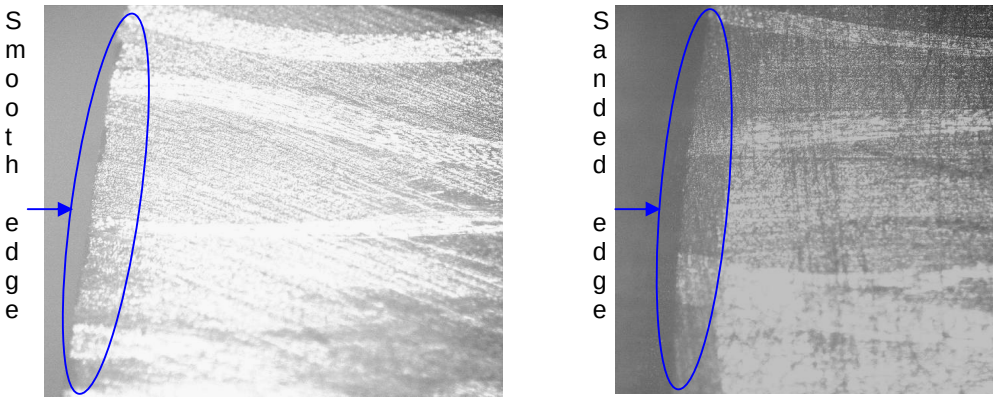

a) Non-over sized hole edge b) Treated over sized hole edge

Figure I - 13 Treated over sized edge comparison

Based on the above study, the over-sizing was done in two steps. The first step involved drilling the hole using standard drill bits. In the second step the hole surface was sanded to provide a smooth finish. The sanding was performed as shown in Figure I - 14. To get even surface finish along the thickness of the hole, the tool was rotated about its axis while being pushed in and out of the hole. Two different sand paper grades (600 and 1200) were used to achieve an optimum result. The rough sand paper was used first to remove the larger pieces and the fine grit was used later to remove remaining small pieces and provide a smooth surface.

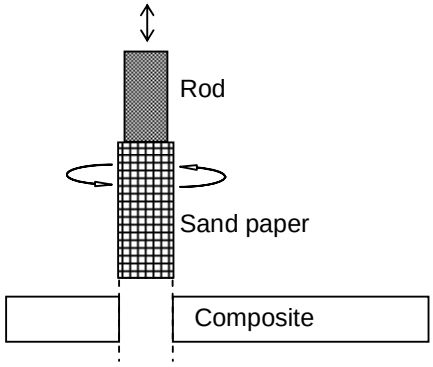

Figure I - 14 Edge sanding

I.I.III. Torque wrench calibration

As bolt torque was one of the variables in the test regime, it was important to determine the exact bolt torque. In this project a Warren and Brown® bending type torque wrench was used. A conventional torque wrench socket (see Figure I - 15) does not allow an

Allen key to pass through, which is required to assemble a Hi-Lok fastening system. Therefore a new attachment for the torque wrench was designed to allow the use of an Allen key during joint assembly. The attachment was manufactured by cutting the head from a normal spanner and drilling an attachment hole in the spanner head to attach it to the torque wrench. Comparing Figure I - 15 and Figure I - 16, it can be seen that the conventional socket covers the nut leaving no room for an Allen key, however the new attachment allowed the use of an Allen key with the torque wrench. The attachments for different bolt/nut assembly are shown Figure I - 17.

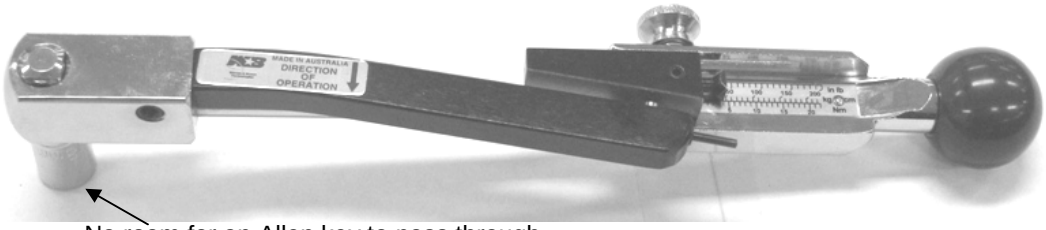

Figure I - 15 Conventional torque wrench

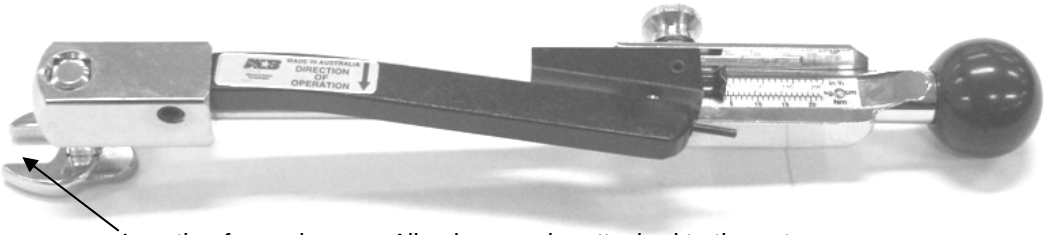

Figure I - 16 Modified torque wrench

Figure I - 17 Attachments for different bolt/nut assemblies

The new attachment increased the length of the torque wrench by 10 mm which required slight adjustment to the calibrated scale of the torque wrench. The calibration factor was determined using a simple device capable of providing consistent and repeated torque for a given rotation. The linear stiffness of the springs was converted to torque by the use of a disc as shown in Figure I - 18. The torque rating (θ^{o}/Nm) for conventional wrench (torque

wrench with standard socket) and modified torque wrench (torque wrench with new attachment) were recorded using the designed calibration device. Multiple values were measured for different torques up to 5 Nm. The conventional torque wrench had a rating of 15.7^{o}/Nm whereas the modified torque wrench had a rating of 16.5^{o}/Nm. The adjustment factor was calculated to be 0.951. The adjusted values of torque up to 5 Nm are shown in Table I - 5.

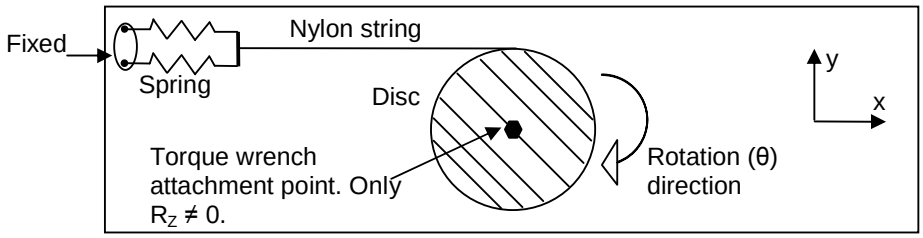

Figure I - 18 Torque wrench calibration device

Table I - 5 Torque calibration table

Conventional Wrench (Nm)	Modified Wrench (Nm)
1	1.051
2	2.103
3	3.154
4	4.206
5	5.257

APPENDIX II.

This appendix shows the stress concentration factor distribution in various plies. The locations of plies are shown in Figure II-1. The stress concentration factor was calculated using following equation:

Stress concentration factor $= \frac{Acting\ Stress}{Bearing\ Stress}$

Acting stress = Local radial or tangential stress from FE model

Bearing stress $= \frac{Acting\ load}{D * t}$

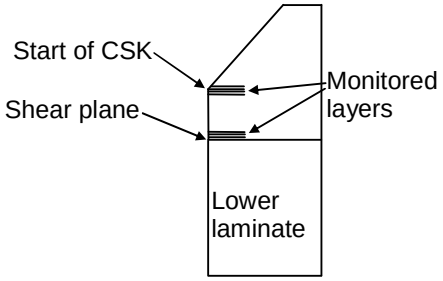

Figure II- 1 Layers used to plot stress concentration factor distribution

BT1

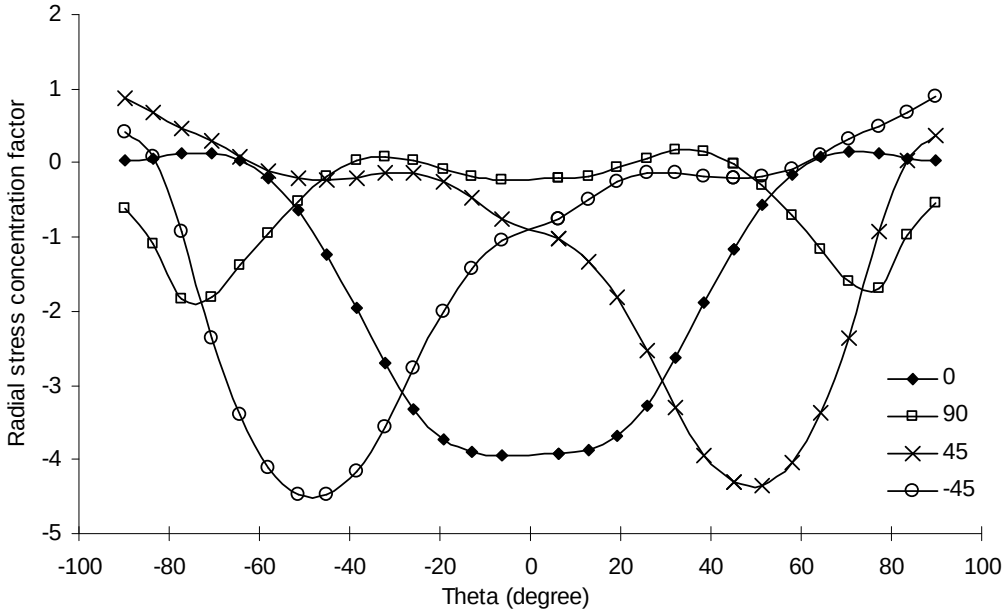

Figure II- 2 Radial stress concentration factor in shear plane of BT1 joint at ~1.5 kN

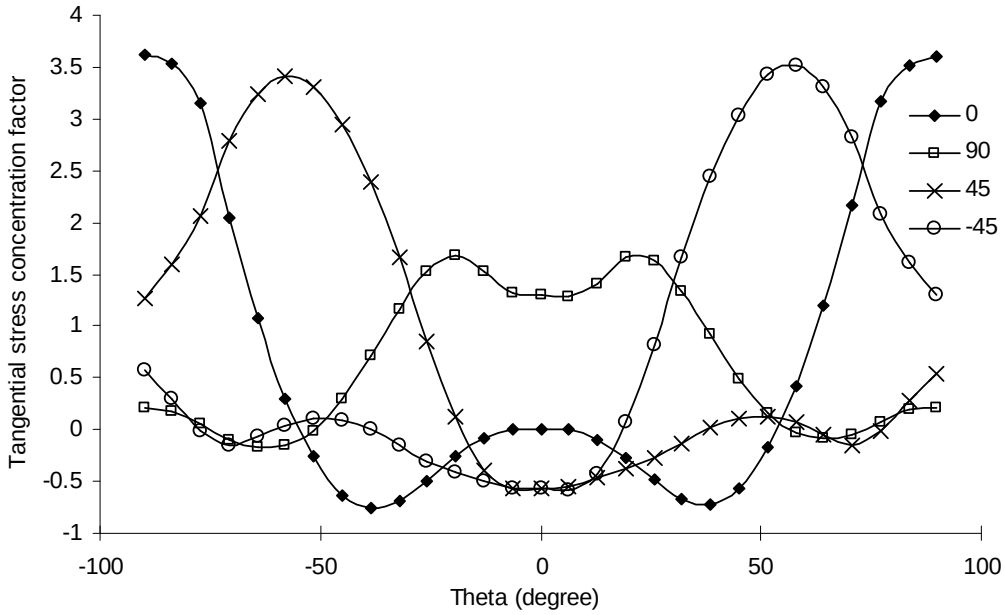

Figure II- 3 Tangential stress concentration factor in shear plane of BT1 joint at ~1.5 kN

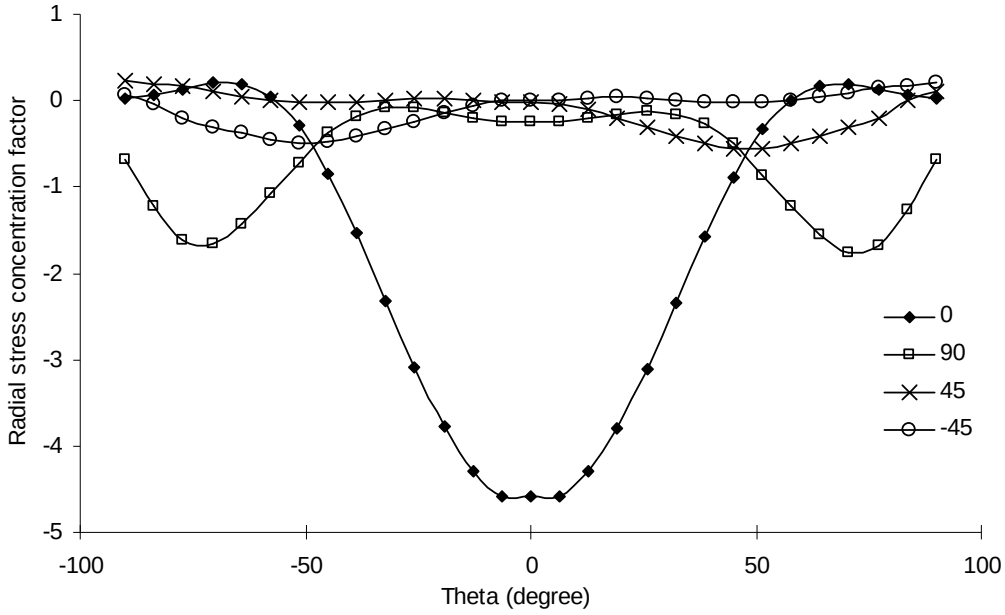

Figure II- 4 Radial stress concentration factor at start of CSK of BT1 joint at ~1.5 kN

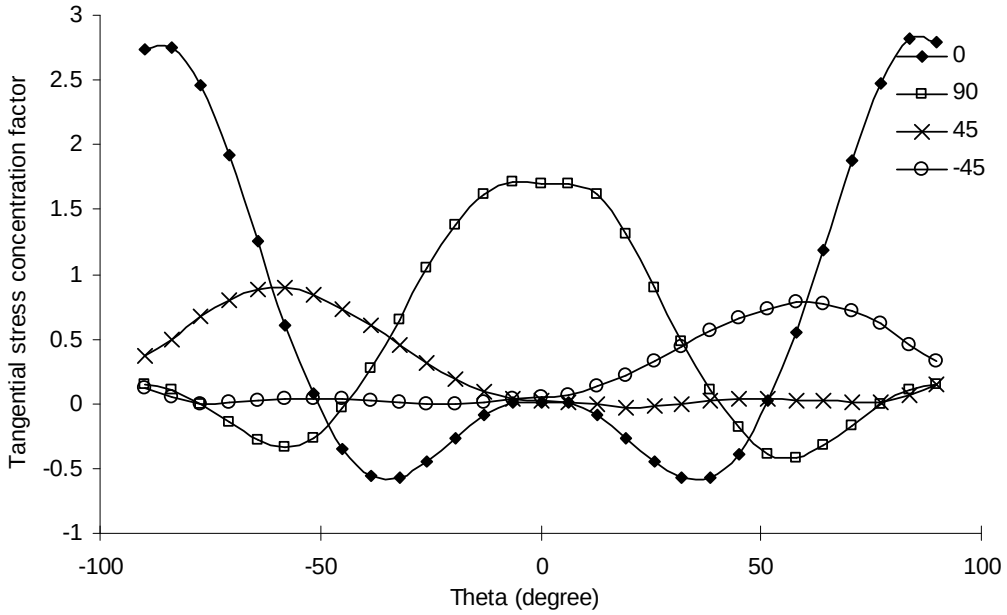

Figure II- 5 Tangential stress concentration factor at start of CSK of BT1 joint at ~1.5 kN

BT2/CL1/HT2

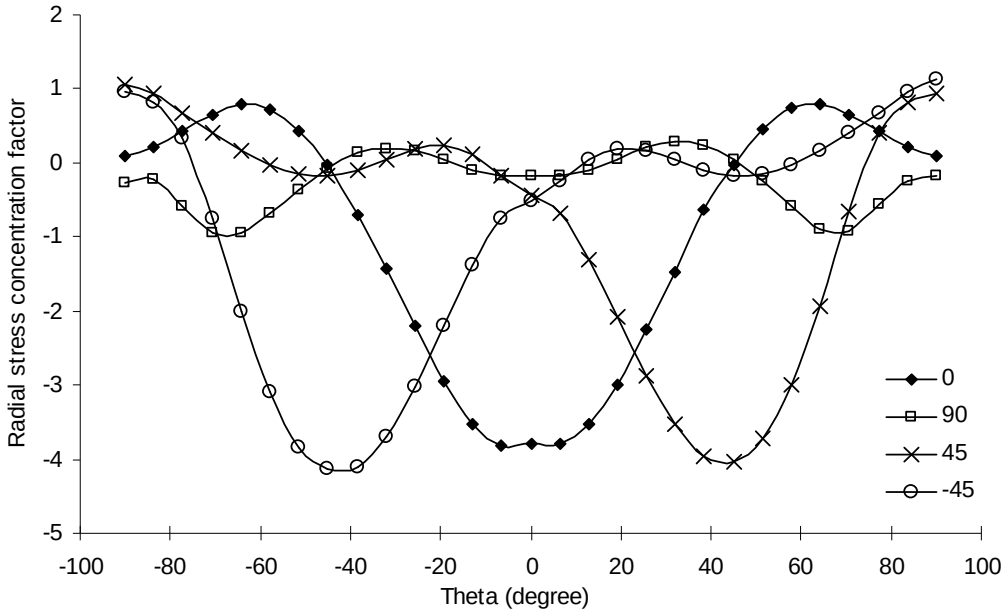

Figure II- 6 Radial stress concentration factor in shear plane of BT2 joint at ~1.5 kN

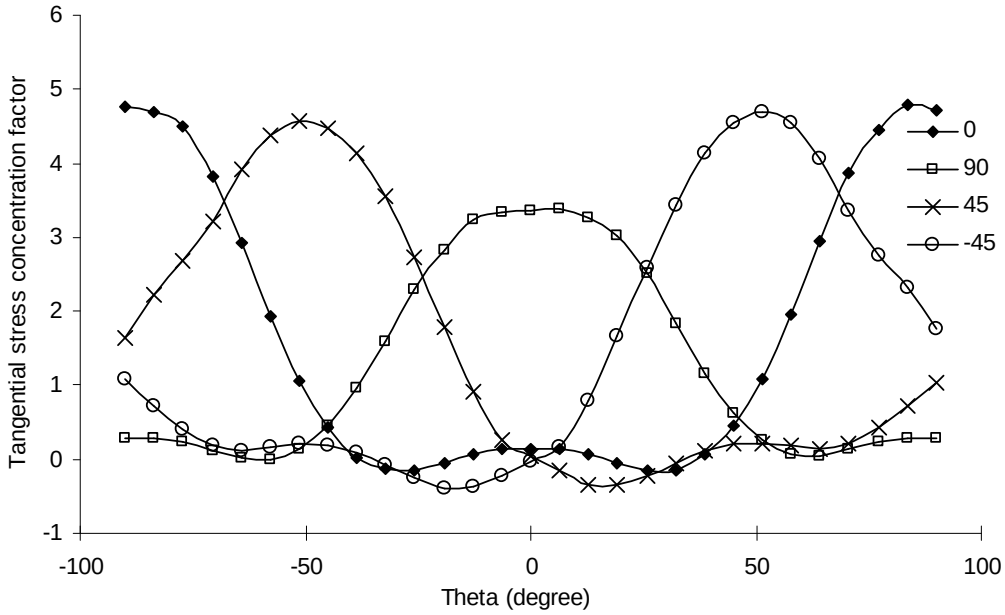

Figure II- 7 Tangential stress concentration factor in shear plane of BT2 joint at ~1.5 kN

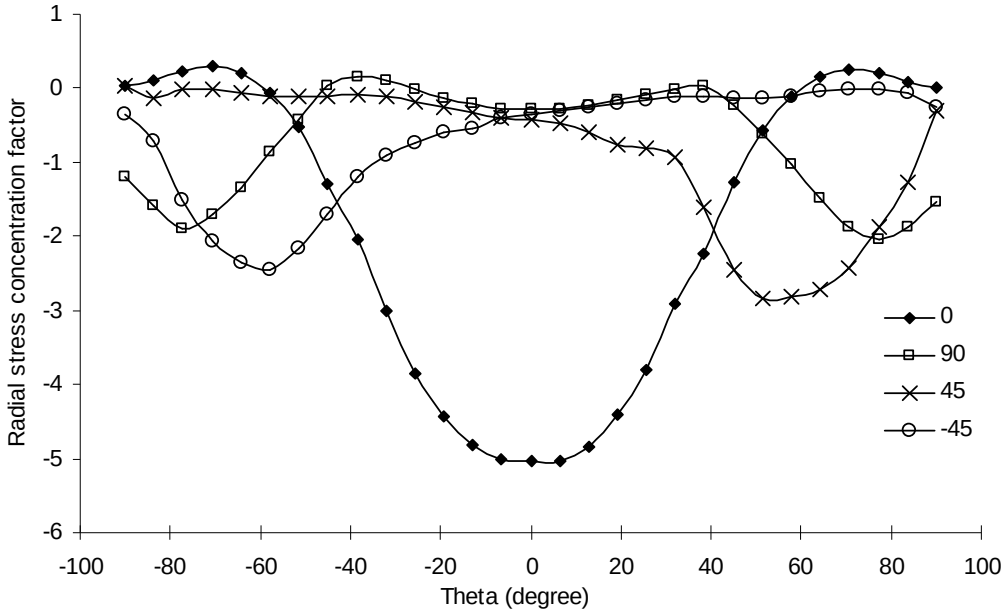

Figure II- 8 Radial stress concentration factor at start of CSK of BT2 joint at ~1.5 kN

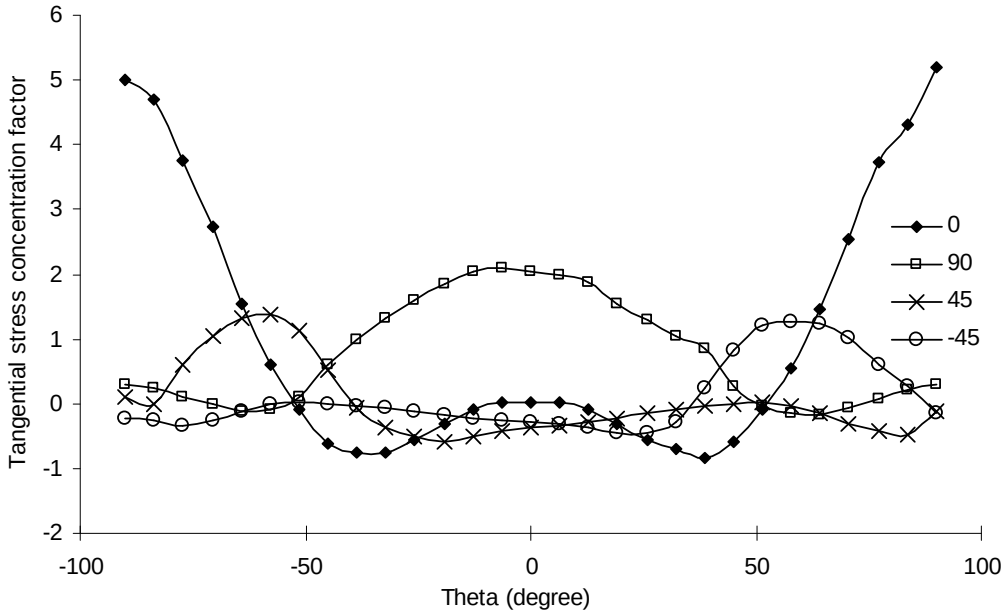

Figure II- 9 Tangential stress concentration factor at start of CSK of BT2 joint at ~1.5 kN

BT3

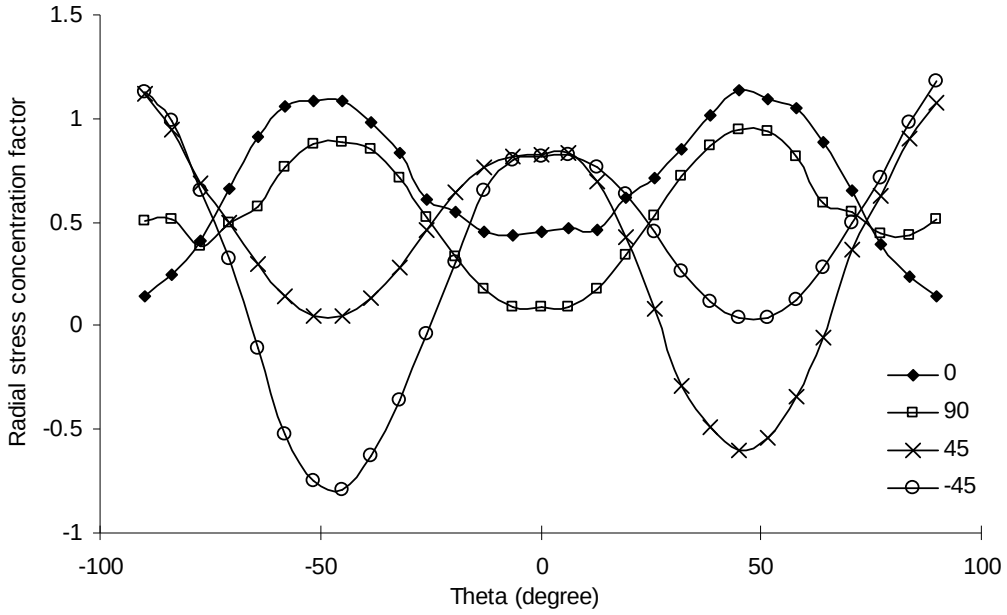

Figure II- 10 Radial stress concentration factor in shear plane of BT3 joint at ~1.5 kN

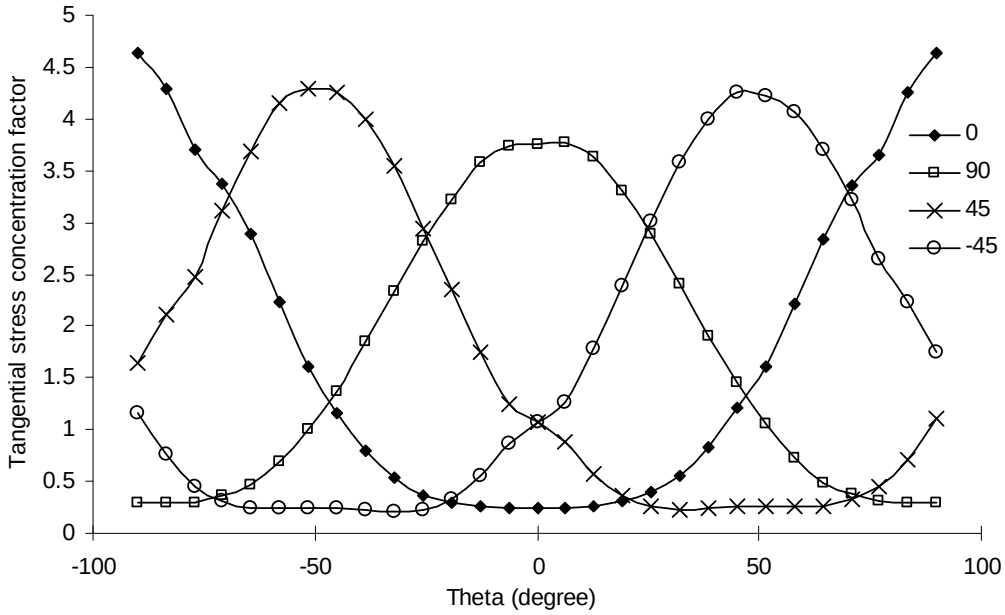

Figure II- 11 Tangential stress concentration factor in shear plane of BT3 joint at ~1.5 kN

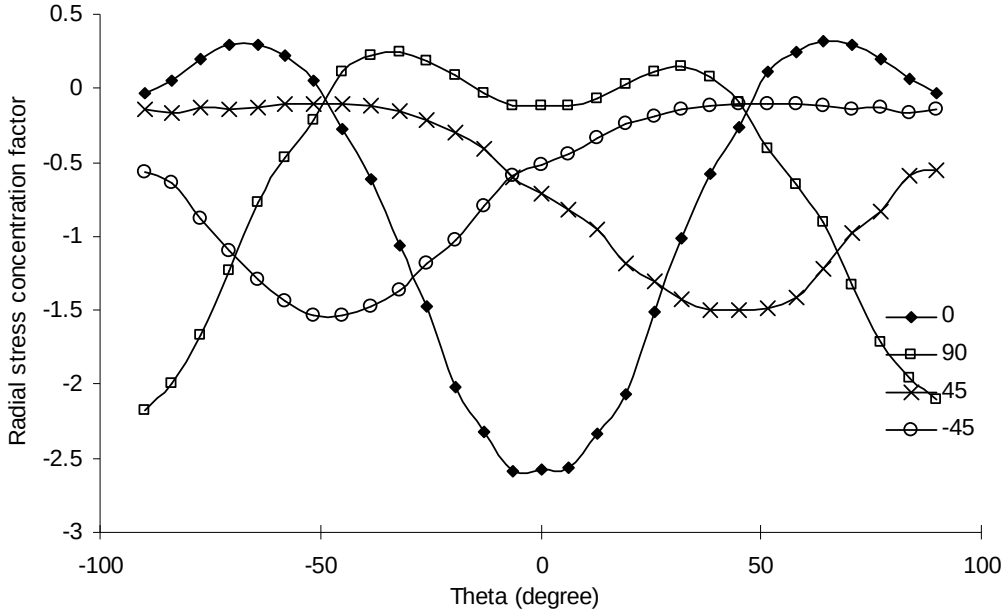

Figure II- 12 Radial stress concentration factor at start of CSK of BT3 joint at ~1.5 kN

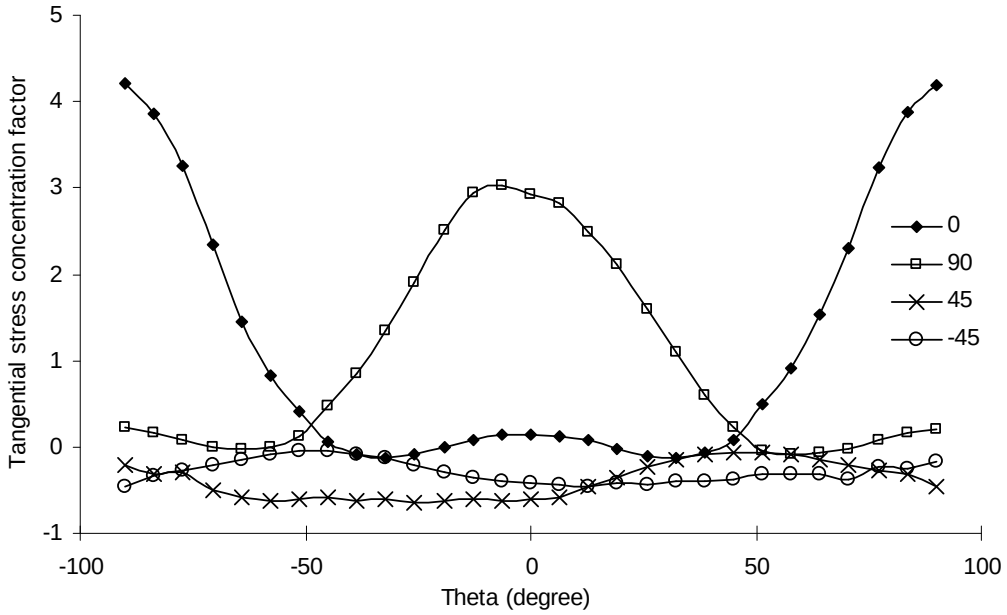

Figure II- 13 Tangential stress concentration factor at start of CSK of BT3 joint at ~1.5 kN

CL2

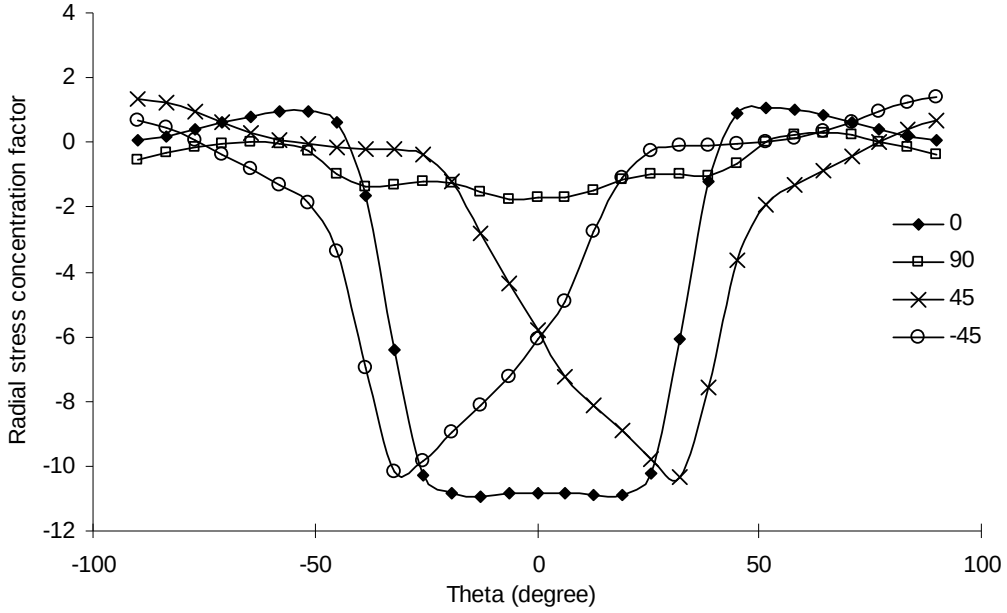

Figure II- 14 Radial stress concentration factor in shear plane of CL2 joint at ~1.5 kN

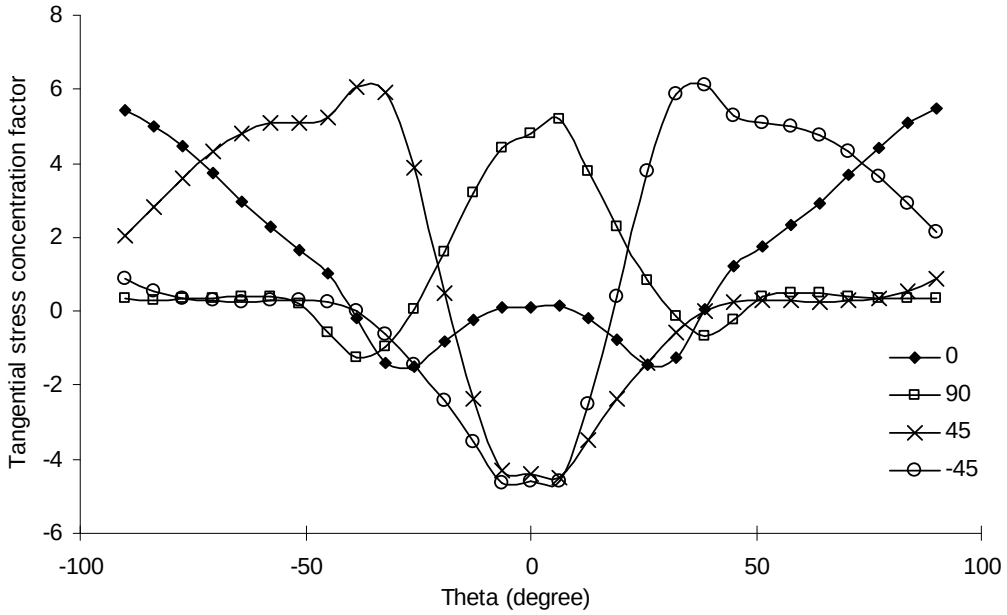

Figure II- 15 Tangential stress concentration factor in shear plane of CL2 joint at ~1.5 kN

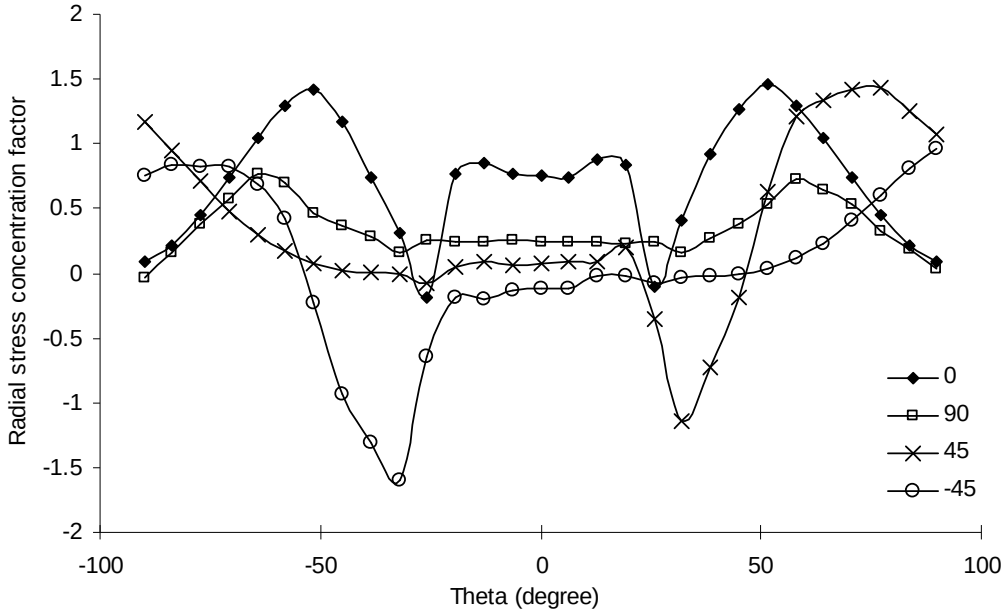

Figure II- 16 Radial stress concentration factor at the start of CSK of CL2 joint at ~1.5 kN

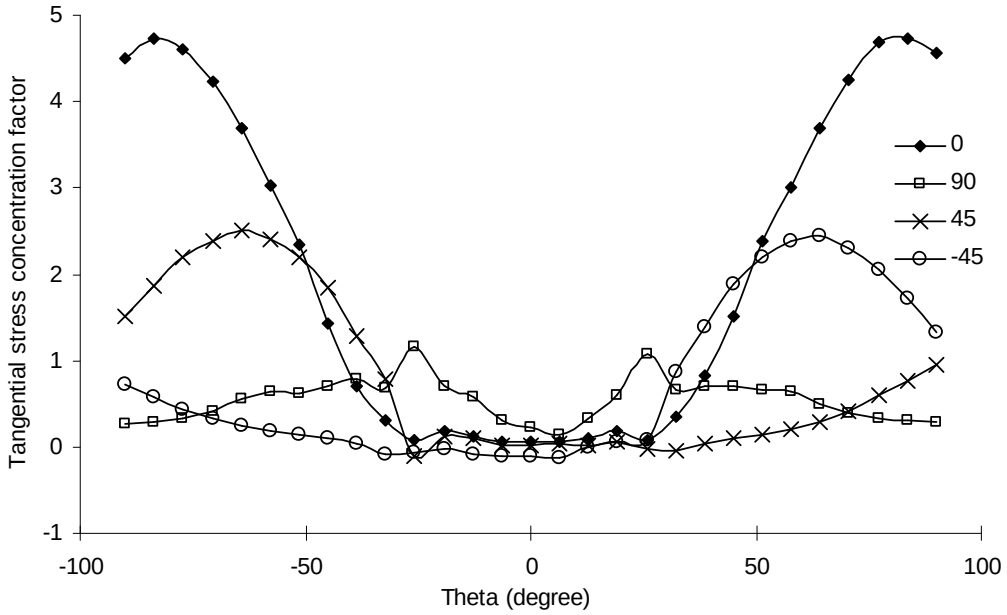

Figure II- 17 Tangential stress concentration factor at the start of CSK of CL2 joint at ~1.5 kN

CL3

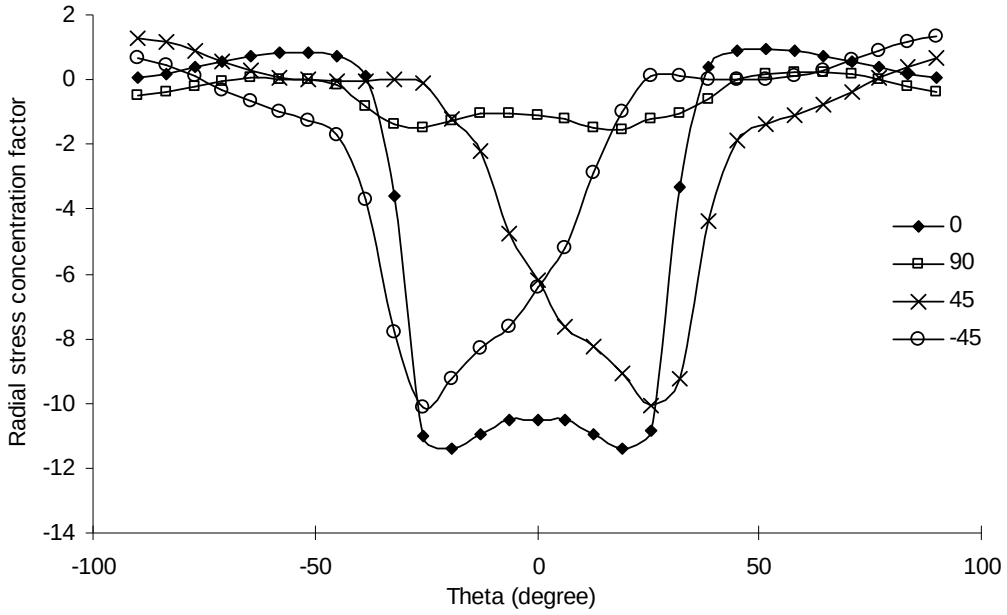

Figure II- 18 Radial stress concentration factor in shear plane of CL3 joint at ~1.5 kN

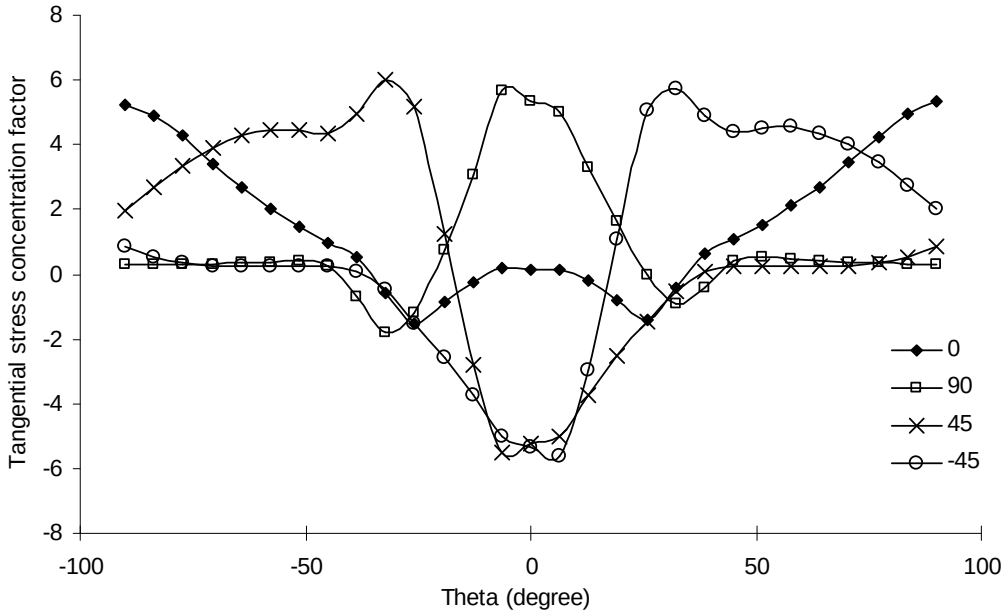

Figure II- 19 Tangential stress concentration factor in shear plane of CL3 joint at ~1.5 kN

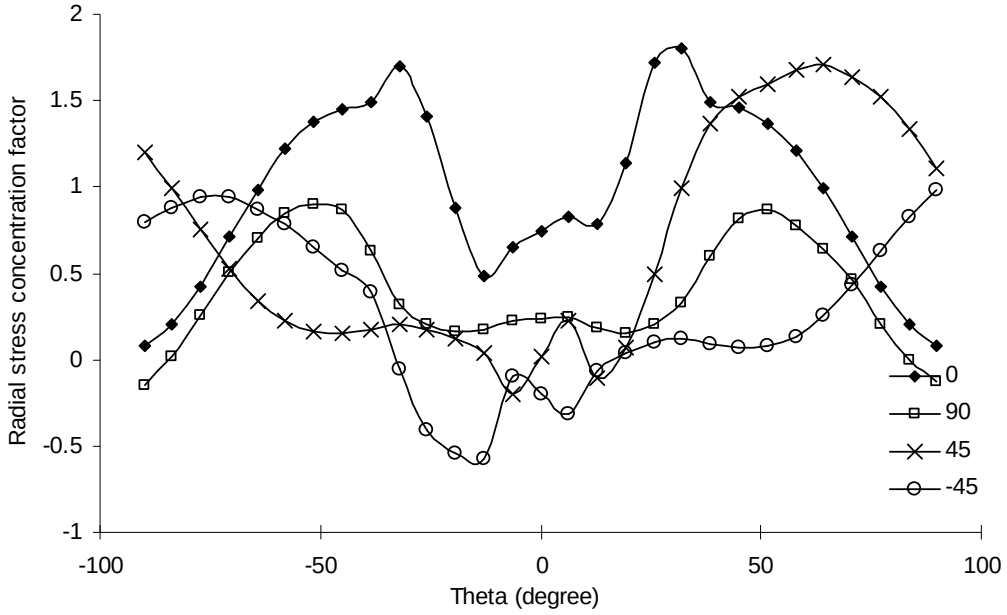

Figure II- 20 Radial stress concentration factor at the start of CSK of CL3 joint at ~1.5 kN

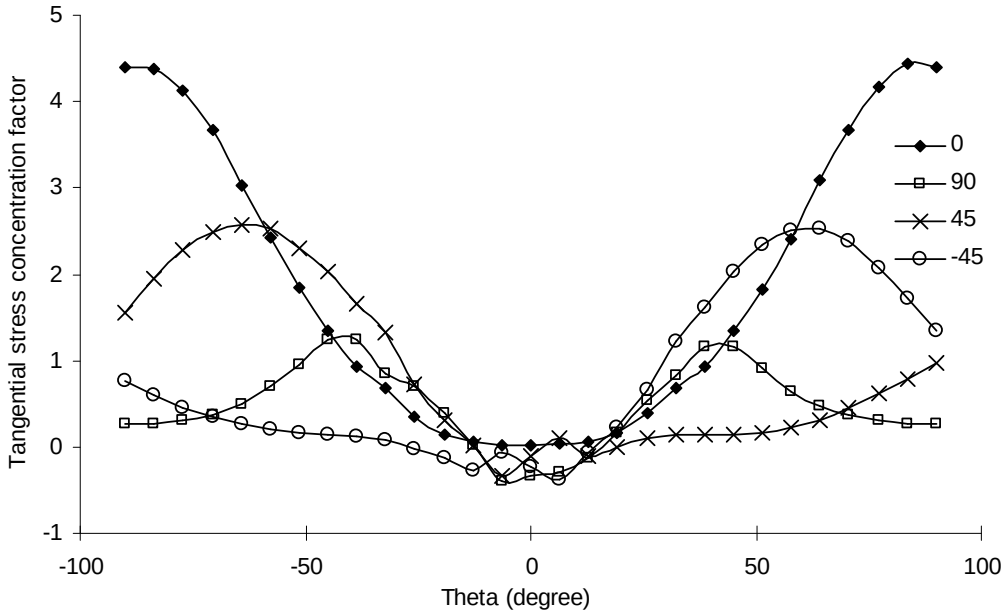

Figure II- 21 Tangential stress concentration factor at the start of CSK of CL3 joint at ~1.5 kN

HT1

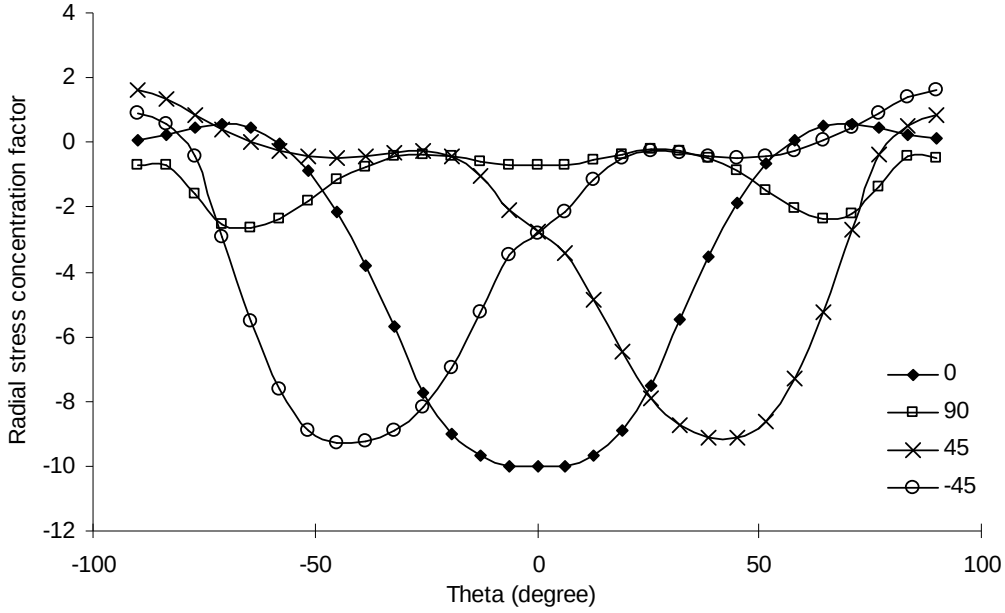

Figure II- 22 Radial stress concentration factor in shear plane of HT1 joint at ~1.5 kN

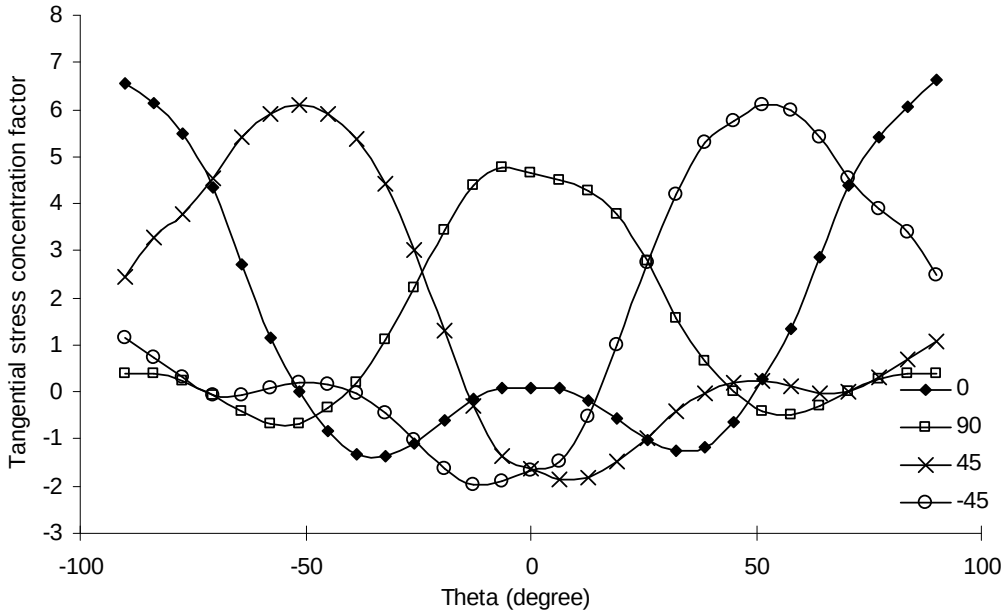

Figure II- 23 Tangential stress concentration factor in shear plane of HT1 joint at ~1.5 kN

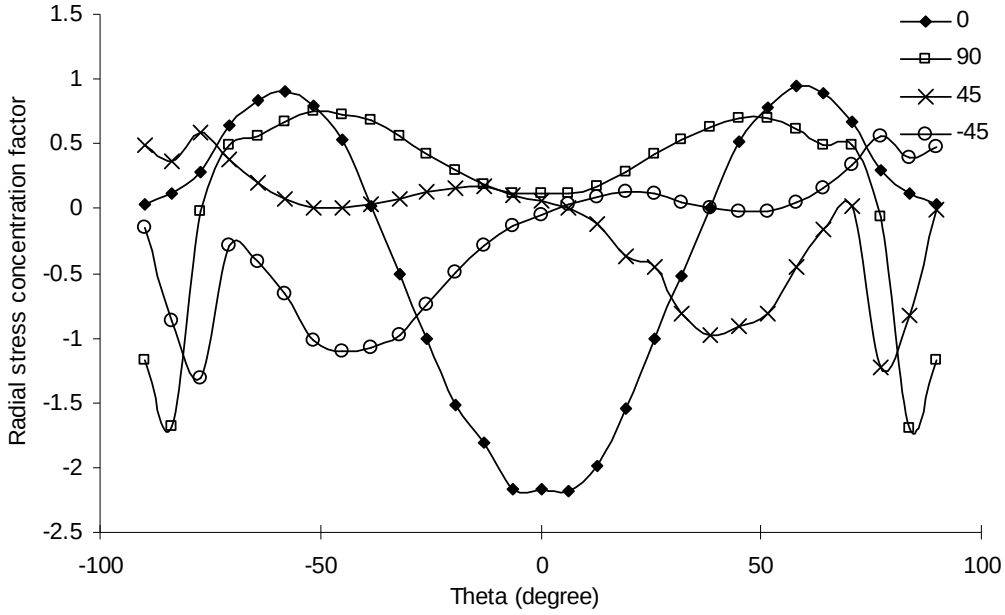

Figure II- 24 Radial stress concentration factor at the start of CSK of HT1 joint at ~1.5 kN

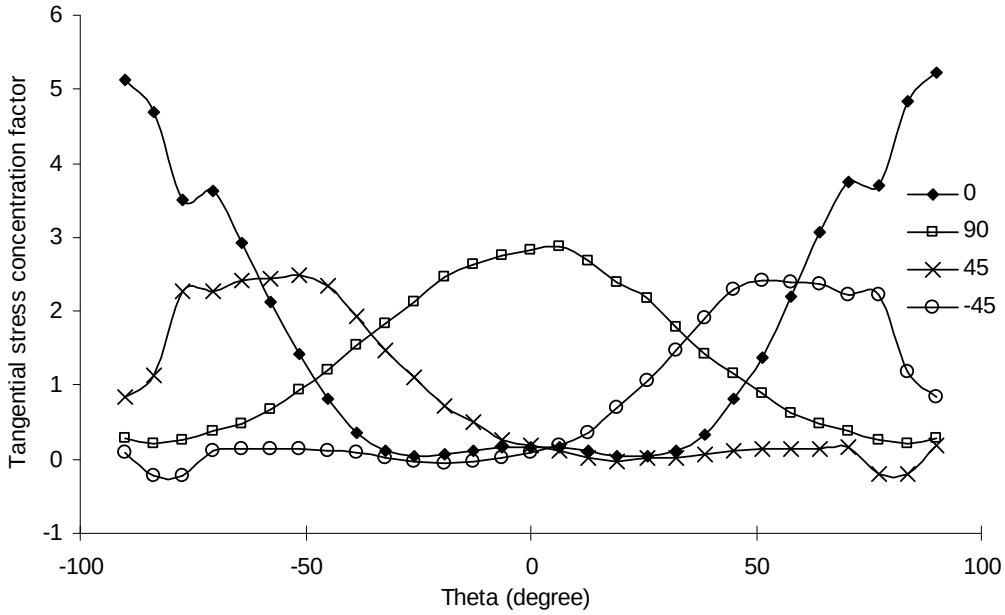

Figure II- 25 Tangential stress concentration factor at the start of CSK of HT1 joint at ~1.5 kN

HT3

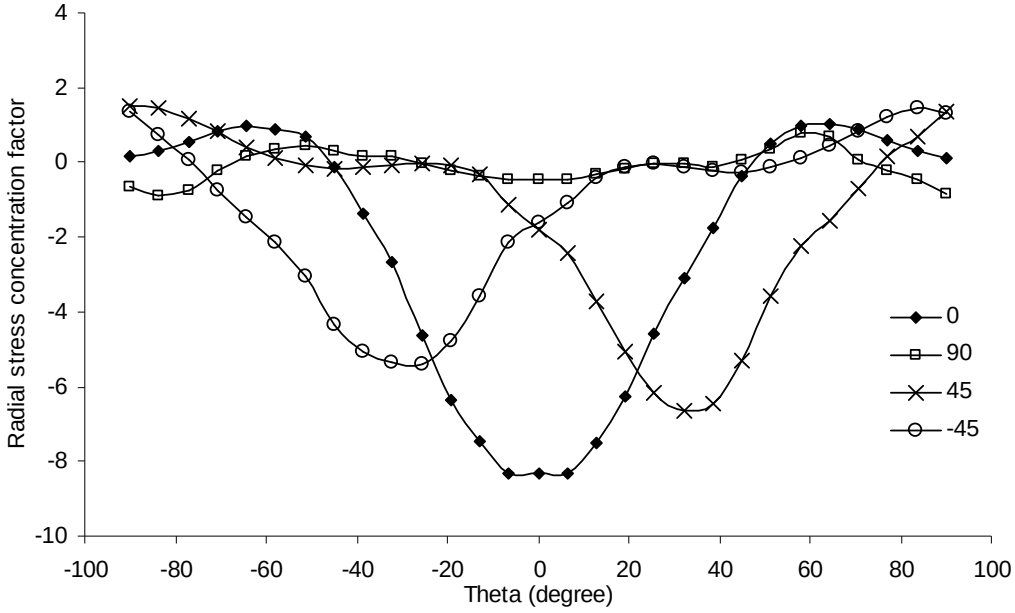

Figure II- 26 Radial stress concentration factor in shear plane of HT3 joint at ~1.5 kN

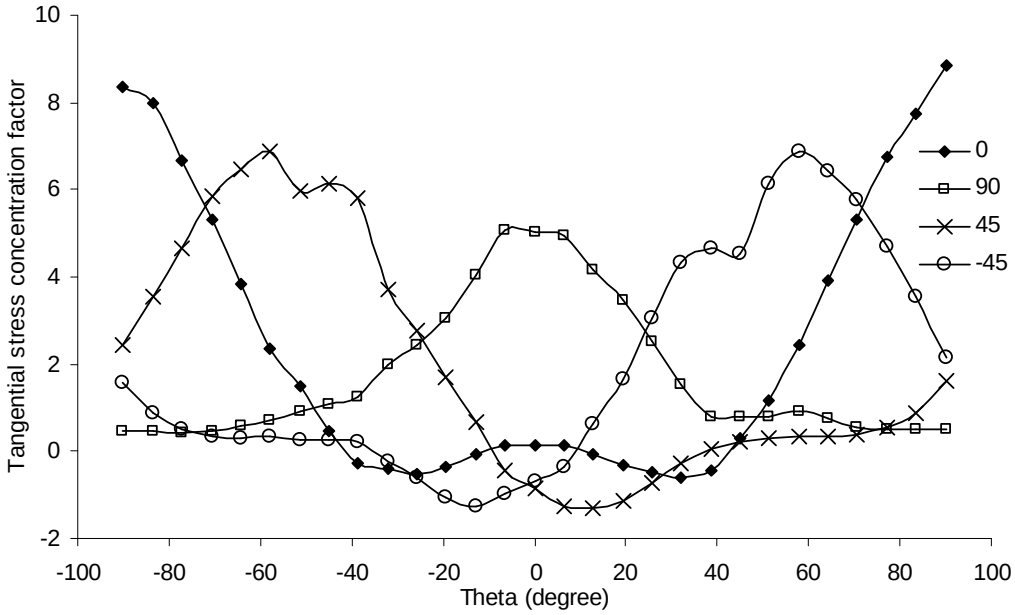

Figure II- 27 Tangential stress concentration factor in shear plane of HT3 joint at ~1.5 kN

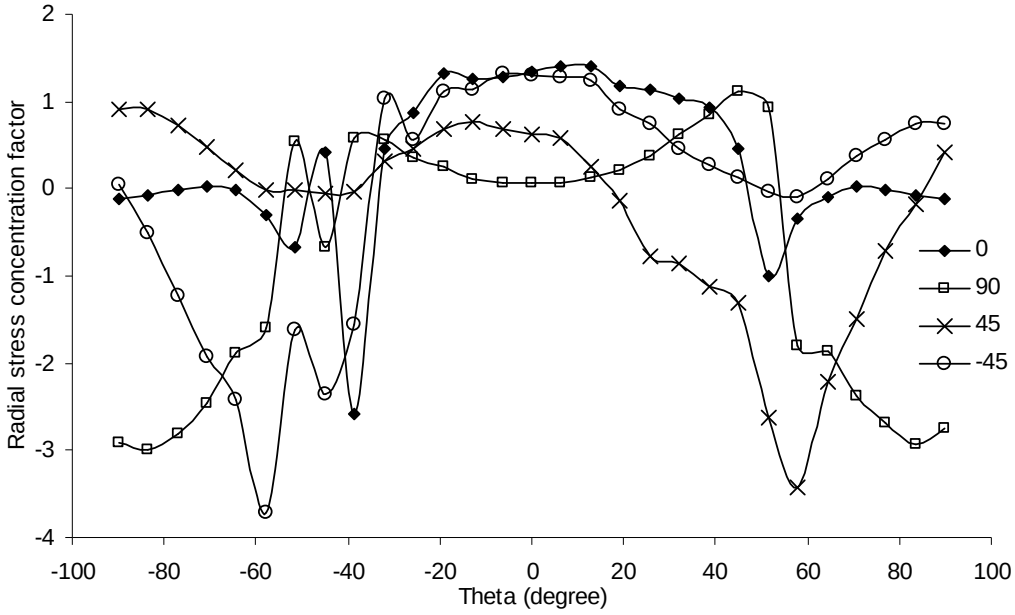

Figure II- 28 Radial stress concentration factor at the start of CSK of HT3 joint at ~1.5 kN

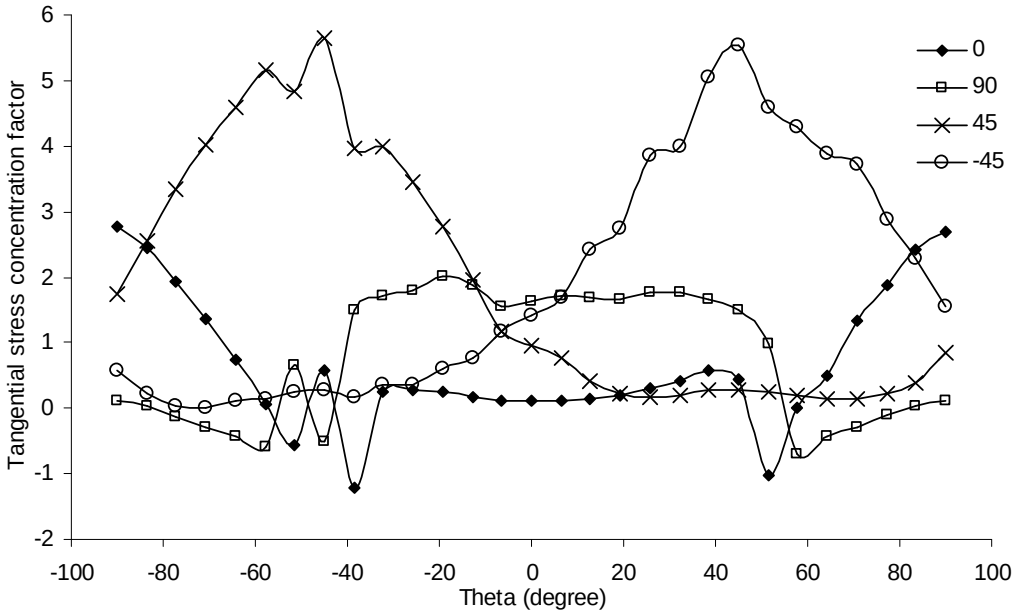

Figure II- 29 Tangential stress concentration factor at the start of CSK of HT3 joint at ~1.5 kN

HT3FE

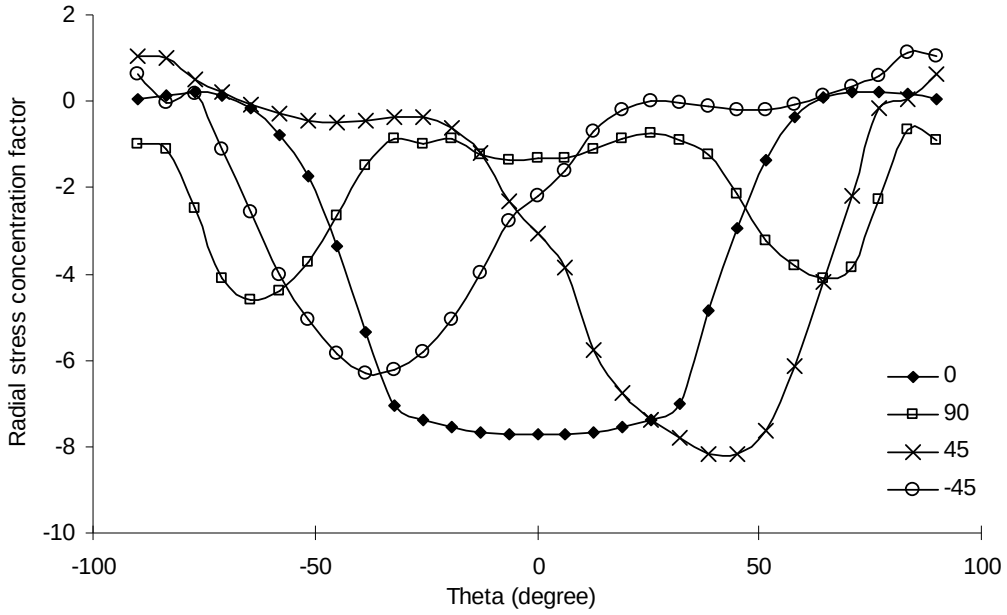

Figure II- 30 Radial stress concentration factor in shear plane of HT3FE joint at ~1.5 kN

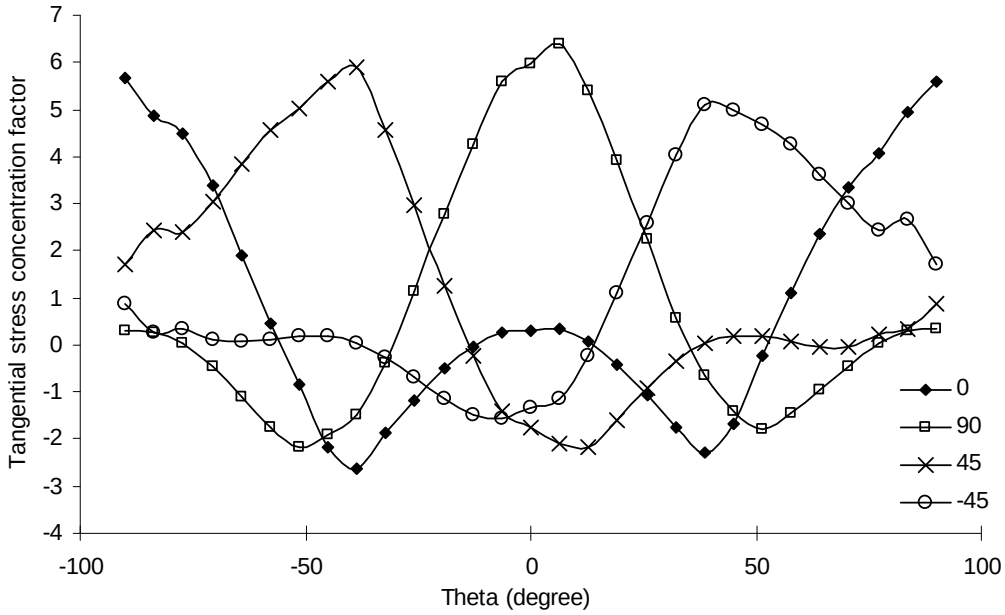

Figure II- 31 Tangential stress concentration factor in shear plane of HT3FE joint at ~1.5 kN

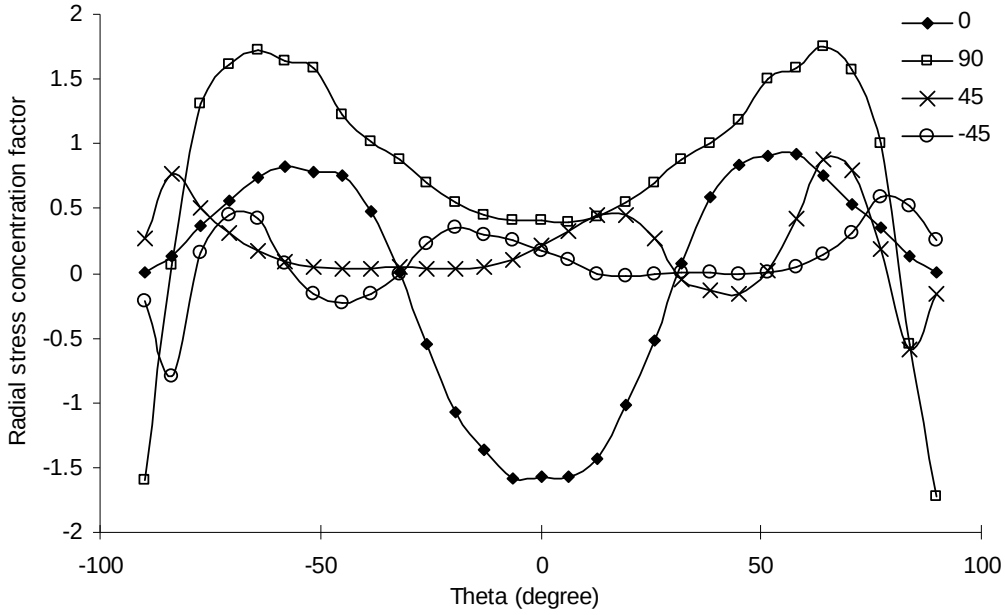

Figure II- 32 Radial stress concentration factor at the start of CSK of HT3FE joint at ~1.5 kN

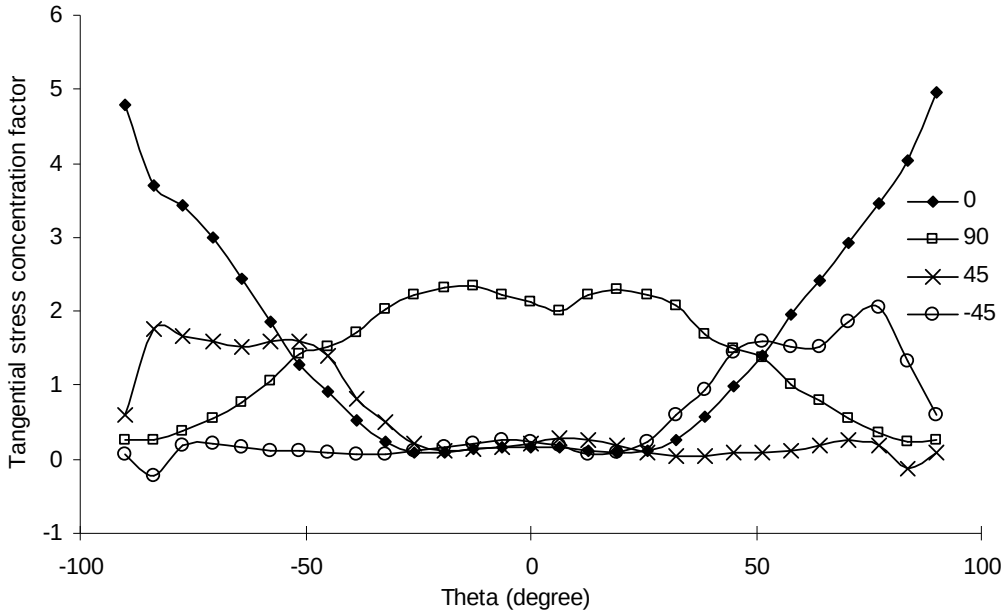

Figure II- 33 Tangential stress concentration factor at the start of CSK of HT3FE joint at ~1.5 kN